



HAL
open science

Modeling and identification of the constitutive behaviour of magneto-rheological elastomers

Jean-Pierre Voropaieff

► **To cite this version:**

Jean-Pierre Voropaieff. Modeling and identification of the constitutive behaviour of magneto-rheological elastomers. Solid mechanics [physics.class-ph]. Université Paris Saclay (COMUE), 2018. English. NNT: 2018SACLX051 . tel-01968073

HAL Id: tel-01968073

<https://pastel.hal.science/tel-01968073>

Submitted on 2 Jan 2019

HAL is a multi-disciplinary open access archive for the deposit and dissemination of scientific research documents, whether they are published or not. The documents may come from teaching and research institutions in France or abroad, or from public or private research centers.

L'archive ouverte pluridisciplinaire **HAL**, est destinée au dépôt et à la diffusion de documents scientifiques de niveau recherche, publiés ou non, émanant des établissements d'enseignement et de recherche français ou étrangers, des laboratoires publics ou privés.

Modeling and identification of the constitutive behaviour of magnetorheological elastomers

Thèse de doctorat de l'Université Paris-Saclay
préparée à l'École Polytechnique

Ecole doctorale n°579 Sciences mécaniques et énergétiques, matériaux et
géosciences (SMEMAG)
Spécialité de doctorat : Mécanique des Solides

Thèse présentée et soutenue à Palaiseau, le 14/09/2018, par

JEAN-PIERRE VOROPAIEFF

Composition du Jury :

Michel JABBOUR Enseignant Chercheur, École Polytechnique (LMS)	Président
Pedro REIS Professeur, EPFL (FLEXLAB)	Rapporteur
Jean-Claude MICHEL Directeur de recherche, CNRS (LMA)	Rapporteur
Sundeeep KANKANALA PhD, World Wide Vice-President of Becton Dickinson Medical R&D	Examinateur
Laurence BODELOT Maître de conférence, École Polytechnique (LMS)	Directeur de thèse
Nicolas TRIANTAFYLLIDIS Directeur de recherche, CNRS (LMS)	Directeur de thèse
Kostantinos DANAS Chargé de recherche, CNRS (LMS)	Invité

Modeling and identification of the constitutive behaviour of magnetorheological elastomers

LABORATOIRE DE MECANIQUE DES SOLIDES
ECOLE POLYTECHNIQUE, PALAISEAU

PhD Student:
Jean-Pierre VOROPAIEFF

Advisors :
Laurence BODELOT

Kostantinos DANAS

Nicolas TRIANTAFYLLIDIS

Contents

I	Introduction	9
I.1	MREs among smart materials	10
I.2	Classification within MREs	10
I.3	A brief review of existing work on MREs	12
I.4	Modeling approaches	15
I.4.1	Micro-mechanically based description of MREs	16
I.4.2	Phenomenological continuum modeling	16
I.5	Difficulties associated with MRE experiments	17
I.5.1	Description of previous experimental studies on MREs	18
I.5.2	Existing attempts to experimentally characterize MREs using continuum models	20
I.6	Scope and organization of the present thesis	21
II	Experimental investigation of the coupled magneto-mechanical behavior in magnetorheological elastomers	23
II.1	Introduction	24
II.1.1	Context of the study	24
II.1.2	Bibliographic background on MREs	25
II.1.3	Aim of the study and structure of the chapter	26
II.2	Physical mechanisms arising in MREs	26
II.2.1	Mechanical behavior of MREs as particle-filled composites	26
II.2.2	Magnetic response of MREs	27
II.2.3	Deformation under magnetic field	27
II.2.4	Magnetic field-dependent modulus	29
II.3	Samples	31
II.3.1	Sample shape for coupled magneto-mechanical testing	31
II.3.2	Materials	34
II.3.3	Fabrication procedure	37
II.4	Experimental methods	39
II.4.1	General setup	39
II.4.2	Mechanical diagnostics	41
II.4.3	Magnetic diagnostics	42
II.4.4	Testing protocol	44
II.5	Results and discussion	45
II.5.1	Purely mechanical testing	45

II.5.2	Coupled magneto-mechanical testing	48
II.6	Conclusions and perspectives	54
Appendix II.A	Correction of magnetic measurements	56
II.A.1	Elliptical coordinate system	56
II.A.2	Problem to solve	57
II.A.3	Resolution of Laplace equation	59
III	Modeling and Identification of the constitutive behavior of Magnetorheological Elastomers	63
III.1	Introduction	64
III.2	Experiments	66
III.2.1	Tests description	66
III.2.2	Sample design	67
III.2.3	Fabrication procedure	67
III.2.4	Measurement techniques	68
III.2.5	Experimental verification of negligible dissipation	69
III.3	Theory	71
III.3.1	Overview of governing equations	71
III.3.2	Variational formulation alternatives	74
III.3.2.a	Formulation using \mathbf{B} (free energy $\psi_B(\mathbf{F}, \mathbf{B})$)	74
III.3.2.b	Formulation using \mathbf{H} (free energy $\psi_H(\mathbf{F}, \mathbf{H})$)	77
III.3.2.c	Formulation using \mathbf{M} (free energy $\psi_M(\mathbf{F}, \mathbf{M})$)	79
III.3.3	Equivalence between formulations	82
III.3.4	Type of Energies considered	85
III.4	Numerical Implementation	88
III.4.1	Coulomb gauge for the magnetic vector potential	88
III.4.2	Boundary conditions	89
III.4.3	Symmetry conditions for the magnetic vector potential	93
III.5	Results	95
III.5.1	Free energy determination using the F-B formulation ($\psi_B(\mathbf{F}, \mathbf{B})$)	95
III.5.1.a	Purely Mechanical Experiments and FEM simulations	95
III.5.1.b	Coupled Magneto-Mechanical Experiments and FEM simulations	96
III.5.2	Predictive capabilities of the model	99
III.5.3	Free energy in other formulations (ψ_H, ψ_M)	100
III.6	Conclusions	106
Appendix III.A	Complement Theory	106
III.A.1	F-B Theory	106
III.A.2	F-H Theory	109
III.A.3	Details of Calculation	110
III.A.4	Calculation of the total stress tensor $\mathbf{\Pi}$	111
Appendix III.B	Importance of specimen geometry	113
IV	On 3D FEM finite strain formulations for magnetorheological elastomers	119
IV.1	Introduction	120

IV.2 F-B Theory	121
IV.2.1 Variational formulation	121
IV.2.2 Form of energy density functions	122
IV.2.3 Finite element discretization	123
IV.3 F-M Theory	125
IV.3.1 Variational formulation	125
IV.3.2 Form of energy density functions	126
IV.3.3 Finite element discretization	126
IV.4 Solving a boundary value problem	129
IV.4.1 Boundary conditions	129
IV.4.2 Symmetry conditions for the perturbed magnetic vector potential $\tilde{\mathbf{A}}$	129
IV.5 Code testing	131
IV.5.1 Purely mechanical patch test	131
IV.5.2 Purely magnetic patch test	134
IV.5.3 Coupled magneto-mechanical patch test on an infinite medium (uniform field case)	137
IV.5.4 Coupled magneto-mechanical patch test on a sphere (non-uniform field case)	138
IV.6 Conclusions	144
Appendix IV.A Complement for the F-B Theory	145
IV.A.1 First and second derivatives of the energy density, and of the invariants	145
IV.A.2 ABAQUS UEL implementation	149
IV.A.2.a Element jacobian and coordinate transformations	150
IV.A.2.b Derivative of matrices	151
IV.A.2.c Expression of the force vector	155
IV.A.2.d Expression of the stiffness matrix	156
IV.A.2.e Numerical Integration	157
IV.A.3 Shape functions and their derivatives for an 8-node isoparametric cubic element (C3D8)	159
IV.A.4 ABAQUS UEL implementation for a 10-node isoparametric tetrahedral element	160
Appendix IV.B Complement for the F-M Theory	163
IV.B.1 First and second derivatives of the energy density, and of the invariants	163
IV.B.2 ABAQUS UEL implementation	166
V Conclusion and perspectives	169
V.1 Conclusion	169
V.2 Future work	171

Abstract: Modeling and Identification of the constitutive behavior of Magnetorheological Elastomers

In this thesis, we study a class of ‘active materials’ called Magnetorheological Elastomers (MRE) which are ferromagnetic impregnated rubbers whose mechanical properties are altered by the application of external magnetic fields. With the purpose of characterizing the behavior of MREs up to large strains and high magnetic fields, this work brings a completely novel experimental, theoretical and numerical approach.

The first part of this study focuses on an experimental investigation of MRE where multiple microstructures (isotropic and transversely isotropic materials) and multiple particles’ volume fraction are tested. A special sample geometry is designed in order to increase the uniformity of internal magnetic and mechanical fields measured during coupled-field experiments. The interfacial adhesion between the iron fillers and the silicone matrix is investigated and we show that when specimens are subjected to external magnetic fields, a silane primer treatment of the particles is needed to prevent debonding at the interface particle/matrix. Then, we present the magneto-mechanical testing setup that allows simultaneous 3D mechanical and magnetic measurements before discussing the results. Even if it is found that instabilities are ubiquitous in MREs, lots of useful data are collected and will be used to compute the parameters proposed in the material model.

The second part of the thesis is dedicated to the modeling of isotropic MREs. The continuum description proposed by Kankanala, Triantafyllidis and Danas [90, 40, 41] to derive constitutive laws that account for finite strains is used and, in particular, the energetic approach (that requires an energy density function) is chosen. Multiple equivalent variational formulation alternatives (based on different choices of the independent magnetic variable used in the energy function: \mathbf{B} , \mathbf{H} or \mathbf{M}) are given and implemented into 3D finite element (FEM) codes. Based on the use of FEM simulation in combination with least square optimization methods, the previously collected experimental data are fitted and all three energy functions ψ_B , ψ_H and ψ_M are computed. The obtained material model proves to have excellent predictive capabilities when compared to other experiments not used in the fitting process. The use of numerical tools is necessary to make sure that the calculated material parameters are not influenced by the shape of experimental specimens.

The last part of this work details the numerical implementation of the different variational formulations. For each one of them, it is found that isoparametric elements are well suited to simulate coupled magneto-mechanical boundary value problems. We show that special care is needed when implementing variational formulations using the displacement vector and the magnetic vector potential as independent variables. Indeed, ensuring the uniqueness of the vector potential requires to numerically enforce the Coulomb gauge, which leads to numerical complications that are addressed in this thesis. Before describing the different patch tests that have been considered to validate the numerical codes, we show which are the valid boundary conditions for the magnetic vector potential and how to use the symmetry properties of a given boundary value problem to reduce its complexity and the computational resources needed to solve it.

Résumé: Modélisation et identification de la loi de comportement des élastomères Magnéto-Rhéologiques

Ce travail de thèse porte sur une catégorie de matériaux actifs dénommés Elastomères Magnéto-Rhéologiques (EMR). Ces derniers sont composés de particules micrométriques et magnétisables imprégnées dans une matrice élastomère isolante. Il est possible de modifier les propriétés mécaniques de tels matériaux en les soumettant à un champ magnétique externe. Avec pour objectif d'aboutir à une caractérisation couplée (magnéto-mécanique) du comportement des EMRs en grandes déformations et en présence de champs magnétiques élevés, ce travail propose une approche à la fois expérimentale, théorique et numérique.

La première partie de ce travail s'intéresse à des aspects expérimentaux où l'influence de la microstructure (isotrope et transverse isotrope) et l'influence de la fraction volumique de particules sont étudiées. Un échantillon dédié est développé afin d'obtenir simultanément des champs mécaniques et magnétiques les plus homogènes possibles dans celui-ci lors d'une caractérisation couplée. La question de l'adhésion interfaciale entre les particules de fer doux et la matrice en silicone est également traitée et il est montré qu'un traitement chimique des particules est nécessaire afin d'éviter toute décohésion avec la matrice lorsque le matériau est soumis à un champ magnétique externe. Avant d'analyser les données obtenues, le dispositif expérimental permettant d'obtenir de manière simultanée une mesure du champ de déformation en trois dimensions et une mesure des champs magnétiques internes, est décrit. Malgré l'ensemble des difficultés expérimentales en grande partie dûes à des phénomènes d'instabilité qui sont omniprésents chez les EMRs, de nombreuses données sont collectées et serviront à la calibration des lois de comportement.

La seconde partie de cette thèse couvre la modélisation couplée magnéto-mécanique des EMRs en s'appuyant sur le cadre théorique général des solides magnéto-élastiques proposé par Kankanala, Triantafyllidis et Danas [90, 40, 41]. En particulier, la méthode énergétique (qui s'appuie sur l'utilisation d'une fonction d'énergie libre) est préférée et des formulations variationnelles équivalentes (qui diffèrent entre elles simplement par le choix de la variable magnétique indépendante utilisée pour décrire le problème : \mathbf{B} , \mathbf{H} ou \mathbf{M}) sont proposées et implémentées dans des codes numériques 3D s'appuyant sur la méthode des éléments finis. Ces outils numériques sont combinés à la méthode de minimisation des moindres carrés afin d'obtenir l'ensemble des paramètres matériaux du modèle de comportement des EMRs. L'utilisation de simulations numériques est nécessaire car une approche purement analytique ne permettrait pas de modéliser 'l'effet de forme' observé expérimentalement. En effet, il est primordial de modéliser ce dernier car dans le cas contraire les paramètres identifiés dépendraient de la forme de l'échantillon expérimental et ne décriraient pas uniquement le matériau.

La troisième partie de cette étude décrit en détail l'implémentation numérique des différentes formulations variationnelles proposées précédemment. Dans chacun des cas, il est prouvé que l'utilisation d'éléments isoparamétriques est bien adaptée. De nombreuses difficultés numériques ont été observées dans le cas des formulations variationnelles utilisant le champ de déplacement et le potentiel vecteur magnétique comme variables indépendantes. L'ensemble de ces difficultés est surmonté dans ce travail. Par exemple, la minimisation de

l'énergie potentielle sous la contrainte imposée par la jauge de Coulomb (nécessaire pour assurer l'unicité du potentiel vecteur magnétique) est réalisée grâce à la méthode de pénalisation. Avant de décrire les différents problèmes tests utilisés pour s'assurer de la validité et de la précision des codes numériques, les différentes étapes nécessaires à la simulation d'un problème aux limites sont expliquées. Plus précisément, les questions liées aux spécificités des conditions aux limites à appliquer sur le potentiel vecteur magnétique ou encore aux conditions de symétries, sont traitées.

Acknowledgment

I would like to express my deep sense of gratitude to my supervisors at the LMS: Professor Nicolas Triantafyllidis, who indicated the right directions and helped me with his immense theoretical background. Professor Laurence Bodelot, who always was there for any questions with her accurate help and guidance during the three years of my doctoral thesis. Professor Kostas Danas, who introduced and guided me through the formulation of the FEM methodology and who was there if I had questions. I would also like to mention and thank Professor Patrick Le Tallec, head of the lab, who always showed an honest interest on the work of all the PhD students at the LMS.

I would also like to mention the very interesting weekly seminars at the LMS, the excellent courses at the Ecole Polytechnique and the well organized on-site assistance and courses of the graduate school and thank the people responsible therefore. Next, I would like to thank all engineers and technicians, who generously offered their great expertise and technical support: the mechatronic engineers Vincent De Greef especially, Hakim Gharbi and Jean-Christophe Eytard. The technicians from the machine shop François Lelong and Antoine Soler, the designing engineer Jean-Erik Guimbretière and the research engineers and specialists in Scanning Electron Microscopy Alexandre Tanguy and Simon Hallais. I would also like to thank the doctoral students and employees at the LMS for the helpful and friendly working atmosphere. Particular thanks to Alexandra Joly, Anna Johnsson, Christiane Periam and Danielle Elizabeth for their help on administration procedures.

Finally, I am so thankful to my family, especially my mother Patricia, my father Pierre, my sister Clara, and my girlfriend Di, who enormously enrich my life and without who all this wouldn't be possible. Also a big thank you to all my friends in Corsica, in France and elsewhere.

Contents

I.1	MREs among smart materials	10
I.2	Classification within MREs	10
I.3	A brief review of existing work on MREs	12
I.4	Modeling approaches	15
I.4.1	Micro-mechanically based description of MREs	16
I.4.2	Phenomenological continuum modeling	16
I.5	Difficulties associated with MRE experiments	17
I.5.1	Description of previous experimental studies on MREs	18
I.5.2	Existing attempts to experimentally characterize MREs using con- tinuum models	20
I.6	Scope and organization of the present thesis	21

Magnetorheological elastomers (MREs) are smart materials composed of an elastomeric matrix filled with magnetic particles. The combination of the magnetic characteristics of the particles and the mechanical properties of the matrix allow to obtain high level of deformations with relatively low externally applied magnetic fields. The rapid characteristic response time and the possibility to control these deformations by adjusting the applied field make these materials very promising for modern engineering applications [24]. For instance, one could envision to use MREs for the following applications: novel actuators, smart sensors, artificial muscles, sound control, shape control, product health or lifetime monitoring, etc ... (see the review by [77]). However, the efficient design of such devices is so far very limited since, to the best of our knowledge, there exists no full characterization of the magneto-mechanical properties of MREs for finite strains and high magnetic fields.

In this introductory chapter, after presenting MREs and their benefits over other types of smart materials in Section I.1, a sorting within the class of MRE is proposed in Section

I.2. The main research topics, as well as some practical use cases of MREs are presented in Section I.3. In Section I.4, we briefly present the different modeling approaches that can be divided into two categories with either microscopic based models or phenomenological continuum descriptions. Since the latter approach is the one used in this thesis and requires experimental data of quality to properly compute magneto-elastic material properties, we analyze in Section I.5 what has previously been done in terms of experiments. Finally, the scope of the present work is presented and the organization of the manuscript is detailed to guide the reader through the following chapters in Section I.6.

I.1 MREs among smart materials

A stimulus from a given physical domain can induce in some materials called ‘smart’, ‘intelligent’ or ‘active’ a response to their environment which can sometimes produce a useful effect in another physical domain. Common materials that formally have the label of being smart include piezo-electric materials, electro-strictive materials, magneto-strictive materials, electro-rheological materials, magneto-rheological materials, thermo-responsive materials, shape memory alloys, etc... The applied driving forces for smart materials can be broadly identified as mechanical fields, electrical fields, magnetic fields, thermal fields, chemical fields, etc... Therefore, an important feature related to smart materials is that they encompass almost all fields of science and engineering.

While electro-active materials usually require high voltages to obtain small deformations [8], low magnetic fields which can be economically generated (using permanent magnets, solenoids) are used to stimulate magneto-active materials (see [65, 64, 144, 141]). As a branch of this kind of active materials, electro- and magneto-rheological materials consist of an insulating or non magnetic matrix (either a fluid, a foam or an elastomer) into which electrically or magnetically polarizable particles are embedded, respectively [77]. Among the benefits of MREs over other types of smart materials, one can think of the absence of electric charges, the possibility to obtain large deformations and the fact that these materials can be bio-compatible (depending on the choice of matrix).

A brief history covering the development of magneto-rheological (MR) materials from its early stages as MR fluids to its current state that includes a broader range of materials (foam and elastomers) is provided in the introduction of Chapter II.

I.2 Classification within MREs

Subjecting MREs to magnetic fields during manufacturing leads to materials with different microscopic architectures and anisotropic properties. These materials are called field-structured MREs and it has been observed that they are anisotropic in terms of mechanical, magnetic, electrical, and thermal properties [29]. More specifically, applying a uni-axial magnetic field produces chain like particle structures¹: for low volume fractions the particles

¹ In the following, MREs structured by an externally applied, uni-axial magnetic field are termed field-structured or transversely isotropic whereas isotropic MREs designate composites with a random distribution of particles (where no structuring field is applied during fabrication).

initially form chains that slowly coalesce into columns, as shown in Fig. I.1, whereas for high volume fractions the morphology slightly complexifies, with possible branching between columns and a slight loss in anisotropy [106, 13]. A bi-axial (e.g. rotating) field produces sheet-like particle structures [108]. Finally, with the generation of triaxial magnetic fields during processing, multiple isotropic and anisotropic particle structures can be envisioned [107].

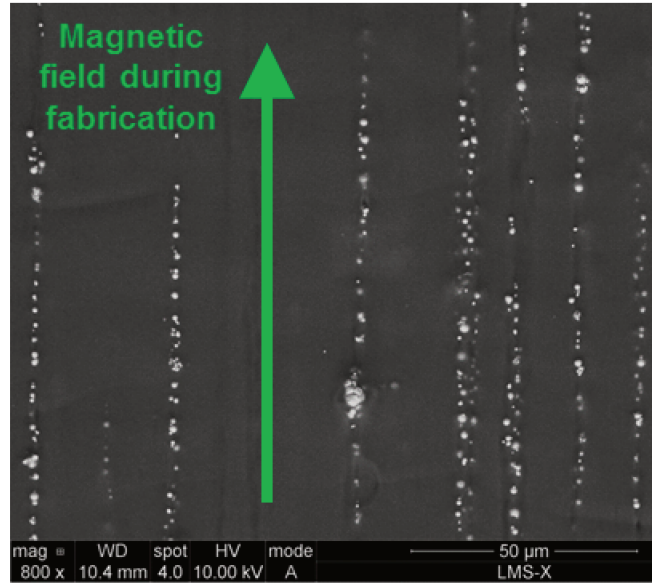


Figure I.1: Scanning electron micrograph of a transversely isotropic MRE with low particle volume fraction. The particles appear as white dots aligned by the externally applied magnetic field in the elastomeric matrix appearing as the black background.

MREs can be further classified based on the inherent properties of their constituents, i.e. the non-magnetic matrix and the magnetic filler particles. These composite elastomers are usually composed of a solid, electrically insulating² matrix, such as silicone rubber, natural rubber, polyurethane or thermoplastic elastomers [88, 80, 31, 151, 86]. In fact, a great variety of matrix materials covering a wide range of properties in shear modulus or viscosity can be found on the market and in the literature. However, among these materials, MREs based on silicone rubber are the most popular due to their excellent processability, a good balance between mechanical, thermal and aging properties, as well as their widespread use in industrial applications. Furthermore, relatively soft matrices with low elastic moduli are achievable in silicon rubbers and tend to ease the magneto-mechanical coupling [88, 66, 44, 134]. It is interesting to note that the class of ‘soft magneto-rheological elastomers’ has been claimed, which comprises MREs with elastically soft matrices. This class of materials includes magnetic gels consisting of magnetic particles dispersed in a gel-like polymeric matrix (sometimes called

² Conductive or graphite-particle-doped MREs are not considered within the scope of this thesis. In addition, we will neglect the phenomenon of magneto-electrical resistance. The interested reader is referred to the papers of Bica [11] and Ausanio et al. [7], for more details on that topic.

ferro-gels). Gel materials (which consist of a fluid within a three-dimensional weakly cross-linked network) can be much softer than typical elastomers, but there are some drawbacks associated with their use. They usually have a wet and sticky consistency, and when agitated, these materials start to flow (thixotropy), thereby resulting in poor mechanical properties [156, 129, 157].

A broad range of magnetic filler particles are used in MREs, among which: magnetostrictive or magnetic shape memory particles, as well as hard or soft magnetic particles. Quite a number of researchers employed highly magnetostrictive particles, usually Terfenol-D [50]. This alloy made out of rare earth crystals is the most effective but a cost-intensive magnetostrictive material, capable of generating reversible strains in the order of 10^{-3} in response to a magnetic loading [73]. The use of particles with magnetic shape memory yields both temperature and magnetic field-driven MRE composites [133]. The dispersion of hard magnetic particles in an elastomeric matrix, magnetized during fabrication, produces anisotropic, magnetically-poled MREs similar to a flexible permanent magnet [96]. However, the most widely used particles in MREs fabrication (in particular spherically shaped carbonyl iron powder (CIP), [88, 18, 44, 134]) are made of soft ferromagnetic materials such as nickel, cobalt or iron and their alloys [6, 5]. Iron presents the benefit of having a high magnetic susceptibility and saturation magnetization, providing high inter-particle interaction forces, as well as a low remanent magnetization required in order to obtain a quick and reversible behavior for MRE applications.

The size of the magnetic particles further distinguishes MREs from ferro-gels³ (as well as ferro-fluids) that tend to include nano-sized particles which are magnetic mono-domains. According to the definition in the review by Carlson and Jolly [29], MREs rather embed micron-sized particles possessing a high number of magnetic domains that, overall, are harder to magnetize [29, 105].

I.3 A brief review of existing work on MREs

Considering the large amount of possible matrix-filler combinations in the literature, a lot of research effort is dedicated to find an optimal composition that will maximize the magneto-mechanical coupling, as well as improving the fabrication procedure. Optical microscopy [54], scanning electron microscopy [67, 32] or X-ray micro-tomography [16] are used to investigate the obtained micro-structures. The processing conditions and (field-)curing mechanisms are crucial parameters for the manufacturing of MREs. More specifically, the mixed viscosity - a measure of the thickness of the blended composite constituents -, the temperature and the magnetic field will determine the competition between gravitational settling and the alignment of the particles during curing [4, 72]. Each of these parameters dictate the final structure of the material, which complicates the comparison of experimental results in the literature.

Furthermore, extensive studies have investigated the dynamic small strain behavior of MREs, especially the influence of an externally applied magnetic field on mechanical properties such as storage, loss and viscoelastic moduli [139, 84, 64, 101, 88, 53, 92]. Since it has

³Ferro-gels are sometimes considered as MREs.

been found that MREs alter their dynamic moduli in response to the field, their performance as tunable vibration absorbers and tunable stiffness devices has been widely studied and prototype applications have been developed [52, 55, 38, 109, 95], such as a prosthetic foot [144] shown in Fig. I.2.

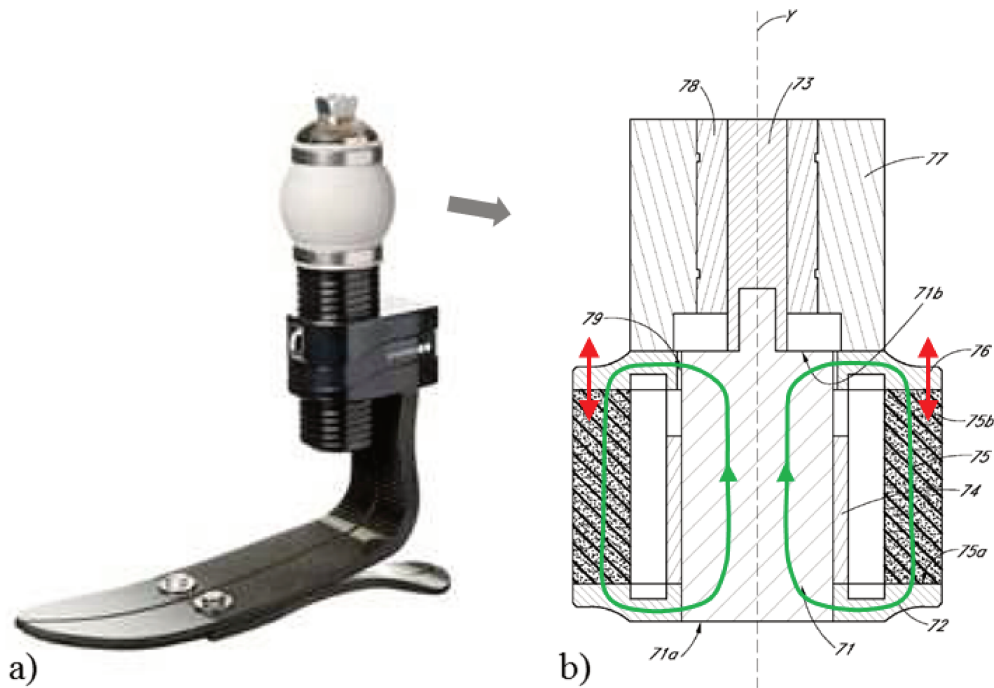


Figure I.2: a) Picture of a smart prosthetic foot device and b) cross section of the integrated tunable MRE spring (from reference [144]). The motion (red arrows) resistance of the MRE spring (75) can be adjusted by the magnetic flux (green circuit) generated by the coil (74).

In parallel, a large body of research has been devoted to the investigation of the deformation of MRE materials exposed to a magnetic field. The attraction of magnetically soft and mechanically flexible MREs by magnetic field gradients has been discovered early [155]. Large out-of-plane deformation could be achieved in response to a spatially localized magnetic field and used in haptic devices such as a tactile interface [150]. For example, patterns can be displayed on a surface by placing a matrix of solenoids or permanent magnets underneath a soft MRE surface (see Fig. I.3), as already achieved with magneto-rheological fluids [82, 15, 99] or electro-rheological elastomers [98].

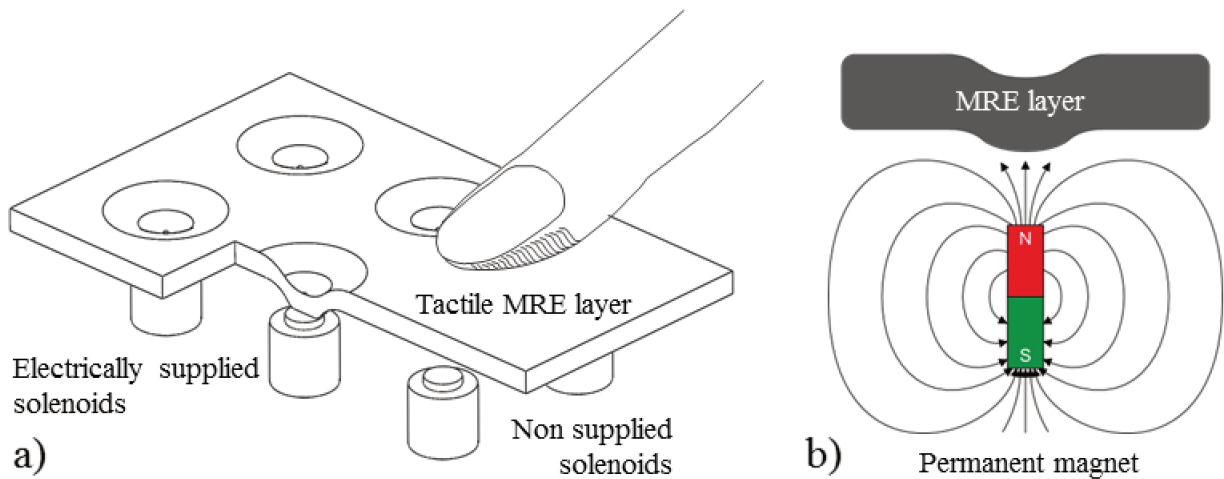


Figure I.3: Schematics of the working principle for tactile interfaces (from reference [125]) with patterns created a) by a matrix of solenoids placed underneath a MRE layer or b) by a permanent magnet.

Another use of this attracting effect has been proposed in smart high-strain actuators [19, 23]. Fig. I.4 shows the example of an MRE device enabling flow control [141].

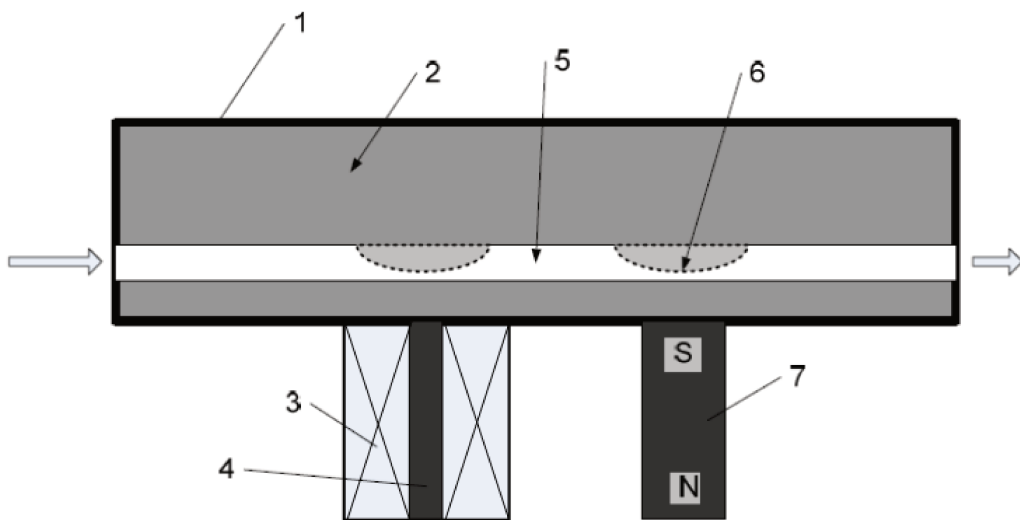


Figure I.4: Schematic of a smart fluid valve (from reference [141]). The flow (large arrows) of the medium inside a channel (5) can be adjusted by attracting the MRE material (6) by means of an electromagnet (3,4) or a permanent magnet (7).

Recently, a study by Psarra and Danas [127] reported an interesting instability phenomena in MREs. The stability and post-bifurcation of a non-linear magnetoelastic film/substrate block is experimentally exploited to obtain active control of surface roughness. Cooperation of two otherwise independent loading mechanisms - mechanical pre-compression and magnetic

field - is used to bring the structure near a marginally stable state and then destabilize it with either magnetic or mechanical fields (see Fig. I.5). It is experimentally demonstrated that the critical magnetic field is a decreasing function of pre-compression and vice versa. The magneto-elastic coupling allows for the reversible on/off control of surface wrinkling under adjustable critical magnetic and mechanical fields. This study constitutes a first step towards a new kind of active haptic and morphing devices where surface patterns are activated at the threshold of instability.

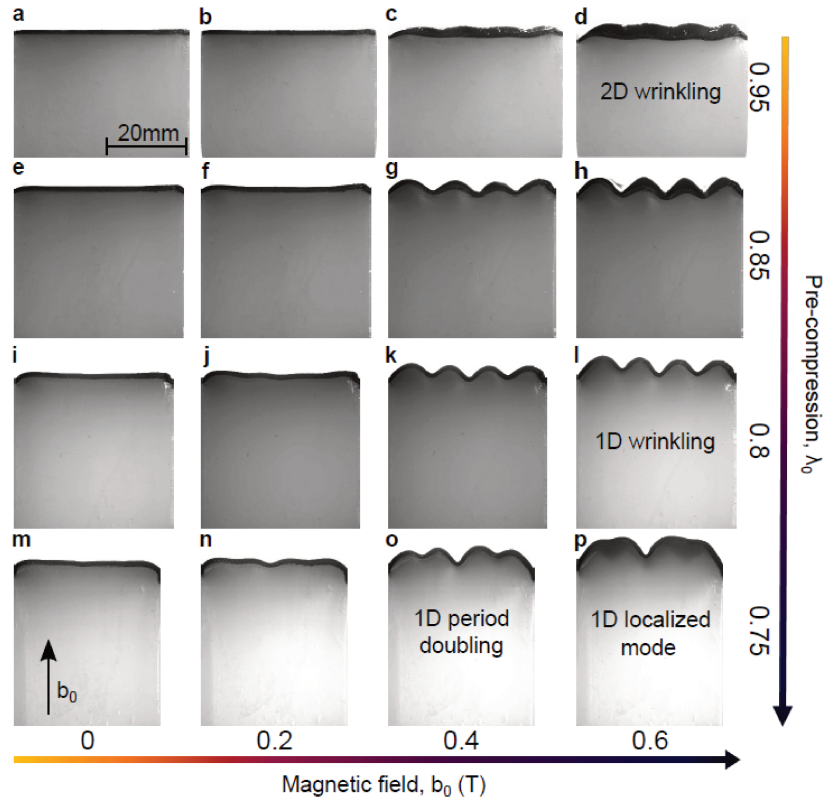


Figure I.5: Experimental influence of the magneto-mechanical coupling on bifurcation and post-bifurcation (from reference [127]). Optical images of the morphological pattern evolution versus the magnetic field \mathbf{b}_0 , under different pre-compressions λ_0 .

Finally, an important part of the literature on MREs is concerned with the modeling of these materials, and is briefly described in the next Section.

I.4 Modeling approaches

The highly coupled magneto-mechanical behavior of MREs makes their mathematical modeling a difficult task. Geometrical non-linearities are introduced in association with the large deformations that these elastomer-based materials are capable of developing. Additionally, constitutive non-linearities due to the hysteretic behavior of the viscoelastic matrix as well

as a hysteretic, saturating magnetic response further complicate the modeling of such composites. Basically, the approaches used to model these materials can be partitioned into two main categories: micro-mechanical or structural models on the one hand and continuum or phenomenological models on the other hand. They are briefly reviewed in the following.

I.4.1 Micro-mechanically based description of MREs

The first kind of model provides a microscopic description of MREs. In most cases, the magnetic filler particles are considered as rigid spheroids randomly distributed (to describe isotropic materials) [17], or with a preferred alignment (to describe transversely isotropic materials) [42, 153], within the elastomeric matrix. The magneto-mechanical interactions for a large set of particles is then extrapolated to obtain global expressions for a body. The powerful technique called homogenization can determine the effective macroscopic constitutive model for a magneto-elastic composite based on the properties of the constituent phases and their relative arrangement [124, 39]. The main benefit of that type of models is that the obtained mathematical expressions can provide insight into the underlying microscopic physical mechanisms responsible for the coupling in MREs. However, the major drawback lies in the complexity of these expressions, even when a series of simplifications is adopted (only the fields of closely neighboring particles or isolated evenly distributed particle chains affect each other; see Jolly et al. [84], Yin et al. [153] for inclusions in dilute limit, Corcolle et al. [37] using small strain Hashin-Strikman homogenized MRE model; etc...). Due to technical difficulties associated with large kinematics, most of the micro-mechanically based studies are in the small strain context, save for the recent work by Ponte Castañeda and Galipeau [124, 59, 60], Lefèvre and Lopez-Pamies [100] and Danas [39]. Recently, quite a number of computational homogenization results have been reported for rubber filled with periodic/hexagonal arrays (Galipeau et al. [61], Javili et al. [83], Keip and Rambašek [93]) and approximately isotropic distributions (Danas [39], Kalina et al. [87]) of circular particles in two dimensions and with periodic cubic arrays of spherical particles (Javili et al. [83], Miehe et al. [114]) in three dimensions.

I.4.2 Phenomenological continuum modeling

The advantage with the second kind of models called continuum models is that they don't have to describe all the microstructural phenomena to accurately capture the material's behavior. Since the magnetic particles are very small in comparison to the overall size of the investigated bodies, a continuous description of isotropic or field-structured MREs can be assumed.

Some magneto-mechanical problems in MREs are solved within the framework of a relatively simple macroscopic theory, in which the MRE composite is considered as a magnetizable elastic continuum, whose equations of magnetic and elastic state are uncoupled [155, 129, 45]. Other models account for stress-induced changes in the magnetic behavior, but without a comprehensive field theory, they are limited to one dimensional (small) deformations or to particular geometrical shapes [105, 157, 92]. Fully coupled non-linear field theories for isotropic MREs [47, 90, 26, 119, 132] and field-structured magneto-elastic con-

tinua [25, 40] have also been developed based on only one underlying continuum . To establish the corresponding governing equations (i.e. the relations between the stress, the strain, the displacement and the magnetic fields), use is made of equations belonging to different fields of science, namely: global balances of linear and angular momentum, the first and second law of thermodynamics, as well as Maxwell’s equations for electromagnetism. At the heart of these theories (which neglect the hysteretic and dissipative behavior of MREs), a free energy density function that depends in a coupled fashion on mechanical deformations and magnetic fields describes the materials constitutive behavior. In this approach that is the theoretical basis for what has been done in this thesis, the material constitutive behavior needs to be identified with the help of magneto-mechanical experiments. Once the material parameters of these models have been identified and implemented numerically, it will be possible to simulate boundary-value problems in complex geometries and complex loading conditions [49, 41].

The main problem at the moment, however, is the lack of an accurate experimental characterization. Indeed, in Section I.5, a review of the available experimental data will show that magneto-elastic coupled behavior up to high strain and high magnetic fields has not been well explored yet due to the difficulties encountered in experiments (due non-uniform fields created by shape effects for instance) and fabrication (for example, we will show in this thesis that a particle treatment is necessary to avoid debonding at the interface ‘matrix/particle’). Hence the design of smart devices capable of high deformations has been limited so far and very few applications allow the MRE material to deform up to 20 percent [38, 144, 141].

I.5 Difficulties associated with MRE experiments

Several difficulties need to be addressed when characterizing MREs experimentally. The first issue lies in the fact that uniform mechanical fields within a test specimen that are required by (standard) mechanical testing methods of elastomers [30, 116], have to be combined with uniform magnetic field distribution within the same sample when subjected to complex magneto-mechanical loading conditions. Secondly, another difficulty is linked to the fact that completely capturing the behavior of MREs requires tests up to large strains and under high magnetic fields. Further complicating this task, the magnetic material properties have to be measured during sample deformation to properly account for the magneto-elastic coupling. Last but not least, different deformation modes should be evaluated to accurately identify the materials constitutive behavior. In the literature, one can find a large number of tests (quasi-static, large strains, high magnetic field) for various MRE materials. Most of these studies are oriented in a purely experimental fashion without the idea yet of a general constitutive description in mind.

In what follows, the most significant studies are classified according to the magnetic field generation. Unless otherwise indicated, measurements of the magnetic properties - if done at all - are performed separately from mechanical ones (i.e. no coupling). Additionally, ‘strains’ implies nominal strain and ‘magnetic field’ designates the excitation magnetic field $\mathbf{b}_0 = \mu_0 \mathbf{h}_0$ in [T], if not otherwise specified.

I.5.1 Description of previous experimental studies on MREs

Magnetic field created by permanent magnets

The use of permanent magnets is probably the most simple way of applying an external magnetic field. In such setups, quasi-static double lap shear tests were performed by Shen et al. [138] (strains up to 80%, magnetic fields up to 0.4 T), and quasi-static compression tests by Farshad et al. [54, 56] (strains up to 30%, magnetic fields up to 0.4 T). Schematics of these two experiments are presented in Fig. I.6a and Fig. I.6b, respectively. The main drawback of the approach used here is that only fixed values of magnetic loads can be applied. Indeed, it is not possible to vary the value of the applied magnetic without modifying the setup. Moreover, it is usually difficult to obtain a constant, homogenous field distribution with the help of these commonly rectangular-shaped permanent magnets.

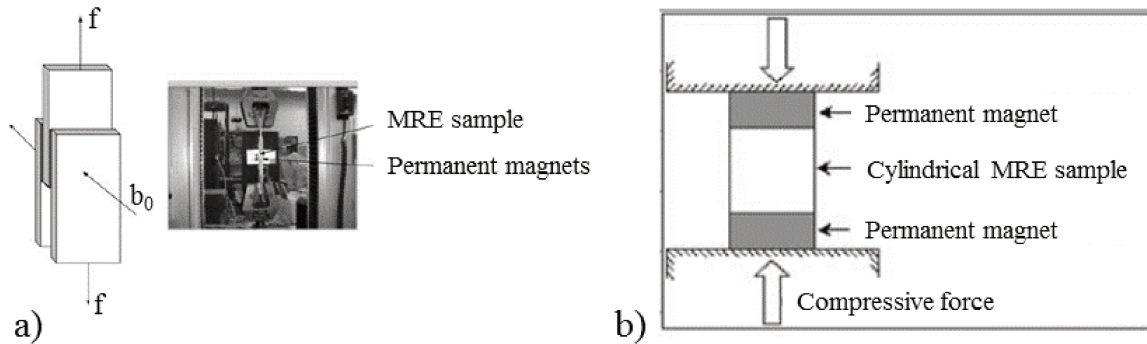


Figure I.6: Schematics of setups in which MREs are subjected to a magnetic field generated by permanent magnets. a) Case of a double-lap shear test (from reference [138]). b) Case of a compression test (from reference [54]).

Magnetic field created by solenoids

Static compression tests (up to 6.5% strain) combined to an external magnetic field (up to 0.5 T) created with a ring-shaped solenoid around the MRE specimen and applied in the same direction that the compressive force were performed by Kallio [88]. However, due to the small length of the solenoid and the asymmetrical positioning of the sample inside it (see Fig. I.7a), non-uniform magnetic fields influenced the measurements.

Bossis et al. [20, 9], as well as Coquelle [34] (see Fig. I.7b), also placed their MRE sample within a solenoid (magnetic fields of up to 0.15 T). The uniformity of the magnetic field in the region where the sample is placed is ensured by the elongated shape of the solenoid together with the central position of the long cylindrical specimen. However, it blocked the access for experimental diagnostics that would be needed to extract the necessary strain data characterizing field-structured MREs. Hence, only one-dimensional tensile stress-strain measurements (up to 25% strain) were performed.

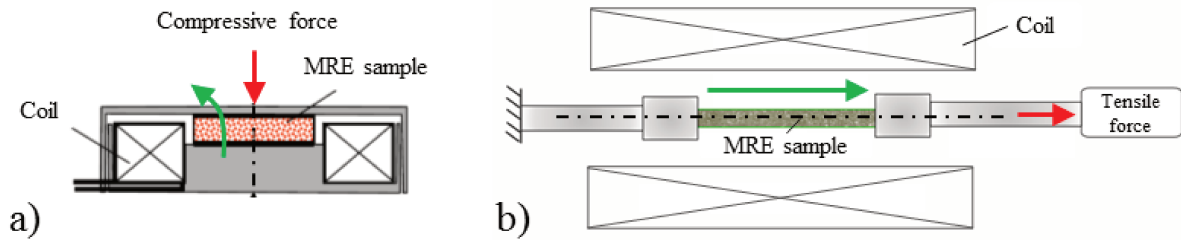


Figure I.7: Schematics of setups in which MRE samples are placed within a solenoid-generated magnetic field (green arrow). a) Case of a compression test (from reference [88]). b) Case of a tension test (from reference [34]).

Magnetic field created by Helmholtz coil systems

An interesting Helmholtz coil system has been designed by Martin et al. [105] to enable deformation measurements during coupled magneto-mechanical tests on MREs (see Fig. I.8).

Two paired solenoids create a homogeneous magnetic field in the region of interest while providing access for measurements, despite being restricted to lower magnetic field values (up to 0.12 T). A rectangular-shaped MRE sample (shape that leads to non-uniform internal magnetic fields \mathbf{b} and mechanical fields) is suspended from a cantilever and centered within the two coils. By adding weights to the cantilever, a constant mechanical pre-stretch could be imposed (on the sample attached on the bottom end) and a one-dimensional deformation upon the application of the magnetic field was recorded by an optical apparatus.

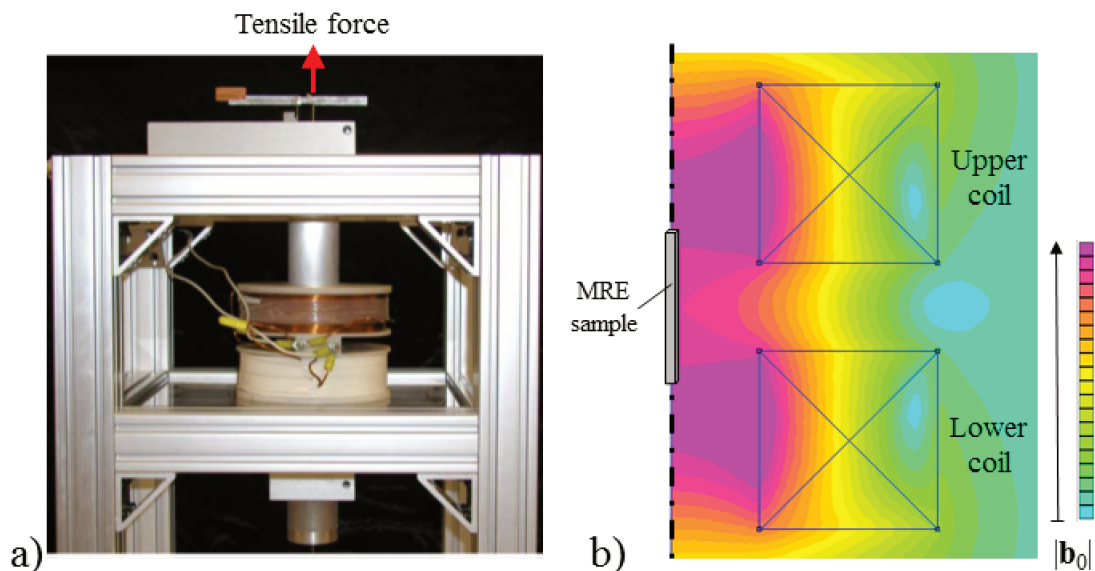


Figure I.8: a) Schematics of the Helmholtz coil combined with a uniaxial tension system designed by Martin et al. [105]. b) FEM visualization (2D axisymmetric, [112]) of the magnetic field distribution $|\mathbf{b}_0|$ generated by the combination of both the upper and lower coils.

Magnetic field created by open magnetic circuits

Another common way to perform experiments on MREs is to place the sample between the two poles of an electromagnet. Usually, tapered pole shapes guide the nearly uniform and elevated magnetic field (above 1 T), created by solenoids integrated in a high susceptibility magnetic circuit, through an accessible air gap. Multiple experiments have been conducted in such setups, including double-lap shear tests (up to 10% strain, [84, 65, 63, 89], see Fig. I.9), uniaxial deformation tests (up to 10% strain, [89, 44]), and compression tests of an MRE cube (up to 10% strain, [148, 149]). A more detailed description of this kind of experimental setups is given in Chapter II since this setting, adapted for uni-axial tensile tests, has been used in this study.

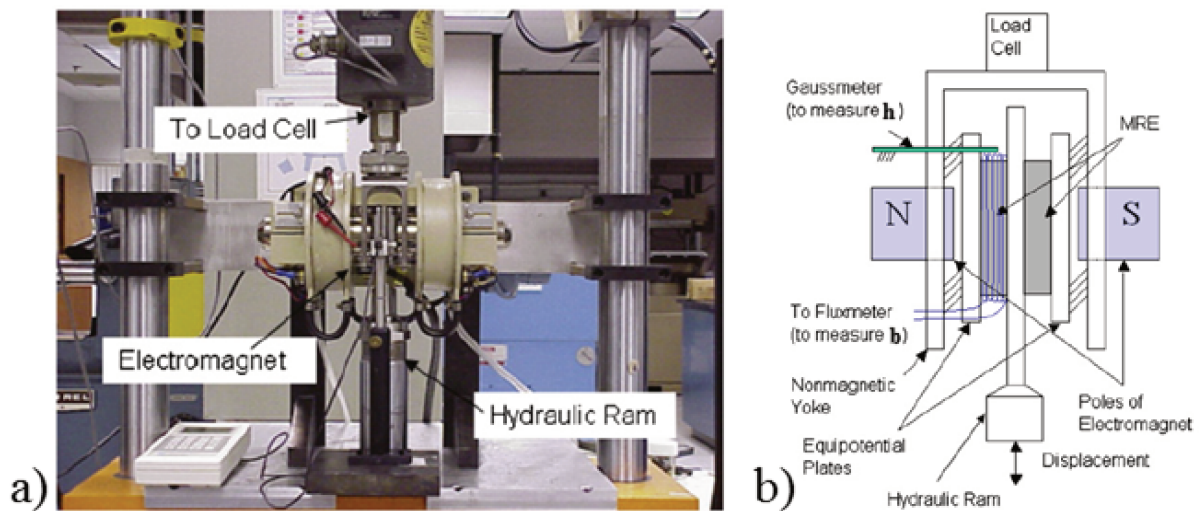


Figure I.9: Double-lap shear setup with the MRE sample located between the two poles of an open electromagnetic circuit (from reference [89]): a) photograph and b) schematic.

I.5.2 Existing attempts to experimentally characterize MREs using continuum models

Recently, some research groups have started working on a full magneto-mechanical experimental characterization for continuum models.

Large-strain experimental data (up to 100% strain) for MREs under various deformation modes, both without and with the application of external magnetic fields, were collected by Schubert et al. [137, 134]. Isotropic and fields-structured MREs were prepared and tested under uniaxial compression and tension, pure shear and equi-biaxial tension (see Fig. I.10). However, due to the use of permanent magnets, the applied magnetic fields (up to 0.3 T) were non-uniform and different in each setup. Furthermore, mechanical experimental issues were recorded (e.g. friction and buckling in compression tests and non-ideal deformation kinematics in pure shear). Though the purely mechanical response of isotropic MREs could be described by a common constitutive model (Ogden), data fitting of several transversely isotropic models were not successful, even in the purely mechanical case. As a consequence,

neither did they proceed to characterize magneto-mechanical constitutive models nor did they measure magnetic material properties depending on sample deformation.

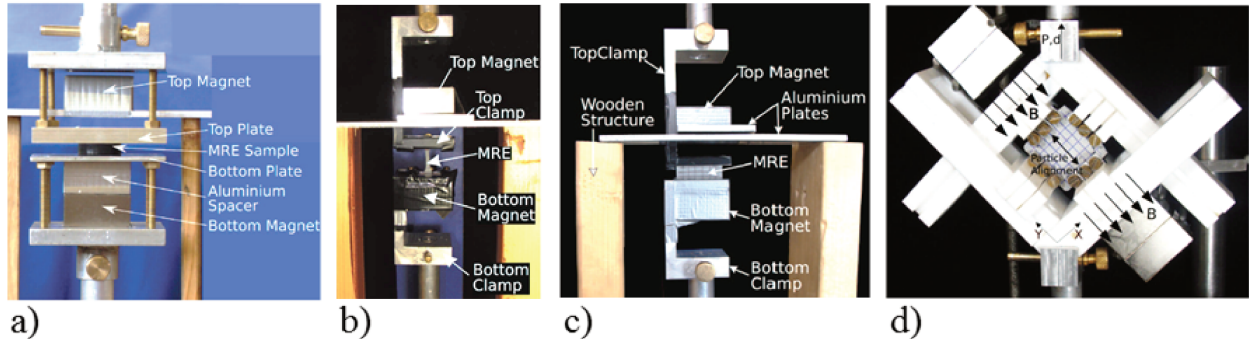


Figure I.10: Photographs of MRE experimental setups (from reference [134]) for large strains under magnetic fields generated by permanent magnets: a) uniaxial compression, b) uniaxial tension, c) pure shear and d) equi-biaxial tension.

Similarly, during a PhD-thesis at the Ecole Polytechnique in Paris, Pössinger et al. [125] conducted experiments in which specimens (both isotropic and transversely isotropic) were subjected whether to a purely mechanical uniaxial tension (up to large strains) or to a coupled magneto-mechanical loading in which an externally applied magnetic field was imposed in a direction perpendicular to the axis of the samples while the forces were kept equal to zero. However, as we will show in this thesis, many improvements are necessary to get reliable data. For instance, the manufacturing procedure needs to be adapted to improve the interfacial adhesion between the particles and the matrix. Secondly, the way magnetic measurements are corrected to account for the fact the probe is not placed exactly at the discontinuity interface between the air and the sample has to be improved. Due to these issues, the proposed constitutive model cannot describe the behavior of MREs in a satisfactory manner.

I.6 Scope and organization of the present thesis

The goal of the present work is to characterize the behavior of MREs with a main focus on their coupled magneto-mechanical response up to large strains and under high magnetic fields. Having in mind the design of smart devices capable of high deformations, the phenomenological material model proposed by Kankanala, Danas and Triantafyllidis [90, 40, 41] needs to be accurately identified and implemented in numerical codes.

For that purpose, this work encompasses experimental, theoretical and numerical developments. These topics are detailed in this manuscript as follows:

- In Chapter II, aspects pertaining to the experimental investigation of MREs are presented. Material selection, fabrication process of isotropic and field-structured MREs, as well as sample design and particle/matrix adhesion are discussed. We also describe the experimental setup, the measurement techniques and the testing protocol. Finally, the results are analyzed and discussed.

- Chapter III covers the actual magneto-mechanical characterization. After introducing the general theoretical framework for isotropic (and transversely isotropic) magneto-elastic continua, the coupled magneto-mechanical constitutive laws for both isotropic and field-structured MREs are derived (using the energetic approach) in order to determine the sets of material parameters to be identified. The second part of this chapter is dedicated to the determination of these material constants for isotropic materials, using the experimental data obtained in Chapter II.
- In Chapter IV, we explain how to implement into finite element codes the different variational formulations discussed in Chapter III. It is to be noted that such codes are used in Chapter III since the determination of material parameters cannot be done analytically and requires to compare experimental data with numerical simulations as it will be explained.
- Finally, Chapter V provides concluding remarks as well as perspectives for future work regarding the specific subjects treated in this thesis. The numerical study of an haptic device that has already been prototyped and experimentally tested is proposed.

CHAPTER II

EXPERIMENTAL INVESTIGATION OF THE COUPLED MAGNETO-MECHANICAL BEHAVIOR IN MAGNETORHEOLOGICAL ELASTOMERS

Contents

II.1	Introduction	24
II.1.1	Context of the study	24
II.1.2	Bibliographic background on MREs	25
II.1.3	Aim of the study and structure of the chapter	26
II.2	Physical mechanisms arising in MREs	26
II.2.1	Mechanical behavior of MREs as particle-filled composites	26
II.2.2	Magnetic response of MREs	27
II.2.3	Deformation under magnetic field	27
II.2.4	Magnetic field-dependent modulus	29
II.3	Samples	31
II.3.1	Sample shape for coupled magneto-mechanical testing	31
II.3.2	Materials	34
II.3.3	Fabrication procedure	37
II.4	Experimental methods	39
II.4.1	General setup	39
II.4.2	Mechanical diagnostics	41
II.4.3	Magnetic diagnostics	42
II.4.4	Testing protocol	44
II.5	Results and discussion	45
II.5.1	Purely mechanical testing	45

II.5.2	Coupled magneto-mechanical testing	48
II.6	Conclusions and perspectives	54
Appendix II.A	Correction of magnetic measurements	56
II.A.1	Elliptical coordinate system	56
II.A.2	Problem to solve	57
II.A.3	Resolution of Laplace equation	59

II.1 Introduction

II.1.1 Context of the study

This work pertains to the technologically important area of active materials, also commonly named smart materials. These can be broadly defined as materials in which a stimulus from a given physical domain (mechanical, electrical, magnetic, thermal, etc) generates a response belonging to another domain. Piezoelectricity is a clear illustration of this concept whereby a mechanical stimulus yields an electrical response in the form of a potential variation. As a branch of active materials, magnetorheological materials consist of a non-magnetic matrix into which magnetically polarizable particles are mixed [75]. The first reported magnetorheological materials had a fluid matrix [128]. In these so-called magnetorheological fluids (MRFs), the particles form columnar structures parallel to the externally applied uniaxial magnetic field. As the field increases, it becomes more and more difficult for the fluid to flow through the formed structures. This field-dependent rheological behavior, which can be rapidly and reversibly controlled, has been exploited in a variety of vibration control or torque transfer devices [28, 10]. However, the drawbacks of MRFs are the settling of their particles over time and the fact that they need to remain enclosed. An answer to these drawbacks was to use an elastomer as the matrix: magnetizable particles are mixed into the initially fluid-like polymer blend and remain locked in place within the cross-linked network of the cured elastomer. Hence magnetorheological elastomers (MREs) are often considered as the solid analogs of MRFs. The first researchers who conducted preliminary tests on MREs were Rigbi and Jilken [130]. They studied the behavior of a ferrite elastomer composite under the combined influence of elastic stresses and magnetic fields and described the previously unknown magneto-mechanical effects. Indeed, the soft characteristics of the matrix combined with the magnetic properties of the particles allow these flexible composites to both deform and alter their stiffness in response to a rather low external magnetic field. Their rapid response, their high level of deformations and the possibility to control their deformations by adjusting the field make these materials of special interest in a variety of advanced engineering applications such as tunable damping systems, actuators, sensors, artificial muscles, sound control or shape control (see the review by Hamrock [75] and also Bustamante [24]).

II.1.2 Bibliographic background on MREs

Considering the variety of possible matrix-filler combinations, many experimental studies have been dedicated to the composition and processing of MREs along with the investigation of the obtained microstructures [54, 67, 31]. Among all possible matrix materials, it stands out that silicone rubbers are preferred due to their excellent processability, their good thermal and aging properties, as well as their low elastic modulus that tend to facilitate the magneto-mechanical interaction [88, 66]. As far as particles are concerned, micron-sized iron particles are the most common since they exhibit high magnetic susceptibility and high saturation magnetization, thus providing high inter-particle interaction forces, as well as low remanent magnetization, a property required to obtain quick and reversible control by the magnetic field in MRE devices [29]. Extensive studies have also been conducted to investigate the influence of an external magnetic field on the damping properties of MREs such as storage, loss and viscoelastic moduli [84, 64, 102]. In particular, their performances as tunable vibration absorbers and tunable stiffness devices have been analyzed and prototypes have been developed [52, 55, 38, 109, 95, 144].

In contrast and despite a potential for slower time response applications in artificial muscles or shape control, only a handful of experimental studies have focused on characterizing the coupled magneto-mechanical behavior of MREs under low-rate loadings. One of the difficulties lies in the fact that standard mechanical testing methods yielding uniform mechanical fields within the elastomer test specimen have to be combined with externally applied magnetic loadings inducing a uniform magnetic field distribution inside the sample. Additionally, in order to analyze the magneto-mechanical couplings, both magnetic and mechanical quantities have to be measured during sample deformation. Since the first experimental studies regarding MREs often approached their behavior without the prospect of a general macroscopic coupled constitutive description, one can find in the literature a large number of tests (quasi-static, large strains, high magnetic field) for various MRE materials but measurements of the magnetic properties, if done at all, are performed separately from mechanical ones (i.e. no coupling). Some studies indeed focused on the deformation of MREs under purely magnetic loading [45, 46]. Other studies explored the mechanical response of MREs under magnetic field but performed experiments in which either the magnetic field was not homogenous [54, 138, 105, 135, 136] and/or in which there was no access to all mechanical quantities [20, 9, 35, 89, 40]. Additionally, an important mechanical effect arising in filled elastomers (the Mullins effect, see Section II.2.1) is ignored in these study and may explain some of the unexpected and unrepeatable results [71].

Finally, an important part of the literature on MREs focuses on their modeling under monotonic loadings. The chosen approaches can be partitioned in micro-mechanical or structural models on the one hand [42, 17, 153, 124] and continuum or phenomenological models on the other hand [24, 45, 47, 90, 119, 132]. A review of theoretical and numerical works is beyond the scope of this article and it is only important to emphasize here that, in the continuum approach, the material constitutive behavior include parameters that need to be identified with the help of consistent magneto-mechanical experiments.

II.1.3 Aim of the study and structure of the chapter

Hence there exist, to our knowledge, no precise and complete characterization of the fully-coupled magneto-mechanical properties of MREs, thus hindering the further design of MRE-based devices. Through this work, we therefore aim at understanding the macroscopic response of MREs under combined magnetic and mechanical loading conditions. For this purpose, we developed a framework for characterizing experimentally the coupled magneto-mechanical behavior of MREs up to large strains and up to high magnetic fields, relying on both specially designed samples and a dedicated experimental setup providing precise in-situ coupled data. Although this is beyond the scope of this chapter, note that we will also seek to derive coupled magneto-mechanical continuum constitutive laws, for which the obtained coupled magneto-mechanical experimental data will be necessary.

The chapter is organized as follows: in Section II.2, a short review of physical mechanisms arising in MREs is given in order to provide the necessary background for discussing the results. In Section II.3, the investigated materials as well as aspects pertaining to samples design and fabrication are presented. Section II.4 is dedicated to the experimental setup and metrological aspects involved in the coupled magneto-mechanical characterization of MREs. Experimental results obtained on MREs with different particle volume fractions are detailed in Section II.5. These results provide material to discuss the underlying microstructural mechanisms responsible for the macroscopic deformation of MREs under combined magnetic and mechanical loading conditions. Finally, remarks regarding parameters identification of a constitutive model and conclusions on further aspects to be studied are developed in Section II.6.

II.2 Physical mechanisms arising in MREs

II.2.1 Mechanical behavior of MREs as particle-filled composites

Even before considering coupled magneto-mechanical aspects, purely mechanical phenomena arise in MREs that are solely due to matrix-filler interactions. Under large deformations, a softening and a permanent deformation between the first and the subsequent load cycles are reported in filled rubbers and MREs [117, 118, 113, 36]. This phenomenon, which depends on the maximum applied strain, is known as the ‘Mullins effect’ and corresponds to the breaking of the initial bonds between the fillers and the matrix. The highest softening occurs after the first load cycle and the hysteresis loop then decreases in area until stabilization after a few cycles. The propensity of the Mullins effect, along with the composite stiffness, both increase with particle content. Particle size and shape also have a significant influence on the composite mechanical behavior [57]. Another important aspect, mainly influencing the mechanical strength, is the interfacial adhesion between the filler particles and the matrix [57, 43]. Indeed, beyond a critical stress level, debonding acts as a distinct failure phenomenon in a polymer containing rigid inclusions due to stress concentrations at the weak particle-matrix interface [62]. Finally, filler networks such as the particle chains in field-structured MREs, as well as possible aggregates due to fabrication process, can further affect the composite mechanical behavior.

II.2.2 Magnetic response of MREs

Important variables commonly used in the magnetics-related literature are recalled here. In vacuum, the magnetic field $\mathbf{b}_0 = \mu_0 \mathbf{h}_0$ corresponds to the externally applied field \mathbf{h}_0 multiplied by the magnetic permeability of the free space $\mu_0 = 4\pi \cdot 10^{-7}$ [N/A²]. If a finite ferromagnetic body is exposed to the excitation field \mathbf{h}_0 , the body becomes magnetized and generates a perturbation field $\tilde{\mathbf{h}}$, also known as demagnetizing field or stray field [120]. The macroscopic magnetic constitutive relation can then be defined, following the SI system, as

$$\mathbf{b} = \mu_0(\mathbf{h}_0 + \tilde{\mathbf{h}} + \mathbf{m}) = \mu_0(\mathbf{h} + \mathbf{m}), \quad (\text{II.2.1})$$

where $\mathbf{b} = \mathbf{b}_0 + \tilde{\mathbf{b}}$ is the total magnetic field, also called magnetic induction or magnetic flux density, expressed in Tesla [T = N/A·m] and $\tilde{\mathbf{b}} = \mu_0(\tilde{\mathbf{h}} + \mathbf{m})$ is the magnetic perturbation field. The state of magnetic polarization within the body is described by the magnetization field \mathbf{m} [A/m]. $\mathbf{h} = \mathbf{h}_0 + \tilde{\mathbf{h}}$ is the total h-field, also called magnetic field intensity or magnetic field strength, expressed in [A/m]. The nonlinear relation between \mathbf{h} and \mathbf{m} for a ferromagnetic bulk material can be determined experimentally and usually takes the form of a hysteresis loop.

In the case of micrometric iron particles usually used in MREs, remanence magnetization (remaining magnetization when applied field vanishes) and coercive field (value of applied field at which magnetization becomes non-zero) are small (in the order of 10^{-3} T) and magnetic hysteresis is usually neglected [105]. The dimensionless volume susceptibility χ [–] corresponding to the initial slope of the \mathbf{m} - \mathbf{h} curve can then be introduced, as well as the following linear constitutive relations

$$\mathbf{m} = \chi \mathbf{h}, \quad \mathbf{b} = \mu_0(1 + \chi) \mathbf{h} = \mu_0 \mu_r \mathbf{h} = \mu \mathbf{h}, \quad (\text{II.2.2})$$

where μ_r and μ are the relative and magnetic permeability of the body, respectively.

It has been shown that the susceptibility of MRE composites is small compared to the bulk values of iron [134]. Moreover, it has been observed that both the initial susceptibility and the saturation magnetization increase with increasing particle content. The saturation magnetization is often assumed to be a linear function of the particle content and the saturation magnetization of the bulk particle material [46, 105].

II.2.3 Deformation under magnetic field

Experimental studies of MREs report deformations up to 10^{-1} [46], and show either stretching or contracting of MREs along the uniformly applied field [105, 40]. This deformation due to the magnetic field is often referred to as magnetostriction. Note that since the 19th century, the term magnetostriction has been used in physics to designate the deformation caused by intra-granular spin-orbit interaction in crystalline ferromagnets [85]. In this case, deformations at play are several orders of magnitude lower (10^{-6}) than in MREs. In what follows, the underlying mechanisms involved in MRE's magnetostriction are clarified.

Magnetostriction (here referring to the definition used in physics) is inherently present in the ferromagnetic filler particles of MREs. However, the magnetostriction of the individual particles is several orders lower than the strains reported in MREs. Therefore, this mechanism

is usually neglected in investigations of standard MREs [45] and the word magnetostriction often used in the MRE literature solely designates the observed macroscopic effect.

Another mechanism that can arise at the microscopic scale is the rotation of the particles due to magnetic torques. Such torques apply predominantly to particles with an elongated shape. Because of their spherical shape, the carbonyl iron particles used in this study cannot experience magnetic torques. However, if care is not taken during fabrication, particle aggregates may arise in MRE materials and contribute to the occurring deformation through torques [142].

The remaining physical mechanisms are the magneto-dipolar interactions between the particles. To summarize, these interactions try to enhance the overall magnetic susceptibility of the body by diminishing the magnetic part of its energy, in competition with the mechanical strain energy. The deformation of a MRE sample then seems to be the result of two contributions:

- (a) On the one hand, determined by the overall geometry of the sample, the Maxwell stress (second-order tensor describing the electromagnetic force within a magnetic volume) at the discontinuity interface between the air and the sample can induce an elongation of the MRE composite along the field. A significant strain of almost 5% for an MRE sphere has been reported [46] and attributed to this so-called shape-effect. In this case, a demagnetizing factor D relating the internal perturbation field $\tilde{\mathbf{h}}$ to the uniform magnetization \mathbf{m} through $\tilde{\mathbf{h}} = -D \mathbf{m}$ can be introduced [46, 105]. Diguet et al. also reported that large aspect ratios in cylindrical or ellipsoidal samples lead to the lowest demagnetizing energy, hence small strains.
- (b) On the other hand, the sample can change its length in the direction of the field to enhance the magnetic susceptibility determined by the local position of the particles relative to one another. A restoring force between a pair of particles subjected to an externally applied magnetic field tends to align the particles with the field so that they form a magnetic dipole [17]. This contribution is characteristic for MREs (shape-independent material property) and theoretically can lead to either contraction or elongation of the sample, depending on the sample microstructure, pre-stress and the orientation of the field:
 - In isotropic MREs, the general tendency for non pre-stressed cylindrical samples, whose main axis is aligned with the applied magnetic field, is to elongate [63]. This effect seems to generate strains in the order of 10^{-3} . Note that an opposite tendency, i.e. a small contraction, has been reported in parallelepipedic samples even with no pre-strain [105].
 - In field-structured MREs, different possible magnetic and mechanical loading conditions further complicate the situation. If the magnetic field is applied parallel to the direction of particle chains, there should be no deformation effect since the particles have reached their preferred arrangement during curing and have been trapped as such in the matrix. However, small elongations have been reported for non pre-stressed cylindrical samples, whose main axis and particle chains are aligned with the applied magnetic field [40]. If an applied mechanical load disturbs

this state of equilibrium and changes the inter-particle distances, the magnetic susceptibility decreases. For an applied pre-tension, possibly up to a certain strain threshold, the magnetic interactions can try to restore the preferred state and the sample tends to be compressed [105, 35, 40]. Conversely, for an applied pre-compression, the sample usually expands [40]. Typical values of strains in this case are in the order of 10^{-3} . Note again that studies focused on parallelepipedic samples reported different effects, namely compression when no pre-stress is applied [154] as well as much larger strains for this case than for the isotropic case [105]. If the magnetic field is applied transverse to the structuring direction, the induced deformation can even be higher. Due to the presence of the particle chains normal to the applied field, the particles tend to move more significantly in order to form dipole-pairs aligned with the applied field, typically leading to an overall extension of the sample [40]. Typical values of strains here are in the order of 10^{-2} .

Finally it is important to emphasize that when characterizing MREs, a uniform field distribution within the sample should be achieved since field gradients can have an important influence on the behavior of MREs. If a magnetic material is placed in a non-uniform magnetic field, the material experiences a magnetic body force to decrease its interaction energy with the magnetic field. When a MRE composite is placed in a gradient of external magnetic field, these forces act on the filler particles. The particles, together with the polymer matrix that they drag along, are therefore displaced towards the highest amplitude of the field. Depending on both the shape of the sample and the geometrical arrangement of the filler particles, elongation, contraction, bending or rotation can be achieved and used to create motion [155]. In experimental MRE characterization in contrast, one has to keep in mind that these parasite field gradients can lead to additional deformation of the material on top of the original magnetostriction. Furthermore, even if the externally applied field \mathbf{h}_0 is perfectly uniform, the magnetized MRE sample can further create field gradients within itself. Magneto-static field equations and the corresponding boundary conditions indeed prescribe the field distribution within a body, which strongly depends on its geometry. Only for ellipsoids of revolution are the magnetization \mathbf{m} as well as the perturbation $\tilde{\mathbf{h}}$ and hence the total magnetic field \mathbf{b} uniform within the body [120].

II.2.4 Magnetic field-dependent modulus

The field-dependent modulus is closely related to the coupled magneto-mechanical behavior and attributed to the same physical mechanisms. The deformation exclusively due to an externally applied magnetic field can be defined as the free deformation of the MRE material. If such a deformation is restricted by imposed mechanical boundary conditions, additional work has to be exerted to act upon the material, thus leading to a field-induced increase in stiffness. This corresponds to the so-called magneto-rheological (MR) effect introduced by many researchers. Very different results are reported about the relative MR effect: from as low as a few dozen percent [13] up to more than a thousand percent [140]. Due to the great variety of investigated materials, manufacturing techniques and testing conditions, it

is difficult to compare objectively all these results. However, some tendencies regarding the field-dependent modulus of MREs can be outlined:

- Generally speaking, the MR effect results from an overall competition between the mechanical stiffness of the composite and the magnetic interactions between the particles and the field: a lower composite stiffness leads to a larger MR effect.
- The modulus usually increases with iron-filler content. An optimal proportion of particles, resulting from a competition between the stiffening of the composite and the magnetic interactions (within the linear regime), is estimated between 20% and 30% particle volume fraction [88, 46, 42].
- The MR effect increases with increasing magnetic field but saturates above a certain level of applied magnetic field [88, 63] due to the saturation magnetization of the particles.
- The modulus increase tends to be highest in the small-strain region (from 0 to 5%) while it tends to decrease in the mid-strain region (around 15%) [135, 9].
- The MR effect can be further enhanced in field-structured MREs [9, 148] thereby meaning that it is affected by the microstructure of the sample.

II.3 Samples

Due to the scarcity of coupled magneto-mechanical characterization existing in the literature, there has been so far no typical or ideal sample specially devised for carrying a coupled characterization. Considering this is the main goal of the present study, the crucial topic of the sample shape is first addressed in what follows. Then, aspects pertaining to material selection and fabrication protocols for both isotropic and transversely isotropic MRE samples are presented

II.3.1 Sample shape for coupled magneto-mechanical testing

In order to ensure reproducibility in material testing, norms provide guidelines for sample shape design depending on both the tested material and the type of loading. Behind a sample's shape for mechanical material properties evaluation lies the Saint Venant's principle according to which the difference between the effects of two different but statically equivalent loads becomes very small at sufficiently large distances from the load [131]. Practically, this means that for long tensile samples, the stress is homogeneous in the gage area of the sample far away from the clamping. If the sample is to be shorter, stress localization at the clamping needs to be attenuated by smooth root-corner radii from the sample's head to its gage area, hence yielding the well-known dog-bone (or dumbbell) shape samples for tensile testing. For elastomers tested in tension, the corresponding (and equivalent) norms are the American ASTM D412 and its European counterpart ISO 37. The cross-section of the proposed samples is rectangular since, in polymer testing, samples are often punched out of large sheets of the material of interest. However, as mentioned in Section II.2.3, the shape of a body influences the distribution of the total magnetic field \mathbf{b} , even when submitted to a uniform external magnetic field \mathbf{b}_0 . A numerical simulation, performed with the Finite Element Method (FEM) software ANSYS and reported in Fig. II.1a, shows that the magnetic perturbation field $\tilde{\mathbf{b}}$ (and thus \mathbf{b} when the sample is magnetized by a uniform external magnetic field \mathbf{b}_0) is not homogeneous in the gage area of a dog-bone shape sample with a rectangular cross-section.

Following common usage in tensile testing of metals (ASTM E8/ISO 6892 [51, 1]), the same type of dog-bone shape sample, but with a circular cross-section, could be used, as it does not affect the homogeneity of the mechanical quantities in the gage area. The dimensions of this sample are reported in Fig. II.2a. Note that its heads are flattened rather than cylindrical in order to adapt to the clamps of the setup used in this study. In this case, the FEM simulation reported in Fig. II.1b shows that the magnetic perturbation field $\tilde{\mathbf{b}}$ is now homogeneous in the gage area when the sample is uniformly magnetized transverse to its longitudinal axis. Nevertheless, this sample still exhibits a non-homogeneous magnetic field \mathbf{b} in its heads. As a matter of fact, only magnetic bodies of ellipsoidal (or as a subset, spherical) shapes can exhibit a homogeneous magnetic field \mathbf{b} throughout their whole body [120, 21]. Though in mechanics, homogeneity is sufficient in the gage area to ensure proper material characterization, it has to be verified experimentally whether this is also the case when magneto-mechanical coupling is considered as the magnetization of the heads may influence the sample's behavior.

Based on the design of the dog-bone shape sample with a circular cross-section (Fig. II.2a), the sample heads are replaced by non-magnetic 3D-printed plastic insets while only the cylindrical gage area is made of MRE and terminated at both ends by an ellipsoidal cap (see Fig. II.2b, Fig. II.2c and further details in Section II.3.3 dedicated to fabrication). This thus brings the body of the sample as close as possible to an ellipsoid while retaining the homogeneity of mechanical quantities in the gage area. A FEM simulation, reported in Fig. II.1c, confirms that the magnetic perturbation field $\tilde{\mathbf{b}}$ is almost homogeneous in the nearly ellipsoidal MRE body of this modified sample as the heads do not interact with the magnetic field. Before looking at the impact of this modification on the magneto-mechanical coupling, it is first checked whether it affects the mechanical response. To this end, purely mechanical tests are performed on fully-MRE dog-bone shape samples with a circular cross-section and on samples with a nearly ellipsoidal MRE body and plastic heads, for each particle content considered in this study and expressed as phr (per hundred rubber, see Section II.3.2). All the corresponding upload parts of the 3rd stabilized cycles (see Section II.4.4 for details on the testing protocol) are presented in Fig. II.3a. The curves reveal that the mechanical responses of the tested samples are only identical up to a certain threshold, after which the latter sample exhibits a loss of carrying load capacity due to debonding at the interface between the soft MRE body and the stiffer plastic heads. The threshold is the lowest for the highest particle content but for all particle contents studied here, the fully-MRE dog-bone shape sample with a circular cross-section and the sample with a nearly ellipsoidal MRE body and plastic heads show the same mechanical response, within experimental error, up to a 1.4 stretch. To address the question of the magneto-mechanical coupling, the stress response under purely magnetic loading (up to $\mathbf{b}_0 = 0.8$ T) is monitored for the two above-mentioned geometries of MRE samples, in the case of the lowest particle content considered in the study (70 phr), as they are held fixed in the uniform magnetic field, applied transversely to their longitudinal axis, within the dedicated setup that will be described in details in Section II.4.1. The corresponding results are reported in Fig. II.3b and show that the stress exerted by the sample is much higher in the case of the fully MRE dog-bone shape sample with a circular cross-section than in the case of the dog-bone shape sample with a nearly ellipsoidal MRE body and plastic heads. This confirms the large contribution of the magnetization gradients present within the MRE heads to the magneto-mechanical response of the sample: in such a case, the measurements would yield the response of the whole structure rather than that of the material. As a conclusion, in order to perform a coupled magneto-mechanical testing of MREs, fully-MRE dog-bone shape samples with a circular cross-section will be used for purely mechanical tests up to large stretches while samples with a nearly ellipsoidal MRE body and plastic heads will be used for coupled experiments, provided that the overall stretch remains below the threshold identified earlier. Note that this threshold of 1.4 nominal stretch (40% nominal strain) is largely beyond the domain of small strains.

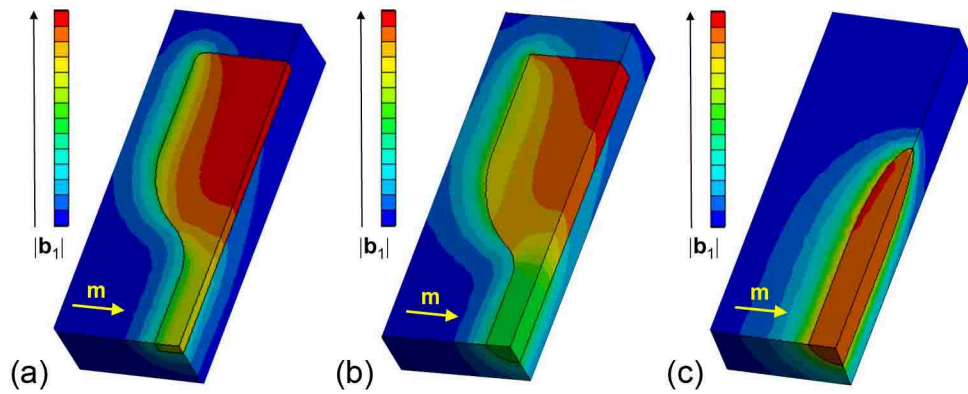


Figure II.1: 3D FEM simulations in ANSYS showing the magnitude of the magnetic perturbation field $|\tilde{\mathbf{b}}|$ in different types of samples uniformly magnetized transversely to their longitudinal axis a) Dog-bone shape sample with rectangular cross-section b) Dog-bone shape sample with circular cross-section c) Cylinder closed with two half-ellipsoids.

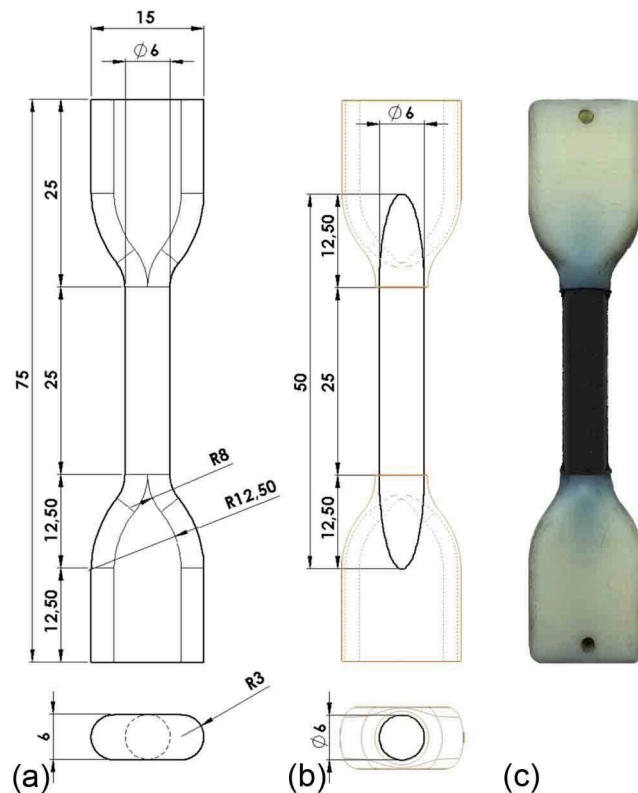


Figure II.2: 2 a) Dimensions of the fully-MRE dog-bone shape sample with a circular cross-section. b) Dimensions of the sample with a nearly ellipsoidal MRE body and non-magnetic heads. All dimensions are in millimeters. c) Picture of the sample with a nearly ellipsoidal MRE body and non-magnetic heads.

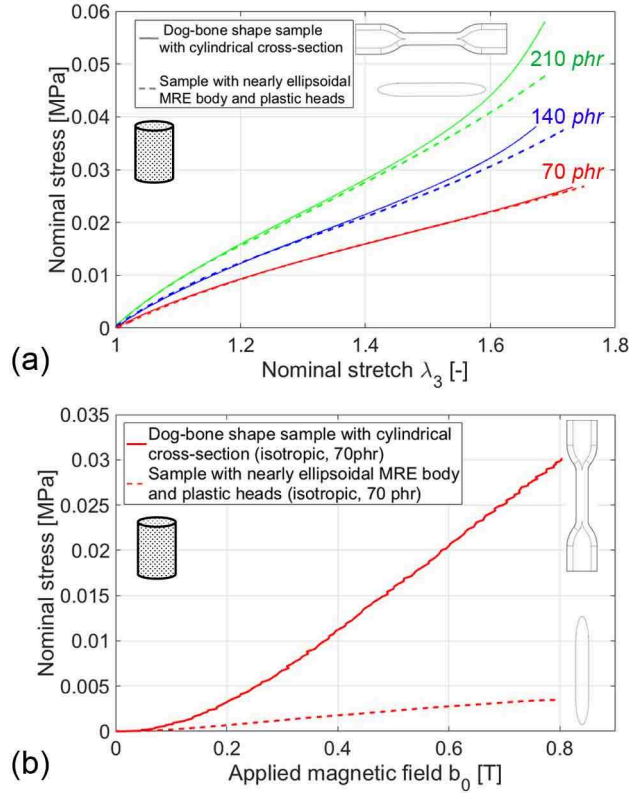


Figure II.3: a) Nominal stress-stretch curve of fully-MRE dog-bone shape samples with a circular cross-section and of samples with a nearly ellipsoidal MRE body and non-magnetic heads, for MRE blends of different particle contents (70 phr, 140 phr and 210 phr). b) Stress response of the two above-mentioned geometries of MRE samples, in the case of the lowest particle content considered (70 phr), as they are held fixed in a uniform magnetic field, applied transversely to their longitudinal axis.

II.3.2 Materials

In the perspective of obtaining a material in which the magneto-mechanical coupling is optimal (i.e. largest deformation produced by the smallest magnetic field), the selected matrix material is a very soft and stretchable silicone elastomer: Ecoflex 00-20 from Smooth-On Inc., USA. This elastomer is a room temperature two-part addition-cured platinum-catalyzed system (RTV-2) with a mixed density ρ_{sil} of 1,070 kg/m³ and a mixed viscosity of 3 Pa.s that offers a good compromise between good dispersion when mixing, easy pouring and minimal settling of particles during accelerated curing.

The filler phase is carbonyl iron powder (CIP) SM from BASF Germany. This powder is made of spherical particles with a median diameter of 3.5 μm and contains up to 99.8% of Fe with low amounts of C, N and O. It is thus considered magnetically ‘soft’ as it does not retain magnetization once the magnetic field is turned off. As soft iron is also known to have a low coercivity and a magnetic saturation $\mu_0 m_s = 2.1 \text{ T}$ [79], these particles are good candidates for MRE applications with optimal coupling. According to the manufacturer, the

bulk density ρ_{bulk} is between 1,500 and 2,500 kg/m³ in the form of powder, while the density of iron (as a solid metal) is 7,874 kg/m³.

The above-mentioned powder bulk density takes into account the presence of air gaps between particles when they occupy a given volume in the form of powder but this becomes irrelevant once the particles are mixed in the viscous liquid elastomer. Hence the density commonly considered in the MRE literature is taken as the one of iron (e.g. [134]) or slightly lower than that of iron (e.g. [68]), probably to account for the exact chemistry of the particles. In practice during fabrication, the different elements of the compound are weighed and one actually works with m_{CIP} , m_A and m_B , that correspond to the mass of CIP particles, Part A silicone and Part B catalyzer, respectively. In the chemistry and polymer literature [33], the particles to silicone ratio is often expressed in Parts per Hundred Rubber (phr), which gives the mass of filler per hundred parts of raw compounded polymer mass ($phr = 100 \times m_{CIP}/(m_A + m_B)$). The CIP density ρ_{CIP} only comes into play to calculate the corresponding particle volume fraction c as follows

$$c = \frac{\frac{m_{CIP}}{\rho_{CIP}}}{\frac{m_{CIP}}{\rho_{CIP}} + \frac{m_A + m_B}{\rho_{sil}}} = \left(1 + \frac{100}{phr} \frac{\rho_{CIP}}{\rho_{sil}}\right)^{-1}. \quad (\text{II.3.1})$$

The particle volume fraction c is actually preferred in the mechanics community because it appears in the constitutive equations. However, considering the fact that it involves the equivalent density of CIP particles once dispersed in silicone, which might be sensitive to the type of particles used, we will compare MRE composite samples on the basis of the particles to silicone mass ratio expressed in phr throughout this chapter. The value taken for the density of CIP should be clearly stated if proper comparisons have to be made or if the volume fraction is needed as input for modeling. In this study, considering $\rho_{CIP} = 7,874$ kg/m³, the different MRE blends contents are 70, 140 and 210 phr, which corresponds to 8.7, 16 and 22.2% volume fraction, respectively.

As mentioned in Section II.2.1, the quality of the interfacial adhesion between the filler particles and the matrix greatly influences the strength of composite materials, especially under large deformations. However this topic has rarely been investigated in details in the case of MREs. The interfacial adhesion between CIP particles and the silicone matrix used in this manuscript was investigated for samples of different particle content submitted to a purely mechanical loading in a previous study of Pössinger and Bodelot [126]. It was found that a silane primer¹ treatment of the particles prior to sample fabrication improved the macroscopic mechanical behavior, in terms of ultimate load carrying capacity, by preventing debonding of the particles from the matrix, but only above a critical stretch threshold that depends on the particles to silicone ratio and decreases with it. Hence, in the stretch and particles to silicone ratio ranges targeted in the present work (i.e. under a nominal stretch of 1.8 and below 210 phr, respectively) particle treatment does not influence the mechanical response. Nevertheless, we discovered in this study that the previous results and thresholds,

¹ A silane coupling agent or primer typically consists of two different reactive groups located at either end of the active molecule, one compatible with the filler particles and the other one with the elastomer matrix. Applied in a thin, theoretically monomolecular layer, the primer serves as an adhesion promoter between the two initially non-bonding surfaces.

found for MRE samples submitted to purely uniaxial mechanical loadings, do not hold when magnetic loadings are at play. Let us focus in Fig. II.4 on the highest particle content used in this study (210 phr) -as this is the case for which the debonding propensity is the highest- and consider MRE samples containing uniformly distributed particles that are either non-treated or treated (solid lines versus dashed lines in the plots). All plots correspond to the upload part of the 3rd stabilized cycle (see details on the testing protocol in Section II.4.4). As mentioned above, under purely mechanical loading, such dog-bone shape samples with cylindrical cross-section exhibit the same nominal stress-nominal stretch response as reported in Fig. II.4a. However, such samples with a nearly ellipsoidal MRE body and non-magnetic heads, if submitted to a uniform magnetic field perpendicular to their main axis while the force is maintained at 0 N, exhibit different stretch responses in all principal directions well before the threshold found under purely mechanical loading, as highlighted in Fig. II.4b. Indeed, treated and non treated samples start exhibiting different stretch responses for a relatively low applied magnetic field \mathbf{b}_0 of 0.2 T while the corresponding stretch values remain very low (a few percent strain). The debonding occurring under magnetic field can be seen more clearly when looking at the Jacobian of the transformation $J = \det(\lambda_1 \lambda_2 \lambda_3)$, where λ_1 , λ_2 , λ_3 are the three principal stretches of the sample. Error bars were added in these plots to quantify the possible error committed when calculating J from the measured principal stretches. This error is on the order of $8 \cdot 10^{-4}$ and confirms that reported values that are slightly below 1 are within experimental error since J cannot theoretically be smaller than 1 (see Section II.4.2 for details on measurement error). In the case of the mechanical test (see Fig. II.4c), the Jacobian remains around 1 with a maximum deviation of 0.003 at a 1.6 stretch whether the sample had its particles treated or not. This confirms that there is very minute to no debonding between the non-treated particles and the matrix during mechanical testing. However, during the application of a magnetic field on a non-treated sample, J steadily increases with the magnetic field and already reaches a value of 1.006 for only a 1.05 stretch in the field direction. The reported increase in volume in the non-treated case indicates that cavities are created in the MRE when the particles interact with the magnetic field, which means that the debonding between the particles and the matrix is much stronger under magnetic loading than under mechanical loading. As a consequence, only particles used in MRE samples dedicated to coupled magneto-mechanical tests will be pre-treated in this study.

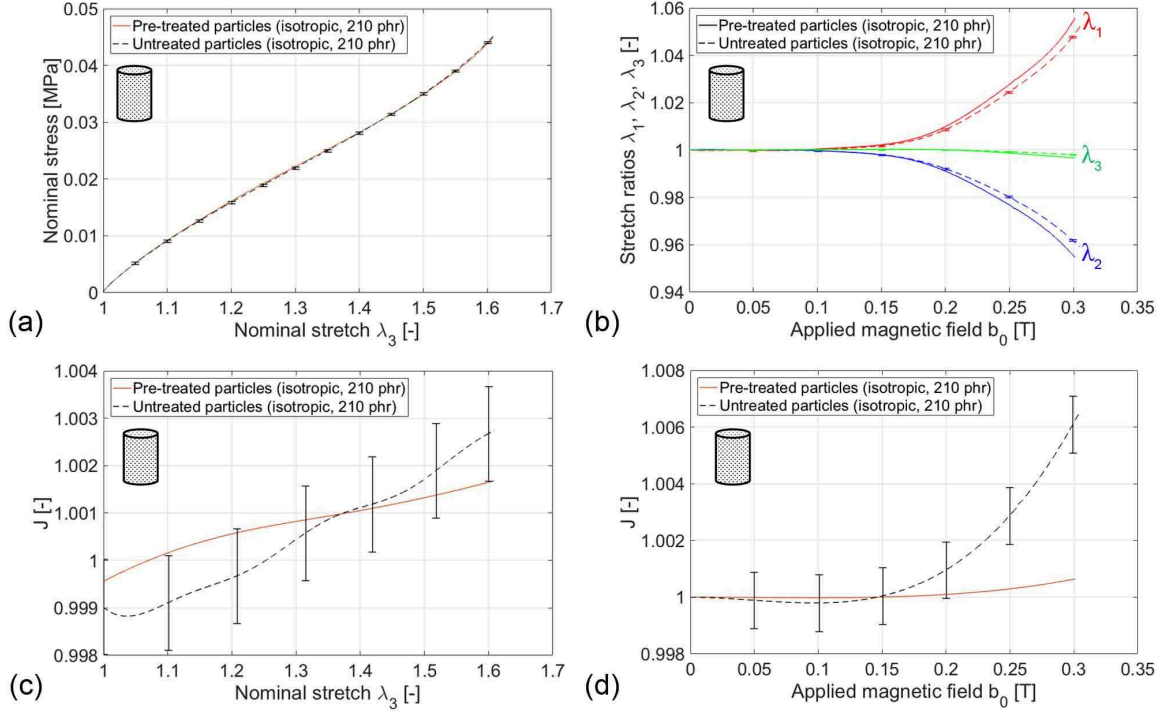


Figure II.4: Comparison of the response of 210 phr MRE samples for which particles have been either treated (solid lines) or untreated (dashed lines). a) Mechanical nominal stress-nominal stretch response of such dog-bone shaped samples with a cylindrical cross-section. b) All principal stretches responses of such samples with a nearly ellipsoidal MRE body and non-magnetic heads when submitted to a uniform magnetic field \mathbf{b}_0 perpendicular to their main axis while the force is maintained at 0 N. c) Jacobian of the transformation during a mechanical test on a treated and a non-treated sample. d) Jacobian of the transformation during a magneto-mechanical test on a treated and untreated sample.

II.3.3 Fabrication procedure

As mentioned in the previous section, only particles used for MRE samples dedicated to coupled magneto-mechanical tests are pre-treated with a silane primer. The silane primer used in this study is vinyltrimethoxysilane 97% from Sigma-Aldrich. Particles are first rinsed: they are soaked in a beaker filled with isopropanol and placed in an ultrasonic bath for 2 min. The mix is then filtrated through a mesh of 3 to 5 μm porosity and the retained particles are transferred to a second beaker. After being filled with vinyltrimethoxysilane, the beaker is placed in an ultrasonic bath for 4 min. This mix is filtrated and the retained particles are again transferred to a new beaker subsequently placed on a hot plate set at 60° C for 1 hour. Once fully dried, the particles are functionalized with silane and ready to use in the remainder of the procedure.

To fabricate pure silicone material, the elastomer (Part A) and the catalyzer (Part B) are first dispensed in a beaker in a one to one weight ratio thanks to a 10 mg-precision scale. In the case of MRE samples, the desired mass of particles and the polymer (Part A) are blended

and mechanically mixed for two minutes to ensure a proper dispersion of the particles among the polymer molecular chains before starting the polymerization of the network by adding the catalyzer (Part B). The obtained blend is then again mixed thoroughly mechanically for three minutes. Mechanical mixing is carried out with a large wing nut mounted on a drill rotating at 400 rpm in order to ensure a homogeneous dispersion of all constituents in the compound. This mixed compound is degassed at 1 bar vacuum for 6 minutes to eliminate any air entrapped during mixing and then poured by hand in a mold. The steps described above are conducted in less than 30 minutes, which is the so-called ‘pot lifetime’ of the Ecoflex 00-20 elastomer, according to the manufacturer. Finally, curing is performed by heating the mold up to 100° C at 10° C/min, maintaining it at this temperature for 60 minutes and letting it cool down back to room temperature. After this, the sample can be removed from the mold. Though this silicone can be cured at room temperature within 24 h, accelerating the curing process via heating has two advantages: lock particles in place quickly to avoid settling down during curing and reduce manufacturing time.

In order to fabricate a sample of the desired shape, dedicated molds were machined out of copper². This material was selected for its high thermal conductivity of 390 W.m⁻¹.K⁻¹ so as to ensure optimized thermal exchanges through a significant thickness. For the dog-bone sample with circular cross-section described in Fig. II.2a, the negative half imprint of the sample was machined out of a pair of plates (each measuring 81 mm × 60 mm × 4.5 mm) thus providing a mold when assembled together. A detachable piece located next to the sample heads provides clearance to fill the material into the mold along the sample height and is reattached before curing. For the sample with nearly ellipsoidal MRE body and plastic heads (Fig. II.2b), the negative half imprint of the fully assembled sample was also machined out of a pair of plates (81 mm × 60 mm × 5.5 mm). The lower 3D-printed plastic head is first inserted before assembling the mold, then the MRE mixture is poured, the upper 3D-printed plastic head is inserted and the whole mold is finally closed before curing. For this sample, the part of the plastic heads in contact with the MRE mixture is coated with a primer (Primer 3 from ACC Silicone) to enhance adhesion between the rigid plastic heads and the soft body of the sample.

In order to obtain a non-magnetic heating system allowing to cure the sample while the mold is placed in an electromagnet, each the above-mentioned molds can be sandwiched between two other copper plates (each measuring 81 mm × 60 mm × 3 mm) that bear, at the center of their external surface, a 30 W copper heating resistance encapsulated in silicon covering an area of 76.2 mm × 41.9 mm. A non-magnetic type T thermocouple with 0.5° C precision is inserted in one of the half imprint of each mold, close to the center of the sample, and connected to a temperature on/off PID regulation system that delivers current to the heating resistance following the heating schedule mentioned earlier.

² Copper is very slightly diamagnetic (i.e. it creates a small magnetic field in opposition to the applied field) but its susceptibility is $-1 \cdot 10^{-5}$ [79]. A relevant comparison is to be made with aluminum: it has a thermal conductivity of 237 W.m⁻¹.K⁻¹ and is paramagnetic (i.e. it creates a small magnetic field in the direction of the applied field) with a susceptibility of $2.2 \cdot 10^{-5}$ [79]. In any case, such values of susceptibilities are so negligible, that under the maximum magnetic field of 0.8 T that we can achieve, such a perturbation remains lower than that of the Earth magnetic field (between 25 and $65 \cdot 10^{-6}$ T).

To fabricate transversely isotropic MRE samples, curing must be conducted under magnetic field. For curing - and the subsequent magneto-mechanical characterization - we use a two-coil electromagnet generating a field of 0.8 T between two 90 mm-diameter poles separated by a 82 mm-air gap. In this gap comes a removable aluminum plate maintained from outside of the magnet by a fixed bracket. Centering pins are installed on this plate for an easy and repeatable positioning of dedicated stands at the center of the magnetic field. These stands permit the fabrication of samples having chains of particles of different orientations, namely along the sample longitudinal direction so that chains are perpendicular to the field during the tests and along the sample transverse direction so that chains are either parallel or perpendicular to the field during the tests. The parts of the stand in contact with the copper mold are made of tubular polyether ether ketone (PEEK) material exhibiting good mechanical strength while having a very low thermal conductivity of $0.25 \text{ W}\cdot\text{m}^{-1}\cdot\text{K}^{-1}$ so that the stand does not act as a heat sink. When curing is conducted under magnetic field, the mold is placed within the poles before the magnetic field \mathbf{b}_0 is linearly increased from 0 to 0.8 T in 340 s. The curing schedule then starts when the maximum field is attained. Note that raising the magnetic field faster or starting the curing before the maximum field was attained led in our samples to either some local aggregates in the microstructure or large zones with fewer particles. Hence the above-mentioned parameters need to be tuned and the microstructures studied under Scanning Electron Microscope to ensure that the desired microstructure of particle chains is actually obtained and can be so in a repeatable fashion. Note also that only one sample at a time can be cured under magnetic field since the presence of neighboring MRE samples in the field would compromise the uniformity of the field within each sample.

II.4 Experimental methods

II.4.1 General setup

To obtain the macroscopic behavior of MREs under coupled magneto-mechanical loading, a dedicated setup, whose overall schematic is given in Fig. II.5a, has been designed. It consists of an electromagnet producing a homogeneous field within an air gap and of a tension setup that brings the sample at the center of the magnet and allows for the application of low rate cyclic tensile loadings while monitoring in-situ mechanical and magnetic quantities.

The electromagnet used in this study was custom-built by Bouhnik SAS and SigmaPhi, two French companies specialized in power electronics and coils systems. The electromagnet consists of two current conducting water-cooled copper coils mounted on a C-frame, each bearing in their center a truncated conical iron pole 90 mm in diameter, so as to concentrate a nearly homogeneous field across the 82 mm air gap between the two poles without induced heating during the experiments. The electromagnet is connected to a four-quadrant bipolar water-cooled power supply of $\pm 70 \text{ V}$ and $\pm 70 \text{ A}$ nominal voltage and intensity, respectively. Generation of the magnetic field is current-controlled (precision $\pm 50 \text{ mA}$) but can also be field-controlled when a probe measuring the magnetic field is installed within the air gap. The intensity delivered by the power supply can be varied either manually or through an

analogic entry and yields a field $\mathbf{b}_0 = 0.8$ T at the center of the air gap for a current of 68 A. The magnetic field \mathbf{b}_0 is homogeneous in the central zone of the air gap for all three directions (± 1 mT at ± 3 mm from the center). It then shows an increase in direction \mathbf{e}_1 towards the poles as well as a decrease in directions \mathbf{e}_2 and \mathbf{e}_3 away from the center (for \mathbf{e}_3 : -28 mT at $+25$ mm and -37 mT at -25 mm at a nominal maximum field of 0.8 T at the center). Note that due to the shape of the frame (C-frame), there is a slight offset of 2.5 mm in the positive direction of \mathbf{e}_3 for the point of maximum magnetic field.

Symmetric tension is applied to the samples thanks to two linear Piezo LEGS motors from PiezoMotor installed in opposition (see Fig. II.5b). Piezoelectric materials have the advantage to be insensitive to magnetic fields and, per the needs of our application, these motors do not contain any ferromagnetic component that could disturb the applied magnetic field. Classical piezoelectric actuators are well known for providing nanometric to micrometric displacements while accommodating large loads; however, in these motors, the long-range motion of the axis is obtained by incremental steps through friction between the axis and piezo-operated driving legs. As a consequence, they can only bear very small loads. Hence, the recommended operating range is between 0 and 3 N with a stall load of 6.5 N while the maximum stroke is 80 mm. Microsteps can be as low as 40 nm but because this technology cannot guarantee equal steps, especially under varying load, the motors have to be operated in a closed-displacement loop. To this end, the axis of each motor is equipped with a laser-engraved graduated glass ruler monitored by optical encoders; both provided by Renishaw (ATOM miniature encoder system). Once integrated in a LabVIEW (National Instruments) in-house interface program, the whole system provides a resolution of $1 \mu\text{m}$ and a precision of $\pm 3 \mu\text{m}$. Each Piezo LEGS motor, along with its encoding system, is mounted at the sensitive end of a LCAE-600G single-point load cell from OMEGA. These load cells, generally used for scales and weighing platforms, are made of aluminum and have a maximum capacity of 6 N and a precision of ± 3 mN. At the end of the motor are attached custom-designed clamps that hold the sample during the test (see Fig. II.5b and Fig. II.6a). They consist of two aluminum plates; the first one is permanently fixed to the motor axis while the second one is free to slide along two vertical guiding rods fixed along the normal axis to the first plate. Once the fully-MRE sample is installed in the clamps, the latter are pinched thanks to a spring system made of a brass thin plate and two non-magnetic bent screws. This spring-loading of the clamps maintains a constant gripping force on the head of the samples -that deform appreciably due to the large deformations they experience and the incompressibility of the material- and thus prevents slippage during tests. In the case of the samples with plastic heads, the latter are directly attached to the second plate before installing the clamps. Finally, this symmetric tension system is attached to an aluminum plate connected to two cylindrical arms gliding within two dry-friction bearings installed outside of the electromagnet, as can be seen in Fig. II.5a and Fig. II.5b. This allows taking the tension system in and out of the electromagnet for mounting the samples outside of the electromagnet prior to testing. With this tension system, mechanical tests can either be carried out in displacement-controlled or force-controlled modes.

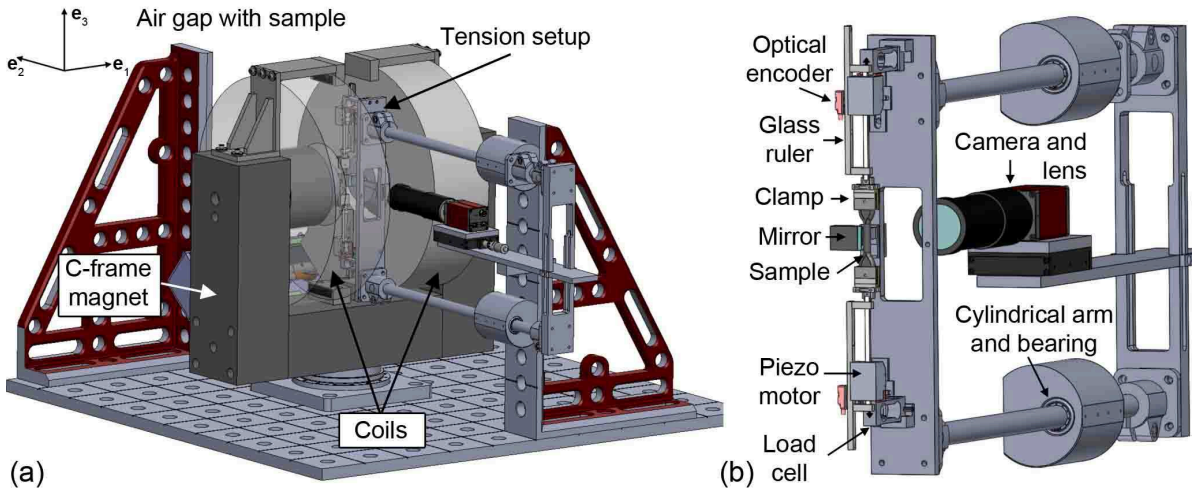


Figure II.5: a) Overall schematic of the magneto-mechanical characterization setup. b) Schematic of the symmetric tensile setup showing the Piezo LEGS motors, the rulers and optical encoders, the load cells, the clamps and the sample. The setup holds a camera for optical diagnostics and can be taken in and out of the electromagnet for mounting the samples outside of the electromagnet prior to testing.

II.4.2 Mechanical diagnostics

Strains in the gage area of the samples are measured via non-contact video extensometry. To this end, a stand is attached perpendicularly to an aluminum plate mounted at the other end of the two cylindrical arms gliding within the bearings, opposite to the plate holding the tension system (see Section II.4.1 and Fig. II.5b). A 5 Megapixels F-505B Pike CCD camera is installed on this stand and equipped with a $0.3\times$ telecentric lens to take images of the sample during testing at a rate of 6.5 frames per second. In the configuration used for the study, the working distance is 173 mm, the field of view is $16\text{ mm} \times 20\text{ mm}$ and the resolution is $12\text{ }\mu\text{m}/\text{pixel}$ while the depth of field is 8 mm. For telecentric lenses, the magnification remains constant throughout the depth of field [70], hence the out-of-plane movement of the sample due to its change in section during tension does not affect the tracking carried out on the sample. Additionally, a mirror making a 45° angle with the camera CCD array is positioned next to the sample and reflects an image of its side towards the camera (see Fig. II.6a). A single image thus contains a front view of the sample as well as a view of its side (Fig. II.6b), which gives access to the strains along the three principal directions of the sample (Fig. II.6c). Note that once the optical components are installed and aligned, they stay in position since both the plate holding the tensile system and mirror, on the one hand, and the plate holding the camera, on the other hand, remain fixed in relation to each other when the whole system glides along the bearings.

To obtain the longitudinal strains (along e_3), markers -consisting in black (for pure silicone samples) or white (for MRE samples) acrylic paint dots applied with a sharp tip- are drawn 6 mm apart from the center along the vertical axis of the sample prior to testing, as represented in Fig. II.6c. To obtain transverse strains (along e_1 and e_2), one makes sure that

the background behind the sample is of the opposite shade than that of the sample so that there is a sharp change of shade at the interface between the sample and the background. A tracking algorithm implemented in LabVIEW then follows in-situ the two vertical dots and the two pairs of borders, thus giving access to the true (Eulerian) strains $\epsilon_i = \ln(\lambda_i)$ along direction \mathbf{e}_3 , \mathbf{e}_1 and \mathbf{e}_2 , respectively (see Fig. II.6). The precision obtained on the stretches values is $2 \cdot 10^{-4}$ for the dots tracking and $3 \cdot 10^{-4}$ for the border tracking (maximum error found during a rigid body motion were the stretch is expected to remain 1).

The force exerted on the sample during loading is measured by the two LCAE-600G single-point load cells from OMEGA mentioned in Section II.4.1. The actual force is obtained by dividing by two the sum of the voltage readings coming out of the cells (calibration was performed by the manufacturer and was checked with calibrated weights before use).

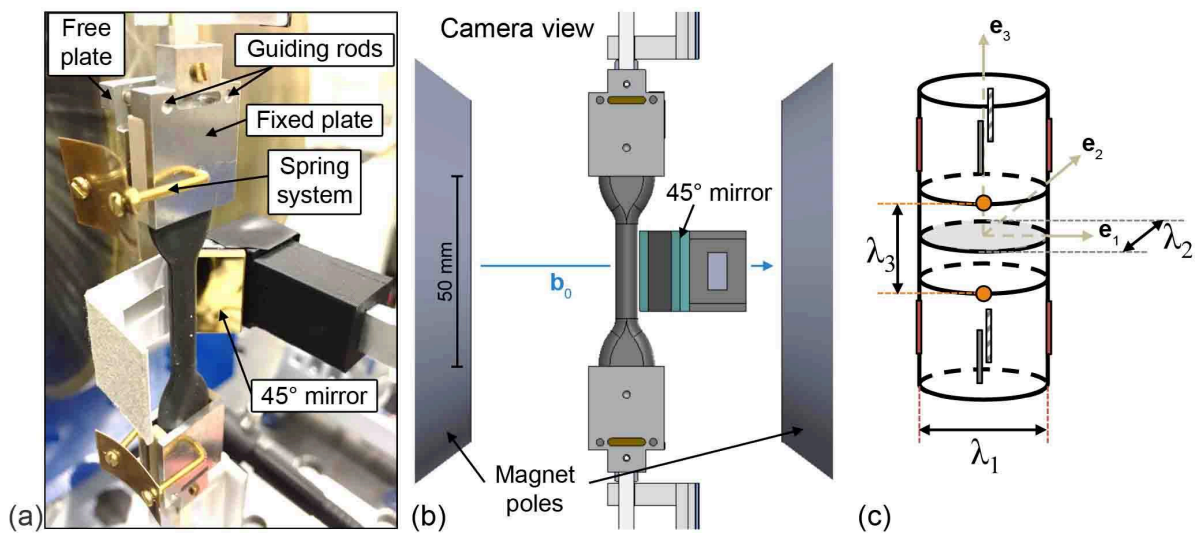


Figure II.6: a) Picture of the setup especially showing the clamps systems holding the specimen and the 45° mirror. b) Schematic of the sample held at the center of the electromagnet airgap and of the 45° mirror from the camera vantage point. c) Schematic of the tracked dots and borders on the sample and principal stretches.

II.4.3 Magnetic diagnostics

In-situ magnetic field measurements are carried out with transversal Hall probes. A Hall sensor consists in a thin semi-conductor. When a current is applied to the semi-conductor and the latter is placed within a magnetic field \mathbf{b} so that the field lines are along its thickness, a voltage develops between the faces across the thickness. This phenomenon, known as the Hall effect, was reported by Edwin H. Hall in 1879 [74]. Because these sensors are sensitive to the magnetic field across their thickness, they need to be placed strictly perpendicular to the lines of the magnetic flux to be probed. Additionally, they need to be calibrated in reference to a known magnetic field. Two HGT-2010 Hall sensors from Lakeshore are used in this study. The sensitive semi-conductor is a $760 \mu\text{m}$ -thick square ($2.28 \text{ mm} \times 2.28 \text{ mm}$) mounted at the end of a plastic stem. Both sensors are calibrated by placing them at the

center of the electromagnet where the same measurement can be done with the Hall probe given and calibrated by the electromagnet manufacturer, and they provide a precision of $\pm 1\%$ at a range of ± 1 T and stable temperature.

For coupled experiments, a fixed bracket placed behind the electromagnet is equipped with displacement stages holding two extension arms carrying each a Hall probe, as depicted in Fig. II.7a. One probe (named probe h) is located behind the sample, in its vertical mid-plane, and can be adjusted along direction \mathbf{e}_2 to come nearly in contact with the sample when at rest. The second probe (named probe m) is located on the side of the sample so that its center is in the other vertical mid-plane of the sample and can be adjusted along directions \mathbf{e}_1 and \mathbf{e}_2 to also come nearly in contact with the sample. In both cases, the normal to the sensing element is along the applied magnetic field \mathbf{b}_0 . Since the samples used for the magnetic measurements have a nearly ellipsoidal MRE body, the perturbation field $\tilde{\mathbf{h}}$ and the magnetization \mathbf{m} , hence the total magnetic field \mathbf{b} , all are uniform within the MRE material. Due to the continuity of the tangential component of \mathbf{h} at the interface between the air and the sample, the Hall probe h placed at the back of the sample gives access to the total field $\mu_0 \mathbf{h}$ [T] inside the material (the externally applied field \mathbf{h}_0 plus the perturbation field $\tilde{\mathbf{h}}$, measured in air), since the contribution of the magnetization \mathbf{m} vanishes at that point. Due to the continuity of the normal component of \mathbf{b} at the interface between the air and the sample, the total magnetic field \mathbf{b} [T] inside the sample - now including the contribution of the total \mathbf{h} -field (measured at the back) plus the contribution of the magnetization \mathbf{m} - is measured by the lateral Hall probe m, which then gives access to the magnetization \mathbf{m} inside the sample. The distribution of the magnetic field \mathbf{b} in the air-gap in the presence of a magnetic sample is sketched in Fig. II.7b along with the positions of the h and m sensors relative to the sample.

Before the test, both probes are positioned with the help of the camera to come nearly in contact with the sample at rest however they cannot be placed exactly at the discontinuity interface between the air and the sample due to geometrical limitations. Additionally, the magnetic quantities also need to be measured for different levels of applied magnetic field that yield the sample to deform and move away from the sensors. Hence measurements need to be systematically corrected to account for the distance between the sensitive part of the probes and sample/air interface. Fortunately, the evolutions of the \mathbf{e}_1 component of \mathbf{h} and \mathbf{b} along direction \mathbf{e}_2 and along direction \mathbf{e}_1 , respectively, can be derived analytically (the equations at play in this correction are detailed in Appendix II.A). The obtained results are plotted in Fig. II.7c, where the top curve corresponds to the evolution of the \mathbf{e}_1 component of the \mathbf{h} field along direction \mathbf{e}_2 and the bottom one to the evolution of the \mathbf{e}_1 component of the \mathbf{b} field along direction \mathbf{e}_1 , with both curves covering the discontinuity interface between the air and the sample. To link the current value measured away from the sample to the actual value at the sample/air interface thanks to the previous curves, the distance between the sensitive part of the probes and sample/air interface is monitored in-situ with the border detection algorithm used in Section II.4.2 to follow the sample dimensions in the transverse directions.

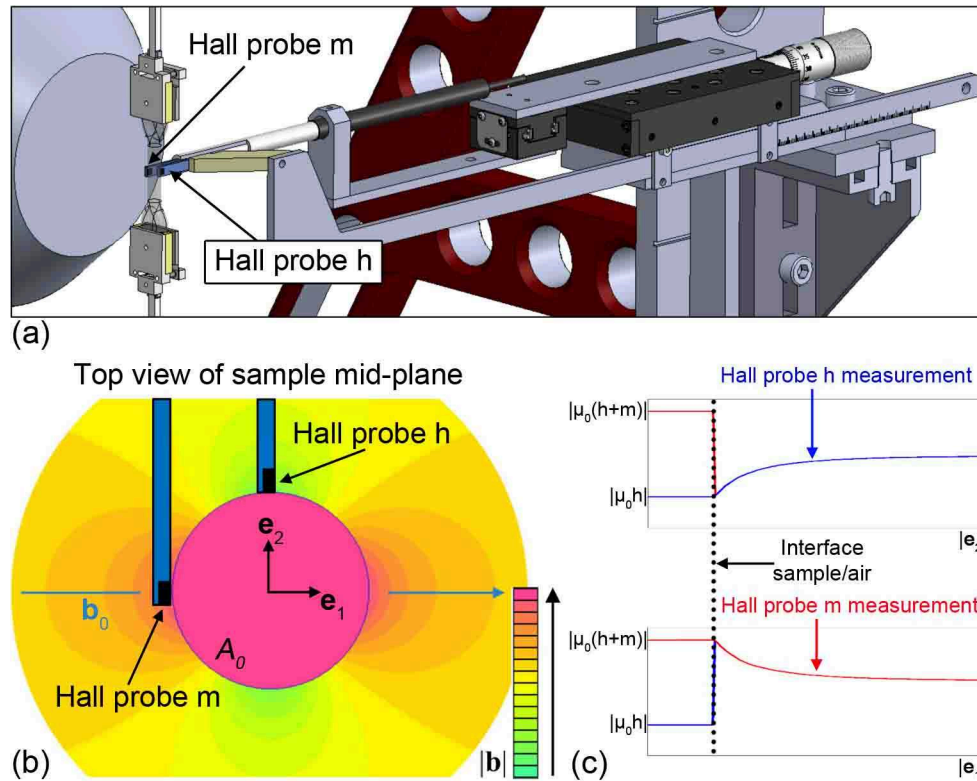


Figure II.7: a) Stand coming from behind the electromagnet and holding the two Hall probes h and m . b) 2D plane FEM simulation of the distribution of the magnetic field \mathbf{b} in the airgap of an electromagnet in the presence of a magnetic sample of circular cross-section having a homogeneous magnetization \mathbf{m} . View from top within the horizontal mid-plane of the sample. c) Evolution of the \mathbf{e}_1 component of the magnetic intensity \mathbf{h} along direction \mathbf{e}_2 (top) and of the \mathbf{e}_1 component of the magnetic field \mathbf{b} along direction \mathbf{e}_1 (bottom). Both curves cover the discontinuity interface between the air and the sample.

II.4.4 Testing protocol

For all tests, a virgin sample of the material of interest is installed and aligned in the tensile setup with the help of the camera as the system is drawn out of the electromagnet. Once the clamps are in place, the setup is glided back inside the electromagnet and latched so that the sample lies exactly at the center of the magnet. At that stage, the force applied on the sample as well as the strains are zero.

In the case of the purely mechanical tests, the sample is first pre-conditioned, which consists in submitting it to cyclic loading prior to the actual test in order to attain a stabilized behavior after the initial cyclic softening known as Mullins effect. The pre-cycling (10 cycles) is conducted in displacement-controlled mode, so that the relative displacement of the two piezo-motors oscillates between 0 and 30 mm following a sinus at a frequency of 0.01 Hz. Following the pre-conditioning, as the sample carries some residual strain, a relaxation time of 10 minutes is allowed before the motors are displaced to get the sample straight while

maintaining the force at 0 N. At this moment, the initial cross-section $A_0 = L_1 L_2 \pi/4$ is determined with the help of the camera, where L_1 and L_2 are the lengths of the sample in direction \mathbf{e}_1 and \mathbf{e}_2 in the gage area, respectively. The actual cyclic test (3 cycles) is then conducted in displacement-controlled mode, so that the relative displacement of the piezo-motors oscillates between 0 and 30 mm following a triangle at a frequency of 0.001 Hz (quasi-static).

In the case of the magneto-mechanical tests, either the force or the displacement can be set and maintained at a given value during the whole test. In this case, the initial state of the sample corresponds to its state after the application of the applied pre-stress or pre-strain. Since the magnetic field leads to deformations within the sample, Mullins effect can be expected. Hence a pre-conditioning is also conducted here, as in the mechanical case. The magnetic field \mathbf{b}_0 is thus cycled between 0 and 0.8 T (by varying the current between 0 and 68 A) so as to perform 10 sinusoidal pre-cycles at a frequency of 0.001 Hz followed by a relaxation time of 10 minutes and finally 3 triangular test cycles at a frequency of 0.001 Hz (quasi-static).

II.5 Results and discussion

In this section, the experimental data obtained during the tests described above are presented and discussed. The plotted quantities are the longitudinal nominal stress T , stretches λ_i along the principal directions \mathbf{e}_1 , \mathbf{e}_2 and \mathbf{e}_3 (λ_3 being the nominal stretch), the Jacobian of the transformation $J = \det \mathbf{F} = \det(\lambda_1 \lambda_2 \lambda_3)$ as well as the magnetization \mathbf{m} and the magnetic field \mathbf{h} . In particular, the nominal stress T [MPa] is obtained by dividing the measured force F [N] by the sample initial cross-section A_0 [mm²]. The stretch λ [-] corresponds to the variation of length divided by the initial probed length. As the in-situ extensometer returns results in true (Eulerian) strain ϵ , the following conversion is performed: $\lambda = \exp(\epsilon)$. Finally magnetic measurements from probes h and m both yield magnetic field data in [T].

II.5.1 Purely mechanical testing

In Fig. II.8a, we first plot the nominal stress-stretch curve of the whole test (i.e. including the 10 pre-conditioning cycles and the subsequent 3 test cycles) for isotropic samples with varying particle content i.e. 0, 70, 140 and 210 phr. The responses of the 140 and 210 phr particle-filled elastomers clearly show an initial softening known as the Mullins effect while the 70 phr sample shows much less softening and the pure silicone exhibits a steady response throughout the whole test. For higher content particle filled-elastomers, the nominal stress-stretch response of the first cycle differs significantly from the following cycles; the second cycle also differs from the following ones but less significantly; then softening diminishes with the following cycles to finally be negligible after about 6 cycles. Since the first 10 preconditioning cycles are carried out at a higher frequency, the data is noisier. Hence for better clarity, we limit the plot in Fig. II.8b to the 3 test cycles carried out at a frequency a decade smaller. It can be seen that after pre-conditioning, the subsequent test cycles are very close. The stiffness of the material increases with particle content since the rigidity of the fillers is much higher than that of the matrix material. The same trend is observed for

the stabilized hysteresis loops since higher particle content leads to more dissipation due to more friction and rearrangements between the particles and the host matrix. Such results are classically observed in filled elastomers [113].

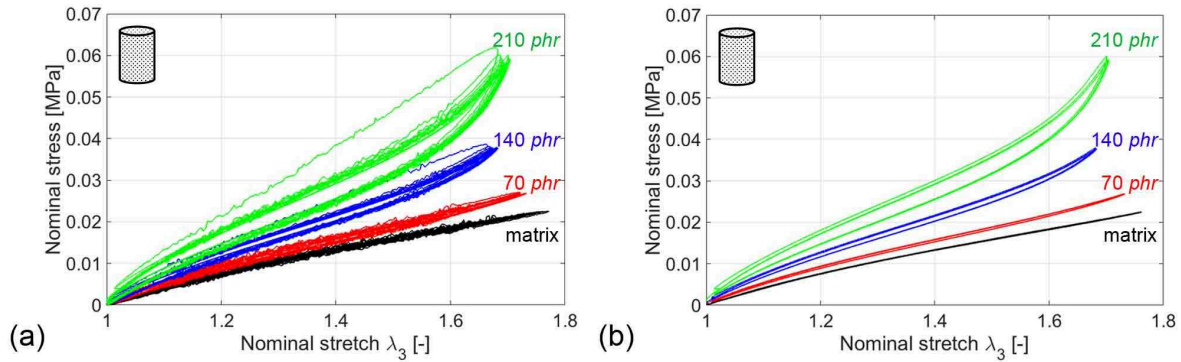


Figure II.8: Nominal stress-stretch curves obtained during purely mechanical tensile tests on isotropic samples with varying particle content: 0, 70, 140 and 210 phr. a) Curves obtained over the whole test, including the 10 pre-conditioning cycles and the subsequent 3 test cycles. b) Curves obtained during the 3 test cycles.

In what follows, we plot in Fig. II.9 the mechanical response obtained during the third test cycle (stabilized cycle) for 70 phr samples that are either isotropic or field-structured in directions \mathbf{e}_1 , \mathbf{e}_2 and \mathbf{e}_3 . The minimum stiffness is obtained for the isotropic sample, the maximum stiffness for the sample having particle chains in the loading direction, while samples having chains in either the \mathbf{e}_1 or \mathbf{e}_2 direction exhibit an intermediate stiffness that is nevertheless identical since the orientation of their structuration is the same from a mechanical standpoint. Such behavior is typically observed in fiber-reinforced composites [78]. However it is interesting to note that particle chains are not continuous like fibers. Hence if the increase in stiffness is due to the higher load-bearing capacity of the fibers in fiber-reinforced composites, a different mechanism is at play in field-structured MREs. In this case, it is rather friction arising at the microscopic level that leads to the observed increase in stiffness and it is when particles form columns in the loading direction that they impinge the most on polymer chain motion in the loading direction, preventing them from unwinding freely.

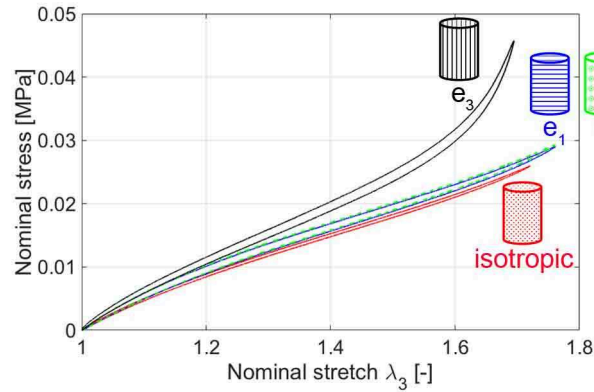


Figure II.9: Stabilized stress-stretch curve obtained during purely mechanical tensile tests on 70 phr samples with different microstructures: isotropic or field-structured in directions \mathbf{e}_1 , \mathbf{e}_2 and \mathbf{e}_3 .

To complete the mechanical analyses, we now plot in Fig. II.10a through Fig. II.10c the principal stretches λ_1 and λ_2 as a function of λ_3 during the upload part of the stabilized cycle for 70 phr samples that are either isotropic (Fig. II.10a) or field-structured in directions \mathbf{e}_3 (Fig. II.10b) and \mathbf{e}_1 and \mathbf{e}_2 (Fig. II.10c). As expected, λ_1 and λ_2 are superimposed for the axisymmetric test cases (isotropic and field-structured in direction \mathbf{e}_3). When the particle chains are aligned transversely to the tensile direction \mathbf{e}_3 (Fig. II.10c), the λ_1 response of the sample having particle chains in the \mathbf{e}_2 direction is superimposed to the λ_2 response of the sample having particle chains in the \mathbf{e}_1 direction, and conversely, since these samples are identical by a 90° rotation along the \mathbf{e}_3 axis. In both cases, the contraction in the particle chain direction is smaller than along the other transverse direction since the sample exhibits the highest stiffness along the particle alignment. However, this time, particle chains and local friction do not primarily impinge on chain unwinding but rather on the general motion of separated chains trying to get closer to each other.

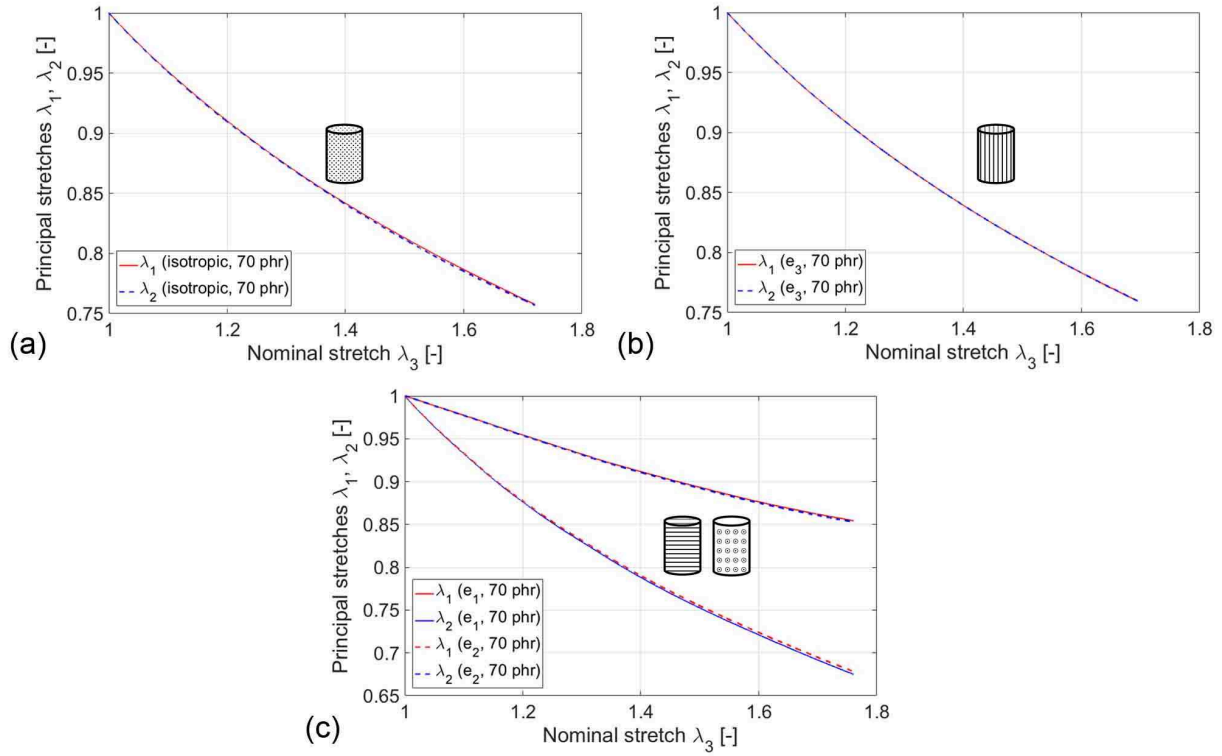


Figure II.10: Evolution of principal stretches λ_1 and λ_2 as a function of the applied stretch λ_3 during the upload part of a purely mechanical tensile stabilized cycle for 70 phr MRE samples exhibiting different microstructural structurations a) isotropic b) transversely isotropic with chains along direction \mathbf{e}_3 c) transversely isotropic with chains either along direction \mathbf{e}_1 or direction \mathbf{e}_2 .

II.5.2 Coupled magneto-mechanical testing

Magneto-mechanical tests are now performed as the force is maintained at 0 N on 70 phr samples exhibiting different microstructural structurations. The interest of maintaining the force at 0 N is to impose traction free boundary conditions, thus simulating a condition where the sample hangs free at the center of a uniform magnetic field. These tests, similar to the purely mechanical ones, are composed of 10 pre-conditioning cycles at 0.001 Hz followed by 3 cycles at 0.001 Hz, where the varying parameter is the applied field \mathbf{b}_0 .

In the case of the sample that is field-structured in direction \mathbf{e}_3 , a macroscopic instability occurs, causing the sample to bend symmetrically in the direction of the applied magnetic field (for an applied field \mathbf{b}_0 of 120 mT), as reported in Fig. II.11a. Such an instability is comparable to that of an elongated body subjected to a magnetic field transverse to its long axis and that is well-known as the compass effect in magnetism [115], though the role of the elongated body is here played by the chains of particles. In the case of the sample that is field-structured in direction \mathbf{e}_2 , a rotation of the body of the sample around the \mathbf{e}_3 axis is observed and here too attributed to the compass effect. The angle of rotation increases with the applied magnetic field to attain 90° at an maximum applied field $\mathbf{b}_0 = 99$ mT and

remains stable thereafter, as reported in Fig. II.11b. Note that because the heads of the sample are clamped, the generatrices of the MRE body transform into helicoids that are symmetrical about the $(\mathbf{e}_1, \mathbf{e}_2)$ plane as outlined on the last snapshots of Fig. II.11b.

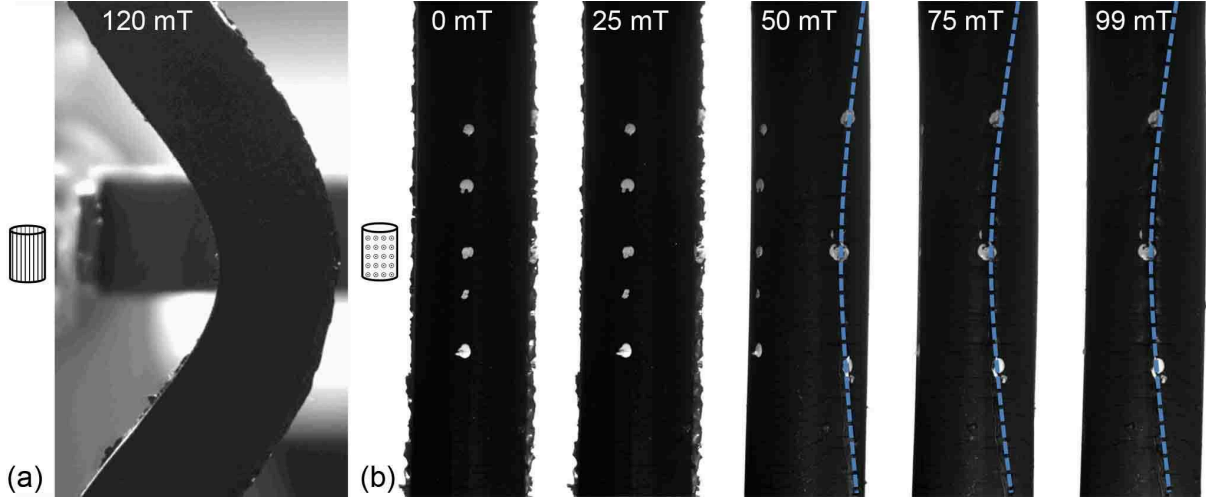


Figure II.11: a) Macroscopic instability observed in a 70 phr MRE sample field-structured in direction \mathbf{e}_3 . b) Snapshots of the macroscopic rotation observed in a 70 phr MRE sample field-structured in direction \mathbf{e}_2 .

In the case of the 70 phr isotropic sample, the whole test mentioned above can be carried out without the occurrence of any instability on samples that are either isotropic or field-structured along direction \mathbf{e}_1 . We can thus compare the principal stretches of an isotropic sample (Fig. II.12a) with those of an \mathbf{e}_1 field-structured sample (Fig. II.12b) during a coupled magneto-mechanical test as the force is maintained at 0 N, for which the 3rd stabilized cycle is plotted.

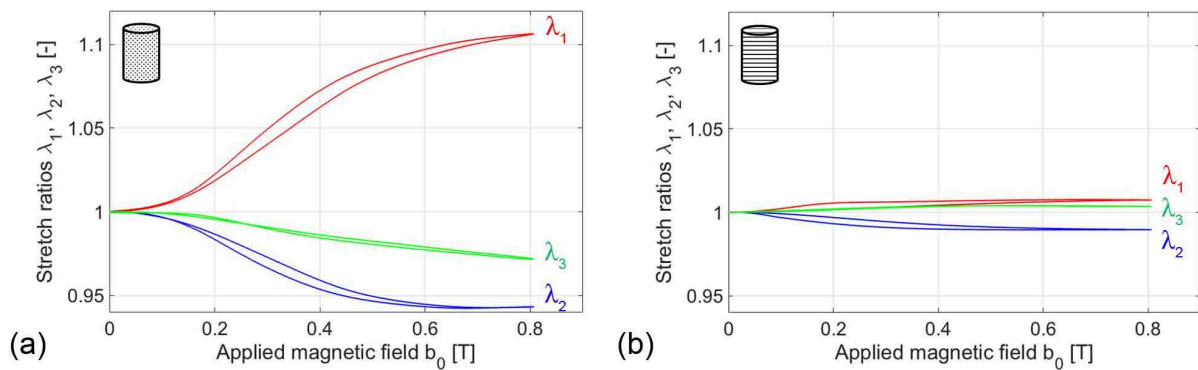


Figure II.12: Principal stretches as a function of the applied magnetic field \mathbf{b}_0 obtained during the 3rd stabilized cycled for 70 phr samples exhibiting different microstructural structurations and submitted to a coupled magneto-mechanical test as the force is maintained at 0 N, a) isotropic sample, b) sample field-structured in direction \mathbf{e}_1 .

In the isotropic case (Fig. II.12a), the maximum stretch is along the field direction (\mathbf{e}_1) ; it corresponds to an elongation in the field direction and is accompanied by a contraction in the other two transverse directions. Note that because the sample elongates along \mathbf{e}_1 and contracts along \mathbf{e}_2 , the originally circular cross-section transforms into a quasi elliptic cross-section. Additionally, even though the two transverse directions are of equivalent orientation relative to the magnetic field they do not behave the same: the sample contracts more along \mathbf{e}_1 than along \mathbf{e}_3 . These deformations are macroscopic manifestation of the motions of the particles at the microstructural scale as they try to align along the lines of the magnetic field in order to minimize the energy of the whole sample. It also suggest that despite the uniform magnetic field achieved within the sample, the overall response still suffers from a shape effect though, according to [46], the demagnetizing factor of the used sample is very low due to its high aspect ratio of 8.3. As reported in Fig. II.12b, the sample field-structured in direction \mathbf{e}_1 exhibits its larger deformation as a contraction along direction \mathbf{e}_2 while it shows a small elongation in the field direction \mathbf{e}_1 and also to an even lesser extent along \mathbf{e}_3 . Nevertheless, all these deformations remain very small ($< 0.7\%$) even at saturation. It actually seems that the particles have already attained a stable equilibrium position during the curing of the sample and that these strains are due to the fact that even though the relative orientation sample/field was the same, the absolute orientation was different during curing (we indeed tried to minimize the number of stands needed for fabricating field-structured samples). These experimental observations are similar to what was observed for cylindrical samples whose main axis was aligned along the magnetic field (see Section II.2.3), namely we report elongation in the direction of the applied field and a stronger magnetostriction for isotropic samples. In particular, for an applied field of 0.8 T, the magnetostriction is 10.5% in the field direction for isotropic samples and only 0.7% for samples that are field-structured in the magnetic field direction. Compared to other studies, the main difference here is that the sample's main axis is perpendicular to the magnetic field. Nevertheless, to further confirm the previous results, a nearly ellipsoidal 70 phr isotropic MRE body with plastic heads removed was placed in a holder (covered with oil to minimize friction) at the center of the magnetic field with its main axis in the direction of the magnetic field and it also exhibited elongation as the field increased. The observation was only qualitative but a short-term perspective of this work is to adapt the setup to perform fully-coupled tests instrumented with mechanical and magnetic in-situ diagnostics as the sample is submitted to a magnetic field along its long axis.

In parallel, it is interesting to look at the magnetization curves of the two above-mentioned samples. They are both reported in Fig. II.13. The \mathbf{e}_1 field-structured sample magnetizes itself much faster than the isotropic sample and attains saturation whereas the isotropic samples does not. We interpret this as follows: the \mathbf{e}_1 field-structured sample magnetizes itself and reaches saturation fast because it stabilizes very early due to the small amount of motion among its particles. On the other hand, in the case of the isotropic sample, magnetization is slower, hence the overall composite is less susceptible, because the particles keep moving locally throughout the increase of the magnetic field in order to keep minimizing the energy of the whole sample as it deforms. As a result, samples for which the microstructure interacts feebly with the magnetic field (because they are already in an optimal state regarding the field) exhibit (counter-intuitively) a higher initial susceptibility and a faster saturation. On

the contrary, samples that interact the most with the magnetic field (because the particles need significant rearrangement to reach an optimal state regarding the field) exhibit a lower initial susceptibility but the microstructure is being rearranged to correct this, thus in turn delaying the saturation in the sample. Additionally, it might be useful to recall that in both Fig. II.12 and Fig. II.13, the part of the curves obtained as the magnetic field increases is located at the bottom of the loops while the part obtained as the magnetic field decreases is located above the loops, as can be observed in classical magnetization curves of ferromagnetic bulk materials. Finally, for our samples, both the stretch and the magnetization go readily back to 1 and 0, respectively, when the magnetic field vanishes. The latter observation indicates that the MRE composite, whose fillers do not have remnant magnetization, does not exhibit any remnant magnetization either. The former observation actually only shows that there is no residual stretch induced by particle debonding. Note that in the case of samples with untreated particles, the magnetization also goes back to zero but the samples exhibit residual strains as the applied magnetic field vanishes. This confirms that the observed residual strains are not linked to remanence as initially suggested by Guan [71] but to mechanical phenomena arising in the samples and in particular to debonding which has been shown here to play an important role in the MREs response during coupled tests.

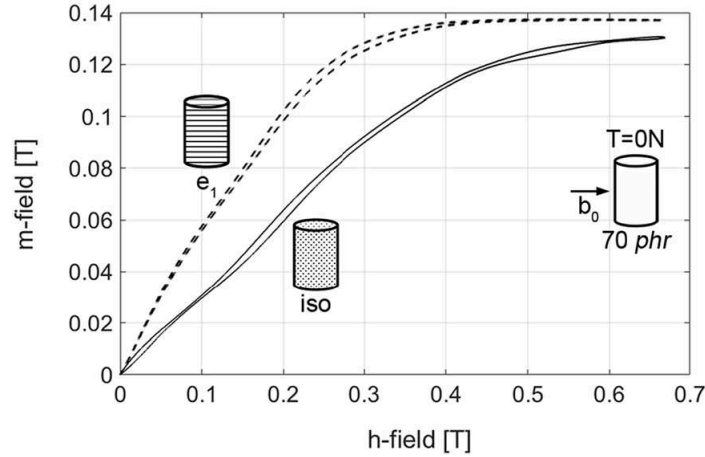


Figure II.13: Magnetization curves of a 70 phr isotropic sample and a 70 phr sample field-structured in direction \mathbf{e}_1 obtained during the 3rd stabilized cycle of a coupled magneto-mechanical test as the force is maintained at 0 N.

Since the isotropic sample exhibit the highest magnetostriction, the effect of particle content will only be studied on these samples. However the magneto-mechanical test in which the force is maintained at 0 N suffers an instability that arises at smaller and smaller magnetic field as the particle content increases from 70 phr (0.45 T for 140 phr and 0.3 T for 210 phr). This instability takes the same form than the one depicted in Fig. II.11a: the sample first starts to deform like the 70 phr sample but it eventually tries to align its whole body along the magnetic field while its two extremities remained clamped in the tensile setup. Note that, for all particle contents studied here, no instability was observed for the \mathbf{e}_1 field-structured samples. In fact, the instability occurring in the isotropic samples, for which the field direc-

tion is perpendicular to the sample’s long axis, is a topic that has been largely investigated theoretically, mainly though in the idealized case of a rectangular block in plane strain [91]. Instability arises at a critical magnetic field threshold that is reported to increase monotonically with the aspect ratio of the sample. In our case, since the aspect ratio of the sample is high, both the demagnetizing factor and the risk of occurrence of such an instability are lowered. Since the contribution of these two shape-related effects are minimized, the devised experiments, more than any reported to date, approach the ideal goal of an actual material characterization. Since this experimental study is conducted in the broader perspective of providing data for identifying constitutive models for MREs, it is important to keep in mind that the fitting procedure will need to be supplemented by numerical simulations to account for the contribution of the above-mentioned shape-related effects and thus ensure that the obtained parameters are intrinsic to the material.

Nevertheless, the influence of particle content on magnetostriction can still be studied since the reported instabilities can be delayed or even cancelled when a sufficient pre-stress or pre-stretch is applied on the studied samples so as to increase their aspect ratio. In order for the only varying parameter to be the particle content, the same pre-stretch needs to be applied to all samples so that they have the same aspect ratio when the coupled test starts. In order to select the maximum pre-stretch that can be applied to all samples, we refer to Fig. II.3a that gives, for each particle content, the maximum stretch that can be applied to the sample designed for the coupled tests while ensuring that there is no debonding at the plastic heads/MRE body interface, hence that its mechanical response is representative of the material. This pre-stretch is 1.4 for the present study. Then, the maximum field that can be applied without triggering an instability must be determined for an isotropic sample with the highest particle content submitted to a pre-stretch of 1.4, that is 0.65 T here. Finally, magneto-mechanical tests (including pre-cycling and cycling) up to a maximum field of 0.65 T can be carried out on 70 phr, 140 phr and 210 phr isotropic samples that were initially submitted to a 1.4 pre-stretch and for which the corresponding force then remained fixed throughout the rest of the test.

The evolution of the λ_1 stretch (stretch in the field direction) as a function of the applied magnetic field \mathbf{b}_0 during the 3rd stabilized cycle is plotted in Fig. II.14a, for isotropic samples of 70 phr, 140 phr and 210 phr. Note that the state of the sample after the application of the pre-stretch is considered as the reference configuration (hence the plotted λ_1 starts from 1). For all tested samples, the λ_1 stretch evolution has the shape of a hysteresis loop (with again a clear return to the initial state), whose area increases slightly with particle content. The maximum amplitude of stretch is attained for the highest particle content, but the value of the maximum stretch does not increase linearly with particle content. In fact, beyond a given particle content, often called ‘optimal filling factor’ (see Section II.2.4), increasing further the particle content would not lead to more magnetostriction as the amount of filler would render the composite too stiff. In parallel, we plot in Fig. II.14b the magnetization curves obtained during these tests. The initial slope or magnetic susceptibility increases with particle content, regardless of the overall stiffness of the composite, but saturation is not reached since the ideal stabilized state of the sample would happen post-instability. These experimental results may thus shed some light on the macroscopic instability mechanism. As the magnetic field

increases, particles first rearrange themselves to align along the lines of the magnetic field. If saturation is reached at the maximum applied magnetic field, only magnetostriction is observed. However if the sample is still far away from saturation, beyond the microscopic rearrangement of the particles, a macroscopic realignment of the whole sample through the compass effect is needed to reach its ideal stabilized state in regard of the applied magnetic field (that is perpendicular to the sample). Hence, because saturation increases with particle content, the macroscopic instability in isotropic samples happens at lower magnetic field in samples with higher particle content.

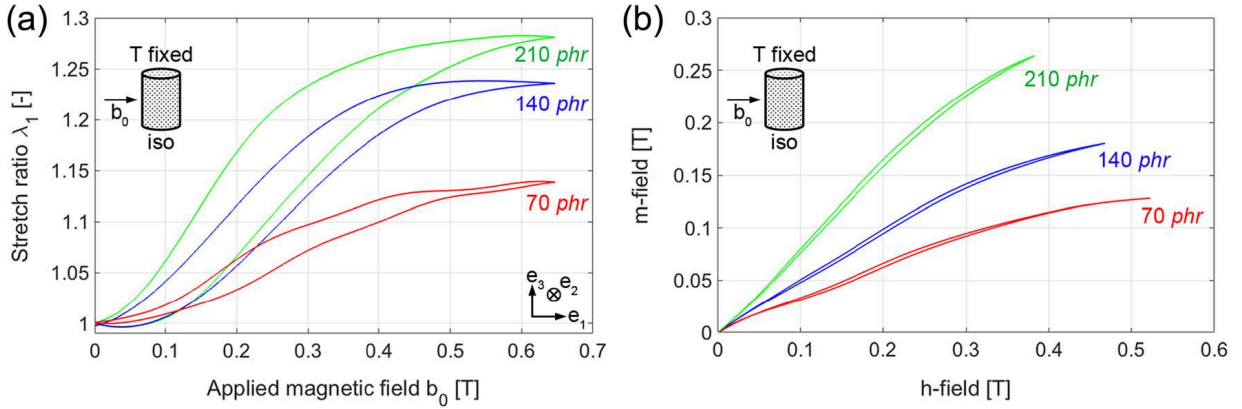


Figure II.14: a) Evolution of the λ_1 stretch (stretch in the field direction) as a function of the applied magnetic field \mathbf{b}_0 during the 3rd stabilized cycle for 70 phr, 140 phr and 210 phr isotropic samples. These tests are all carried out after a 1.4 pre-stretch was applied on the samples in their long axis direction and the reference configuration is taken post pre-stretch. b) Magnetization curves of isotropic samples of a 70 phr, 140 phr and 210 phr obtained during the 3rd stabilized cycle of a coupled magneto-mechanical test after the samples were submitted to a 1.4 pre-stretch.

Finally, a last interesting aspect that can be clarified thanks to the specially designed setup and samples is the effect of a pre-stretch or a pre-stress on the magnetic behavior of MRE composites. It was indeed recently suggested [76] that MREs might exhibit a change in their magnetic susceptibility when subjected to a mechanical stress (Villari effect or inverse magnetostrictive effect). The reported experimental results showed indeed a little sensitivity but the involved samples did not have their particles pre-treated. In order to investigate experimentally the effect of pre-stress, which was predicted numerically to have no effect on the magnetization [9], a 70 phr isotropic sample was submitted to a full coupled test as the force was maintained at different values: 0 N, 0.1 N and 0.2 N. The corresponding magnetization curves obtained during the 3rd stabilized cycle are plotted in Fig. II.15. They are superimposed, thus confirming that pre-stress does not influence the magnetic response of the sample.

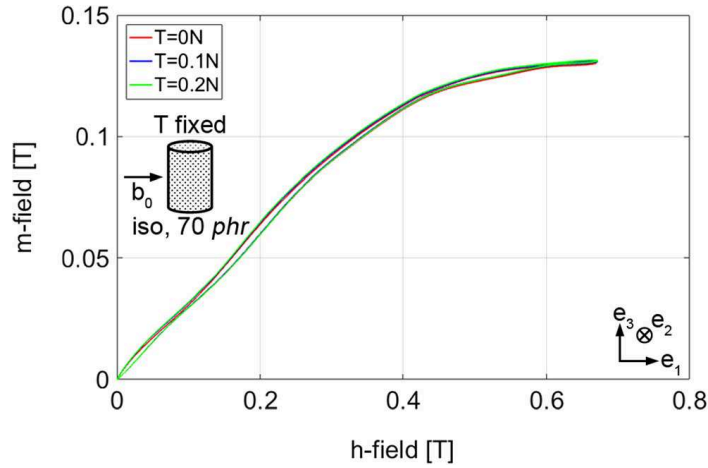


Figure II.15: Magnetization curves obtained during the 3rd stabilized cycle for a 70 phr isotropic sample submitted to a coupled test as the force is maintained at 0 N, 0.1 N and 0.2 N.

II.6 Conclusions and perspectives

The present study proposes an experimental setup in which coupled magneto-mechanical tests can be carried out while measuring in-situ both mechanical and magnetic quantities with precision and without impinging on the sample deformation. Considering the multitude of effects arising within MRE samples when submitted to a magnetic field, a special sample was designed. Within this sample, mechanical and magnetic uniform loadings can be obtained concurrently and known structural-dependent effects can be minimized in order to focus on the characterization of the actual material properties of MREs.

This study of MREs was also carried out from the perspective of the mechanics of filled polymers to ensure the reliability and repeatability of the results. In particular, MRE samples were systematically pre-cycled, both for purely mechanical and coupled tests, to prevent the Mullins effect from disrupting the results. It was also found that debonding between the particles and the matrix, though less of an issue under purely mechanical tests, can lead to significant volume change during magnetic tests and render false the incompressibility assumption if ignored. Hence the preparation of MRE samples is crucial. It involves not only the pre-treatment of the particles but also a careful study of the obtained microstructures according to the curing schedule and the rate of application of the magnetic field during curing.

The conducted experiments highlight that instabilities are ubiquitous in MREs. Hence low power applications may benefit greatly from these instabilities if they are properly harnessed. The experiments also demonstrate that, despite uniform magnetic and mechanical fields within the sample, the latter is still affected by shape-related effects (demagnetizing factor and macroscopic instabilities due to the compass effect). However, these effects are minimal compared to the previous state of the art and can even be further minimized by pre-stretching the samples before testing.

Tests conducted on MREs samples of various microstructures showed that the only sam-

ples remaining macroscopically stable during the experiments are the isotropic ones and the one that are field-structured in the direction of the applied field. In fact, the field-structured samples experience little to no magnetostriction when submitted to a magnetic field similar to the one applied during fabrication. Only the isotropic samples exhibit significant magnetostriction along the direction of the applied field. The results also showed that, in these samples, the maximal magnetostriction increases with particle content. Nevertheless, the rate of increase is not linear and tends to saturate as the amount of filler stiffens the matrix too much. Finally it was demonstrated that the magnetization response of the sample is independent on the pre-stress applied on the sample prior to testing.

The reported experimental work was conducted within the broader challenge of building a dedicated framework, based on a strong experimental-numerical dialog, in order to carefully address MRE material optimization and structural design. Further experimental developments include significant modifications of the setup to permit the application of the magnetic field along the main axis of the sample and study of the optimal filling factor for varying matrix materials. The conducted experiments will also be exploited to calibrate coupled magneto-mechanical phenomenological constitutive laws.

Acknowledgments

For this experimental work, I acknowledge my supervisor Laurence Bodelot, LMS research engineers Vincent De Greef for tailoring the LMS acquisition software to the specificity of the magneto-mechanical experiments, Erik Guimbretiere for his contribution to the mechanical design of the setup as well as François Lelong and Antoine Soler for machining the molds and many parts of the setup. I also thank my supervisors Kostas Danas and Nick Triantafyllidis for their precious help on theoretical and numerical aspects. The contribution of Lingjie Cai during his master internship at LMS is also acknowledged.

II.A Correction of magnetic measurements

In this Appendix, the derivation of the formulas used to correct the magnetic measurements are detailed. First, it is to be noted that in the range of deformation that we consider in this study, we can show numerically that the eulerian magnetic quantities are fairly uniform inside the sample (this will be further shown in Chapter IV). Moreover, during deformation, the approximation of the sample's cross-section remaining very close to an ellipse is of good accuracy. As a result, we consider the general 2D problem where a sample with an ellipsoidal cross section is placed within a uniform magnetic field $\mathbf{h}_0 = h_0 \mathbf{e}_1$. The objective here is to calculate how the external magnetic field outside of the sample is influenced by the presence of the sample. This will allow us to evaluate the field at the interface between the sample and the air from measurements taken away from the interface.

II.A.1 Elliptical coordinate system

The elliptical coordinate system is well suited to solve problems involving ellipsoidal geometries, so we will use it in what follows (see Fig. II.16).

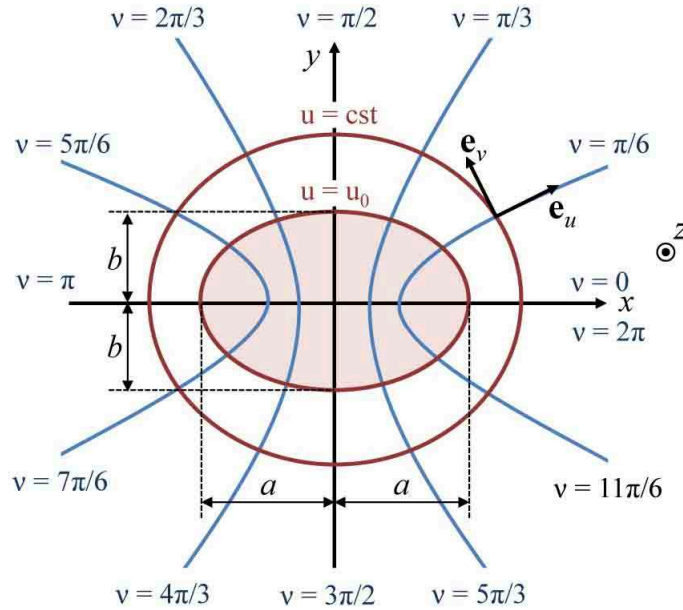


Figure II.16: *Elliptical coordinate system.*

$$\begin{cases} x = c \cosh(u) \cos(v) \\ y = c \sinh(u) \sin(v) \end{cases}, \quad (u, v) \in [0, +\infty[\times [0, 2\pi[, \quad (\text{II.A.1})$$

with the normalized basis vectors ($\mathbf{e}_u, \mathbf{e}_v$) expressed in the cartesian basis ($\mathbf{e}_1, \mathbf{e}_2$):

$$\begin{cases} \mathbf{e}_u = \frac{\cos(v) \sinh(u)}{\sqrt{\sinh^2(u) + \sin^2(v)}} \mathbf{e}_1 + \frac{\sin(v) \cosh(u)}{\sqrt{\sinh^2(u) + \sin^2(v)}} \mathbf{e}_2, \\ \mathbf{e}_v = -\frac{\sin(v) \cosh(u)}{\sqrt{\sinh^2(u) + \sin^2(v)}} \mathbf{e}_1 + \frac{\cos(v) \sinh(u)}{\sqrt{\sinh^2(u) + \sin^2(v)}} \mathbf{e}_2. \end{cases} \quad (\text{II.A.2})$$

As can be noticed, the lines of constant u describe a family of confocal ellipses (i.e. ellipses with common foci). Indeed, from eq.(II.A.1), it is clear that:

$$\frac{x^2}{c^2 \cosh^2(u)} + \frac{y^2}{c^2 \sinh^2(u)} = 1 \Leftrightarrow \frac{x^2}{a^2} + \frac{y^2}{b^2} = 1 \quad \text{with} \quad \begin{cases} a = c \cosh(u) \\ b = c \sinh(u) \end{cases}, \quad (\text{II.A.3})$$

which is the equation of an ellipse of:

- semi-major axis $a = c \cosh(u)$,
- semi-minor axis $b = c \sinh(u)$,
- foci $F = \begin{vmatrix} \pm \sqrt{a^2 - b^2} \\ 0 \end{vmatrix} = \begin{vmatrix} \pm c \sqrt{\cosh^2(u) - \sinh^2(u)} \\ 0 \end{vmatrix} = \begin{vmatrix} \pm c \\ 0 \end{vmatrix}$,
- aspect ratio $w = b/a = \tanh u$.

The discontinuity interface between the air and the sample that has an ellipsoidal geometry will be described as follows with the help of parameter $u_0 > 0$:

$$\begin{cases} x = c \cosh(u_0) \cos(v) \\ y = c \sinh(u_0) \sin(v) \end{cases}, \quad \forall v \in [0, 2\pi[. \quad (\text{II.A.4})$$

The interior of the sample is described by the set of points $C_{in} = \{(u, v) \text{ st. } (u, v) \in [0, u_0[\times [0, 2\pi[\}$, whereas the exterior, i.e. the air, is described by $C_{out} = \{(u, v) \text{ st. } (u, v) \in]u_0, +\infty[\times [0, 2\pi[\}$.

II.A.2 Problem to solve

Since the samples used for the magneto-mechanical tests have a nearly ellipsoidal MRE body, the \mathbf{h}_{in} -field, the magnetization \mathbf{m}_{in} and the total magnetic field \mathbf{b}_{in} , are all nearly uniform within the material (this approximation is accurate in the range of deformation considered in the present study).

$$\begin{cases} \mathbf{h}_{in}(u, v) = h_{in} \mathbf{e}_1 \\ \mathbf{m}_{in}(u, v) = m_{in} \mathbf{e}_1 \\ \mathbf{b}_{in}(u, v) = \mu_0(\mathbf{h}_{in} + \mathbf{m}_{in}) = \mu_0(h_{in} + m_{in}) \mathbf{e}_1 \end{cases}, \quad \forall (u, v) \in C_{in}, \quad (\text{II.A.5})$$

where (h_{in}, m_{in}) are the constants to be determined from measurements made outside of the sample. They correspond to the total h_{in} field (magnetic field intensity) and the magnetization inside the sample, respectively.

Outside of the sample (i.e. $\forall(u, v) \in C_{out}$), magnetic quantities are indicated with the “out” subscript and the following equations apply:

$$\mathbf{b}_{out} = \mu_0 \mathbf{h}_{out}, \quad (\text{II.A.6})$$

$$\mathbf{m}_{out} = \mathbf{0}, \quad (\text{II.A.7})$$

$$\nabla \times \mathbf{h}_{out} = \mathbf{0}, \quad (\text{II.A.8})$$

$$\nabla \cdot \mathbf{b}_{out} = 0 = \nabla \cdot \mathbf{h}_{out}. \quad (\text{II.A.9})$$

Eq.(II.A.8) yields that there exists a potential φ such that $\forall(u, v) \in C_{out}$:

$$\mathbf{h}_{out} = -\nabla\varphi(u, v). \quad (\text{II.A.10})$$

If we substitute the previous expression in eq.(II.A.9), it comes that $\forall(u, v) \in C_{out}$:

$$\nabla \cdot \mathbf{h}_{out} = -\nabla \cdot (\nabla\varphi)(u, v) = -\nabla^2\varphi(u, v) = 0. \quad (\text{II.A.11})$$

The problem to solve here is a boundary value problem. We first need to make sure that, far away from the interface, the influence of the sample on the \mathbf{h} -field vanishes:

$$\lim_{u \rightarrow \infty} \mathbf{h}_{out} = h_0 \mathbf{e}_1, \forall v \in [0, 2\pi[\Leftrightarrow \varphi \underset{u \rightarrow \infty}{\sim} -h_0 x = -h_0 c \cosh(u) \cos(v). \quad (\text{II.A.12})$$

Additionally, magnetostatics theory imposes the following relations to be satisfied at the discontinuity interface between the air and the sample (i.e. $\forall(u, v)$ such that $u = u_0$ and $v \in [0, 2\pi[$):

$$\mathbf{n} \cdot \llbracket \mathbf{b} \rrbracket = 0 \Leftrightarrow \mathbf{e}_u \cdot \mathbf{b}_{out} = \mathbf{e}_u \cdot \mathbf{b}_{in} \Leftrightarrow \mathbf{e}_u \cdot \mathbf{h}_{out} = (h_{in} + m_{in}) \mathbf{e}_u \cdot \mathbf{e}_1, \quad (\text{II.A.13})$$

$$\mathbf{n} \times \llbracket \mathbf{h} \rrbracket = \mathbf{0} \Leftrightarrow \mathbf{e}_u \times \mathbf{h}_{out} = \mathbf{e}_u \times \mathbf{h}_{in} \Leftrightarrow \mathbf{e}_u \times \mathbf{h}_{out} = h_{in} \mathbf{e}_u \times \mathbf{e}_1. \quad (\text{II.A.14})$$

If we now substitute the expression of \mathbf{e}_u from eq.(II.A.2), we can rewrite the discontinuity interface conditions as follows: for $u \rightarrow u_0$, and $\forall v \in [0, 2\pi[$

$$-\mathbf{e}_u \cdot \nabla\varphi(u, v) = -\frac{1}{c\sqrt{\sinh^2(u) + \sin^2(v)}} \frac{\partial\varphi}{\partial u} = (h_{in} + m_{in}) \frac{\cos(v) \sinh(u)}{\sqrt{\sinh^2(u) + \sin^2(v)}}, \quad (\text{II.A.15})$$

$$-\mathbf{e}_u \times \nabla\varphi(u, v) = -\frac{1}{c\sqrt{\sinh^2(u) + \sin^2(v)}} \frac{\partial\varphi}{\partial v} \mathbf{e}_3 = -h_{in} \frac{\cosh(u) \sin(v)}{\sqrt{\sinh^2(u) + \sin^2(v)}} \mathbf{e}_3. \quad (\text{II.A.16})$$

Finally, the boundary value problem to be solved is the following:

$$\left\{ \begin{array}{l} \nabla^2 \varphi(u, v) = 0, \quad \forall (u, v) \in C_{out}, \\ \varphi \underset{u \rightarrow \infty}{\sim} -h_0 c \cosh(u) \cos(v), \quad \forall v \in [0, 2\pi[, \\ \lim_{u \rightarrow u_0} \frac{\partial \varphi}{\partial u} = -c(h_{in} + m_{in}) \cos(v) \sinh(u_0), \quad \forall v \in [0, 2\pi[, \\ \lim_{u \rightarrow u_0} \frac{\partial \varphi}{\partial v} = c h_{in} \cosh(u_0) \sin(v), \quad \forall v \in [0, 2\pi[. \end{array} \right. \quad (\text{II.A.17})$$

II.A.3 Resolution of Laplace equation

The equation to solve $\forall (u, v) \in C_{out}$ is:

$$\nabla^2 \varphi = 0 \Leftrightarrow \frac{1}{c^2(\sinh^2(u) + \sin^2(v))} \left[\frac{\partial^2 \varphi}{\partial u^2} + \frac{\partial^2 \varphi}{\partial v^2} \right] = 0 \Leftrightarrow \left[\frac{\partial^2 \varphi}{\partial u^2} + \frac{\partial^2 \varphi}{\partial v^2} \right] = 0. \quad (\text{II.A.18})$$

This equation is exactly the same as the Laplace equation in cartesian coordinates and, as a result, can be solved using the separation of variables method. We look thus for a potential that takes the following form:

$$\varphi(u, v) = U(u)V(v), \quad \forall (u, v) \in C_{out}, \quad (\text{II.A.19})$$

$V(v)$ being a 2π -periodic function of the variable v .

Under this condition, the general solution for both U and V is well known:

$$U(u) = \begin{cases} e_n \cosh(nu) + f_n \sinh(nu) & \text{if } n \geq 1 \\ e_0 u + f_0 & \text{if } n = 0, \end{cases} \quad (\text{II.A.20})$$

$$V(v) = \begin{cases} g_n \cos(nv) + h_n \sin(nv) & \text{if } n \geq 1, \\ g_0 & \text{if } n = 0. \end{cases} \quad (\text{II.A.21})$$

Without loss of generality, the solution of eq.(II.A.17)₁ can be rewritten as:

$$\begin{aligned} \varphi(u, v) = & (a_0 u + b_0) + \sum_{n=1}^{\infty} [a_n \cosh(nu) + b_n \sinh(nu)] \cos(nv) + \\ & \sum_{n=1}^{\infty} [c_n \cosh(nu) + d_n \sinh(nu)] \sin(nv), \end{aligned} \quad (\text{II.A.22})$$

where (a_n, b_n, c_n, d_n) are constants that need to be calculated to satisfy the boundary conditions. Because the only quantity of interest is $\mathbf{h}_{out} = -\nabla \varphi(u, v)$, we can choose to impose $b_0 = 0$.

From the first boundary condition (see eq.(II.A.17)₂), we get that:

$$\begin{cases} a_1 + b_1 = -h_0 c, \\ a_n = -b_n & \text{for } n \geq 2, \\ c_n = -d_n & \text{for } n \geq 1. \end{cases} \quad (\text{II.A.23})$$

From the second boundary condition (eq.(II.A.17)₃), we necessarily have:

$$\begin{cases} a_0 = 0, \\ a_n = b_n = 0 & \text{for } n \geq 2, \\ c_n = d_n = 0 & \text{for } n \geq 1, \\ a_1 \sinh(u_0) + b_1 \cosh(u_0) = -c(h_{in} + m_{in}) \sinh(u_0), \end{cases}, \quad (\text{II.A.24})$$

and from the third boundary condition (eq.(II.A.17)₄), we get:

$$a_1 \cosh(u_0) + b_1 \sinh(u_0) = -c h_{in} \cosh(u_0). \quad (\text{II.A.25})$$

So far, with eq.(II.A.23), eq.(II.A.24) and eq.(II.A.25), we end up with the following system:

$$\begin{cases} a_0 = b_0 = 0, \\ a_n = b_n = 0 & \text{for } n \geq 2, \\ c_n = d_n = 0 & \text{for } n \geq 1, \\ a_1 + b_1 + c h_0 = 0, \\ a_1 \cosh(u_0) + b_1 \sinh(u_0) + c \cosh(u_0) h_{in} = 0, \\ a_1 \sinh(u_0) + b_1 \cosh(u_0) + c \sinh(u_0) h_{in} + c \sinh(u_0) m_{in} = 0. \end{cases}, \quad (\text{II.A.26})$$

In the system formed by eq.(II.A.26)₄, eq.(II.A.26)₅ and eq.(II.A.26)₆, $u_0 = \text{arctanh}(w)$ and $c = a\sqrt{1-w^2}$ are known quantities since the major semi-axis a and the minor semi-axis b of the cross-section are measured at each step of the experiment. In this system, the constants that need to be calculated are $(a_1, b_1, h_0, h_{in}, m_{in})$. In order to solve for those unknowns, we perform two magnetic measurements outside of the sample to get the two more equations needed.

As reported in Fig. II.7b, the magnetic measurements are taken by Hall probes h and m , away from the sample, along axes \mathbf{e}_2 and \mathbf{e}_1 , respectively.

From what precedes, we know that $\forall (u, v) \in C_{out}$:

$$\begin{aligned} \mathbf{h}_{out}(u, v) &= -\nabla\varphi(u, v) \\ &= -\frac{\left((a_1 \sinh(u) + b_1 \cosh(u)) \cos(v) \mathbf{e}_u - (a_1 \cosh(u) + b_1 \sinh(u)) \sin(v) \mathbf{e}_v \right)}{c\sqrt{\sinh^2(u) + \sin^2(v)}}. \end{aligned} \quad (\text{II.A.27})$$

Along the axis of interest \mathbf{e}_2 and \mathbf{e}_1 , we can now easily express the magnetic intensity in elliptical coordinates as well as in cartesian coordinates.

Outside the sample, along the \mathbf{e}_2 axis:

$$\begin{cases} \mathbf{h}_{out}(0, y) = \frac{-1}{a\sqrt{1-w^2}} \left(a_1 + b_1 \left(1 + \frac{a^2(1-w^2)}{y^2} \right)^{-1/2} \right) \mathbf{e}_1, & \text{for } y > b = aw, \\ \mathbf{b}_{out}(0, y) = \mu_0 \mathbf{h}_{out}(0, y), & \text{for } y > b = aw. \end{cases} \quad (\text{II.A.28})$$

Outside the sample, along the \mathbf{e}_1 axis:

$$\begin{cases} \mathbf{h}_{out}(x, 0) = \frac{-1}{a\sqrt{1-w^2}} \left(a_1 + b_1 \left(1 - \frac{a^2(1-w^2)}{x^2} \right)^{-1/2} \right) \mathbf{e}_1, & \text{for } x > a, \\ \mathbf{b}_{out}(x, 0) = \mu_0 \mathbf{h}_{out}(x, 0), & \text{for } x > a. \end{cases} \quad (\text{II.A.29})$$

So in the end the system that we have to solve is:

$$\begin{cases} a_1 + b_1 + c h_0 = 0, \\ a_1 \cosh(u_0) + b_1 \sinh(u_0) + c \cosh(u_0) h_{in} = 0, \\ a_1 \sinh(u_0) + b_1 \cosh(u_0) + c \sinh(u_0) h_{in} + c \sinh(u_0) m_{in} = 0, \end{cases}, \quad (\text{II.A.30})$$

$$\text{with } \begin{cases} b_1 = \frac{-a\sqrt{1-w^2} (h_{out}(0, y_0) - h_{out}(x_0, 0))}{\left(1 + \frac{a^2(1-w^2)}{y_0^2} \right)^{-1/2} - \left(1 - \frac{a^2(1-w^2)}{x_0^2} \right)^{-1/2}}, & x_0 > a, \quad y_0 > b = aw, \\ a_1 = -a\sqrt{1-w^2} h_{out}(0, y_0) - b_1 \left(1 + \frac{a^2(1-w^2)}{y_0^2} \right)^{-1/2}, & y_0 > b = aw, \end{cases} \quad (\text{II.A.31})$$

where $(x_0, 0)$ and $(0, y_0)$ represent the positions of Hall probes m and h respectively (those positions are known and remain fixed during the test). And $h_{out}(0, y_0)$ is the measurement of the magnetic intensity by Hall probe h along the \mathbf{e}_2 axis (respectively $h_{out}(x_0, 0)$ is the measurement of the magnetic intensity by Hall probe m along the \mathbf{e}_1 axis). We can note that this system is linear with respect to the unknowns (h_0, h_{in}, m_{in}) , so we can solve it very easily and hence have access to the magnetic quantities inside the sample.

The variations of \mathbf{h} and \mathbf{b} along axes \mathbf{e}_2 and \mathbf{e}_1 are plotted in Fig. II.7c of the article.

To validate the correction method derived here, magnetic measurements were taken by Hall probes h and m at increasing distances away from the sample as it was submitted to a steady uniform magnetic field of 0.35 T. The experimental data for probes h and m are reported, along with the theoretically derived predictions, in **Fig. II.17a** and **Fig. II.17b**,

respectively. They both show very good agreement, with a maximum deviation of 0.1% and 0.2%, respectively.

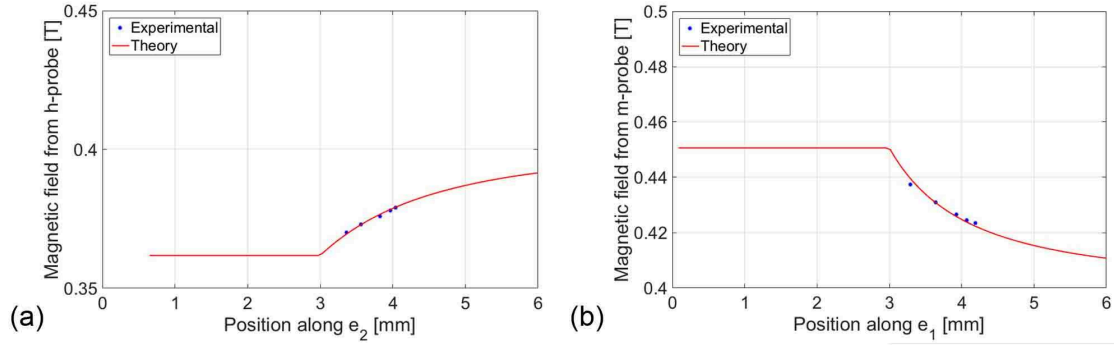


Figure II.17: Theoretical predictions and measurements of the magnetic field evolution outside of the sample: a) \mathbf{h} -field and its \mathbf{e}_1 component evolution along the \mathbf{e}_2 axis, b) \mathbf{b} -field and its \mathbf{e}_1 component evolution along the \mathbf{e}_1 axis.

CHAPTER III

MODELING AND IDENTIFICATION OF THE CONSTITUTIVE BEHAVIOR OF MAGNETORHEOLOGICAL ELASTOMERS

Contents

III.1	Introduction	64
III.2	Experiments	66
III.2.1	Tests description	66
III.2.2	Sample design	67
III.2.3	Fabrication procedure	67
III.2.4	Measurement techniques	68
III.2.5	Experimental verification of negligible dissipation	69
III.3	Theory	71
III.3.1	Overview of governing equations	71
III.3.2	Variational formulation alternatives	74
III.3.3	Equivalence between formulations	82
III.3.4	Type of Energies considered	85
III.4	Numerical Implementation	88
III.4.1	Coulomb gauge for the magnetic vector potential	88
III.4.2	Boundary conditions	89
III.4.3	Symmetry conditions for the magnetic vector potential	93
III.5	Results	95
III.5.1	Free energy determination using the F-B formulation ($\psi_B(\mathbf{F}, \mathbf{B})$)	95
III.5.2	Predictive capabilities of the model	99
III.5.3	Free energy in other formulations (ψ_H, ψ_M)	100

III.6 Conclusions	106
Appendix III.A Complement Theory	106
III.A.1 F-B Theory	106
III.A.2 F-H Theory	109
III.A.3 Details of Calculation	110
III.A.4 Calculation of the total stress tensor $\mathbf{\Pi}$	111
Appendix III.B Importance of specimen geometry	113

III.1 Introduction

Magnetorheological elastomers (MRE) are soft composite materials which consist of an elastomeric matrix and (sub-)micron sized magnetic inclusions. These composites are members of a wide class of materials called ‘active materials’, in virtue of their strong magneto-elastic coupling properties. Since the mechanical properties can be altered rapidly and reversibly when subjected to external magnetic fields, MREs have been proposed and tested for a variety of applications in which it is desirable to continuously and controllably vary the effective stiffness of a device under different operating conditions. In particular, MREs have been manufactured and studied as adaptive engine mounts and tunable shock absorbers (see Ginder et al. [65, 64]).

In dealing with these materials, it has been observed experimentally that the magneto-mechanical response of an MRE specimen is mainly driven by two effects. The first is due to the conformation of the MRE’s microstructure in the sense of inclusion distribution (Danas et al. [40]). The second effect is due to the specimen’s shape and reveals itself through the interaction of the specimen with its surrounding (Diguet et al. [46], Bodelot et al. [14]). The shape effects pose a challenge for the experimental determination of the effective material properties since the magneto-mechanical interaction of the specimen with its environment plays a crucial role for its overall coupled response and depends on both the properties of the material and the shape of the specimen. While this is already complicated for undeformed specimens, the situation is even more delicate at finite strains. The existence of shape-dependencies in the context of MREs was first addressed in the work by Diguet [46], and attempts to use numerical simulations to develop ideas on how to design experimental procedures for the precise characterization of MRE properties at large deformations have been proposed by Keip and Rambauser [93, 94]. In the recent past, analytical models were successfully fitted to experimental measurements on MRE devices. Indeed we highlight the works of Galipeau and Ponte Castañeda [58], Danas et al. [40], Ivaneyko et al. [81], Maas and Uhlenbusch [104] and Xin et al. [152] who adjusted analytical models to experiments on particular specimens and applications. The fitted parameters, however, cannot be classified as material parameters since they are strictly related to the specific MRE specimen or device. This means, that when the design of the device is changed (for instance by modifying its shape), the parameters have to be adjusted again. To our knowledge, Pössinger [125] and Bodelot [14] are the only ones who tackled this issue by developing a novel, almost ellipsoidal

MRE specimen to reduce the shape effects, and their experimental data will be used in this study to compute the material parameters of isotropic MREs.

The above experimental studies are completed by significant theoretical achievements (started back in the 1950s and 1960s) in the area of magneto-elasto-statics at finite strains. Although a literature review of continuum as well as micro-mechanically based magneto-elasticity is beyond the scope of this study, a few comments are helpful to put the present work in perspective and motivate the particular continuum model used here. The modeling approaches can be broadly classified into two categories. The first is the ‘direct’ method which uses conservation laws of continuum mechanics, e.g. Truesdell and Toupin [147], Tiersten [145], Maugin and Eringen [110, 111], Pao and Yeh [122], Pao [121]. The second method is an energetic approach which uses the calculus of variations to extremize an appropriate potential energy, e.g. Tiersten [146], Brown [22], Maugin and Eringen [110, 111]. Recently, based on the work of Brown [22], Kankanala [90] proved that the direct and variational approaches result in the same set of governing equations. At the heart of these theories is a free energy density that depends on a magnetic variable (Kankanala [90] and Danas [40] chose the magnetization per unit mass \mathbf{M} , Dorfmann and Ogden [47] used the magnetic field \mathbf{B}). In addition to the continuum based approach, a number of micro-mechanically based studies have recently been reported on MREs. Their purpose is to provide mean (or homogenized) field theories for the macroscopic behavior of MREs using a wide variety of simplifying assumptions about local strain and magnetic fields, e.g. Jolly et al. [84], Yin et al. [153] for inclusions in dilute limit, Corcolle et al. [37] using small strain Hashin-Strikman homogenized MRE model. Due to technical difficulties associated with large kinematics, the previously mentioned micro-mechanically based studies are in the small strain context, save for the recent work by Ponte Castañeda and Galipeau [124, 59, 60], Lefèvre and Lopez-Pamies [100] and Danas [39].

Currently, we have only limited knowledge on how to determine intrinsic MRE properties. Thus the goal of our research is to propose a complete road map to compute and validate an energy density for isotropic MREs.

The outline of the Chapter is as follows. First, we present the experimental data (obtained in Bodelot [14]) that will be used to compute the material parameters of isotropic MREs in Section III.2. In Section III.3, the theoretical formulation using the energetic approach proposed by Kankanala [90] is extended and proposed for all three possible choices of the magnetic independent variable. In the same section, we prove that all three formulations are equivalent, and we propose appropriate forms for the free energies to describe the experiments. Next, Section III.4 explains how to numerically implement the proposed variational formulations, and shows which are the correct boundary conditions to impose to properly simulate MRE boundary value problems. Lastly, in Section III.5, we use finite element simulations in combination with least square optimization algorithms to compute the material parameters. The use of numerical tools is necessary to make sure that the shape effect seen in experiments is taken into account in the simulation so that the material parameters proposed are not influenced by the shape of the specimens. The proposed material model is validated by testing its predictive capabilities on other experimental data. In Appendix, the interested reader can find extensive discussions on the influence of the shape effect.

III.2 Experiments

This section explains the experimental procedure used to characterize the coupled magneto-mechanical response of magnetorheological elastomers. More specifically we describe the tests, the samples' design, the fabrication procedure and the measurement techniques. The section is concluded by experimental evidence of negligible dissipation supporting the proposed theoretical formulation. For a more detailed study on the experimental investigation of these materials, the interested reader is referred to Bodelot et al. [14].

III.2.1 Tests description

The characterization of the fully coupled magneto-mechanical response of isotropic MREs requires two different tests.

A purely mechanical uniaxial tensile test as depicted in Figure III.1a is first performed, in which the axial displacement is controlled (i.e. λ_2 is applied) and the sample is stress-free in the directions transverse to its axis. The associated force F_2 (and thus the nominal traction T_2) is measured as well as the principal transverse stretch ratios λ_1 and λ_3 .

Next, a coupled magneto-mechanical test is conducted. Due to geometric constraints imposed by the experimental equipment, we choose a purely magnetostrictive test in which the sample is subjected to a uniform magnetic field \mathbf{b}_0 applied far from its boundaries, in a direction transverse to its axis (see Figure III.1b). The axial force F_2 is maintained at 0 N to impose traction free boundary conditions, thus approximating the conditions of a freely suspended sample in a uniform magnetic field. The perturbations caused by the sample on the magnetic field \mathbf{b} , the magnetic intensity \mathbf{h} , the magnetization vector \mathbf{m} in the sample and the three principal stretch ratios λ_i are measured.

The two above described experiments (purely mechanical and purely magnetostrictive) are sufficient to fully characterize isotropic MREs. However, more data are needed to test the predictive capabilities of the obtained constitutive model. For this purpose, coupled experiments similar to the purely magnetostrictive test are conducted using different axial forces F_2 (maintained constant during the test).

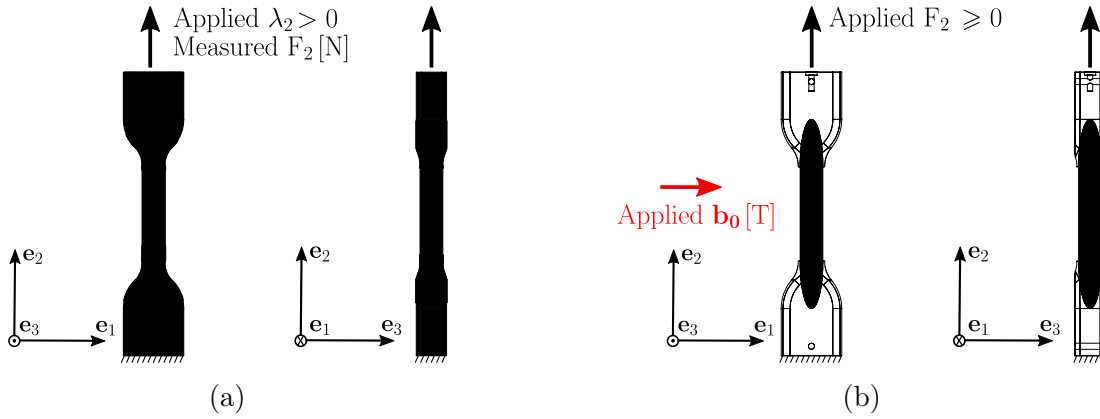


Figure III.1: Schematic of the two types of experiments. Purely mechanical tests are based on a “dog bone” sample with MRE heads (a) while coupled magneto-mechanical (magnetostrictive) tests use cylindrical specimens with ellipsoidal ends bonded to specially designed non-magnetizable 3D printed polymer grips (b).

III.2.2 Sample design

As one can notice in Figure III.1, the sample’s shape is specific for each test. Sample shapes for the evaluation of purely mechanical properties are designed to achieve a uniform state of stress in the gage area of the sample away from the heads. We hence use a dog-bone shaped sample with a gage area of circular cross-section as shown in Figure III.1a. However, using the same specimen (Figure III.1a) for the coupled magnetostrictive tests results in large Maxwell stresses in the two heads, rendering impossible the stress calculations in the gage area. To counter this, a different design for the heads is necessary. Only ellipsoidally shaped uniform rigid bodies subjected to constant remote external magnetic fields result in uniform internal magnetic fields (see Osborn [120] and Tejedor [143]). Hence we design magnetostriction specimens with ellipsoidal ends, while keeping a cylindrically shaped gage area (see Figure III.1b). This allows the accurate calculation of the stresses in the gage area. The grips which are made by a non-magnetic 3D-printed polymer are then glued to the ellipsoidal ends of the MRE specimen as shown in Figure III.1b. In conclusion, the dog-bone specimen of Figure III.1a is kept for the purely mechanical tests, especially since we impose large strains that would lead to debonding of the plastic heads of the magnetostriction sample. The ellipsoidal head specimen of Figure III.1b is used for the coupled magneto-mechanical (magnetostrictive) tests since the applied tractions are low enough to keep the integrity of the specimen.

III.2.3 Fabrication procedure

The MREs of interest here consist of nearly spherical carbonyl iron particles (with a median size of $3.5\mu m$) embedded in a soft and stretchable silicone elastomer. The particles are first pre-treated with a silane primer in order to avoid debonding from the elastomer matrix when subjected to a coupled magneto-mechanical loading, due to the large inter-particle axial strains as discussed by Danas [39]. The desired quantity of particles, polymer and catalyzer are then mixed. The final blend is degassed (to eliminate air entrapped during mixing) and

poured in a mold of the desired shape. Finally, curing is performed by heating the mold (see Bodelot et al. [14]).

III.2.4 Measurement techniques

A specific setup has been designed to investigate the response of MREs under large strains and high magnetic fields. It comprises an electromagnet that produces a uniform magnetic field, and a tension setup that brings the sample in the magnetic field (see Figures III.2a and III.2b) and imposes either a displacement or an axial force. To avoid interference of the strong magnetic fields, the tension setup is equipped with piezoelectric motors. The overall deformation quantities of the sample are measured in-situ via non-contact video extensometry. A mirror inclined at a 45° with respect to the camera's axis is positioned next to the sample and reflects an image of its side (see Figure III.2a and III.2b). The measurements taken from the front and the side of the sample allow the calculation of stretch ratios in the three principal directions. The longitudinal elongation along \mathbf{e}_2 is obtained by depositing markers consisting of a pair of white paint dots along the sample's vertical axis prior to testing. The diameter changes of the initially circular section along \mathbf{e}_1 and \mathbf{e}_3 are measured using an edge detection technique. A tracking algorithm follows in-situ the two vertical dots and the two pairs of borders, giving access to the three principal stretch ratios λ_i ; ratios of corresponding final to initial lengths (see Figure III.2c). It is important to note that such macroscopic measurements are not necessarily representative of the corresponding local values. According to our numerical simulations discussed in Appendix III.B, nearly uniformly magnetized MRE samples exhibit heterogeneities in their strain fields (see Figure III.17a), and hence the λ_i are average stretch ratios.

The measurement of the magnetic quantities take advantage of the specimen's ellipsoidal heads which guarantee fairly uniform internal magnetic fields and magnetization even for the deformable magnetic bodies at hand (see Figure III.17b). The continuity of the tangential component of \mathbf{h} , and the continuity of the normal component of \mathbf{b} at the interface sample/air allows the measurements of the two magnetic quantities of interest using two Hall probes positionned at the back and the side of the middle section of the specimen (see Figure III.2c). The difference of these measurements gives the sought magnetization field $\mathbf{m} = m_1 \mathbf{e}_1 = [(b_1/\mu_0) - h_1] \mathbf{e}_1$. In practice the sensitive elements of the Hall probes cannot be placed exactly at the interface due to geometrical limitations, requiring us to correct the measurement's systematic error. A detailed derivation of this correction based on the analytical solution of Laplace's equation governing the \mathbf{h} -field outside the specimen is presented in Bodelot et al. [14].

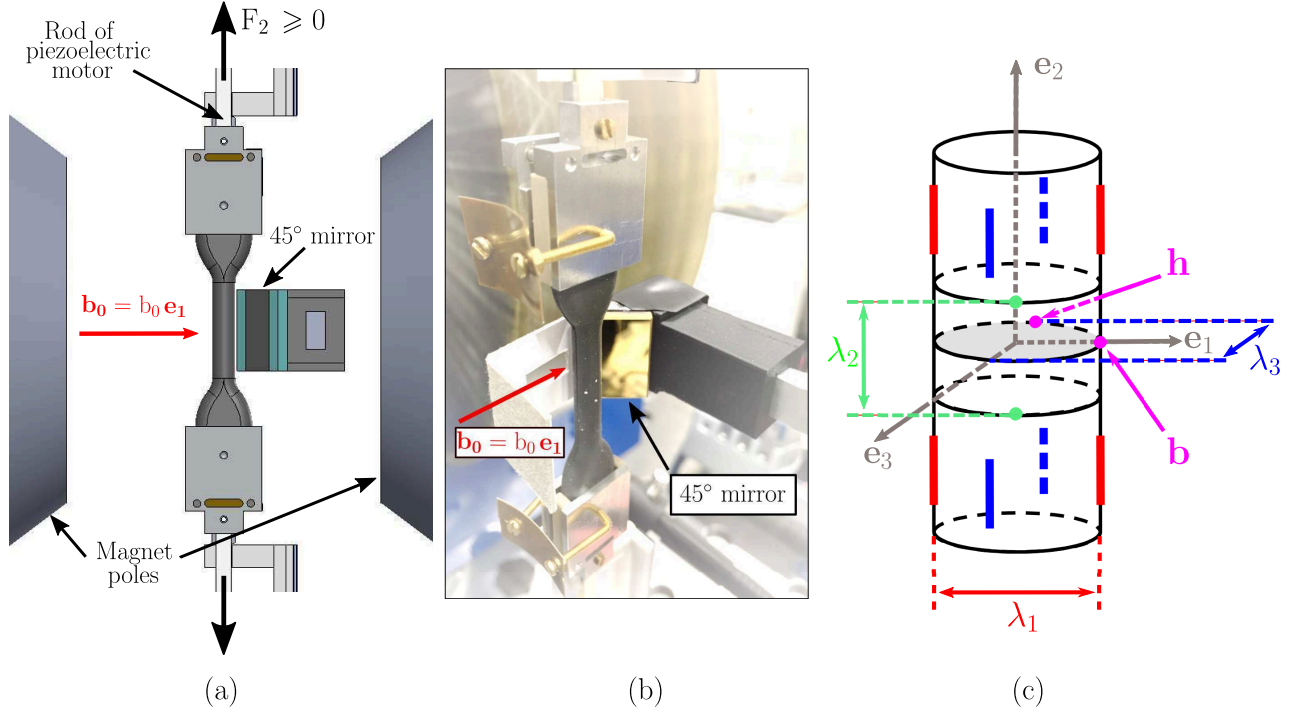


Figure III.2: Experimental setup and measurements. In (a) schematics of the tension setup that allows for the imposition and measurement of the axial force F_2 and the side mirror allowing tracking of specimen borders. In (b) a picture of the tension setup and the side mirror. The figure (c) illustrates average stretch ratios λ_i and indicates locations for measuring b_1 and h_1 (the components along \mathbf{e}_1 of \mathbf{b} and \mathbf{h} respectively).

III.2.5 Experimental verification of negligible dissipation

The proposed continuum modeling of the isotropic MRE at hand is based on a Helmholtz free energy where the independent variables are the deformation gradient \mathbf{F} and the magnetic field \mathbf{B} (or equivalently the \mathbf{H} -field or the magnetization \mathbf{m}). Note that \mathbf{B} (resp. \mathbf{H}) is the Lagrangian counterpart of \mathbf{b} (resp. \mathbf{h}). No internal variable is necessary in the theoretical formulation in view of the absence of any rate and hysteretic phenomena in either the mechanical or the magnetic response of the tested isotropic MRE specimens (which contained 8.7% Fe particles in volume fraction), for loading rates up to $8.6 \times 10^{-4} \text{ s}^{-1}$ (for the purely mechanical tests) and $4.0 \times 10^{-4} \text{ T/s}$ (for the magnetostrictive test), stretch ratios up to 1.72 (for the purely mechanical tests) and magnetic fields up to 0.8 T and constant axial forces up to 0.2 N (in the magnetostrictive test). It should also be noted here that the particle volume fraction of 8.7% is the highest that allows the purely magnetostrictive tests to be carried out without the occurrence of any buckling phenomena.

The results of the purely mechanical uniaxial loading/unloading tensile test under imposed λ_2 are presented in Figure III.3. The nominal stress-stretch curve for an entire cycle is plotted in Figure III.3a, where one can notice a practically hyperelastic behavior in view of a negligible hysteretic loop for strain rates up to $8.6 \times 10^{-4} \text{ s}^{-1}$. As expected from

incompressibility, the stretch ratios λ_1 and λ_3 in the transverse directions are almost equal and show no hysteric loop as seen in Figure III.3b.

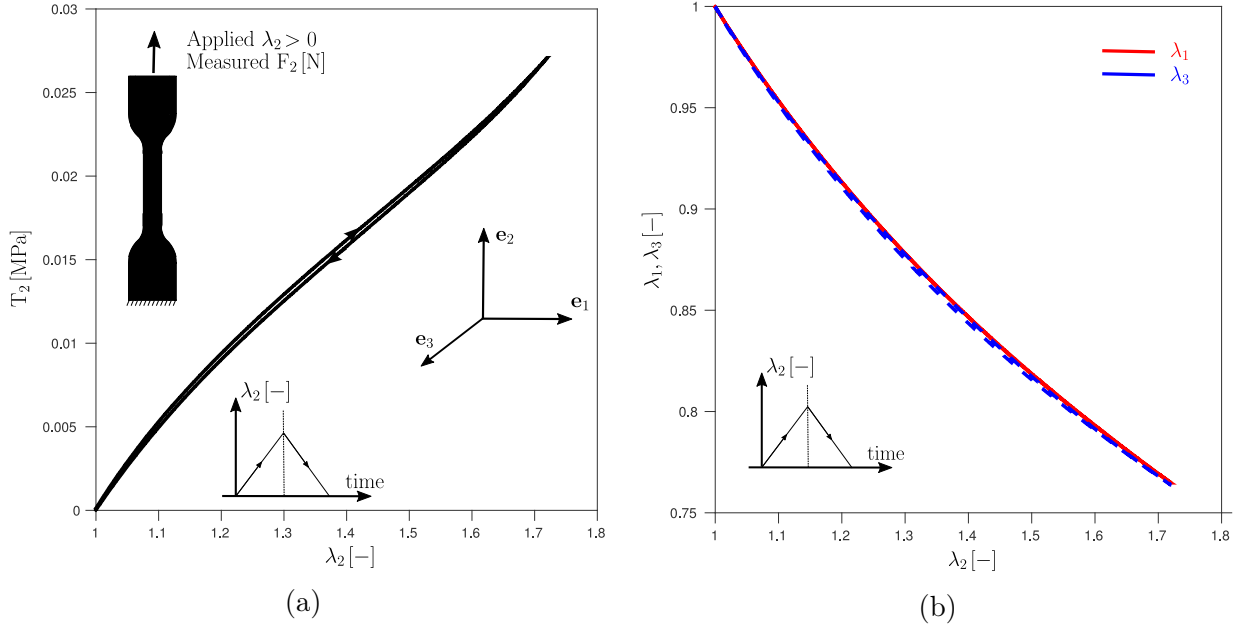


Figure III.3: Experimental verification of negligible dissipative phenomena in the purely mechanical tests. The nominal traction T_2 - stretch ratio λ_2 in a uniaxial experiment is shown in (a) and the lateral stretch ratios λ_1 , λ_3 in (b). Notice the negligible difference between loading and unloading paths in (a), and the coincidence of λ_1 , λ_3 loading and unloading paths in (b).

For the results of the purely magnetostrictive test, measurements under imposed \mathbf{b}_0 , are plotted in Figure III.4. The largest average stretch ratio occurring along the applied field direction \mathbf{e}_1 , and the average stretch ratios in the other two transverse directions are plotted in Figure III.4a. Notice the negligible hysteric loop in the loading/unloading portions of λ_2 and the small hysteric loops in the λ_1 and λ_3 curves. Due to the shape effect, $\lambda_2 \neq \lambda_3$ contrary to what one could expect from isotropy in a specimen with uniform strain fields. An almost total absence of a hysteric loop is also observed in the magnetization \mathbf{m} versus remotely applied magnetic field \mathbf{b}_0 curves depicted in Figure III.4b where the loading/unloading portions of the curve are practically coincident. It is worth noticing that for magnetic fields up to 0.4 T the magnetization response of the MRE is linear, while saturation is almost reached at about 0.8 T (higher magnetic fields cannot be applied due to equipment limitations). The insert in Figure III.4b plots the magnetization \mathbf{m} versus \mathbf{h} -field inside the specimen, clearly showing the initial linear range of the response (the initial slope of the \mathbf{m} - \mathbf{h} curve is χ , the initial magnetic susceptibility of the MRE). Finally Figure III.4c emphasizes the fact that the eulerian magnetic field \mathbf{b} inside the sample must not be confused with the magnetic field \mathbf{b}_0 applied far from its boundaries. Indeed, \mathbf{b}_0 is a loading parameter that is controlled via the electromagnet whereas \mathbf{b} , measured on the surface of the specimen, accounts for the perturbation caused by the MRE sample.

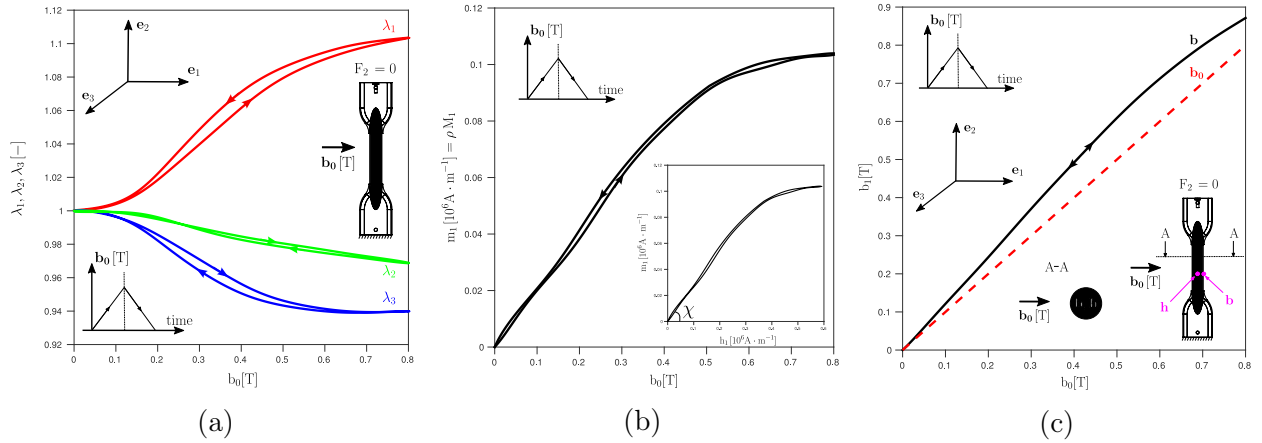


Figure III.4: Experimental verification of the negligible dissipative phenomena in the purely magnetostrictive test ($F_2 = 0$). The macroscopic stretch ratios λ_i as functions of the remotely applied magnetic field \mathbf{b}_0 are presented in (a). The corresponding results for the magnetization m_1 inside the specimen are shown in (b) where the loading/unloading curves are almost coincident. Finally in (c) we show the difference between the remotely applied field \mathbf{b}_0 and the measured magnetic field \mathbf{b} inside the specimen.

The above presented data provide evidence that hysteretic effects are weak. However they are not inexistant and for both tests only half of the cycle where the loading parameter increases will be considered in the fitting process. Nevertheless, at a first approximation dissipative phenomena can be neglected in our model, thus explaining the adopted energy formulation without the need of using internal variables.

III.3 Theory

This section pertains to the energy-based theoretical formulation used for solving the MRE boundary value problem associated to our experiments. The first part presents an overview of the governing equations in Eulerian and Lagrangian formulations. The second part gives the three different versions, depending on the choice for the magnetic independent variables in the energy density, of the variational formulation needed for the numerical solution of the MRE boundary value problem. The third part shows the equivalence between the different formulations. The fourth part presents the specific forms adopted for the energy densities and used in FEM calculations to fit the experimental data.

III.3.1 Overview of governing equations

Although the governing equations for finite strain magnetoelasticity are known [90, 40, 47, 49, 26, 39], a brief presentation is given here for completeness of the presentation. Henceforth the usual continuum mechanics conventions are adopted, according to which all field quantities associated with the current configuration are denoted by small letters, while capitals are used for their reference configuration counterparts. Moreover scalar quantities are denoted by script symbols while bold symbols are used for vector and tensor quantities.

Consider a 3D magnetoelastic body that occupies a region V (resp v) with boundary ∂V (∂v) and outward normal \mathbf{N} (\mathbf{n}) in the undeformed reference (deformed current) configuration as seen in Figure III.5. A material point of initial position vector \mathbf{X} in V has a current position vector $\mathbf{x} = \mathbf{x}(\mathbf{X}) = \mathbf{X} + \mathbf{u}(\mathbf{X})$, where \mathbf{u} is the displacement field vector.

The deformation gradient \mathbf{F} and its determinant J needed to quantify the mechanical strain contribution to MRE's free energy are defined by,

$$\mathbf{F} \equiv \nabla \mathbf{x} = \mathbf{I} + \nabla \mathbf{u}, \quad J \equiv \det \mathbf{F} > 0; \quad \forall \mathbf{x} \in v, \quad (\text{III.3.1})$$

where $\nabla \equiv \partial/\partial \mathbf{X}$ denotes the reference configuration gradient operator and \mathbf{I} the rank 3 identity tensor.

The reference density of the solid ρ_0 is related to the current density ρ through mass conservation by equation

$$\rho_0 = \rho J. \quad (\text{III.3.2})$$

The mechanical quantities needed for setting the MRE boundary value problem are the total Cauchy stress measure $\boldsymbol{\sigma}$, the mechanical body force \mathbf{f} and the mechanical traction \mathbf{t} in the deformed configuration (that might be imposed at a boundary/interface¹). They satisfy (see Kankanala [90] and Dorfmann [47]) the following equation and boundary/interface condition

$$\nabla \cdot \boldsymbol{\sigma} + \rho \mathbf{f} = \mathbf{0}; \quad \forall \mathbf{x} \in v, \quad \mathbf{n} \cdot \llbracket \boldsymbol{\sigma} \rrbracket = \mathbf{t}; \quad \forall \mathbf{x} \in \partial v. \quad (\text{III.3.3})$$

The magnetic quantities introduced in Section III.2 are the magnetic field \mathbf{b} , the magnetic intensity \mathbf{h} also termed \mathbf{h} -field and the magnetization vector \mathbf{m} , and are related by

$$\mathbf{b} = \mu_0 (\mathbf{h} + \mathbf{m}), \quad \mathbf{m} \neq \mathbf{0}; \quad \forall \mathbf{x} \in v; \quad \mathbf{b} = \mu_0 \mathbf{h}, \quad \mathbf{m} = \mathbf{0}; \quad \forall \mathbf{x} \in \mathbb{R}^3 \setminus v, \quad (\text{III.3.4})$$

where μ_0 is the magnetic permeability in vacuum. The fields \mathbf{b} and \mathbf{h} are Eulerian fields that satisfy the following differential equations and boundary/interface¹ conditions in magnetostatics [90, 40, 47, 26, 39]. From the no magnetic monopole law and Gauss's divergence theorem, one obtains

$$\nabla \cdot \mathbf{b} = 0; \quad \forall \mathbf{x} \in \mathbb{R}^3, \quad \mathbf{n} \cdot \llbracket \mathbf{b} \rrbracket = 0; \quad \forall \mathbf{x} \in \partial v, \quad (\text{III.3.5})$$

where $\nabla \equiv \partial/\partial \mathbf{x}$ is the current configuration gradient operator, $\nabla \cdot$ is the corresponding divergence operator and $\llbracket f \rrbracket \equiv f^+ - f^-$ is the jump of any field quantity f evaluated at either side of the solid/air interface. From Ampère's circuit law and Stokes theorem, we can derive the following equations in the absence of external current density

$$\nabla \times \mathbf{h} = \mathbf{0}; \quad \forall \mathbf{x} \in \mathbb{R}^3, \quad \mathbf{n} \times \llbracket \mathbf{h} \rrbracket = \mathbf{0}; \quad \forall \mathbf{x} \in \partial v. \quad (\text{III.3.6})$$

Since the variational formulation used here is based on the Lagrangian description of the MRE boundary value problem, it is important to remind that both the mechanical and the magnetic Eulerian quantities can be 'pulled back' from v to V to their Lagrangian

¹ NOTE: The only interface that needs to be considered is the MRE solid/air interface, which coincides with ∂v . Magnetic fields as well as Maxwell stress fields exist in both the solid and the surrounding air and hence the boundary conditions in MRE's are interface conditions.

counterparts. The relation between the total Cauchy stress and the total first Piola-Kirchhoff stress tensor $\mathbf{\Pi}$ reads

$$\mathbf{\Pi} = J\boldsymbol{\sigma} \cdot \mathbf{F}^{-T}. \quad (\text{III.3.7})$$

The Lagrangian counterparts of the Eulerian magnetic fields \mathbf{b} and \mathbf{h} , denoted by \mathbf{B} and \mathbf{H} respectively are defined by (see for instance Dorfmann [47], Bustamante [26] and Danas [39]))

$$\mathbf{B} = J\mathbf{F}^{-1} \cdot \mathbf{b}, \quad \mathbf{H} = \mathbf{F}^T \cdot \mathbf{h}. \quad (\text{III.3.8})$$

These Lagrangian variables satisfy equations and boundary/interface conditions analogous to their Eulerian counterparts

$$\nabla \cdot \mathbf{\Pi} + \rho_0 \mathbf{f} = \mathbf{0}; \quad \forall \mathbf{X} \in V, \quad \mathbf{N} \cdot \llbracket \mathbf{\Pi} \rrbracket = \mathbf{T}; \quad \forall \mathbf{X} \in \partial V, \quad (\text{III.3.9})$$

where \mathbf{T} is the reference mechanical traction on the boundary of the solid. Hence the reference configuration counterpart of (III.3.5) reads,

$$\nabla \cdot \mathbf{B} = \mathbf{0}; \quad \forall \mathbf{X} \in \mathbb{R}^3, \quad \mathbf{N} \cdot \llbracket \mathbf{B} \rrbracket = \mathbf{0}; \quad \forall \mathbf{X} \in \partial V, \quad (\text{III.3.10})$$

and the reference configuration counterpart of (III.3.6) is

$$\nabla \times \mathbf{H} = \mathbf{0}; \quad \forall \mathbf{X} \in \mathbb{R}^3, \quad \mathbf{N} \times \llbracket \mathbf{H} \rrbracket = \mathbf{0}; \quad \forall \mathbf{X} \in \partial V. \quad (\text{III.3.11})$$

Moreover, as it has been mentioned in the literature (see Dorfmann [49] and Danas [39]), the magnetization vector \mathbf{m} is a Eulerian variable. A Lagrangian form for \mathbf{m} would be non unique since Eq. (III.3.4) is not invariant under current-to-reference configuration transformations.

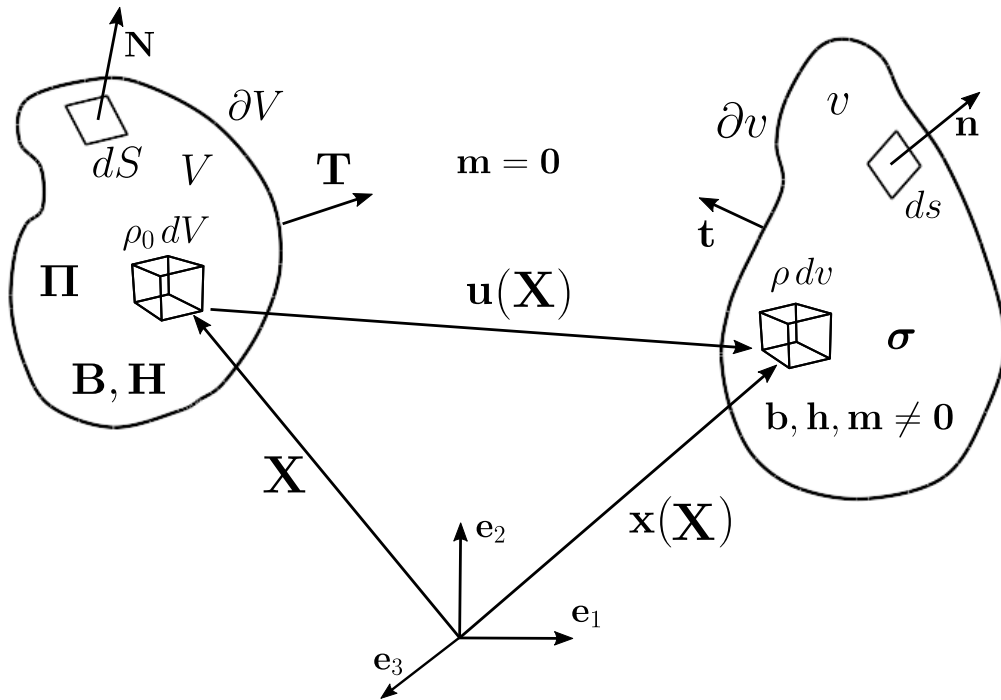


Figure III.5: Schematic diagram of reference and current configurations with associated mechanical and magnetic variables.

III.3.2 Variational formulation alternatives

In the previous section we establish the governing equations and the boundary/interface conditions for the finitely strained magnetoelastic solid. The description of its constitutive response is the missing link to complete the setting for the solution of the corresponding boundary value problem. The variational formulation adopted requires an energy density for the MRE solid. Here, unlike the mechanical contribution which is characterized by the deformation gradient \mathbf{F} , one has the possibility of different choices for the magnetic contribution, resulting in alternative variational formulations of the boundary value problem.

As explained by Brown [22] and Kankanala [90], a Lagrangian setting is necessary to capture Maxwell stresses in the coupled variational formulation of the magnetoelastic problem. Consequently the solid's Helmholtz free energy ψ can depend (in addition to \mathbf{F}) on \mathbf{B} or \mathbf{H} . An additional alternative based on \mathbf{m} is also possible. Each formulation has its own advantages as discussed in length by Danas [39] and hence all three will be given here. Moreover, the approach introduced by Brown [22] using the perturbed magnetic field is presented here, in view of its computational advantages (see Danas [39]).

III.3.2.a Formulation using \mathbf{B} (free energy $\psi_B(\mathbf{F}, \mathbf{B})$)

We assume that the specific free energy density is a function of the reference configuration magnetic field \mathbf{B} . Consequently the total energy stored in the system (solid and surrounding air) \mathcal{E}_B is the sum of the energy stored in the MRE solid (integral over V) plus the magnetic energy of the entire space (integral over \mathbb{R}^3) namely

$$\mathcal{E}_B = \int_V \rho_0 \psi_B(\mathbf{F}, \mathbf{B}) \, dV + \frac{1}{2\mu_0} \int_{\mathbb{R}^3} \frac{1}{J} \mathbf{B} \cdot \mathbf{C} \cdot \mathbf{B} \, dV, \quad (\text{III.3.12})$$

where $\psi_B(\mathbf{F}, \mathbf{B})$ is the MRE's specific Helmholtz free energy for the \mathbf{B} -formulation and $\mathbf{C} = \mathbf{F}^T \cdot \mathbf{F}$ is the right Cauchy-Green tensor. The potential of the externally applied mechanical loads, i.e. the body force \mathbf{f} per unit mass in V and the surface nominal traction \mathbf{T} per unit reference area on ∂V is

$$\mathcal{W} = \int_V \rho_0 \mathbf{f} \cdot \mathbf{u} \, dV + \int_{\partial V} \mathbf{T} \cdot \mathbf{u} \, dS. \quad (\text{III.3.13})$$

Hence the potential energy \mathcal{P}_B of the system (solid plus surrounding free space) is from Eq. (III.3.12) and Eq. (III.3.13)

$$\mathcal{P}_B = \mathcal{E}_B - \mathcal{W} = \int_V (\rho_0 \psi_B(\mathbf{F}, \mathbf{B}) - \rho_0 \mathbf{f} \cdot \mathbf{u}) \, dV + \frac{1}{2\mu_0} \int_{\mathbb{R}^3} \frac{1}{J} \mathbf{B} \cdot \mathbf{C} \cdot \mathbf{B} \, dV - \int_{\partial V} \mathbf{T} \cdot \mathbf{u} \, dS. \quad (\text{III.3.14})$$

Using Eq. (III.3.8) (and $dv = JdV$), the second term of the potential energy \mathcal{P}_B can be rewritten as

$$\frac{1}{2\mu_0} \int_{\mathbb{R}^3} \frac{1}{J} \mathbf{B} \cdot \mathbf{C} \cdot \mathbf{B} \, dV = \frac{1}{2\mu_0} \int_{\mathbb{R}^3} \mathbf{b} \cdot \mathbf{b} \, dv. \quad (\text{III.3.15})$$

We decompose the magnetic field \mathbf{b} (resp. \mathbf{B}) as the sum of an externally applied magnetic field \mathbf{b}_0 (resp. \mathbf{B}_0) (in the absence of the MRE solid) and a perturbation magnetic field $\tilde{\mathbf{b}}$

(resp. $\tilde{\mathbf{B}}$) (created by the presence of the MRE solid), i.e. $\mathbf{b} = \mathbf{b}_0 + \tilde{\mathbf{b}}$ (resp. $\mathbf{B} = \mathbf{B}_0 + \tilde{\mathbf{B}}$)², thus obtaining from (III.3.15)

$$\frac{1}{2\mu_0} \int_{\mathbb{R}^3} \mathbf{b} \cdot \mathbf{b} \, dv = \frac{1}{2\mu_0} \int_{\mathbb{R}^3} \mathbf{b}_0 \cdot \mathbf{b}_0 \, dv + \frac{1}{\mu_0} \int_{\mathbb{R}^3} \mathbf{b}_0 \cdot \tilde{\mathbf{b}} \, dv + \frac{1}{2\mu_0} \int_{\mathbb{R}^3} \tilde{\mathbf{b}} \cdot \tilde{\mathbf{b}} \, dv. \quad (\text{III.3.16})$$

The first term of Eq. (III.3.16): $\frac{1}{2\mu_0} \int_{\mathbb{R}^3} \mathbf{b}_0 \cdot \mathbf{b}_0 \, dv$ represents the energy of the externally applied magnetic field before the introduction of the MRE solid. This term is finite and depends on \mathbf{b}_0 , and as a constant can be omitted from the potential energy. Moreover, as we show in Appendix III.A.1, the second term of Eq. (III.3.16): $\frac{1}{\mu_0} \int_{\mathbb{R}^3} \mathbf{b}_0 \cdot \tilde{\mathbf{b}} \, dv$ is equal to zero, and hence from Eq. (III.3.15) and Eq. (III.3.16), the potential energy \mathcal{P}_B can be rewritten as

$$\mathcal{P}_B = \int_{\mathbb{R}^3} \tilde{W}_B(\mathbf{F}, \tilde{\mathbf{B}}) \, dV - \int_V \rho_0 \mathbf{f} \cdot \mathbf{u} \, dV - \int_{\partial V} \mathbf{T} \cdot \mathbf{u} \, dS, \quad (\text{III.3.17})$$

where the energy density \tilde{W}_B is defined as

$$\tilde{W}_B(\mathbf{F}, \tilde{\mathbf{B}}) = \begin{cases} \rho_0 \psi_B(\mathbf{F}, \tilde{\mathbf{B}} + J\mathbf{F}^{-1} \cdot \mathbf{b}_0) + \frac{1}{2\mu_0 J} \tilde{\mathbf{B}} \cdot \mathbf{C} \cdot \tilde{\mathbf{B}}; & \forall \mathbf{X} \in V, \\ \frac{1}{2\mu_0 J} \tilde{\mathbf{B}} \cdot \mathbf{C} \cdot \tilde{\mathbf{B}}; & \forall \mathbf{X} \in \mathbb{R}^3 \setminus V. \end{cases} \quad (\text{III.3.18})$$

The perturbation magnetic field $\tilde{\mathbf{b}}$ is divergence free since both the total magnetic field \mathbf{b} and the externally applied magnetic field \mathbf{b}_0 are divergence free, according to Eq. (III.3.5), i.e. $\nabla \cdot \tilde{\mathbf{b}} = 0$, $\forall \mathbf{x} \in \mathbb{R}^3$. From Eq. (III.3.8), this differential constraint holds for the Lagrangian magnetic fields as well (see Dorfmann [47], Bustamante [26] and Danas [39]), i.e. $\nabla \cdot \tilde{\mathbf{B}} = 0$, $\forall \mathbf{X} \in \mathbb{R}^3$, and hence one can express $\tilde{\mathbf{B}}$ in term of a vector potential $\tilde{\mathbf{A}}$

$$\tilde{\mathbf{B}} = \nabla \times \tilde{\mathbf{A}}, \quad \forall \mathbf{X} \in \mathbb{R}^3. \quad (\text{III.3.19})$$

As the perturbation field must vanish far away from the solid, i.e. $\|\tilde{\mathbf{B}}\| \rightarrow 0$ as $\|\mathbf{X}\| \rightarrow \infty$, it is reasonable to choose $\tilde{\mathbf{A}}$ that does the same, i.e. $\|\tilde{\mathbf{A}}\| \rightarrow 0$ as $\|\mathbf{X}\| \rightarrow \infty$.

By using Eq. (III.3.19), one can rewrite³ the potential energy \mathcal{P}_B in terms of independent variables \mathbf{u} and $\tilde{\mathbf{A}}$

$$\mathcal{P}_B = \int_{\mathbb{R}^3} \left(\tilde{W}_B(\mathbf{F}, \tilde{\mathbf{B}}) - \rho_0 \mathbf{f} \cdot \mathbf{u} \right) \, dV - \int_{\partial V} \mathbf{T} \cdot \mathbf{u} \, dS, \quad (\text{III.3.20})$$

based on the \mathbf{B} -formulation for the Helmholtz free energy $\psi_B(\mathbf{F}, \mathbf{B})$. Taking variations of the above potential energy $\mathcal{P}_B(\mathbf{u}, \tilde{\mathbf{A}})$, with respect to its independent variables $\tilde{\mathbf{A}}$ and \mathbf{u} , one

² NOTE: A similar decomposition holds for \mathbf{H} (resp. \mathbf{h}): $\mathbf{h} = \mathbf{h}_0 + \tilde{\mathbf{h}}$ (resp. $\mathbf{H} = \mathbf{H}_0 + \tilde{\mathbf{H}}$).

³ NOTE: $\mathbf{f} = \mathbf{0}$, $\forall \mathbf{X} \in \mathbb{R}^3 \setminus V$.

obtains two Euler-Lagrange equations respectively: Ampère's and equilibrium, combined with the corresponding magnetics and mechanics constitutive laws.

Indeed, by taking the variation of \mathcal{P}_B with respect to $\tilde{\mathbf{A}}$ one obtains after considerable algebraic manipulation

$$\mathcal{P}_{B, \tilde{\mathbf{A}}} \delta \tilde{\mathbf{A}} = \int_{\mathbb{R}^3} \left[\left(\nabla \times \frac{\partial \tilde{W}_B}{\partial \tilde{\mathbf{B}}} \right) \cdot \delta \tilde{\mathbf{A}} \right] dV + \int_{\partial V} \left[\left(\mathbf{N} \times \left[\frac{\partial \tilde{W}_B}{\partial \tilde{\mathbf{B}}} \right] \right) \cdot \delta \tilde{\mathbf{A}} \right] dS = 0. \quad (\text{III.3.21})$$

Upon comparing the resulting Euler-Lagrange equations and interface conditions with Eq. (III.3.11) and recalling that $\mathbf{H} = \mathbf{H}_0 + \tilde{\mathbf{H}}$, one obtains

$$\nabla \times \tilde{\mathbf{H}} = \mathbf{0}, \quad \forall \mathbf{X} \in \mathbb{R}^3, \quad \mathbf{N} \times [\tilde{\mathbf{H}}] = \mathbf{0}, \quad \forall \mathbf{X} \in \partial V; \quad \tilde{\mathbf{H}} = \frac{\partial \tilde{W}_B}{\partial \tilde{\mathbf{B}}}(\mathbf{F}, \tilde{\mathbf{B}}). \quad (\text{III.3.22})$$

Similarly by taking the variation of \mathcal{P}_B with respect to \mathbf{u} one obtains after considerable algebraic manipulation

$$\begin{aligned} \mathcal{P}_{B, \mathbf{u}} \delta \mathbf{u} = & - \int_{\mathbb{R}^3} \left[\left(\nabla \cdot \left(\frac{\partial \tilde{W}_B}{\partial \mathbf{F}} \right)^T + \rho_0 \mathbf{f} \right) \cdot \delta \mathbf{u} \right] dV + \\ & \int_{\partial V} \left[\left(\mathbf{N} \cdot \left[\left(\frac{\partial \tilde{W}_B}{\partial \mathbf{F}} \right)^T \right] - \mathbf{T} \right) \cdot \delta \mathbf{u} \right] dS = 0. \end{aligned} \quad (\text{III.3.23})$$

Upon comparing the resulting Euler-Lagrange equations and interface conditions with Eq. (III.3.9), one obtains

$$\nabla \cdot \tilde{\mathbf{\Pi}} + \rho_0 \mathbf{f} = \mathbf{0}, \quad \forall \mathbf{X} \in \mathbb{R}^3, \quad \mathbf{N} \cdot [\tilde{\mathbf{\Pi}}] = \mathbf{T}, \quad \forall \mathbf{X} \in \partial V; \quad \tilde{\mathbf{\Pi}}^T = \frac{\partial \tilde{W}_B}{\partial \mathbf{F}}(\mathbf{F}, \tilde{\mathbf{B}}). \quad (\text{III.3.24})$$

At this point it is instructive to see how the general constitutive equations obtained from \tilde{W}_B , which are valid for any $\mathbf{X} \in \mathbb{R}^3$, can be expressed inside and outside the MRE solid using the Helmholtz free energy ψ_B . From Eq. (III.3.18), one gets

$$\begin{cases} \tilde{\mathbf{H}} = \rho_0 \frac{\partial \psi_B}{\partial \tilde{\mathbf{B}}}(\mathbf{F}, \tilde{\mathbf{B}} + J\mathbf{F}^{-1} \cdot \mathbf{b}_0) + \frac{1}{\mu_0 J} \mathbf{C} \cdot \tilde{\mathbf{B}} = \rho_0 \frac{\partial \psi_B}{\partial \mathbf{B}} \Big|_{\mathbf{F}}(\mathbf{F}, \mathbf{B}) + \frac{1}{\mu_0 J} \mathbf{C} \cdot \tilde{\mathbf{B}}, & \forall \mathbf{X} \in V, \\ \tilde{\mathbf{H}} = \frac{1}{\mu_0 J} \mathbf{C} \cdot \tilde{\mathbf{B}}, & \forall \mathbf{X} \in \mathbb{R}^3 \setminus V, \end{cases} \quad (\text{III.3.25})$$

$$\left\{ \begin{array}{l} \tilde{\boldsymbol{\Pi}}^T = \rho_0 \frac{\partial \psi^B}{\partial \mathbf{F}} (\mathbf{F}, \tilde{\mathbf{B}} + J\mathbf{F}^{-1} \cdot \mathbf{b}_0) - \frac{1}{2\mu_0 J} (\tilde{\mathbf{B}} \cdot \mathbf{C} \cdot \tilde{\mathbf{B}}) \mathbf{F}^{-T} + \frac{1}{\mu_0 J} (\mathbf{F} \cdot \tilde{\mathbf{B}}) \tilde{\mathbf{B}}, \\ = \rho_0 \left[\frac{\partial \psi_B}{\partial \mathbf{F}} \Big|_{\mathbf{B}} + \left\{ \frac{\partial \psi_B}{\partial \mathbf{B}} \Big|_{\mathbf{F}} \cdot (J\mathbf{F}^{-1} \cdot \mathbf{b}_0) \right\} \mathbf{F}^{-T} - \left(\frac{\partial \psi_B}{\partial \mathbf{B}} \Big|_{\mathbf{F}} \cdot \mathbf{F}^{-1} \right) (J\mathbf{F}^{-1} \cdot \mathbf{b}_0) \right] + \\ \frac{1}{\mu_0 J} (\mathbf{F} \cdot \tilde{\mathbf{B}}) \tilde{\mathbf{B}} - \frac{1}{2\mu_0 J} (\tilde{\mathbf{B}} \cdot \mathbf{C} \cdot \tilde{\mathbf{B}}) \mathbf{F}^{-T}, \quad \forall \mathbf{X} \in V, \\ \tilde{\boldsymbol{\Pi}}^T = \frac{1}{\mu_0 J} (\mathbf{F} \cdot \tilde{\mathbf{B}}) \tilde{\mathbf{B}} - \frac{1}{2\mu_0 J} (\tilde{\mathbf{B}} \cdot \mathbf{C} \cdot \tilde{\mathbf{B}}) \mathbf{F}^{-T}, \quad \forall \mathbf{X} \in \mathbb{R}^3 \setminus V. \end{array} \right. \quad (\text{III.3.26})$$

These constitutive equations give the change in magnetic field and stress tensor due to the presence of the MRE solid. To find the corresponding total magnetic intensity, one has to add \mathbf{H}_0 . In addition, one can define a total stress $\boldsymbol{\Pi}$ (resp. $\boldsymbol{\sigma}$) which can be related to $\tilde{\boldsymbol{\Pi}}$ (resp. $\tilde{\boldsymbol{\sigma}}$) as explained in Appendix III.A.4. Of importance is the fact that the reference mechanical traction \mathbf{T} can be computed whether with $\boldsymbol{\Pi}$ or $\tilde{\boldsymbol{\Pi}}$ (see Appendix III.A.4), i.e. $\mathbf{N} \cdot \llbracket \boldsymbol{\Pi} \rrbracket = \mathbf{N} \cdot \llbracket \tilde{\boldsymbol{\Pi}} \rrbracket = \mathbf{T}$.

III.3.2.b Formulation using \mathbf{H} (free energy $\psi_H(\mathbf{F}, \mathbf{H})$)

Choosing the Lagrangian \mathbf{H} -field as the magnetic independent variable in the specific free energy density leads to an alternative variational formulation which is presented next.

The total energy \mathcal{E}_H stored in the system can still be expressed as the sum of the solid's energy plus the magnetic energy of the entire space (see Dorfmann [47, 49], Bustamante [27] and Danas [39])

$$\mathcal{E}_H = \int_V \rho_0 \psi_H(\mathbf{F}, \mathbf{H}) dV - \frac{\mu_0}{2} \int_{\mathbb{R}^3} J \mathbf{H} \cdot \mathbf{C}^{-1} \cdot \mathbf{H} dV, \quad (\text{III.3.27})$$

where $\psi_H(\mathbf{F}, \mathbf{H})$ is the MRE's specific Helmholtz free energy for the \mathbf{H} -formulation. Hence, from Eq. (III.3.13) and (III.3.27), the potential energy \mathcal{P}_H of the system reads

$$\mathcal{P}_H = \mathcal{E}_H - \mathcal{W} = \int_V (\rho_0 \psi_H(\mathbf{F}, \mathbf{H}) - \rho_0 \mathbf{f} \cdot \mathbf{u}) dV - \frac{\mu_0}{2} \int_{\mathbb{R}^3} J \mathbf{H} \cdot \mathbf{C}^{-1} \cdot \mathbf{H} dV - \int_{\partial V} \mathbf{T} \cdot \mathbf{u} dS. \quad (\text{III.3.28})$$

Using Eq. (III.3.8), we can write the second term of \mathcal{P}_H as

$$\frac{\mu_0}{2} \int_{\mathbb{R}^3} J \mathbf{H} \cdot \mathbf{C}^{-1} \cdot \mathbf{H} dV = \frac{\mu_0}{2} \int_{\mathbb{R}^3} \mathbf{h} \cdot \mathbf{h} dv. \quad (\text{III.3.29})$$

Similarly to the derivation in the F-B theory, we decompose the magnetic intensity \mathbf{h} (resp. \mathbf{H}) as the sum of the externally applied magnetic intensity \mathbf{h}_0 (resp. \mathbf{H}_0) (in the absence of the magnetoelastic solid), and a perturbation magnetic intensity $\tilde{\mathbf{h}}$ (resp. $\tilde{\mathbf{H}}$) (created by the presence of the MRE solid), i.e. $\mathbf{h} = \mathbf{h}_0 + \tilde{\mathbf{h}}$ (resp. $\mathbf{H} = \mathbf{H}_0 + \tilde{\mathbf{H}}$). By substituting this decomposition into Eq. (III.3.29), one obtains

$$\frac{\mu_0}{2} \int_{\mathbb{R}^3} \mathbf{h} \cdot \mathbf{h} dv = \frac{\mu_0}{2} \int_{\mathbb{R}^3} \mathbf{h}_0 \cdot \mathbf{h}_0 dv + \mu_0 \int_{\mathbb{R}^3} \mathbf{h}_0 \cdot \tilde{\mathbf{h}} dv + \frac{\mu_0}{2} \int_{\mathbb{R}^3} \tilde{\mathbf{h}} \cdot \tilde{\mathbf{h}} dv. \quad (\text{III.3.30})$$

The energy of the externally applied field in the entire space: $\frac{\mu_0}{2} \int_{\mathbb{R}^3} \mathbf{h}_0 \cdot \mathbf{h}_0 \, dv$, can be omitted from \mathcal{P}_H since it is finite and constant. The second term of Eq. (III.3.30): $\mu_0 \int_{\mathbb{R}^3} \mathbf{h}_0 \cdot \tilde{\mathbf{h}} \, dv$ is equal to zero as proved in Appendix III.A.2, and as a result, from Eq. (III.3.29) and (III.3.30), we can rewrite the potential energy \mathcal{P}_H as

$$\mathcal{P}_H = \int_{\mathbb{R}^3} \tilde{W}_H(\mathbf{F}, \tilde{\mathbf{H}}) \, dV - \int_V \rho_0 \mathbf{f} \cdot \mathbf{u} \, dV - \int_{\partial V} \mathbf{T} \cdot \mathbf{u} \, dS, \quad (\text{III.3.31})$$

where the energy density \tilde{W}_H is defined as

$$\tilde{W}_H(\mathbf{F}, \tilde{\mathbf{H}}) = \begin{cases} \rho_0 \psi_H(\mathbf{F}, \tilde{\mathbf{H}} + \mathbf{F}^T \cdot \mathbf{h}_0) - \frac{J\mu_0}{2} \tilde{\mathbf{H}} \cdot \mathbf{C}^{-1} \cdot \tilde{\mathbf{H}}, & \forall \mathbf{X} \in V, \\ -\frac{J\mu_0}{2} \tilde{\mathbf{H}} \cdot \mathbf{C}^{-1} \cdot \tilde{\mathbf{H}}, & \forall \mathbf{X} \in \mathbb{R}^3 \setminus V. \end{cases} \quad (\text{III.3.32})$$

Since the perturbation magnetic intensity has to satisfy Eq. (III.3.11), one can express $\tilde{\mathbf{H}}$ as the gradient of a scalar potential $\tilde{\phi}$. And as the perturbation field must vanish far from the solid, i.e. $\|\tilde{\mathbf{H}}\| \rightarrow 0$ as $\|\mathbf{X}\| \rightarrow \infty$, we choose $\tilde{\phi}$ that does the same

$$\tilde{\mathbf{H}} = -\nabla \tilde{\phi}, \quad \forall \mathbf{X} \in \mathbb{R}^3, \quad \lim_{\|\mathbf{X}\| \rightarrow +\infty} \tilde{\phi} = 0. \quad (\text{III.3.33})$$

Using Eq. (III.3.33), one can rewrite³ the potential energy in terms of its independent variables \mathbf{u} and $\tilde{\phi}$

$$\mathcal{P}_H = \int_{\mathbb{R}^3} \left(\tilde{W}_H(\mathbf{F}, \tilde{\mathbf{H}}) - \rho_0 \mathbf{f} \cdot \mathbf{u} \right) \, dV - \int_{\partial V} \mathbf{T} \cdot \mathbf{u} \, dS, \quad (\text{III.3.34})$$

based on the \mathbf{H} -formulation for the Helmholtz free energy $\psi_H(\mathbf{F}, \mathbf{H})$. At this point, all the machinery is in place to derive the governing equations. Taking variations of the above potential energy $\mathcal{P}_H(\mathbf{u}, \tilde{\phi})$ with respect to its independent variables $\tilde{\phi}$ and \mathbf{u} , one obtains two Euler-Lagrange equations respectively: divergence-free magnetic field (i.e. absence of magnetic monopole) and equilibrium combined with the corresponding magnetics and mechanics constitutive laws.

Indeed, by taking the variation of \mathcal{P}_H with respect to $\tilde{\phi}$, one obtains after some algebraic manipulation

$$\mathcal{P}_{H, \tilde{\phi}} \delta \tilde{\phi} = \int_{\mathbb{R}^3} \left[\left(\nabla \cdot \frac{\partial \tilde{W}_H}{\partial \tilde{\mathbf{H}}} \right) \delta \tilde{\phi} \right] \, dV + \int_{\partial V} \left[\left(\mathbf{N} \cdot \left[\frac{\partial \tilde{W}_H}{\partial \tilde{\mathbf{H}}} \right] \right) \delta \tilde{\phi} \right] \, dS = 0. \quad (\text{III.3.35})$$

If we compare the resulting Euler-Lagrange equation and interface condition with (III.3.10) and recalling that $\mathbf{B} = \mathbf{B}_0 + \tilde{\mathbf{B}}$, we get

$$\nabla \cdot \tilde{\mathbf{B}} = 0, \quad \forall \mathbf{X} \in \mathbb{R}^3, \quad \mathbf{N} \cdot [\tilde{\mathbf{B}}] = 0, \quad \forall \mathbf{X} \in \partial V; \quad \tilde{\mathbf{B}} = -\frac{\partial \tilde{W}_H}{\partial \tilde{\mathbf{H}}}(\mathbf{F}, \tilde{\mathbf{H}}). \quad (\text{III.3.36})$$

Similarly by taking the variation of \mathcal{P}_H with respect to \mathbf{u} one obtains after some algebraic manipulation

$$\begin{aligned} \mathcal{P}_{H,\mathbf{u}} \delta \mathbf{u} = & - \int_{\mathbb{R}^3} \left[\left(\nabla \cdot \left(\frac{\partial \widetilde{W}_H}{\partial \mathbf{F}} \right)^T + \rho_0 \mathbf{f} \right) \cdot \delta \mathbf{u} \right] dV + \\ & \int_{\partial V} \left[\left(\mathbf{N} \cdot \left[\left(\frac{\partial \widetilde{W}_H}{\partial \mathbf{F}} \right)^T \right] - \mathbf{T} \right) \cdot \delta \mathbf{u} \right] dS = 0. \end{aligned} \quad (\text{III.3.37})$$

Upon comparing the resulting Euler-Lagrange equations and interface conditions with Eq. (III.3.9), one obtains

$$\nabla \cdot \widetilde{\boldsymbol{\Pi}} + \rho_0 \mathbf{f} = \mathbf{0}, \quad \forall \mathbf{X} \in \mathbb{R}^3, \quad \mathbf{N} \cdot \llbracket \widetilde{\boldsymbol{\Pi}} \rrbracket = \mathbf{T}, \quad \forall \mathbf{X} \in \partial V; \quad \widetilde{\boldsymbol{\Pi}}^T = \frac{\partial \widetilde{W}_H}{\partial \mathbf{F}}(\mathbf{F}, \widetilde{\mathbf{H}}). \quad (\text{III.3.38})$$

At this stage, it is instructive to see how the general constitutive equations obtained from \widetilde{W}_H , which are valid for any $\mathbf{X} \in \mathbb{R}^3$, can be expressed inside and outside the MRE solid using the Helmholtz free energy ψ_H . From Eq. (III.3.32), one gets

$$\left\{ \begin{aligned} \widetilde{\mathbf{B}} &= -\rho_0 \frac{\partial \psi_H}{\partial \widetilde{\mathbf{H}}}(\mathbf{F}, \widetilde{\mathbf{H}} + \mathbf{F}^T \cdot \mathbf{h}_0) + \mu_0 J(\widetilde{\mathbf{H}} \cdot \mathbf{C}^{-1}), \\ &= -\rho_0 \frac{\partial \psi_H}{\partial \widetilde{\mathbf{H}}}\Big|_{\mathbf{F}}(\mathbf{F}, \mathbf{H}) + \mu_0 J(\widetilde{\mathbf{H}} \cdot \mathbf{C}^{-1}), \quad \forall \mathbf{X} \in V, \\ \widetilde{\mathbf{B}} &= \mu_0 J(\widetilde{\mathbf{H}} \cdot \mathbf{C}^{-1}), \quad \forall \mathbf{X} \in \mathbb{R}^3 \setminus V, \end{aligned} \right. \quad (\text{III.3.39})$$

$$\left\{ \begin{aligned} \widetilde{\boldsymbol{\Pi}}^T &= \rho_0 \frac{\partial \psi_H}{\partial \mathbf{F}}(\mathbf{F}, \widetilde{\mathbf{H}} + \mathbf{F}^T \cdot \mathbf{h}_0) + \mu_0 J(\mathbf{F}^{-T} \cdot \widetilde{\mathbf{H}})(\mathbf{C}^{-1} \cdot \widetilde{\mathbf{H}}) - \\ &\quad \frac{\mu_0 J}{2}(\widetilde{\mathbf{H}} \cdot \mathbf{C}^{-1} \cdot \widetilde{\mathbf{H}}) \mathbf{F}^{-T}, \\ &= \rho_0 \left[\frac{\partial \psi_H}{\partial \mathbf{F}}\Big|_{\mathbf{H}} + \mathbf{h}_0 \frac{\partial \psi_H}{\partial \mathbf{H}}\Big|_{\mathbf{F}} \right] + \\ &\quad \mu_0 J(\mathbf{F}^{-T} \cdot \widetilde{\mathbf{H}})(\mathbf{C}^{-1} \cdot \widetilde{\mathbf{H}}) - \frac{\mu_0 J}{2}(\widetilde{\mathbf{H}} \cdot \mathbf{C}^{-1} \cdot \widetilde{\mathbf{H}}) \mathbf{F}^{-T}, \quad \forall \mathbf{X} \in V, \\ \widetilde{\boldsymbol{\Pi}}^T &= \mu_0 J(\mathbf{F}^{-T} \cdot \widetilde{\mathbf{H}})(\mathbf{C}^{-1} \cdot \widetilde{\mathbf{H}}) - \frac{\mu_0 J}{2}(\widetilde{\mathbf{H}} \cdot \mathbf{C}^{-1} \cdot \widetilde{\mathbf{H}}) \mathbf{F}^{-T}, \quad \forall \mathbf{X} \in \mathbb{R}^3 \setminus V. \end{aligned} \right. \quad (\text{III.3.40})$$

Similarly to the \mathbf{B} -formulation, these constitutive equations give the change in magnetic field and stress tensor due to the presence of the MRE solid. To find the corresponding total magnetic field, one has to add \mathbf{B}_0 . Moreover, one can define a total stress $\boldsymbol{\Pi}$ (resp. $\boldsymbol{\sigma}$) which can be related to $\widetilde{\boldsymbol{\Pi}}$ (resp. $\widetilde{\boldsymbol{\sigma}}$) and such that $\mathbf{N} \cdot \llbracket \boldsymbol{\Pi} \rrbracket = \mathbf{N} \cdot \llbracket \widetilde{\boldsymbol{\Pi}} \rrbracket = \mathbf{T}$.

III.3.2.c Formulation using \mathbf{M} (free energy $\psi_M(\mathbf{F}, \mathbf{M})$)

The derivation of the constitutive equations based on the \mathbf{m} -formulation is already explained in details in Kankanala [90]. Here, we will simply write the variational formulation following

the same procedure used in previous sections and remind the main equations. Since it is convenient to use the magnetization per unit mass \mathbf{M} instead of the magnetization per unit volume \mathbf{m} (see Kankanala [90]) in the variational formulation of the magnetoelastic boundary value problem, we define it here

$$\mathbf{m} = \rho\mathbf{M}. \quad (\text{III.3.41})$$

The total energy \mathcal{E}_M stored in the system is decomposed as the sum of the solid's energy and the magnetic energy of the entire space such that

$$\mathcal{E}_M = \int_V \rho_0 \psi_M(\mathbf{F}, \mathbf{M}) dV + \int_{\mathbb{R}^3} \frac{J\mu_0}{2} \mathbf{H} \cdot \mathbf{C}^{-1} \cdot \mathbf{H} dV, \quad (\text{III.3.42})$$

where ψ_M is the MRE's specific Helmholtz free energy for the \mathbf{M} -formulation. Hence from Eq. (III.3.13) and (III.3.42), the potential energy \mathcal{P}_M of the system can be written as

$$\mathcal{P}_M = \mathcal{E}_M - \mathcal{W} = \int_V (\rho_0 \psi_M(\mathbf{F}, \mathbf{M}) - \rho_0 \mathbf{f} \cdot \mathbf{u}) dV + \int_{\mathbb{R}^3} \frac{J\mu_0}{2} \mathbf{H} \cdot \mathbf{C}^{-1} \cdot \mathbf{H} dV - \int_{\partial V} \mathbf{T} \cdot \mathbf{u} dS. \quad (\text{III.3.43})$$

If we substitute Eq. (III.3.8) into the second term of \mathcal{P}_M , and if we use the decomposition of the magnetic intensity introduced in previous section (i.e. $\mathbf{h} = \mathbf{h}_0 + \tilde{\mathbf{h}}$), we get

$$\int_{\mathbb{R}^3} \frac{J\mu_0}{2} \mathbf{H} \cdot \mathbf{C}^{-1} \cdot \mathbf{H} dV = \frac{\mu_0}{2} \int_{\mathbb{R}^3} \mathbf{h}_0 \cdot \mathbf{h}_0 dv + \mu_0 \int_{\mathbb{R}^3} \tilde{\mathbf{h}} \cdot \mathbf{h}_0 dv + \frac{\mu_0}{2} \int_{\mathbb{R}^3} \tilde{\mathbf{h}} \cdot \tilde{\mathbf{h}} dv. \quad (\text{III.3.44})$$

Since this formulation is based on the magnetization \mathbf{M} , we need to express $\tilde{\mathbf{h}}$ as a function of \mathbf{M} (and $\tilde{\mathbf{b}}$). From Eq. (III.3.4), if we use the decomposition of the magnetic field and magnetic intensity introduced above and recalling the fact that $\mathbf{b}_0 = \mu_0 \mathbf{h}_0$, we get

$$\tilde{\mathbf{h}} = \frac{1}{\mu_0} \tilde{\mathbf{b}} - \rho\mathbf{M}. \quad (\text{III.3.45})$$

Now, substituting Eq. (III.3.45) into Eq. (III.3.44) leads to

$$\begin{aligned} \int_{\mathbb{R}^3} \frac{J\mu_0}{2} \mathbf{H} \cdot \mathbf{C}^{-1} \cdot \mathbf{H} dV &= \frac{1}{2\mu_0} \int_{\mathbb{R}^3} \mathbf{b}_0 \cdot \mathbf{b}_0 dv + \frac{1}{\mu_0} \int_{\mathbb{R}^3} \tilde{\mathbf{b}} \cdot \mathbf{b}_0 dv - \\ &\int_{\mathbb{R}^3} \rho_0 \mathbf{M} \cdot \mathbf{b}_0 dV + \int_{\mathbb{R}^3} \frac{1}{2\mu_0 J} \left\| \mathbf{F} \cdot \tilde{\mathbf{B}} - \mu_0 \rho_0 \mathbf{M} \right\|^2 dV. \end{aligned} \quad (\text{III.3.46})$$

Similarly to what has been done for the previous formulations, the energy of the externally applied magnetic field in the entire space: $\frac{1}{2\mu_0} \int_{\mathbb{R}^3} \mathbf{b}_0 \cdot \mathbf{b}_0 dv$ can be omitted from \mathcal{P}_M since it is finite and constant, and the second term of Eq. (III.3.46): $\frac{1}{\mu_0} \int_{\mathbb{R}^3} \tilde{\mathbf{b}} \cdot \mathbf{b}_0 dv$ is equal to zero (see Appendix III.A.1). Hence, from Eq. (III.3.46), the potential energy \mathcal{P}_M can be rewritten as

$$\mathcal{P}_M = \int_{\mathbb{R}^3} \tilde{W}_M(\mathbf{F}, \tilde{\mathbf{B}}, \mathbf{M}) dV - \int_V \rho_0 \mathbf{f} \cdot \mathbf{u} dV - \int_{\partial V} \mathbf{T} \cdot \mathbf{u} dS, \quad (\text{III.3.47})$$

where the total potential $\widetilde{W}_M(\mathbf{F}, \widetilde{\mathbf{B}}, \mathbf{M})$ is defined as

$$\widetilde{W}_M(\mathbf{F}, \widetilde{\mathbf{B}}, \mathbf{M}) = \begin{cases} \rho_0 \psi_M(\mathbf{F}, \mathbf{M}) - \rho_0 \mathbf{M} \cdot \mathbf{b}_0 + \frac{1}{2\mu_0 J} \left\| \mathbf{F} \cdot \widetilde{\mathbf{B}} - \mu_0 \rho_0 \mathbf{M} \right\|^2, & \forall \mathbf{X} \in V, \\ \frac{1}{2\mu_0 J} \left\| \mathbf{F} \cdot \widetilde{\mathbf{B}} \right\|^2 = \frac{1}{2\mu_0 J} \widetilde{\mathbf{B}} \cdot \mathbf{C} \cdot \widetilde{\mathbf{B}}, & \forall \mathbf{X} \in \mathbb{R}^3 \setminus V. \end{cases} \quad (\text{III.3.48})$$

It is interesting to note that contrary to the total potential \widetilde{W}_B (resp. \widetilde{W}_H) in the \mathbf{B} (resp. \mathbf{H}) theory, \widetilde{W}_M depends on two magnetic variables instead of just one.

Now if we use Eq. (III.3.19) and similarly to what is done in Section III.3.2.a, we choose the perturbed magnetic vector potential $\widetilde{\mathbf{A}}$ such that $\left\| \widetilde{\mathbf{A}} \right\| \rightarrow 0$ as $\left\| \mathbf{X} \right\| \rightarrow \infty$. We can then rewrite³ the potential energy in terms of its independent variables \mathbf{u} , $\widetilde{\mathbf{A}}$ and \mathbf{M}

$$\mathcal{P}_M(\mathbf{u}, \widetilde{\mathbf{A}}, \mathbf{M}) = \int_{\mathbb{R}^3} \left(\widetilde{W}_M(\mathbf{F}, \widetilde{\mathbf{B}}, \mathbf{M}) - \rho_0 \mathbf{f} \cdot \mathbf{u} \right) dV - \int_{\partial V} \mathbf{T} \cdot \mathbf{u} dS. \quad (\text{III.3.49})$$

At this stage, we notice that this expression of \mathcal{P}_M corresponds to the one used in Kankanala [90] and so instead of repeating the entire minimization procedure, we will just give the corresponding magnetics and mechanics laws

$$\left\{ \begin{array}{l} \mu_0 \mathbf{h} = \mu_0 (\mathbf{h}_0 + \widetilde{\mathbf{h}}) = \frac{\partial \psi_M(\mathbf{F}, \mathbf{M})}{\partial \mathbf{M}}, \\ \widetilde{\mathbf{\Pi}}^T = \frac{\partial \widetilde{W}_M(\mathbf{F}, \widetilde{\mathbf{B}}, \mathbf{M})}{\partial \mathbf{F}} = \rho_0 \frac{\partial \psi_M(\mathbf{F}, \mathbf{M})}{\partial \mathbf{F}} - \frac{1}{2\mu_0 J} \left\| \mathbf{F} \cdot \widetilde{\mathbf{B}} - \mu_0 \rho_0 \mathbf{M} \right\|^2 \mathbf{F}^{-T} + \\ \quad \frac{1}{\mu_0 J} (\mathbf{F} \cdot \widetilde{\mathbf{B}} - \mu_0 \rho_0 \mathbf{M}) \widetilde{\mathbf{B}} \\ = J \left[\rho \left(\frac{\partial \psi_M(\mathbf{F}, \mathbf{M})}{\partial \mathbf{F}} \right) \cdot \mathbf{F}^T - \frac{\mu_0}{2} (\widetilde{\mathbf{h}} \cdot \widetilde{\mathbf{h}}) \mathbf{I} + \widetilde{\mathbf{h}} \widetilde{\mathbf{b}} \right] \cdot \mathbf{F}^{-T}. \end{array} \right. \quad (\text{III.3.50})$$

These constitutive equations give the total magnetic intensity field and the change in stress tensor due to the presence of the MRE solid. Similarly to the other formulations, we can define a total stress $\mathbf{\Pi}$ which can be related to $\widetilde{\mathbf{\Pi}}$ and such that $\mathbf{N} \cdot \llbracket \mathbf{\Pi} \rrbracket = \mathbf{N} \cdot \llbracket \widetilde{\mathbf{\Pi}} \rrbracket = \mathbf{T}$.

III.3.3 Equivalence between formulations

Each variational formulation presented is admissible for the magnetoelastic problem of interest. In this section, we will provide the relationships between the different energy densities so that the variational formulations are all mathematically equivalent.

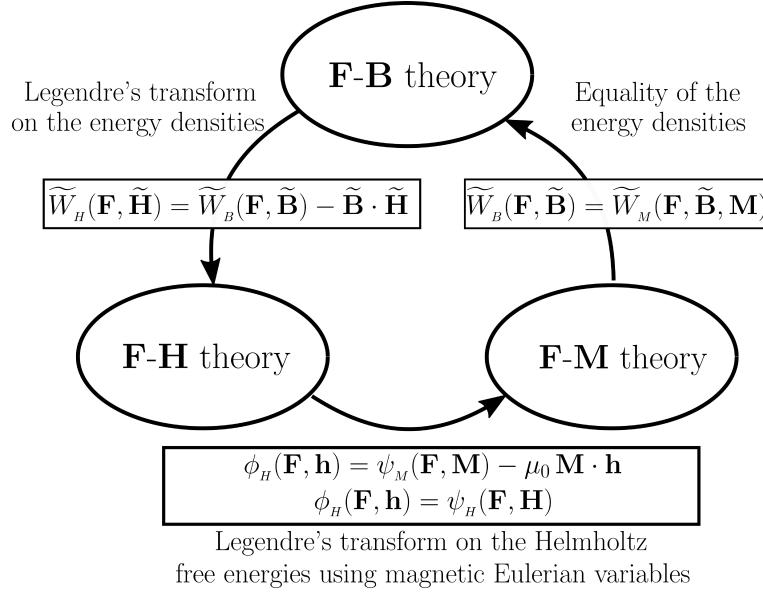


Figure III.6: Schematic representation of equivalence between different energy formulations.

Equivalence between the F-B and F-H theories

First, the equivalence between the \mathbf{B} and the \mathbf{H} -formulation is obtained by the following partial Legendre's transform on the energy densities \widetilde{W}_B and \widetilde{W}_H , namely

$$\widetilde{W}_H(\mathbf{F}, \widetilde{\mathbf{H}}) = \widetilde{W}_B(\mathbf{F}, \widetilde{\mathbf{B}}) - \widetilde{\mathbf{B}} \cdot \widetilde{\mathbf{H}}. \quad (\text{III.3.51})$$

Indeed, based on Eq. (III.3.51) and provided the fact that $\widetilde{\mathbf{B}}$, $\widetilde{\mathbf{H}}$ and \mathbf{F} are all independent variables, we retrieve the following constitutive equations (provided in Eq. (III.3.22) and Eq. (III.3.36))

$$\begin{cases} \widetilde{\mathbf{H}} = \frac{\partial \widetilde{W}_B}{\partial \widetilde{\mathbf{B}}}(\mathbf{F}, \widetilde{\mathbf{B}}), \\ \widetilde{\mathbf{B}} = -\frac{\partial \widetilde{W}_H}{\partial \widetilde{\mathbf{H}}}(\mathbf{F}, \widetilde{\mathbf{H}}). \end{cases} \quad (\text{III.3.52})$$

Moreover, from Eq. (III.3.51) it is obvious to notice that Eq. (III.3.24) is just another expression of Eq (III.3.38) (and vice versa)

$$\widetilde{\boldsymbol{\Pi}}^T = \frac{\partial \widetilde{W}_B}{\partial \mathbf{F}}(\mathbf{F}, \widetilde{\mathbf{B}}) = \frac{\partial \widetilde{W}_H}{\partial \mathbf{F}}(\mathbf{F}, \widetilde{\mathbf{H}}). \quad (\text{III.3.53})$$

Hence, the set of constitutive equations corresponding to the \mathbf{B} -formulation is equivalent to the one obtained with the \mathbf{H} -formulation provided that one uses equivalent in the sense of partial Legendre transformed energy densities for the material at hand.

Equivalence between the \mathbf{F} - \mathbf{H} and \mathbf{F} - \mathbf{M} theories

Secondly, we can derive a similar result between the \mathbf{H} and the \mathbf{M} -formulations. This time, instead of using energy densities, the equivalence between the two formulations is proved using once again a partial Legendre's transform but on the Helmholtz free energies (see Bustamante et al. [27])

$$\begin{aligned}\psi_H(\mathbf{F}, \mathbf{H}) &= \phi_H(\mathbf{F}, \mathbf{h}) = \psi_M(\mathbf{F}, \mathbf{M}) - \mu_0 \mathbf{M} \cdot \mathbf{h}, \\ \Rightarrow \psi_H(\mathbf{F}, \mathbf{H}) &= \psi_H(\mathbf{F}, \tilde{\mathbf{H}} + \mathbf{F}^T \cdot \mathbf{h}_0) = \psi_M(\mathbf{F}, \mathbf{M}) - \mu_0 \mathbf{M} \cdot \left(\mathbf{F}^{-T} \cdot \tilde{\mathbf{H}} + \mathbf{h}_0 \right),\end{aligned}\quad (\text{III.3.54})$$

where $\phi_H(\mathbf{F}, \mathbf{h})$ is the expression of the Helmholtz free energy of the \mathbf{H} -formulation if we use the Eulerian \mathbf{h} -field as a variable instead of its Lagrangian counterpart. The free energies ψ_H and ϕ_H are just expressions of the same quantity (and so they are equal) but using different independent variables. At this point, if we differentiate Eq. (III.3.54) first with respect to \mathbf{M} and then with respect to $\tilde{\mathbf{H}}$ (provided the fact that $\tilde{\mathbf{H}}$, \mathbf{M} and \mathbf{F} are chosen to be independent, and \mathbf{h}_0 is externally imposed), we get

$$\frac{\partial \psi_M}{\partial \mathbf{M}}(\mathbf{F}, \mathbf{M}) = \mu_0 \left(\mathbf{F}^{-T} \cdot \tilde{\mathbf{H}} + \mathbf{h}_0 \right) = \mu_0 \mathbf{h}, \quad (\text{III.3.55})$$

which is already provided in Eq. (III.3.50a), and

$$\frac{\partial \psi_H}{\partial \tilde{\mathbf{H}}}(\mathbf{F}, \tilde{\mathbf{H}} + \mathbf{F}^T \cdot \mathbf{h}_0) = -\mu_0 \mathbf{M} \cdot \mathbf{F}^{-T} = -\mu_0 \mathbf{F}^{-1} \cdot \mathbf{M}. \quad (\text{III.3.56})$$

From Eq. (III.3.45), we know that

$$\mathbf{M} = \frac{J}{\rho_0} \left(\frac{1}{\mu_0} \tilde{\mathbf{b}} - \tilde{\mathbf{h}} \right) = \frac{1}{\rho_0} \left(\frac{1}{\mu_0} \mathbf{F} \cdot \tilde{\mathbf{B}} - J \mathbf{F}^{-T} \cdot \tilde{\mathbf{H}} \right). \quad (\text{III.3.57})$$

If we replace this expression of \mathbf{M} into Eq. (III.3.56), we can retrieve Eq. (III.3.39)

$$\tilde{\mathbf{B}} = -\rho_0 \frac{\partial \psi_H}{\partial \tilde{\mathbf{H}}}(\mathbf{F}, \tilde{\mathbf{H}} + \mathbf{F}^T \cdot \mathbf{h}_0) + \mu_0 J \mathbf{C}^{-1} \cdot \tilde{\mathbf{H}}. \quad (\text{III.3.58})$$

We just proved that based on Eq. (III.3.54), we can retrieve the magnetic constitutive relations of the $\tilde{\mathbf{H}}$ and \mathbf{M} -formulations. Next step consists of taking the derivative of Eq. (III.3.54) with respect to \mathbf{F}

$$\frac{\partial \psi_H}{\partial \mathbf{F}}(\mathbf{F}, \tilde{\mathbf{H}} + \mathbf{F}^T \cdot \mathbf{h}_0) = \frac{\partial \psi_M}{\partial \mathbf{F}}(\mathbf{F}, \mathbf{M}) + \mu_0 \left(\mathbf{F}^{-T} \cdot \tilde{\mathbf{H}} \right) \left(\mathbf{F}^{-1} \cdot \mathbf{M} \right). \quad (\text{III.3.59})$$

Substituting Eq. (III.3.59) into the expression of the perturbed Piola-Kirchhoff obtained from the \mathbf{H} -formulation (see Eq. (III.3.40)), leads to

$$\begin{aligned}\tilde{\mathbf{\Pi}}^T &= \rho_0 \frac{\partial \psi_M}{\partial \mathbf{F}}(\mathbf{F}, \mathbf{M}) + \mu_0 \rho_0 \left(\mathbf{F}^{-T} \cdot \tilde{\mathbf{H}} \right) \left(\mathbf{F}^{-1} \cdot \mathbf{M} \right) - \\ &\quad \frac{\mu_0 J}{2} \left\| \mathbf{F}^{-T} \cdot \tilde{\mathbf{H}} \right\|^2 \mathbf{F}^{-T} + \mu_0 J \left(\mathbf{F}^{-T} \cdot \tilde{\mathbf{H}} \right) \left(\mathbf{C}^{-1} \cdot \tilde{\mathbf{H}} \right).\end{aligned}\quad (\text{III.3.60})$$

At this stage, we need to replace $\tilde{\mathbf{H}}$ by its expression in terms of $\tilde{\mathbf{B}}$ and \mathbf{M} (Lagrangian counterpart of Eq. (III.3.45)), and we obtain

$$\tilde{\mathbf{\Pi}}^T = \rho_0 \frac{\partial \psi_M}{\partial \mathbf{F}}(\mathbf{F}, \mathbf{M}) - \frac{1}{2\mu_0 J} \left\| \mathbf{F} \cdot \tilde{\mathbf{B}} - \mu_0 \rho_0 \mathbf{M} \right\|^2 \mathbf{F}^{-T} + \frac{1}{\mu_0 J} \left(\mathbf{F} \cdot \tilde{\mathbf{B}} - \mu_0 \rho_0 \mathbf{M} \right) \tilde{\mathbf{B}}. \quad (\text{III.3.61})$$

As one can notice, the use of Eq. (III.3.54) allows to retrieve the expression of $\tilde{\mathbf{\Pi}}$ found in the \mathbf{M} -formulation (see Eq. (III.3.50b)) based on the expression of $\tilde{\mathbf{\Pi}}$ in the \mathbf{H} -formulation. In the same way, it is possible to re-derive Eq. (III.3.40) based on Eq. (III.3.54) and Eq. (III.3.50b).

Hence we prove that the set of constitutive equations corresponding to the \mathbf{H} -formulation is equivalent to the one obtained with the \mathbf{M} -formulation provided the fact that the Helmholtz free energies of the considered material in these two formulations are linked by the partial Legendre's transform of Eq. (III.3.54).

Equivalence between the F-M and F-B theories

Finally, eventhough the equivalence between the \mathbf{B} and the \mathbf{M} -formulation can be obtained by a transitive relation based first on the fact that the \mathbf{B} and \mathbf{H} -formulations are equivalent and then on the fact that the \mathbf{H} and the \mathbf{M} -formulations are equivalent, it is interesting to show how the \mathbf{B} and \mathbf{M} -formulations are linked. No Legendre's transform is required and we prove here that the total potentials $\tilde{W}_B(\mathbf{F}, \tilde{\mathbf{B}})$ and $\tilde{W}_M(\mathbf{F}, \tilde{\mathbf{B}}, \mathbf{M})$ simply need to be equal. Indeed, if we substitute Eq. (III.3.54) into Eq. (III.3.51) (keeping in mind the definition of $\tilde{W}_H(\mathbf{F}, \tilde{\mathbf{H}})$ provided in Eq. (III.3.32)), we get

$$\tilde{W}_B(\mathbf{F}, \tilde{\mathbf{B}}) = \rho_0 \psi_M(\mathbf{F}, \mathbf{M}) - \rho_0 \mathbf{M} \cdot \mathbf{b}_0 - \mu_0 \rho_0 \mathbf{M} \cdot \mathbf{F}^{-T} \cdot \tilde{\mathbf{H}} - \frac{\mu_0 J}{2} \tilde{\mathbf{H}} \cdot \mathbf{C}^{-1} \cdot \tilde{\mathbf{H}} + \tilde{\mathbf{B}} \cdot \tilde{\mathbf{H}}. \quad (\text{III.3.62})$$

If we replace $\tilde{\mathbf{H}}$ (resp. \mathbf{b}_0) by its expression in terms of \mathbf{M} and $\tilde{\mathbf{B}}$ (resp. \mathbf{b}_0), one can show that

$$\tilde{W}_B(\mathbf{F}, \tilde{\mathbf{B}}) = \rho_0 \psi_M(\mathbf{F}, \mathbf{M}) - \rho_0 \mathbf{M} \cdot \mathbf{b}_0 + \frac{1}{2\mu_0 J} \left\| \mathbf{F} \cdot \tilde{\mathbf{B}} - \mu_0 \rho_0 \mathbf{M} \right\|^2 = \tilde{W}_M(\mathbf{F}, \tilde{\mathbf{B}}, \mathbf{M}). \quad (\text{III.3.63})$$

At this stage, it is obvious to notice that provided the equality of the energy densities, we can rewrite Eq. (III.3.24) into Eq. (III.3.50b) and vice versa

$$\tilde{\mathbf{\Pi}}^T = \frac{\partial \tilde{W}_B}{\partial \mathbf{F}}(\mathbf{F}, \tilde{\mathbf{B}}) = \frac{\partial \tilde{W}_M}{\partial \mathbf{F}}(\mathbf{F}, \tilde{\mathbf{B}}, \mathbf{M}). \quad (\text{III.3.64})$$

Moreover, we can retrieve the magnetic constitutive relations of both formulations. Equation (III.3.22) can be obtained using Eq. (III.3.48), and by taking the derivative of Eq. (III.3.63) with respect to $\tilde{\mathbf{B}}$ (keeping in mind that we chose \mathbf{F} , $\tilde{\mathbf{B}}$ and \mathbf{M} to be independent variables)

$$\frac{\partial \tilde{W}_B}{\partial \tilde{\mathbf{B}}}(\mathbf{F}, \tilde{\mathbf{B}}) = \frac{\partial \tilde{W}_M}{\partial \tilde{\mathbf{B}}}(\mathbf{F}, \tilde{\mathbf{B}}, \mathbf{M}) = \frac{1}{\mu_0 J} \mathbf{C} \cdot \tilde{\mathbf{B}} - \frac{\rho_0}{J} \mathbf{F}^T \cdot \mathbf{M} = \tilde{\mathbf{H}}. \quad (\text{III.3.65})$$

Similarly, Eq. (III.3.50a) can be obtained using Eq. (III.3.48), and by taking the derivative of Eq. (III.3.63) with respect to \mathbf{M}

$$\begin{aligned} \frac{\partial \widetilde{W}_M}{\partial \mathbf{M}}(\mathbf{F}, \widetilde{\mathbf{B}}, \mathbf{M}) &= \rho_0 \frac{\partial \psi_M}{\partial \mathbf{M}}(\mathbf{F}, \mathbf{M}) - \rho_0 \mathbf{b}_0 - \frac{\rho_0}{J} (\mathbf{F} \cdot \widetilde{\mathbf{B}}) + \frac{\mu_0 \rho_0^2}{J} \mathbf{M} = 0, \\ \Rightarrow \frac{\partial \psi_M}{\partial \mathbf{M}}(\mathbf{F}, \mathbf{M}) &= \mathbf{b}_0 + \frac{1}{J} \mathbf{F} \cdot \widetilde{\mathbf{B}} - \mu_0 \rho \mathbf{M} = \mathbf{b}_0 + \widetilde{\mathbf{b}} - \mu_0 \mathbf{m} = \mu_0 \mathbf{h}. \end{aligned} \quad (\text{III.3.66})$$

Hence, the set of constitutive equations corresponding to the \mathbf{B} -formulation is equivalent to the one obtained with the \mathbf{M} -formulation provided the fact that the energy densities of the material in these two formulations are equal (see Eq. (III.3.63)).

III.3.4 Type of Energies considered

As mentioned above, the proposed continuum modeling relies on a Helmholtz free energy. In this section, we present for each formulation the type of Helmholtz free energy that allows to properly fit experimental data.

Type of Energy for the F-B formulation

First, it is important to recall that due to the properties of objectivity and material symmetry (see Kankanala [90] and Danas [40]), the general form of the specific Helmholtz free energy for isotropic materials in the case of the \mathbf{B} -formulation is given by

$$\psi_B = \psi_B(\mathbf{C}, \mathbf{B}). \quad (\text{III.3.67})$$

Using a known result of representation theory, e.g. Green and Adkins [69], one obtains that an isotropic scalar function which depends on one symmetric rank two tensor \mathbf{C} and one vector argument \mathbf{B} can be expressed as a function of the following six independent invariants, i.e. $\psi_B(\mathbf{C}, \mathbf{B}) = \psi_B(I_i^B)$, $i \in 1, \dots, 6$, with

$$\begin{aligned} I_1 &= \text{tr} \mathbf{C}, & I_2 &= \frac{1}{2} [(\text{tr} \mathbf{C})^2 - \text{tr}(\mathbf{C}^2)], & I_3 &= \det \mathbf{C} = J^2, \\ I_4^B &= \mathbf{B} \cdot \mathbf{B} = J^2 \mathbf{b} \cdot \mathbf{F}^{-T} \cdot \mathbf{F}^{-1} \cdot \mathbf{b} = J^2 \mathbf{b} \cdot \mathcal{B}^{-1} \cdot \mathbf{b}, \\ I_5^B &= \mathbf{B} \cdot \mathbf{C} \cdot \mathbf{B} = J^2 \mathbf{b} \cdot \mathbf{b}, \\ I_6^B &= \mathbf{B} \cdot \mathbf{C}^2 \cdot \mathbf{B} = J^2 \mathbf{b} \cdot \mathbf{F} \cdot \mathbf{F}^T \cdot \mathbf{b} = J^2 \mathbf{b} \cdot \mathcal{B} \cdot \mathbf{b}, \end{aligned} \quad (\text{III.3.68})$$

where $\mathcal{B} = \mathbf{F} \cdot \mathbf{F}^T$, is the left Cauchy-Green strain tensor.

As a first approximation (that remains perfectly reasonable as we will see in Section III.5), we choose not to use invariants I_2 and I_4^B and we propose the following form for the energy density

$$\rho_0 \psi_B = \rho_0 \psi_{mech}(I_1, I_3) + \rho_0 \psi_{coupled}^B(I_3, I_5^B, I_6^B), \quad (\text{III.3.69})$$

where

$$\left\{ \begin{array}{l} \rho_0 \psi_{mech} = \sum_{i=1}^2 \frac{3^{1-\alpha_i}}{2\alpha_i} \mu_i [(I_1 - \ln I_3)^{\alpha_i} - 3^{\alpha_i}] + \frac{G'}{2} (\sqrt{I_3} - 1)^2, \\ \rho_0 \psi_{coupled}^B = \frac{\mu_0 \sqrt{I_3} m_s^2}{\chi^*} [\beta_{1B} \psi_5^B(I_3, I_5^B) + (1 - \beta_{1B}) \psi_6^B(I_3, I_6^B)], \\ \psi_5^B(I_3, I_5^B) = -\ln \left(\cosh \left(\frac{\chi^*}{\mu_0 m_s} \sqrt{\frac{I_5^B}{I_3}} \right) \right), \\ \psi_6^B(I_3, I_6^B) = -\frac{1}{2} \ln \left\{ 1 + \beta_{2B} \left(\left(\frac{\chi^*}{\mu_0 m_s} \right)^2 \frac{I_6^B}{I_3} \right) + (1 - \beta_{2B}) \tanh \left(\left(\frac{\chi^*}{\mu_0 m_s} \right)^2 \frac{I_6^B}{I_3} \right) \right\}. \end{array} \right. \quad (\text{III.3.70})$$

The purely mechanical contribution to the energy, i.e. ψ_{mech} , is the generalization for compressible materials of a hyperelastic model well suited for rubber materials that has been proposed by Lopez-Pamies [103], and that uses as material parameters: α_i , μ_i ($\sum_{i=1}^2 \mu_i = G$ is the shear modulus) and G' is the Lamé constant. For the magneto-mechanical material parameters, we consider four coefficients: m_s , χ^* , β_{1B} and β_{2B} . In the first part of the magneto-mechanical free energy, we use the ‘tanh’ saturation model⁴ ψ_5^B that has been proposed by Danas [39] where m_s is the magnetic saturation of the MRE per unit volume and χ^* is another definition of the magnetic susceptibility used in literature (χ^* is the initial slope of the $(\mathbf{b}-\mu_0\mathbf{m})$ curve) that is linked to the ‘classical’ magnetic susceptibility χ (the initial slope of the $(\mathbf{h}-\mathbf{m})$ curve) through $\chi^* = \chi/(1 + \chi)$. The second part of the coupled free energy, ψ_6^B , depends on the invariant I_6^B that captures the magneto-mechanical coupling. The function ψ_6^B is chosen so that for high magnetic fields (i.e. $I_6^B \rightarrow \infty$), the influence of I_6^B in the governing equations saturates since there are no more magneto-mechanical coupling after magnetic saturation (i.e. the material doesn’t deform anymore after saturation). In the limit of small deformations and small magnetic fields, ψ_{mech} linearizes properly and so does $\psi_{coupled}^B$ (ψ_5^B and ψ_6^B are equivalent in this limit).

Type of Energy for the F-H formulation

Similarly, for the **H**-formulation the Helmholtz free energy can be expressed as a function of six independent invariants

$$\psi_H = \psi_H(\mathbf{C}, \mathbf{H}) = \psi_H(I_i^H), \quad i \in 1, \dots, 6, \quad (\text{III.3.71})$$

⁴ NOTE: We could have used a Langevin model for the saturation, i.e. $\psi_5^B = \frac{1}{3} \left[\ln \left(\frac{3\chi^*}{\mu_0 m_s} \sqrt{\frac{I_5^B}{I_3}} \right) - \ln \left(\sinh \left(\frac{3\chi^*}{\mu_0 m_s} \sqrt{\frac{I_5^B}{I_3}} \right) \right) \right]$. However, the ‘tanh’ model (see Eq. (III.3.70c)) suits better the experimental data since it exhibits a faster growth and reaches the saturation magnetization faster.

where the purely mechanical invariants (i.e. I_i , $i \in [1, 3]$) remain unchanged and where the coupled magneto-mechanical invariants read

$$\begin{aligned} I_4^H &= \mathbf{H} \cdot \mathbf{H} = \mathbf{h} \cdot \mathbf{F} \cdot \mathbf{F}^T \cdot \mathbf{h} = \mathbf{h} \cdot \mathcal{B} \cdot \mathbf{h}, \\ I_5^H &= \mathbf{H} \cdot \mathbf{C}^{-1} \cdot \mathbf{H} = \mathbf{h} \cdot \mathbf{h}, \\ I_6^H &= \mathbf{H} \cdot \mathbf{C}^{-2} \cdot \mathbf{H} = \mathbf{h} \cdot \mathcal{B}^{-1} \cdot \mathbf{h}. \end{aligned} \quad (\text{III.3.72})$$

As a first approximation (that is sufficiently representative as shown in Section III.5), we don't use invariants I_2 and I_6^H in the expression of the Helmholtz free energy ψ_H . For the same reasons that have been explained above, we choose a free energy function that includes a 'tanh' saturation model ψ_5^H and a magneto-mechanical coupling function ψ_4^H whose influence in the governing equation saturates as \mathbf{H} keeps increasing. Since the governing equations of the \mathbf{H} -formulation are similar to the ones of the \mathbf{B} -formulation, the chosen Helmholtz energy resembles the one introduced in Eq. III.3.69 and Eq. III.3.70 and reads

$$\rho_0 \psi_H = \rho_0 \psi_{mech}(I_1, I_3) + \rho_0 \psi_{coupled}^H(I_3, I_4^H, I_5^H), \quad (\text{III.3.73})$$

where ψ_{mech} remains the same as in Eq. (III.3.70a) and

$$\left\{ \begin{aligned} \rho_0 \psi_{coupled}^H &= \frac{\mu_0 \sqrt{I_3} m_s^2}{\chi} [\beta_{1H} \psi_5^H(I_5^H) + (1 - \beta_{1H}) \psi_4^H(I_4^H)], \\ \psi_5^H(I_5^H) &= -\ln \left(\cosh \left(\frac{\chi}{m_s} \sqrt{I_5^H} \right) \right), \\ \psi_4^H(I_4^H) &= -\frac{1}{2} \ln \left\{ 1 + \beta_{2H} \left(\left(\frac{\chi}{m_s} \right)^2 I_4^H \right) + (1 - \beta_{2H}) \tanh \left(\left(\frac{\chi}{m_s} \right)^2 I_4^H \right) \right\}. \end{aligned} \right. \quad (\text{III.3.74})$$

It is interesting to note that in this case we use the 'classical' magnetic susceptibility χ .

Type of Energy for the F-M formulation

For the \mathbf{M} -formulation, the Helmholtz free energy ψ_M is as well expressed as a function of six independent invariants

$$\psi_M = \psi_M(I_i^M), \quad i \in 1, \dots, 6, \quad (\text{III.3.75})$$

where the purely mechanical invariants are given in Eq. (III.3.68), and where the coupled invariants are given by

$$I_4^M = \mathbf{M} \cdot \mathbf{M}, \quad I_5^M = \mathbf{M} \cdot \mathcal{B} \cdot \mathbf{M}, \quad I_6^M = \mathbf{M} \cdot \mathcal{B}^2 \cdot \mathbf{M}. \quad (\text{III.3.76})$$

As a first approximation (which is sufficiently representative to fit experimental data), we choose not to use invariants I_2 and I_6^M and we propose the following free energy form

$$\left\{ \begin{array}{l} \rho_0 \psi_M = \rho_0 \psi_{mech}(I_1, I_3) + \rho_0 \psi_{coupled}^M(I_3, I_4^M, I_5^M), \\ \rho_0 \psi_{coupled}^M = \frac{\mu_0 (M_s \rho_0)^2}{2 \chi \sqrt{I_3}} [\psi_4^M(I_4^M) + \psi_5^M(I_5^M)], \\ \psi_4^M(I_4^M) = \beta_{1M} \frac{I_4^M}{M_s^2} + \beta_{0M} \left\{ \frac{1}{2} \ln \left(1 - \left(\frac{I_4^M}{M_s^2} \right)^2 \right) + \frac{I_4^M}{M_s^2} \operatorname{arctanh} \left(\frac{I_4^M}{M_s^2} \right) \right\}, \\ \psi_5^M(I_5^M) = (1 - \beta_{1M}) \left\{ \frac{I_5^M}{M_s^2} + \beta_{2M} \left(\frac{I_5^M}{M_s^2} \right)^2 + \beta_{3M} \left(\frac{I_5^M}{M_s^2} \right)^3 \right\}, \end{array} \right. \quad (\text{III.3.77})$$

where $M_s = m_s/\rho_0$ is the magnetic saturation per unit mass. The function ψ_4^M is the counterpart of the ‘tanh’ saturation model in the \mathbf{M} -formulation, and uses β_{0M} and β_{1M} as coefficients. In terms of magneto-mechanical coupling, the influence of ψ_5^M in the governing equations doesn’t have to saturate since the independent variable \mathbf{M} saturates by itself (i.e. $\|\mathbf{M}\| < M_s$), and hence a polynomial form (with coefficients β_{2M} and β_{3M}) for ψ_5^M is admissible.

The type of energy densities discussed in this section are obviously not the only ones that can be used to describe the phenomena observed in experiments but are sufficiently representative for the purpose of this study.

III.4 Numerical Implementation

The variational formulations presented above have been implemented in finite element codes for the purpose of simulating complex geometries submitted to complex magneto-mechanical loadings. Indeed, except for some trivial problems, analytical solutions cannot generally be derived due to strong non-linearities in the governing equations and non-uniformities in mechanical and magnetic fields. In this section, we first present the special features of the numerical implementation of the formulations based on a magnetic vector potential (i.e. the \mathbf{F} - \mathbf{B} and \mathbf{F} - \mathbf{M} theory) which require the uniqueness of $\tilde{\mathbf{A}}$. Secondly, we show how to set valid boundary conditions for the magnetic vector potential. The last part explains on a particular example how to use the symetries of a problem to reduce the number of degrees of freedom and execution time to solve it.

III.4.1 Coulomb gauge for the magnetic vector potential

The numerical implementation of each of the formulations presented in Section III.3.2 requires the uniqueness of the potential energy independent variables. The uniqueness of the displacement field \mathbf{u} will not be discussed since no additional care needs to be taken for magneto-mechanical boundary value problems compared to purely mechanical ones.

In terms of magnetic variables, the \mathbf{F} - \mathbf{B} variational formulation (and in exactly the same way the \mathbf{F} - \mathbf{M} variational formulation) needs an additional term to ensure the uniqueness

of the magnetic vector potential $\tilde{\mathbf{A}}$, since according to Eq. (III.3.19), it is defined up to a gradient. Hence, we use the Coulomb gauge

$$\nabla \cdot \tilde{\mathbf{A}} = \mathbf{0}, \quad \forall \mathbf{X} \in \mathbb{R}^3. \quad (\text{III.4.1})$$

To numerically enforce the Coulomb gauge, we choose to add a penalty term in the total potential energy (provided in Eq. (III.3.17)) with penalty $\kappa^5 \ll 1$, so that

$$\mathcal{P}_B = \int_{\mathbb{R}^3} \tilde{W}_B(\mathbf{u}, \tilde{\mathbf{A}}; \mathbf{b}_0) dV - \int_V \rho_0 \mathbf{f} \cdot \mathbf{u} dV - \int_{\partial V} \mathbf{T} \cdot \mathbf{u} dS, \quad (\text{III.4.2})$$

where the energy density is given by

$$\tilde{W}_B(\mathbf{u}, \tilde{\mathbf{A}}; \mathbf{b}_0) = \rho_0 \psi_B(\mathbf{F}, \nabla \times \tilde{\mathbf{A}} + J\mathbf{F}^{-1} \cdot \mathbf{b}_0) + \frac{1}{2\mu_0 J} (\nabla \times \tilde{\mathbf{A}}) \cdot \mathbf{C} \cdot (\nabla \times \tilde{\mathbf{A}}) + \frac{1}{2\mu_0 \kappa} (\nabla \cdot \tilde{\mathbf{A}})^2. \quad (\text{III.4.3})$$

The choice of the penalty approach is motivated by two reasons. First, the total potential energy \mathcal{P}_B remains positive-definite locally. Secondly, unlike the method of Lagrange multipliers, there is no need to solve for any new unknowns. The value of the penalty κ is adjusted so that it doesn't influence the final solution of the boundary value problem. It is important to specify that the penalty term added must be under-integrated to avoid any 'locking phenomena' (similarly to what is done in purely mechanical problems to avoid volumetric locking).

It is interesting to note that to numerically implement the **F-H** theory, the variational formulation presented in Eq. (III.3.34) remains unchanged (i.e. no additional constraint is needed). Indeed, even if the magnetic scalar potential $\tilde{\phi}$ is defined up to a constant, we ensure its uniqueness by imposing boundary conditions (see Eq. (III.3.33)).

III.4.2 Boundary conditions

For the magnetic vector potential

The same boundary conditions can be applied for both the **F-B** and **F-M** formulations since no boundary conditions need to be applied for the magnetization vector **M**. In this section, we focus on $\tilde{\mathbf{A}}$ since no additional care needs to be taken on the boundary conditions of **u** compared to a purely mechanical boundary value problem.

As previously mentioned, the numerical simulation of a MRE boundary value problem requires to simulate not only the response of the magnetoelastic solid but also the influence of its surrounding. Indeed, since magnetic fields exist also outside of the solid V and interact with it through Maxwell stresses at the boundary ∂V (and so there is a strong shape dependence), we need to consider an entire region surrounding the MRE of interest. This system that we simulate is at least composed of the magnetoelastic solid and the surrounding air (see Fig. III.8). It can sometimes contain other components such as a coil that is used to

⁵ NOTE: The final solution of the boundary value problem shouldn't depend on the parameter κ .

apply magnetic loads.

Let's consider a domain \mathcal{D} that contains the system of interest. Generally, \mathcal{D} is finite, simply connected and its boundary $\partial\mathcal{D}$ is at least continuous.

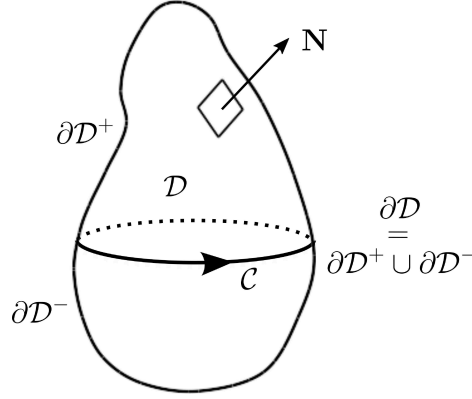


Figure III.7: Domain \mathcal{D} and its boundary $\partial\mathcal{D}$. The closed loop \mathcal{C} that belongs to $\partial\mathcal{D}$ separates the boundary into two parts $\partial\mathcal{D}^+$ and $\partial\mathcal{D}^-$.

At this stage, we want to show that as boundary conditions, only the components of $\tilde{\mathbf{A}}$ that are tangential to $\partial\mathcal{D}$ need to be prescribed to uniquely define the magnetic vector potential in the entire domain \mathcal{D} .

First, it is helpful to recall the equations verified by $\tilde{\mathbf{A}}$ (see Eq. (III.3.10)⁶, (III.3.19) and (III.4.1))

$$\begin{cases} \nabla \times \tilde{\mathbf{A}} = \tilde{\mathbf{B}}, & \forall \mathbf{X} \in \mathcal{D}, \\ \nabla \cdot \tilde{\mathbf{A}} = 0, & \forall \mathbf{X} \in \mathcal{D}, \\ (\nabla \times \tilde{\mathbf{A}}) \cdot \mathbf{N} = 0, & \forall \mathbf{X} \in \partial\mathcal{D}. \end{cases} \quad (\text{III.4.4})$$

Secondly, $\forall \mathbf{X} \in \partial\mathcal{D}$, we can decompose the magnetic vector potential as

$$\tilde{\mathbf{A}} = (\tilde{\mathbf{A}} \cdot \mathbf{N})\mathbf{N} - (\tilde{\mathbf{A}} \times \mathbf{N}) \times \mathbf{N}, \quad (\text{III.4.5})$$

where \mathbf{N} is the outward normal and $(\tilde{\mathbf{A}} \cdot \mathbf{N})\mathbf{N}$ is the normal component of $\tilde{\mathbf{A}}$ on $\partial\mathcal{D}$. Let's now consider a closed loop \mathcal{C} such that $\mathcal{C} \in \partial\mathcal{D}$. This closed loop separates the boundary $\partial\mathcal{D}$ in two parts $\partial\mathcal{D}^+$ and $\partial\mathcal{D}^-$ (see Fig. III.7) such that $\partial\mathcal{D} = \partial\mathcal{D}^+ \cup \partial\mathcal{D}^-$. If we apply Stokes theorem to the third equation of (III.4.4) on the domain $\partial\mathcal{D}^+$, we get

$$\oint_{\mathcal{C}} \tilde{\mathbf{A}} \cdot d\mathbf{l} = - \oint_{\mathcal{C}} [(\tilde{\mathbf{A}} \times \mathbf{N}) \times \mathbf{N}] \cdot d\mathbf{l} = \iint_{\partial\mathcal{D}^+} (\nabla \times \tilde{\mathbf{A}}) \cdot \mathbf{N} dS = 0. \quad (\text{III.4.6})$$

The domain $\partial\mathcal{D}^+ \setminus \mathcal{C}$ is an open set⁷ of \mathbb{R}^2 (subspace topology) and from the arbitrariness of

⁶ NOTE: Without loss of generality, we consider that the normal component of $\tilde{\mathbf{B}}$ is equal to zero at the boundary. In the case where we want to prescribe another boundary condition, i.e. $\tilde{\mathbf{B}} \cdot \mathbf{N} = \tilde{\mathbf{B}}_a \cdot \mathbf{N}$, then the reasoning that is presented remains valid provided the fact that $\tilde{\mathbf{B}}$ is substituted by $\tilde{\mathbf{B}} - \tilde{\mathbf{B}}_a$ and $\tilde{\mathbf{A}}$ is substituted by $\tilde{\mathbf{A}} - \tilde{\mathbf{A}}_a$ (where $\nabla \times \tilde{\mathbf{A}}_a = \tilde{\mathbf{B}}_a$ and $\nabla \cdot \tilde{\mathbf{A}}_a = 0, \forall \mathbf{X} \in \mathcal{D}$).

⁷ NOTE: Careful, $\partial\mathcal{D}^+ \setminus \mathcal{C}$ is not an open set of \mathbb{R}^3 .

\mathcal{C} , we know that Eq. (III.4.6) remains valid for every closed loop belonging to $\partial\mathcal{D}^+$. As a result, we can conclude from the Poincaré's lemma that $(\tilde{\mathbf{A}} \times \mathbf{N}) \times \mathbf{N}$ (which belongs to $\partial\mathcal{D}^+$) is a closed differential form that is locally exact on $\partial\mathcal{D}^+$ (i.e. $\exists \phi^+$ a scalar potential such that $\forall \mathbf{X} \in \partial\mathcal{D}^+$, $(\tilde{\mathbf{A}} \times \mathbf{N}) \times \mathbf{N} = -\nabla\phi^+$). The exact same reasoning can be applied to $\partial\mathcal{D}^-$ and hence we obtain that $\exists \phi^-$ a scalar potential such that $\forall \mathbf{X} \in \partial\mathcal{D}^-$, $(\tilde{\mathbf{A}} \times \mathbf{N}) \times \mathbf{N} = -\nabla\phi^-$. A priori, the scalar potentials ϕ^+ and ϕ^- are defined on different sets. However, we know that locally exact differential forms that are defined on a simply connected domain are exact. Then we can conclude that $\exists \phi$ a scalar potential such that

$$(\tilde{\mathbf{A}} \times \mathbf{N}) \times \mathbf{N} = -\nabla\phi, \quad \forall \mathbf{X} \in \partial\mathcal{D}. \quad (\text{III.4.7})$$

If we substitute Eq. (III.4.7) into Eq. (III.4.5), we end up with

$$\tilde{\mathbf{A}} = (\tilde{\mathbf{A}} \cdot \mathbf{N})\mathbf{N} + \nabla\phi, \quad \forall \mathbf{X} \in \partial\mathcal{D}. \quad (\text{III.4.8})$$

As we can see, the definition of $\tilde{\mathbf{A}}$ on the boundary $\partial\mathcal{D}$ is not unique. At this point, we choose⁸ to consider $\phi = 0$ so that

$$\begin{aligned} \tilde{\mathbf{A}} &= (\tilde{\mathbf{A}} \cdot \mathbf{N})\mathbf{N}, \quad \forall \mathbf{X} \in \partial\mathcal{D}, \\ &\Rightarrow \tilde{\mathbf{A}} \times \mathbf{N} = \mathbf{0}, \quad \forall \mathbf{X} \in \partial\mathcal{D}. \end{aligned} \quad (\text{III.4.9})$$

Based on the work of Biro and Preis [12], we can show that with boundary condition (III.4.9), $\tilde{\mathbf{A}}$ is uniquely defined in \mathcal{D} .

Indeed, if we consider two vector potentials $\tilde{\mathbf{A}}^{(1)}$ and $\tilde{\mathbf{A}}^{(2)}$ both satisfying Eq. (III.4.4a), (III.4.4b) and (III.4.9), then their difference $\tilde{\mathbf{A}}^{(0)} = \tilde{\mathbf{A}}^{(1)} - \tilde{\mathbf{A}}^{(2)}$ verifies

$$\begin{cases} \nabla \times \tilde{\mathbf{A}}^{(0)} = \mathbf{0}, & \forall \mathbf{X} \in \mathcal{D}, \\ \nabla \cdot \tilde{\mathbf{A}}^{(0)} = 0, & \forall \mathbf{X} \in \mathcal{D}, \\ \mathbf{N} \times \tilde{\mathbf{A}}^{(0)} = \mathbf{0}, & \forall \mathbf{X} \in \partial\mathcal{D}. \end{cases} \quad (\text{III.4.10})$$

In view of Eq. (III.4.10a), $\tilde{\mathbf{A}}^{(0)}$ can be written as

$$\tilde{\mathbf{A}}^{(0)} = \nabla\varphi, \quad \forall \mathbf{X} \in \mathcal{D}, \quad (\text{III.4.11})$$

where according to Eq. (III.4.10b), the scalar function φ satisfies the Laplace equation

$$\nabla^2\varphi = 0, \quad \forall \mathbf{X} \in \mathcal{D}. \quad (\text{III.4.12})$$

With the boundary condition (III.4.10c), we can easily show that φ is a constant everywhere in \mathcal{D} (since \mathcal{D} is assumed to be simply connected). Hence, $\tilde{\mathbf{A}}^{(0)} = \mathbf{0}$, which means that $\tilde{\mathbf{A}}$ is

⁸ NOTE: Any choice of scalar function ϕ is allowed (provided some regularity conditions). The important thing is to choose one.

uniquely defined.

As a conclusion, we proved that it is sufficient to impose the tangential components of $\tilde{\mathbf{A}}$ on $\partial\mathcal{D}$ as boundary conditions.

On the particular case of Fig. III.8, if we simulate a region of surrounding air sufficiently large compared to the dimensions of the magnetoelastic solid, and since we know that the influence of the solid on the external magnetic field vanishes far from its boundaries, we can reasonably impose the following boundary conditions on the faces⁹ ‘Top’, ‘Right’ and ‘Front’

$$\begin{cases} \mathbf{u} = \mathbf{0}, \\ \mathbf{N} \times \tilde{\mathbf{A}} = \mathbf{0}. \end{cases} \quad (\text{III.4.13})$$

For the magnetic scalar potential

For the **F-H** theory, both \mathbf{u} and $\tilde{\phi}$ need to be imposed on $\partial\mathcal{D}$. For the boundary problem described in Fig. III.8, the boundary conditions to apply on the faces ‘Top’, ‘Right’ and ‘Front’ are: $\mathbf{u} = \mathbf{0}$ and $\tilde{\phi} = 0$.

⁹ NOTE: Careful on Fig. III.8, the boundary conditions of Eq. (III.4.13) must not be applied on the symmetry planes ‘Bottom’, ‘Left’ and ‘Back’.

III.4.3 Symmetry conditions for the magnetic vector potential

Whenever simulating a boundary value problem, we want to reduce the size of the system as much as possible to minimize the computational resources and time needed to solve it. In this section, we introduce a way to do this by exploiting existing symmetries. For that purpose, we consider the particular case of the MRE sample presented in Section III.2.2 that is used for coupled magneto-mechanical experiments. The magnetoelastic solid is subjected to an externally applied magnetic field \mathbf{b}_0 far from its boundaries and perpendicular to its axis (along the \mathbf{e}_1 direction, see Fig. III.8).

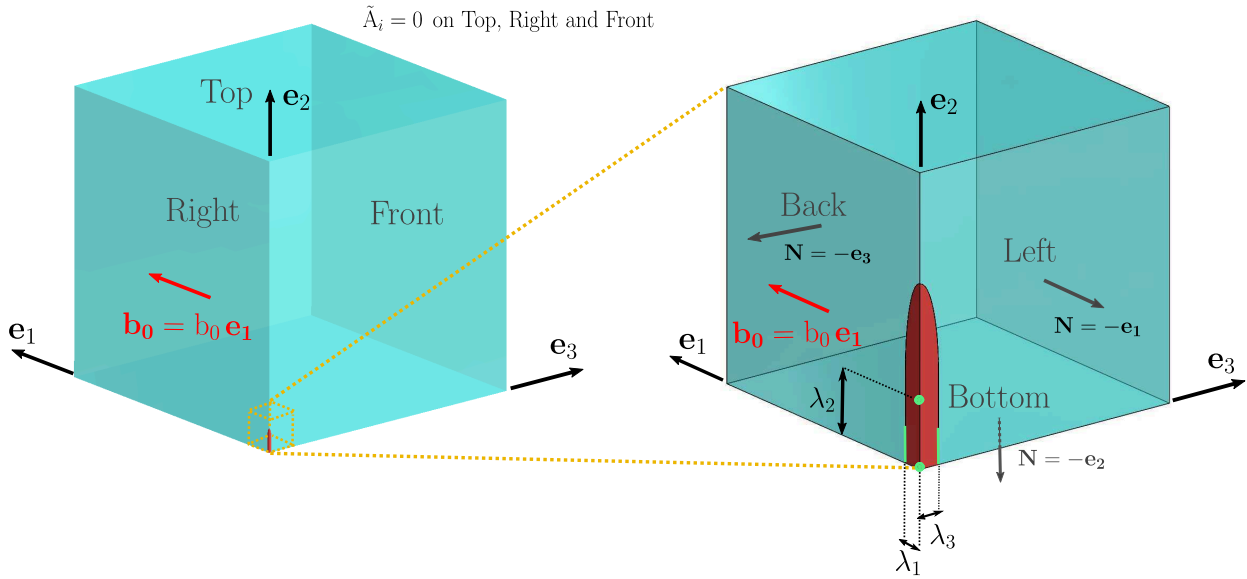


Figure III.8: Schematic of the domain considered for the 3D boundary value problem of a MRE cylindrical specimen with ellipsoidal ends subjected to an externally applied magnetic field \mathbf{b}_0 far from its boundaries; MRE solid in red and surrounding air in blue. The figure on the left shows the entire system whereas the picture on the right is a zoom in that presents the symmetry planes of the problem.

For the magnetic vector potential

First, it is interesting to recall the symmetry properties of the magnetic field (or the perturbed magnetic field). The latter is a pseudovector (as opposed to a polar or ‘true’ vector). Subjected to a reflection through a symmetry plane, it is transformed into the opposite of its mirror image (as opposed to a polar vector which would be transformed into its mirror image). In the case of a reflection through an anti-symmetry plane, it is transformed into its mirror image (as opposed to a polar vector which would be transformed into the opposite of its mirror image). It is important to notice that the symmetry properties of a pseudovector and a polar vector are opposite.

In the three dimensional case, the perturbed magnetic field $\tilde{\mathbf{B}}$ is expressed as the curl of a polar vector, namely the perturbed magnetic vector potential $\tilde{\mathbf{A}}$. As a result $\tilde{\mathbf{A}}$ and $\tilde{\mathbf{B}}$ have

opposite symmetry properties.

In the case of the magnetoelastic MRE sample, as we can see on the schematics in Fig. III.8, there are three remarkable planes (about which the geometry is exactly mirrored). This is the reason why only one-eighth of the problem is shown in this figure. Due to the external magnetic field \mathbf{b}_0 being applied in the direction \mathbf{e}_1 ¹⁰ (perpendicular to the axis of the magnetoelastic solid), we can see that the plane of normal \mathbf{e}_1 named ‘Left’ (see Fig. III.8) is a plane of anti-symmetry whereas the planes of normal \mathbf{e}_2 and \mathbf{e}_3 that are named ‘Bottom’ and ‘Back’ are symmetry planes of the perturbed magnetic field $\tilde{\mathbf{B}}$. Hence, $\tilde{\mathbf{B}}$ verifies the following symmetry properties whereas the ones verified by $\tilde{\mathbf{A}}$ are opposite (anti-symmetry properties)

$$\left\{ \begin{array}{l} \tilde{\mathbf{B}}_1(X_1, X_2, X_3) = \tilde{\mathbf{B}}_1(-X_1, X_2, X_3), \\ \tilde{\mathbf{B}}_1(X_1, X_2, X_3) = \tilde{\mathbf{B}}_1(X_1, -X_2, X_3), \\ \tilde{\mathbf{B}}_1(X_1, X_2, X_3) = \tilde{\mathbf{B}}_1(X_1, X_2, -X_3), \\ \tilde{\mathbf{B}}_2(X_1, X_2, X_3) = -\tilde{\mathbf{B}}_2(-X_1, X_2, X_3), \\ \tilde{\mathbf{B}}_2(X_1, X_2, X_3) = -\tilde{\mathbf{B}}_2(X_1, -X_2, X_3), \\ \tilde{\mathbf{B}}_2(X_1, X_2, X_3) = \tilde{\mathbf{B}}_2(X_1, X_2, -X_3), \\ \tilde{\mathbf{B}}_3(X_1, X_2, X_3) = -\tilde{\mathbf{B}}_3(-X_1, X_2, X_3), \\ \tilde{\mathbf{B}}_3(X_1, X_2, X_3) = \tilde{\mathbf{B}}_3(X_1, -X_2, X_3), \\ \tilde{\mathbf{B}}_3(X_1, X_2, X_3) = -\tilde{\mathbf{B}}_3(X_1, X_2, -X_3), \end{array} \right. \Rightarrow \left\{ \begin{array}{l} \tilde{\mathbf{A}}_1(X_1, X_2, X_3) = -\tilde{\mathbf{A}}_1(-X_1, X_2, X_3), \\ \tilde{\mathbf{A}}_1(X_1, X_2, X_3) = -\tilde{\mathbf{A}}_1(X_1, -X_2, X_3), \\ \tilde{\mathbf{A}}_1(X_1, X_2, X_3) = -\tilde{\mathbf{A}}_1(X_1, X_2, -X_3), \\ \tilde{\mathbf{A}}_2(X_1, X_2, X_3) = \tilde{\mathbf{A}}_2(-X_1, X_2, X_3), \\ \tilde{\mathbf{A}}_2(X_1, X_2, X_3) = \tilde{\mathbf{A}}_2(X_1, -X_2, X_3), \\ \tilde{\mathbf{A}}_2(X_1, X_2, X_3) = -\tilde{\mathbf{A}}_2(X_1, X_2, -X_3), \\ \tilde{\mathbf{A}}_3(X_1, X_2, X_3) = \tilde{\mathbf{A}}_3(-X_1, X_2, X_3), \\ \tilde{\mathbf{A}}_3(X_1, X_2, X_3) = -\tilde{\mathbf{A}}_3(X_1, -X_2, X_3), \\ \tilde{\mathbf{A}}_3(X_1, X_2, X_3) = \tilde{\mathbf{A}}_3(X_1, X_2, -X_3). \end{array} \right. \quad (\text{III.4.14})$$

From Eq. III.4.14, we can deduce the boundary conditions to apply on the symmetry planes ‘Bottom’, ‘Left’ and ‘Back’.

The Dirichlet boundary conditions read

$$\left\{ \begin{array}{l} \tilde{\mathbf{A}}_1 = 0, \quad \forall \mathbf{X} = (0, X_2, X_3) \in \text{‘Left’}, \\ \tilde{\mathbf{A}}_1 = \tilde{\mathbf{A}}_3 = 0, \quad \forall \mathbf{X} = (X_1, 0, X_3) \in \text{‘Bottom’}, \\ \tilde{\mathbf{A}}_1 = \tilde{\mathbf{A}}_2 = 0, \quad \forall \mathbf{X} = (X_1, X_2, 0) \in \text{‘Back’}. \end{array} \right. \quad (\text{III.4.15})$$

As for the Neumann boundary conditions, they are automatically verified and enforced by the variational formulation.

Based on the result derived in previous section, we know that it is sufficient to impose the tangential components of $\tilde{\mathbf{A}}$ on $\partial\mathcal{D}$ and hence it is not necessary to impose the first relation of Eq. III.4.15 (i.e. $\tilde{\mathbf{A}}_1(0, X_2, X_3) = 0$).

For the magnetic scalar potential

For the \mathbf{F} - \mathbf{H} theory, we can as well establish a link between the symmetry properties of the magnetic intensity field $\tilde{\mathbf{H}}$ and the symmetry properties of the scalar potential ϕ . The latter

¹⁰ NOTE: the direction of the externally applied magnetic field dictates the nature of the geometry’s symmetry planes.

is an even function with respect to a symmetry plane of $\tilde{\mathbf{H}}$, and an odd function with respect to an anti-symmetry plane of $\tilde{\mathbf{H}}$.

In the particular case of the boundary value problem described in Fig. III.8, the symmetry properties of $\tilde{\mathbf{H}}$ and $\tilde{\mathbf{B}}$ are the same and are presented in Eq. (III.4.14). Hence $\tilde{\phi}$ is an odd function with respect to the anti-symmetry plane of normal \mathbf{e}_1 ('Left') and an even function with respect to the symmetry planes of normal \mathbf{e}_2 and \mathbf{e}_3 ('Bottom' and 'Back'), i.e.

$$\begin{cases} \tilde{\phi}(X_1, X_2, X_3) = -\tilde{\phi}(-X_1, X_2, X_3), \\ \tilde{\phi}(X_1, X_2, X_3) = \tilde{\phi}(X_1, -X_2, X_3), \\ \tilde{\phi}(X_1, X_2, X_3) = \tilde{\phi}(X_1, X_2, -X_3). \end{cases} \quad (\text{III.4.16})$$

As a result, we can deduce the boundary condition that needs to be applied (only the Dirichlet boundary condition is given since the Neumann boundary conditions are automatically verified)

$$\tilde{\phi} = 0, \quad \forall \mathbf{X} = (0, X_2, X_3) \in \text{'Left'}. \quad (\text{III.4.17})$$

It is to remark that such a reasoning can be applied only for a limited number of problems. Indeed, the geometry (that could be complex) needs to present some symmetries and the applied field has to keep those symmetries.

III.5 Results

In the first part of this Section is described the combined experimental/numerical approach used to obtain an expression for the free energy $\psi_B(\mathbf{F}, \mathbf{B})$ of the MRE solid. A purely mechanical (uniaxial traction) test followed by a coupled magneto-mechanical one (pure magnetostriction, $T_2 = 0$ Pa) are used to obtain the free energy of the MRE in the \mathbf{F} - \mathbf{B} formulation. In the second part, we test the predictive capabilities of the model based on the experimentally obtained free energy for two different coupled magneto-mechanical tests ($T_2 > 0$ Pa). The last part uses a numerical approach to obtain the free energy of the MRE for the remaining formulations, i.e. $\psi_H(\mathbf{F}, \mathbf{H})$ and $\psi_M(\mathbf{F}, \mathbf{M})$.

III.5.1 Free energy determination using the F-B formulation ($\psi_B(\mathbf{F}, \mathbf{B})$)

III.5.1.a Purely Mechanical Experiments and FEM simulations

Results from the purely mechanical test in uniaxial tension are presented in Fig. III.9. The traction (T_2) versus the stretch ratio (λ_2) curve is shown in Fig. III.9a while the transverse stretch ratios (λ_1, λ_3) versus the axial stretch ratio (λ_2) are shown in Fig. III.9b. From these experiments, using a least squares fit in the analytical solution of the problem, one can obtain the coefficients (μ_i, α_i, G')¹¹ (see Eq. (III.3.70a)). The result of this fit is depicted in Fig.

¹¹ NOTE: The numerical value of the computed coefficients are: $\mu_1 = 1.64 \times 10^{-2}$ MPa, $\mu_2 = 3.21 \times 10^{-3}$ MPa, $\alpha_1 = 1.56$, $\alpha_2 = -10.31$ and $G' = 125(\mu_1 + \mu_2)$.

III.9 where the experiments, plotted in dotted line, the analytical solution, plotted in dashed line, and the 3D FEM results plotted in a continuous line, are practically indistinguishable for engineering strains of up to 70%. Note also that the MRE is almost incompressible since $\lambda_1 = \lambda_3 = (\lambda_2)^{-1/2}$, as seen from Fig. III.9b.

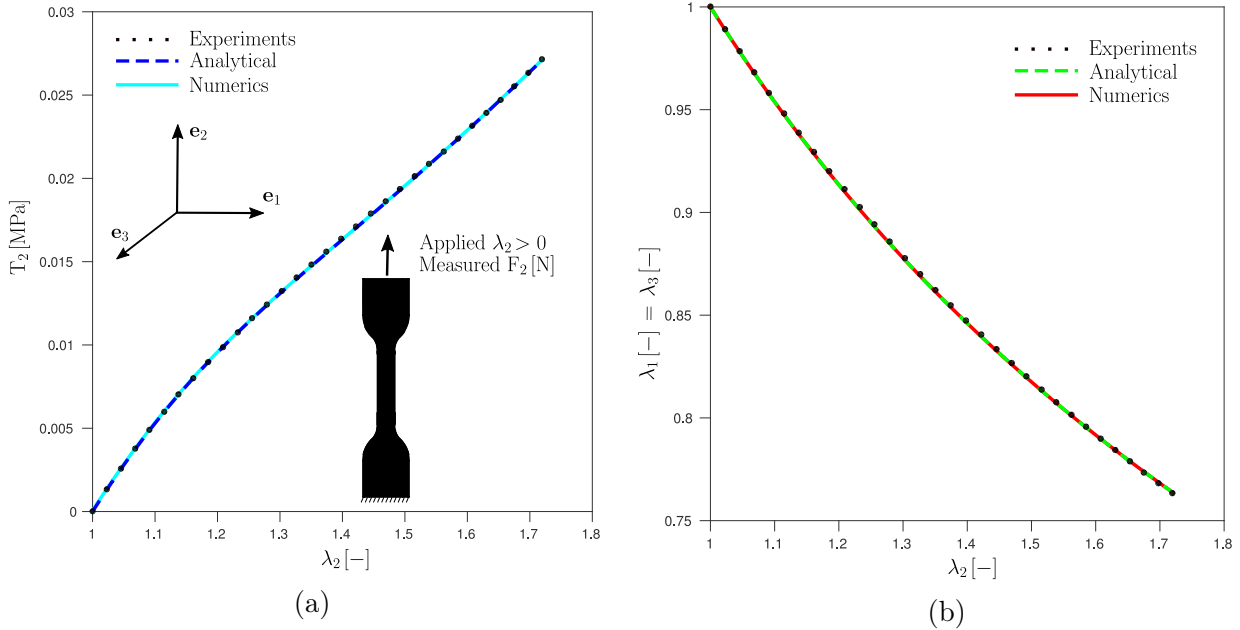


Figure III.9: Purely mechanical (uniaxial tension) test used for obtaining the energy density ψ_B for an isotropic MRE. The traction (T_2) versus stretch ratio (λ_2) curve is shown in (a) while the transverse stretch ratios (λ_1 , λ_3) versus axial stretch ratio (λ_2) are shown in (b). Experimental curves are plotted in dotted lines, analytical predictions in dashed lines and results of FEM calculations in continuous lines.

III.5.1.b Coupled Magneto-Mechanical Experiments and FEM simulations

Results from the coupled magneto-mechanical test in pure magnetostriction are presented in Fig. III.10. The stretch ratio (λ_1) along the direction of the applied magnetic field is shown in Fig. III.10a, the transverse and axial stretch ratios (λ_2 , λ_3) are shown in Fig. III.10b, the magnetic field (b_1) inside the MRE specimen is shown in Fig. III.10c and the magnetization (m_1) is shown in Fig. III.10d. All curves are plotted against the remotely applied field b_0 along the e_1 direction. The insert in Fig. III.10d shows the magnetization response of the MRE, i.e. magnetization (m_1) versus h -field (h_1) along the applied magnetic field direction; the initial slope of this curve is the magnetic susceptibility of the material χ . Notice that for up to about 0.4T the response is linear followed by a sharp drop in the slope as saturation occurs; a full saturation has not occurred up to 0.8T, the maximum value of the applied magnetic field.

From these experiments, in combination with the FEM calculations as described in the previous section (no analytical solution being possible for the corresponding boundary value

problem), one obtains the coefficients $(m_s, \chi^*, \beta_{1B}, \beta_{2B})$ ¹² (see Eq. (III.3.70)). As expected from previous work on MREs [90, 40], the engineering strain for the initial magnetostrictive response $|\lambda_1 - 1|$ has a quadratic dependence on the applied magnetic field b_0 and subsequently saturates for higher b_0 values. A similar behavior is observed for the remaining engineering strains $|1 - \lambda_2|, |1 - \lambda_3|$. The material parameters used for the fitting of ψ_B give an accurate prediction of λ_1 up to 0.4T, but an increasingly higher value (compared to the experiment as seen in Fig. III.10a) for fields $b_0 > 0.4T$. The corresponding predictions for λ_2 and λ_3 are less accurate as seen from Fig. III.10b, given our choice for matching the experimental and predicted value of the axial stretch λ_2 for the highest magnetic field ($b_0 = 0.8T$). The adopted choice of parameters gives much better predictive capabilities for the purely magnetic response, as evidenced by the experimental/numerical comparison in Fig. III.10c and Fig. III.10d, where again we chose to match the experimental and predicted values of the magnetization at the highest magnetic field ($b_0 = 0.8T$).

¹² NOTE: The numerical value of the computed coefficients are: $m_s = 1.265 \times 10^5 \text{ A} \cdot \text{m}^{-1}$, $\chi^* = 0.225$ (corresponding to $\chi = 0.291$), $\beta_{1B} = 0.91$ and $\beta_{2B} = 0.50$.

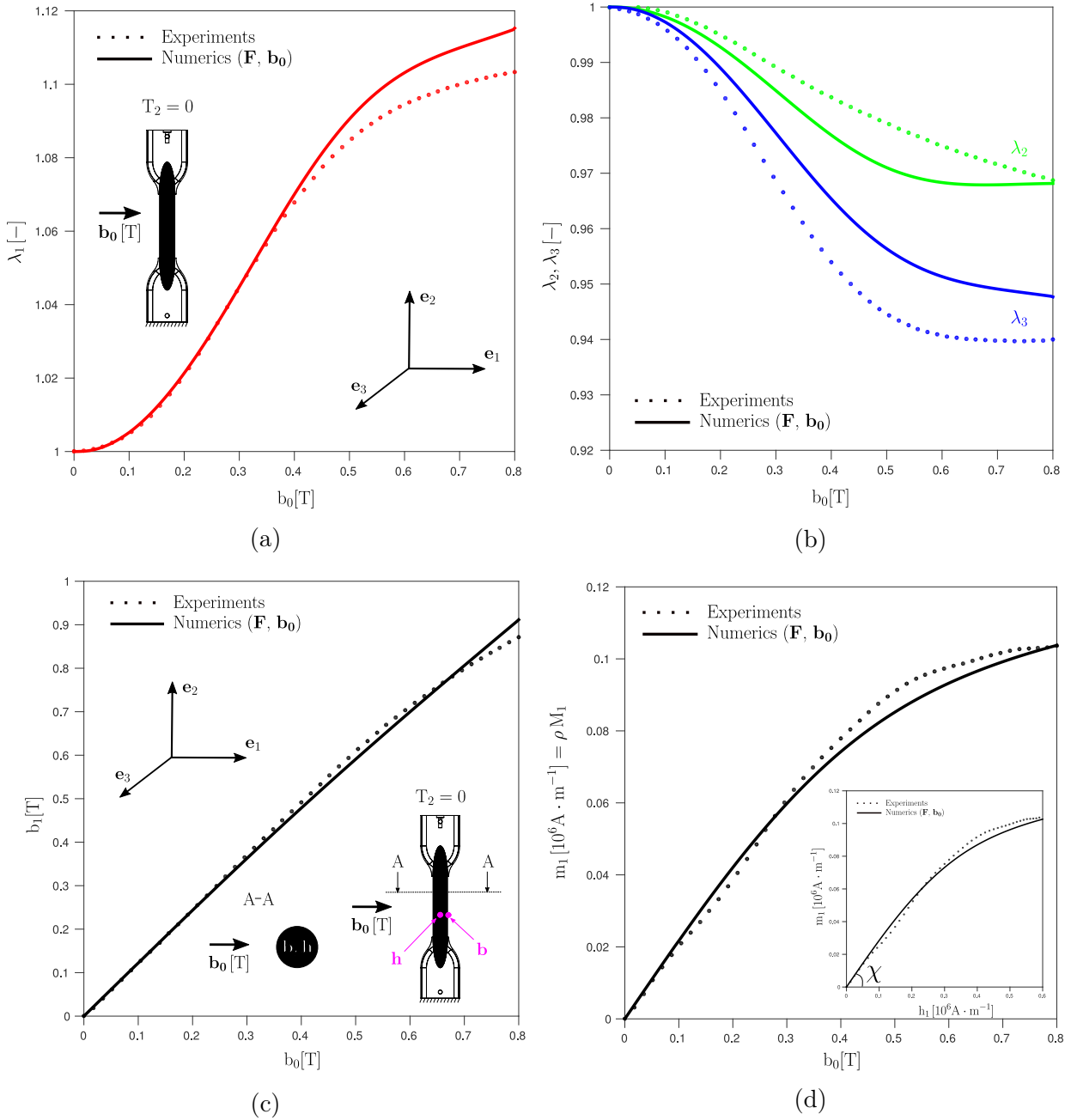


Figure III.10: Coupled magneto-mechanical (pure magnetostriction, $T_2 = 0$) test used for obtaining the energy density ψ_B for an isotropic MRE. The stretch ratio (λ_1) in the direction of the applied magnetic field is shown in (a), the transverse and axial stretch ratios (λ_2, λ_3) are shown in (b), the magnetic field (b_1) inside the MRE specimen is shown in (c) and the magnetization (m_1) is shown in (d). All curves are plotted against the remotely applied field (b_0) along the e_1 direction. Experimental curves are plotted in dotted lines while FEM calculations are in continuous lines.

III.5.2 Predictive capabilities of the model

Following the experimental determination of the free energy $\psi_B(\mathbf{F}, \mathbf{B})$, the obvious next question is about its accuracy in predicting other experiments, different from the ones used to find it. To this end we compare the FEM model's predictions, calculated using the energy density obtained from the purely mechanical and magnetostrictive tests, as described in the previous subsections, to two coupled magneto-mechanical tests where the sample is subjected to fixed axial tractions $F_2 = 0.1\text{N}$, $F_2 = 0.2\text{N}$ and under a transverse magnetic field $0 \leq b_0 \leq 0.8\text{T}$, as shown in Fig. III.11 and Fig. III.12 respectively. More specifically in Fig. III.11a (and Fig. III.12a) are plotted the axial stretch ratio (λ_2) and the transverse stretch ratios (λ_1, λ_3) as functions of the applied magnetic field (b_0) along \mathbf{e}_1 . The magnetic field (b_1) inside the specimen as a function of the applied field (b_0) is plotted in Fig. III.11b (and Fig. III.12b) while the magnetization (m_1) inside the specimen is plotted in Fig. III.11c (and Fig. III.12c). The magnetization (m_1) against the magnetic intensity (h_1) inside the MRE is also plotted in the insert of Fig. III.11c (and Fig. III.12c). The same plotting convention is used in Fig. III.11 and Fig. III.12 as in Fig. III.9 and Fig. III.10, i.e. experimental results in dotted lines and FEM calculations in solid lines.

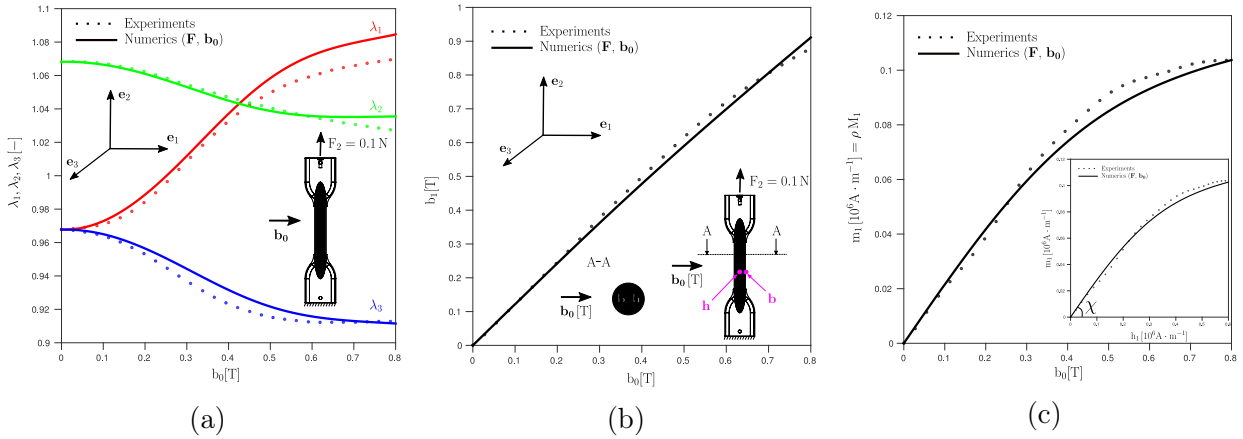


Figure III.11: Predictive capabilities of the model based on the experimentally obtained free energy ψ_B for a coupled magneto-mechanical test under combined axial tension ($F_2 = 0.1\text{N}$) and transverse magnetic field (b_0). The comparison for the stretch ratios is shown in (a), for the magnetic field (b_1) inside the MRE specimen in (b) and for the magnetization (m_1) in (c). All curves are plotted against the remotely applied field (b_0) along the \mathbf{e}_1 direction. Experimental curves are plotted in dotted lines while the FEM calculation results are in solid lines.

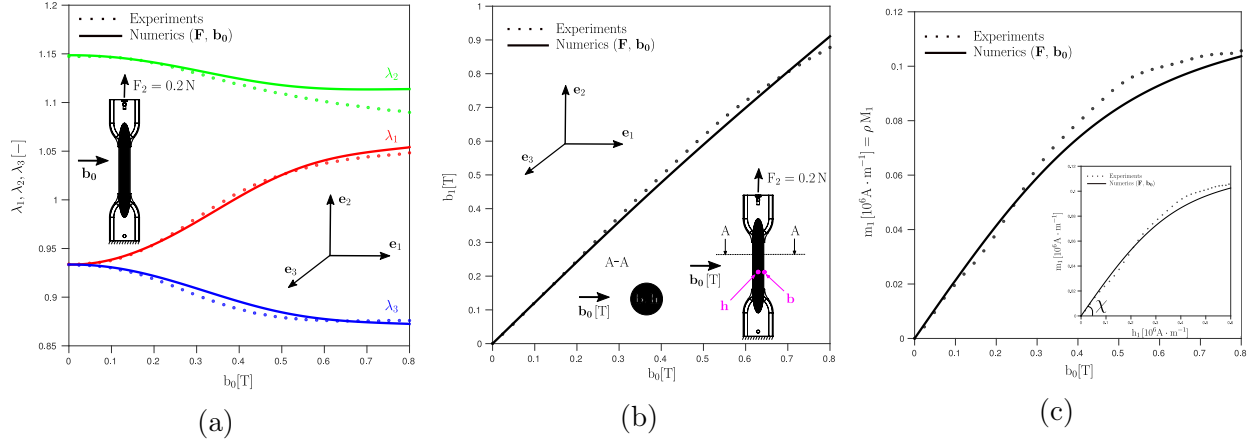


Figure III.12: Predictive capabilities of the model based on the experimentally obtained free energy ψ_B for a coupled magneto-mechanical test under combined axial tension ($F_2 = 0.2\text{N}$) and transverse magnetic field (b_0). The comparison for the stretch ratios is shown in (a), for the magnetic field (b_1) inside the MRE specimen in (b) and for the magnetization (m_1) in (c). All curves are plotted against the remotely applied field (b_0) along the e_1 direction. Experimental curves are plotted in dotted lines while the FEM calculation results are in solid lines.

In the purely magnetostrictive test ($F_2 = 0$) used to obtain the MRE's free energy, the shape effect is the strongest, as evidenced by the difference between the axial stretch (λ_2) and the transverse stretch (λ_3) (had the shape effect been ignored, isotropy would dictate $\lambda_2 = \lambda_3$). In fitting the energy density with the least number of parameters, a choice was made to match the axial stretch (λ_2) at the maximum magnetic field ($b_0 = 0.8\text{T}$) as seen in Fig. III.10b, thus giving the biggest difference between experiments and FEM calculations. In the presence of axial tension $F_2 > 0$, the shape effect is less pronounced and as a result the discrepancy between numerical calculations and experiments is considerably smaller for the axial stretch (λ_2) as well as the transverse stretches (λ_1, λ_3). The predictive capabilities of the FEM model improve with increasing axial tension, thus capturing the coupled magneto-mechanical behaviour and the corresponding shape effect in a very satisfactory manner. The success of predictive capability of the model for the magnetization curve had to be expected since it is not significantly influenced by mechanical effects, as a comparison of experimental results between Fig. III.10c and Fig. III.10d to their counterparts Fig. III.11b and Fig. III.11c (for $F_2 = 0.1\text{N}$) and Fig. III.12b and Fig. III.12c (for $F_2 = 0.2\text{N}$) can easily establish.

III.5.3 Free energy in other formulations (ψ_H, ψ_M)

In Section III.5.1, special attention in the computation of ψ_B was needed to make sure that it only describes the material of interest and is not influenced by the shape of the specimens used to collect experimental data. For that reason, finite element calculations have been used to properly simulate 'shape effects' in our experiments.

The computation of the free energies in the other two formulations (ψ_H and ψ_M), though, can be done much more easily using the analytical equations provided in Section III.3.3.

Indeed, using the fact that the governing equations in each formulations are equivalent and given a common problem to solve analytically, we can use the already known free energy ψ_B to compute ψ_H and ψ_M . In what follows, more details are given on the procedure used.

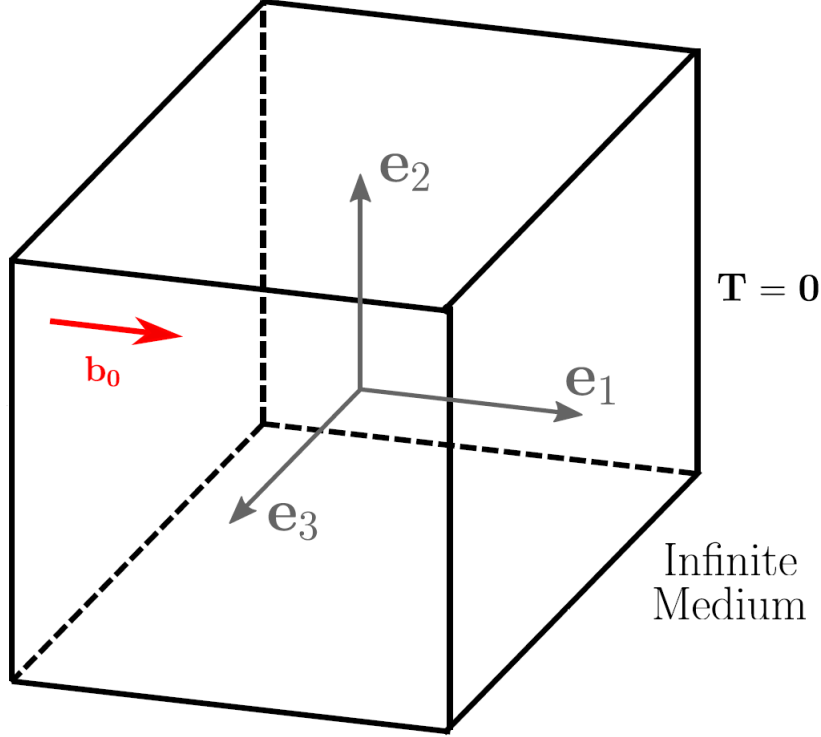


Figure III.13: Schematic of the idealized uniaxial magnetostriction test used to compute the free energies ψ_H and ψ_M . Such a problem of a stress free material subjected to a magnetic field applied in the \mathbf{e}_1 direction can be solved analytically.

Computation of ψ_H

Based on the governing equations provided in Section III.3.2, we can prove (see Danas [39]) that the problem of a stress free material subjected to a magnetic field applied in the \mathbf{e}_1 direction can be obtained by solving a system of equations composed of a magnetic equation and three independent equations of static equilibrium in the reference normal directions $\mathbf{N}_k = \mathbf{e}_k$, $k = 1, 2, 3$, given by

$$\left\{ \begin{array}{l} \mathbf{m} = -\rho_0 \mathbf{F}^{-T} \cdot \frac{\partial \psi_B}{\partial \tilde{\mathbf{B}}}(\mathbf{F}, \tilde{\mathbf{B}} + J\mathbf{F}^{-1} \cdot \mathbf{b}_0) = -\frac{\rho_0}{\mu_0 J} \mathbf{F} \cdot \frac{\partial \psi_H}{\partial \tilde{\mathbf{H}}}(\mathbf{F}, \tilde{\mathbf{H}} + \mathbf{F}^T \cdot \mathbf{h}_0), \\ \mathbf{T} = \rho_0 \left[\frac{\partial \psi_B}{\partial \mathbf{F}}(\mathbf{F}, \tilde{\mathbf{B}} + J\mathbf{F}^{-1} \cdot \mathbf{b}_0) \right] \cdot \mathbf{N} - J \left(\mathbf{m} \cdot \tilde{\mathbf{b}} \right) \mathbf{F}^{-T} \cdot \mathbf{N} + J \left(\mathbf{m} \tilde{\mathbf{b}} \right) \cdot (\mathbf{F}^{-T} \cdot \mathbf{N}) \\ = \rho_0 \left[\frac{\partial \psi_H}{\partial \mathbf{F}}(\mathbf{F}, \tilde{\mathbf{H}} + \mathbf{F}^T \cdot \mathbf{h}_0) \right] \cdot \mathbf{N} - \mu_0 J \left(\tilde{\mathbf{h}} \mathbf{m} \right) \cdot (\mathbf{F}^{-T} \cdot \mathbf{N}) = 0, \end{array} \right. \quad (\text{III.5.1})$$

where \mathbf{T} is the nominal traction.

Given the chosen form of energy for ψ_B (highly non-linear dependence on \mathbf{B} as can be seen in Eq. (III.3.69) and Eq. (III.3.70), and given a prescribed loading path (\mathbf{F}, \mathbf{b}) , finding the exact solution ψ_H of the differential system of Eq. (III.5.1) is a very complicated task. Instead, we look for an approximate solution that belongs to the set of functions of the form suggested in Eq. (III.3.73) and Eq. (III.3.74). A least square optimization (that minimizes the difference between the calculated solutions (λ_i, b_1) to the given problem obtained with the \mathbf{F} - \mathbf{B} and \mathbf{F} - \mathbf{H} theory) is used to compute the material parameters (β_{1H}, β_{2H}) . If the magnetic field is imposed by prescribing the set of variables (b_0, m_1) (see Fig. III.14c), the optimization algorithm provides the following material parameters

$$\beta_{1H} = 0.87, \quad \beta_{2H} = 0.375. \quad (\text{III.5.2})$$

For the considered problem, the obtained free energy ψ_H provides stretch ratios λ_1 and $\lambda_2 = \lambda_3$ (see Fig. III.14a) and magnetic field b_1 (see Fig. III.14b) very similar to the one obtained with free energy ψ_B .

Lastly, we make sure that the partial Legendre's transform of Eq. III.3.51 is verified with a very high accuracy for loading paths of the following form

$$\mathbf{F} = \frac{1}{\sqrt{\lambda}} \mathbf{e}_1 \mathbf{e}_1 + \lambda \mathbf{e}_2 \mathbf{e}_2 + \frac{1}{\sqrt{\lambda}} \mathbf{e}_3 \mathbf{e}_3, \quad \mathbf{b} = b_1 \mathbf{e}_1. \quad (\text{III.5.3})$$

As one can see in Fig. III.14d, the error committed on the partial Legendre's transform defined by

$$\text{Error}^H = 100 \times \left| \frac{\widetilde{W}_H(\mathbf{F}, \widetilde{\mathbf{H}}) - \left(\widetilde{W}_B(\mathbf{F}, \widetilde{\mathbf{B}}) - \widetilde{\mathbf{B}} \cdot \widetilde{\mathbf{H}} \right)}{\widetilde{W}_H(\mathbf{F}, \widetilde{\mathbf{H}})} \right|, \quad (\text{III.5.4})$$

is limited to 3% for stretch ratios $\lambda \in [0.5, 2]$ and magnetic fields $b_1 \in [0, 2\text{T}]$, and is less than 1% for the experimental range used in Section III.5.1. Such a good accuracy means that the chosen energy form for ψ_H can well describe the material behavior.

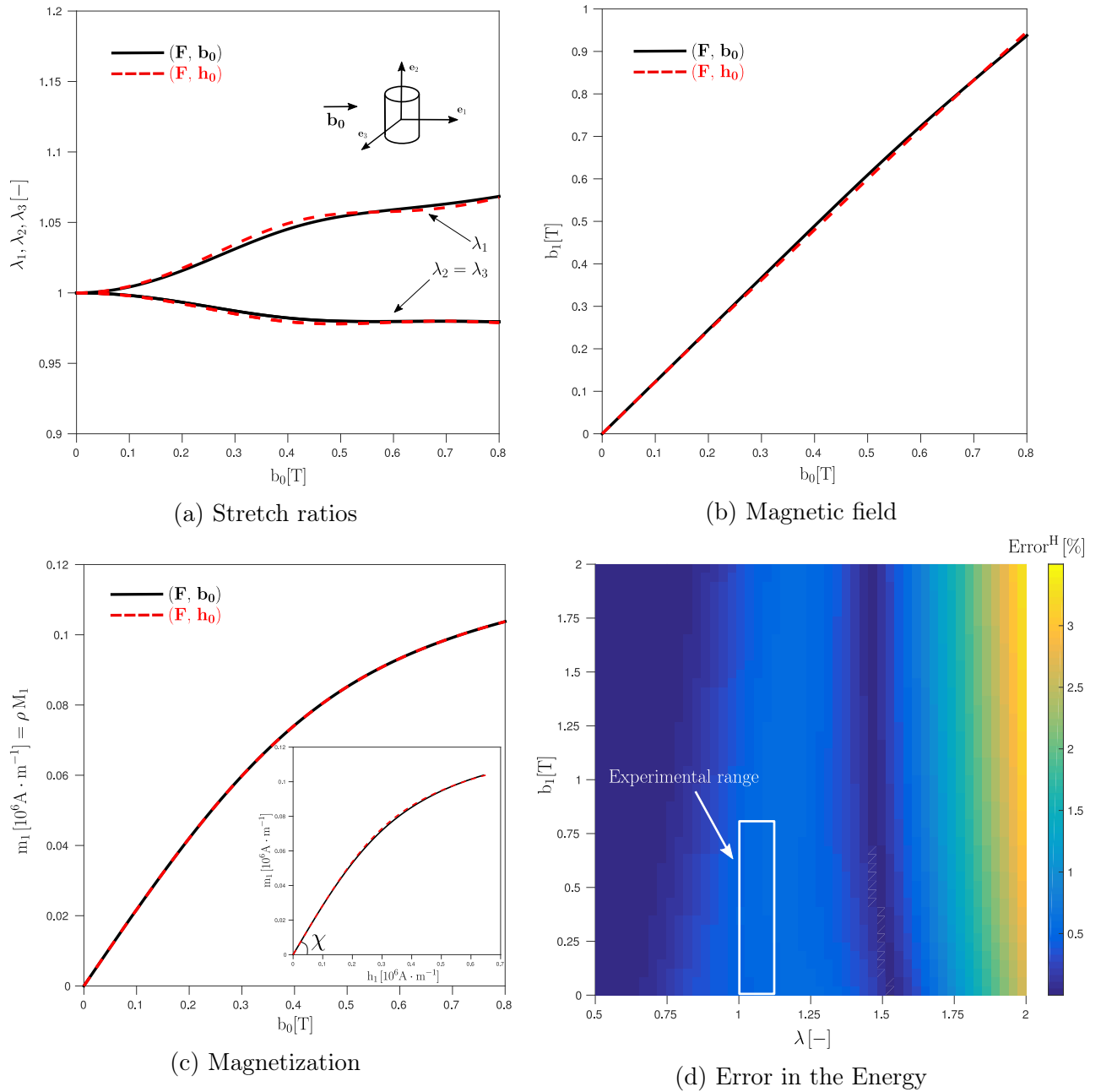


Figure III.14: Analytical solution for the problem of a stress free material subjected to a magnetic field along direction \mathbf{e}_1 computed with both the \mathbf{F} - \mathbf{B} (in black) and \mathbf{F} - \mathbf{H} theory (in red). The comparison between the calculated principal stretch ratios is shown in (a), and the calculated magnetic field b_1 is shown in (b). Fig. (c) defines the applied magnetic loading. In Fig. (d), we plot the accuracy up to which the partial Legendre's transform of Eq. III.3.51 is verified for loading paths given in Eq. III.5.3.

Computation of ψ_M

The exact same procedure is used to compute the Helmholtz free energy of the **F-M** theory. The system of equation describing the same problem of a stress free material subjected to a magnetic field applied along \mathbf{e}_1 is given by

$$\begin{cases} \mathbf{m} = -\rho_0 \mathbf{F}^{-T} \cdot \frac{\partial \psi_B}{\partial \tilde{\mathbf{B}}}(\mathbf{F}, \tilde{\mathbf{B}} + J\mathbf{F}^{-1} \cdot \mathbf{b}_0) = \frac{1}{\mu_0} \left(b_1 \mathbf{e}_1 - \frac{\partial \psi_M}{\partial \mathbf{M}}(\mathbf{F}, \mathbf{M}) \right), \\ \mathbf{T} = \rho_0 \left[\frac{\partial \psi_B}{\partial \mathbf{F}}(\mathbf{F}, \tilde{\mathbf{B}} + J\mathbf{F}^{-1} \cdot \mathbf{b}_0) \right] \cdot \mathbf{N} - J \left(\mathbf{m} \cdot \tilde{\mathbf{b}} \right) \mathbf{F}^{-T} \cdot \mathbf{N} + J \left(\mathbf{m} \tilde{\mathbf{b}} \right) \cdot (\mathbf{F}^{-T} \cdot \mathbf{N}) \\ = \rho_0 \left[\frac{\partial \psi_M}{\partial \mathbf{F}}(\mathbf{F}, \mathbf{M}) \right] \cdot \mathbf{N} = \mathbf{0}. \end{cases} \quad (\text{III.5.5})$$

Once again, given the form of ψ_B , the exact solution to this differential system is quite complex to compute, so we look for an approximate solution ψ_M that belongs to the set of functions of the form suggested in Eq. III.3.77. Then, after imposing the magnetic field by prescribing the set of variables (b_0, b_1) (see Fig. III.15b), a least square optimization provides the material parameters of the approximate solution ψ_M that best solve the differential system among the set of functions considered. We obtain

$$\beta_{1M} = 1.15, \quad \beta_{0M} = 0.77, \quad \beta_{2M} = -0.41, \quad \beta_{3M} = 0.057. \quad (\text{III.5.6})$$

As we can see from Fig. III.15a and Fig. III.15c, the stretch ratios λ_1 and $\lambda_2 = \lambda_3$, and the magnetization m_1 computed with ψ_M for the considered problem are almost the same as the ones obtained with free energy ψ_B .

As a last step, we verify how accurately is the equivalence condition (between the **F-B** and **F-M** theory) provided in Eq. III.3.63 verified. For that purpose, we consider the same loading path described in Eq. III.5.3. As shown in Fig. III.15d, the error defined by

$$\text{Error}^M = 100 \times \left| \frac{\tilde{W}_B(\mathbf{F}, \tilde{\mathbf{B}}) - \tilde{W}_M(\mathbf{F}, \tilde{\mathbf{B}}, \mathbf{M})}{\tilde{W}_B(\mathbf{F}, \tilde{\mathbf{B}})} \right|, \quad (\text{III.5.7})$$

is limited to 11% for stretch ratios $\lambda \in [0.5, 2]$ and magnetic fields $b_1 \in [0, 2\text{T}]$, and is less than 3% for the experimental range used in Section III.5.1. Even if there will always exist other energy functions that can better model the material at hand, the obtained accuracy is very satisfactory.

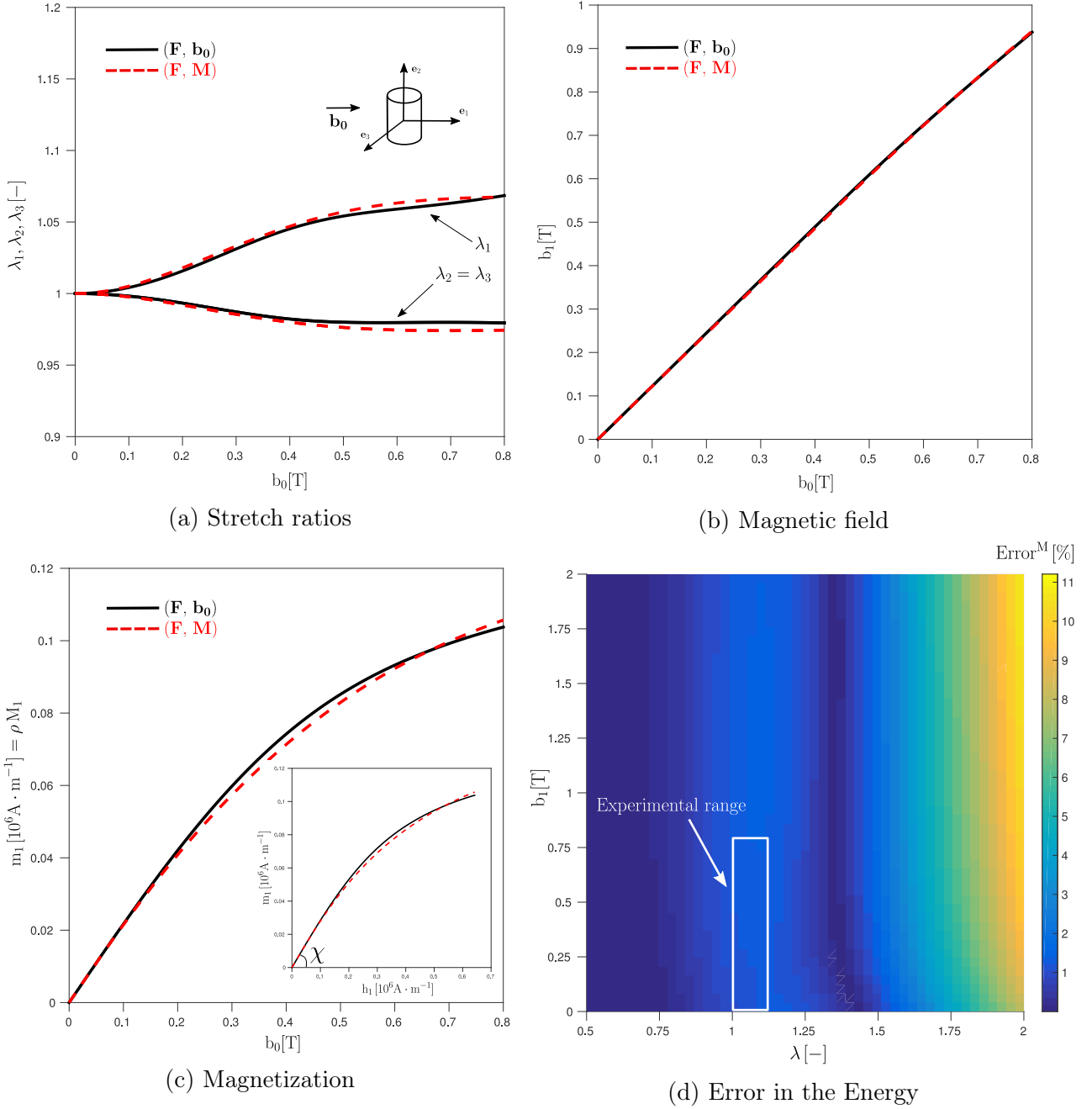


Figure III.15: Analytical solution for the problem of a stress free material subjected to a magnetic field along direction \mathbf{e}_1 computed with both the \mathbf{F} - \mathbf{B} (in black) and \mathbf{F} - \mathbf{M} theory (in red). The comparison between the calculated principal stretch ratios is shown in (a), and the calculated magnetization m_1 is shown in (c). Fig. (b) defines the applied magnetic loading. In Fig. (d), we plot the accuracy up to which the equivalence condition (between the \mathbf{F} - \mathbf{B} and \mathbf{F} - \mathbf{M} theory) given Eq. III.3.63 is verified for loading paths provided in Eq. III.5.3.

III.6 Conclusions

In this work, we present a combined experimental, theoretical and numerical study of the macroscopic response of isotropic MREs. The general continuum framework proposed by Kankanala and Triantafyllidis [90] is extended and multiple and equivalent variational formulations are proposed based on different choices of the independent magnetic variable used in the Helmholtz free energy. These variational formulations are numerically implemented into 3D finite element codes, to properly simulate the significant influence of the specimens shape on characterization results. Indeed, lots of attention is required to make sure that the computed parameters only describe the material and for that reason, shape effects that result from complex magneto-mechanical interactions must not be ignored. We show that it is not possible to fit experimental data using analytical equations, nor is it possible to use a simplified geometry of experimental specimens in numerical calculations. A combination of accurate FEM simulations representative of experiments, together with least square optimization algorithms, is used to compute material parameters. For the variational formulation based on the \mathbf{F} - \mathbf{B} theory, we model both a purely mechanical uni-axial experiment and a coupled magneto-mechanical test under pure magnetostriction with the help of an isotropic energy function which depends on four invariants (out of the six that are theoretically available), two purely mechanical and two magneto-mechanical ones. In order to capture the inherent hyperelastic behavior of MREs under tension, a non-linear dependence of the energy function on the two mechanical invariants is proposed. In terms of the coupled behavior, non-quadratic terms on the magnetic field \mathbf{B} are used in the energy to model the magnetization saturation response of the MRE. The corresponding energy density function is found to have excellent predictive capabilities when compared to other existing experimental results at finite strains and under high magnetic fields. The Helmholtz free energy functions of the other two formulations are calculated much more easily based on equivalence conditions explained in Section III.3.3. Based on these material models and on the 3D finite element codes implemented and used in this study, all the tools necessary to improve the design of MRE-based devices are now available.

III.A Complement Theory

III.A.1 F-B Theory

In this section, we show that the second term of Eq. (III.3.16) is equal to zero (i.e. $\frac{1}{\mu_0} \int_{\mathbb{R}^3} \mathbf{b}_0 \tilde{\mathbf{b}} dv = 0$). Several intermediate results are needed to prove that result.

First, it is useful to recall that the externally imposed Eulerian magnetic \mathbf{b}_0 is independent of the material. It exists even in the absence of the magnetoelastic solid and it is related to the Eulerian magnetic intensity \mathbf{h}_0 far away from the solid through the following equation

$$\mathbf{b}_0 = \mu_0 \mathbf{h}_0, \quad \forall \mathbf{x} \in \mathbb{R}^3. \quad (\text{III.A.1})$$

Secondly, it is worth mentioning that \mathbf{b}_0 (and thus \mathbf{h}_0) vanish at infinity. Indeed, an obvious proof by contradiction using the fact that the energy in the entire space of \mathbf{b}_0 (first

term of Eq. (III.3.16)) is finite gives that result

$$\begin{aligned} \frac{1}{2\mu_0} \int_{\mathbb{R}^3} \mathbf{b}_0 \cdot \mathbf{b}_0 \, dv &= \frac{\mu_0}{2} \int_{\mathbb{R}^3} \mathbf{h}_0 \cdot \mathbf{h}_0 \, dv, \quad \text{is finite,} \\ \Rightarrow \|\mathbf{h}_0\| &\rightarrow 0 \text{ as } \|\mathbf{x}\| \rightarrow \infty, \\ \Rightarrow \forall \epsilon > 0, \quad \exists R > 0 &\text{ such that } (\forall \mathbf{x} : \|\mathbf{x}\| > R, \quad \|\mathbf{h}_0\| \leq \epsilon). \end{aligned} \quad (\text{III.A.2})$$

Then using the fact that the non-magnetic monopole law (see Eq. (III.3.5)) also applies to the perturbation magnetic field $\tilde{\mathbf{b}}$, one can define a Eulerian vector potential $\tilde{\mathbf{a}}$ such that

$$\tilde{\mathbf{b}} = \nabla \times \tilde{\mathbf{a}}, \quad \forall \mathbf{x} \in \mathbb{R}^3. \quad (\text{III.A.3})$$

From Eq. (III.A.1) and Eq. (III.A.3), we can write

$$\frac{1}{\mu_0} \int_{\mathbb{R}^3} \mathbf{b}_0 \cdot \tilde{\mathbf{b}} \, dv = \int_{\mathbb{R}^3} \mathbf{h}_0 \cdot \tilde{\mathbf{b}} \, dv = \int_{\mathbb{R}^3} \mathbf{h}_0 \cdot (\nabla \times \tilde{\mathbf{a}}) \, dv. \quad (\text{III.A.4})$$

Applying a well known identity¹³ of integral calculus to the previous expression yields

$$\frac{1}{\mu_0} \int_{\mathbb{R}^3} \mathbf{b}_0 \cdot \tilde{\mathbf{b}} \, dv = \int_{\mathbb{R}^3} \tilde{\mathbf{a}} \cdot (\nabla \times \mathbf{h}_0) \, dv + \int_{\partial\mathbb{R}^3} (\mathbf{n} \times \mathbf{h}_0) \cdot \tilde{\mathbf{a}} \, ds. \quad (\text{III.A.5})$$

Moreover, \mathbf{h}_0 has to verify Ampere's law (i.e. $\nabla \times \mathbf{h}_0 = \mathbf{0}$, $\forall \mathbf{x} \in \mathbb{R}^3$) and hence

$$\frac{1}{\mu_0} \int_{\mathbb{R}^3} \mathbf{b}_0 \cdot \tilde{\mathbf{b}} \, dv = \int_{\partial\mathbb{R}^3} (\mathbf{n} \times \mathbf{h}_0) \cdot \tilde{\mathbf{a}} \, ds. \quad (\text{III.A.6})$$

At this stage let's consider that the space surrounding the material occupies a sphere of radius R that we call $\mathcal{S}(R)$. For a large enough radius R compared to the dimension of the specimen, we can make the approximation that the magnetoelastic solid behaves like a magnetic dipole. It is well known for the magnetic dipole that if the pair of charges as the source shrinks to a point while keeping the magnetization \mathbf{m} constant, the potential reads (in spherical coordinates)

$$\tilde{\mathbf{a}}(\mathbf{r}) = \frac{\mu_0}{4\pi} \frac{\mathbf{m} \times \mathbf{r}}{r^3}, \quad \forall \mathbf{r} \in \mathcal{S}(R). \quad (\text{III.A.7})$$

If we substitute Eq. (III.A.7) in Eq. (III.A.6), one obtains

$$\begin{aligned} \int_{\partial\mathcal{S}(R)} (\mathbf{n} \times \mathbf{h}_0) \cdot \tilde{\mathbf{a}} \, ds &= \frac{\mu_0}{4\pi} \int_{\partial\mathcal{S}(R)} (\mathbf{n} \times \mathbf{h}_0) \cdot \left(\frac{\mathbf{m} \times \mathbf{r}}{r^3} \right) \, ds, \\ &= \frac{\mu_0}{4\pi} \int_{\theta=0}^{2\pi} \int_{\phi=0}^{\pi} (\mathbf{e}_r \times \mathbf{h}_0) \cdot (\mathbf{m} \times \mathbf{e}_r) \sin\phi \, d\theta \, d\phi, \end{aligned} \quad (\text{III.A.8})$$

where we have used the fact that \mathbf{n} the outward normal of $\mathcal{S}(R)$ is equal to \mathbf{e}_r of the spherical coordinates, and $ds = r^2 \sin\phi \, d\theta \, d\phi$. Using the last relation of Eq. (III.A.2) and the fact

¹³ NOTE: $\int_V \mathbf{c} \cdot (\nabla \times \mathbf{d}) \, dV = \int_V \mathbf{d} \cdot (\nabla \times \mathbf{c}) \, dV + \int_{\partial V} (\mathbf{N} \times \mathbf{c}) \cdot \mathbf{d} \, dS$, where \mathbf{c} , \mathbf{d} are arbitrary vector fields defined in V (and \mathbf{N} the outward normal of the boundary ∂V).

the magnetization \mathbf{m} is constant, we can give an upper bound of the absolute value of Eq. (III.A.8)

$$\begin{aligned} \frac{\mu_0}{4\pi} \left| \int_{\theta=0}^{2\pi} \int_{\phi=0}^{\pi} (\mathbf{e}_r \times \mathbf{h}_0) \cdot (\mathbf{m} \times \mathbf{e}_r) \sin\phi \, d\theta \, d\phi \right| &\leq \frac{\mu_0}{4\pi} \int_{\theta=0}^{2\pi} \int_{\phi=0}^{\pi} \|\mathbf{e}_r \times \mathbf{h}_0\| \|\mathbf{m} \times \mathbf{e}_r\| |\sin\phi| \, d\theta \, d\phi, \\ &\leq \frac{\mu_0 \|\mathbf{m}\|}{4\pi} \int_{\theta=0}^{2\pi} \int_{\phi=0}^{\pi} \|\mathbf{h}_0\| |\sin\phi| \, d\theta \, d\phi, \\ &\leq \frac{\mu_0 \|\mathbf{m}\|}{2} \left(\int_{\phi=0}^{\pi} |\sin\phi| \, d\phi \right) \epsilon = \mu_0 \|\mathbf{m}\| \epsilon. \end{aligned} \quad (\text{III.A.9})$$

So we prove that

$$\begin{aligned} \forall \tilde{\epsilon} > 0, \exists R > 0 \text{ such that : } 0 &\leq \left| \int_{\partial S(R)} (\mathbf{n} \times \mathbf{h}_0) \cdot \tilde{\mathbf{a}} \, ds \right| \leq \tilde{\epsilon} = \mu_0 \|\mathbf{m}\| \epsilon, \\ \Rightarrow \lim_{R \rightarrow +\infty} \left(\int_{\partial S(R)} (\mathbf{n} \times \mathbf{h}_0) \cdot \tilde{\mathbf{a}} \, ds \right) &= 0, \\ \Rightarrow \int_{\partial \mathbb{R}^3} (\mathbf{n} \times \mathbf{h}_0) \cdot \tilde{\mathbf{a}} \, ds &= \frac{1}{\mu_0} \int_{\mathbb{R}^3} \mathbf{b}_0 \cdot \tilde{\mathbf{b}} \, dv = 0. \end{aligned} \quad (\text{III.A.10})$$

This result is valid for any vector potential $\tilde{\mathbf{a}}$ that vanishes as fast as the function $f : x \rightarrow 1/x^2$.

Let's now obtain the same result when the surrounding air occupies a finite domain \mathcal{D} . This case is of great interest since it is impossible to consider an infinite domain surrounding the material in numerical simulations. If the size of \mathcal{D} is sufficiently big with respect to the specimen dimensions, the error caused by this approximation is negligible.

If we substitute \mathbb{R}^3 with \mathcal{D} , Eq. (III.A.1) and Eq. (III.A.3) - Eq. (III.A.6) remain valid

$$\frac{1}{\mu_0} \int_{\mathcal{D}} \mathbf{b}_0 \cdot \tilde{\mathbf{b}} \, dv = \int_{\partial \mathcal{D}} (\mathbf{n} \times \mathbf{h}_0) \cdot \tilde{\mathbf{a}} \, ds. \quad (\text{III.A.11})$$

The major difference with the previous situation lies in the fact that the energy of the externally applied field $\frac{1}{2\mu_0} \int_{\mathcal{D}} \mathbf{b}_0 \cdot \mathbf{b}_0 \, dv$ is finite $\forall \mathbf{b}_0 \in \mathbb{R}^3$ since the domain \mathcal{D} is finite. So we don't necessarily have $\lim_{\mathbf{x} \rightarrow \partial \mathcal{D}} \|\mathbf{h}_0\| = 0$. But we impose that the perturbation vector potential $\tilde{\mathbf{a}}$ vanishes on the boundary $\partial \mathcal{D}$ far from the specimen

$$\tilde{\mathbf{a}} = \mathbf{0}, \quad \forall \mathbf{x} \in \partial \mathcal{D}. \quad (\text{III.A.12})$$

Then if we substitute Eq. (III.A.12) in Eq. (III.A.11), we get the desired result

$$\frac{1}{\mu_0} \int_{\mathcal{D}} \mathbf{b}_0 \cdot \tilde{\mathbf{b}} \, dv = 0. \quad (\text{III.A.13})$$

III.A.2 F-H Theory

Similarly, we prove in this section that the second term of Eq. (III.3.30) is equal to zero (i.e. $\mu_0 \int_{\mathbb{R}^3} \mathbf{h}_0 \cdot \tilde{\mathbf{h}} dv = 0$).

Using the Eulerian counterpart of Eq. (III.3.33), we know that $\exists \tilde{\varphi}$ such that

$$\tilde{\mathbf{h}} = -\nabla \tilde{\varphi}, \quad \forall \mathbf{x} \in \mathbb{R}^3; \quad \lim_{\|\mathbf{x}\| \rightarrow +\infty} \tilde{\varphi} = 0. \quad (\text{III.A.14})$$

From Eq. (III.A.1) and Eq. (III.A.14), we can write that

$$\mu_0 \int_{\mathbb{R}^3} \mathbf{h}_0 \cdot \tilde{\mathbf{h}} dv = - \int_{\mathbb{R}^3} \mathbf{b}_0 \cdot \nabla \tilde{\varphi} dv. \quad (\text{III.A.15})$$

At this stage, we use a well known identity¹⁴ of integral calculus to rewrite Eq. (III.A.15) as follows

$$\mu_0 \int_{\mathbb{R}^3} \mathbf{h}_0 \cdot \tilde{\mathbf{h}} dv = \int_{\mathbb{R}^3} \tilde{\varphi} (\nabla \cdot \mathbf{b}_0) dv - \int_{\partial \mathbb{R}^3} \tilde{\varphi} (\mathbf{b}_0 \cdot \mathbf{n}) ds. \quad (\text{III.A.16})$$

As \mathbf{b}_0 verifies the no magnetic monopole law (see Eq. (III.3.5)), we can simplify the previous expression as

$$\mu_0 \int_{\mathbb{R}^3} \mathbf{h}_0 \cdot \tilde{\mathbf{h}} dv = - \int_{\partial \mathbb{R}^3} \tilde{\varphi} (\mathbf{b}_0 \cdot \mathbf{n}) ds. \quad (\text{III.A.17})$$

Just like in previous section, we consider a scalar potential $\tilde{\varphi}$ that vanishes far from the sample in the following way

$$\tilde{\varphi} = \frac{\mathbf{d} \cdot \mathbf{r}}{r^3}, \quad (\text{III.A.18})$$

where \mathbf{d} is a constant vector field. It is interesting to remark that such a scalar potential describes an electric dipole ($\tilde{\varphi} = \frac{1}{4\pi\epsilon_0} \frac{\mathbf{d} \cdot \mathbf{r}}{r^3}$) where \mathbf{d} would be the electric dipole moment. Then, using the result of Eq. (III.A.2), we can derive the following upper bound

$$0 \leq \left| \int_{\partial S(R)} \tilde{\varphi} (\mathbf{b}_0 \cdot \mathbf{n}) ds \right| \leq \int_{\partial S(R)} |\tilde{\varphi}| \|\mathbf{b}_0\| ds \leq \epsilon \|\mathbf{d}\| \int_{\theta=0}^{2\pi} \int_{\phi=0}^{\pi} |\sin\phi| d\theta d\phi = 4\pi \|\mathbf{d}\| \epsilon. \quad (\text{III.A.19})$$

So we prove that

$$\begin{aligned} \forall \tilde{\epsilon} > 0, \quad \exists R > 0 \text{ such that : } 0 &\leq \left| \int_{\partial S(R)} \tilde{\varphi} (\mathbf{b}_0 \cdot \mathbf{n}) ds \right| \leq \tilde{\epsilon} = 4\pi \|\mathbf{d}\| \epsilon, \\ \Rightarrow \lim_{R \rightarrow +\infty} \left(\int_{\partial S(R)} \tilde{\varphi} (\mathbf{b}_0 \cdot \mathbf{n}) ds \right) &= 0, \\ \Rightarrow \int_{\partial S(R)} \tilde{\varphi} (\mathbf{b}_0 \cdot \mathbf{n}) ds &= \mu_0 \int_{\mathbb{R}^3} \mathbf{h}_0 \cdot \tilde{\mathbf{h}} dv = 0. \end{aligned} \quad (\text{III.A.20})$$

This result is valid for any scalar potential $\tilde{\varphi}$ that vanishes as fast as the function $f : x \rightarrow 1/x^2$.

¹⁴ NOTE: $\int_V \mathbf{d} \cdot \nabla \varphi dV = - \int_V \varphi (\nabla \cdot \mathbf{d}) dV + \int_{\partial V} (\mathbf{N} \cdot \mathbf{d}) \varphi dS$, where φ (resp. \mathbf{d}) is an arbitrary scalar (resp. vector) field defined in V .

Moreover, we can easily show that this result is also true when the air surrounding the material occupies a finite domain \mathcal{D} in the case where we impose the following boundary condition

$$\tilde{\varphi} = 0, \quad \forall \mathbf{x} \in \partial\mathcal{D}. \quad (\text{III.A.21})$$

III.A.3 Details of Calculation

In this section, we will detail the calculation of the derivative of the total potential $\tilde{W}_M(\mathbf{F}, \tilde{\mathbf{B}}, \mathbf{M})$ used in the \mathbf{M} -formulation (see section III.3.2.c). In what follows the Einstein notation will be used.

From Eq. (III.3.48), we show that

$$\begin{aligned} \tilde{W}_M(\mathbf{F}, \mathbf{M}, \tilde{\mathbf{B}}) = & \rho_0 \psi_M(\mathbf{F}, \mathbf{M}) - \rho_0 M_s(\mathbf{b}_0)_s + \\ & \frac{1}{2\mu_0 J} \left(F_{mn} F_{mr} \tilde{B}_n \tilde{B}_r - 2\mu_0 \rho_0 M_m F_{mn} \tilde{B}_n + \mu_0^2 \rho_0^2 M_m^2 \right). \end{aligned} \quad (\text{III.A.22})$$

Now, if we take the derivative of that expression with respect to the deformation gradient \mathbf{F} (keeping in mind that we chose in this formulation $\tilde{\mathbf{B}}$ and \mathbf{M} to be independent of \mathbf{F}), $\forall \{i, j\} \in \{1, 3\}^2$

$$\begin{aligned} \frac{\partial \tilde{W}_M}{\partial F_{ij}}(\mathbf{F}, \mathbf{M}, \tilde{\mathbf{B}}) = & \rho_0 \frac{\partial \psi_M}{\partial F_{ij}}(\mathbf{F}, \mathbf{M}) + \frac{1}{2\mu_0} \frac{\partial}{\partial F_{ij}} \left(\frac{1}{J} \right) \left\| \mathbf{F} \cdot \tilde{\mathbf{B}} - \mu_0 \rho_0 \mathbf{M} \right\|^2 + \\ & \frac{1}{2\mu_0 J} \left(\frac{\partial F_{mn}}{\partial F_{ij}} \tilde{B}_n F_{mr} \tilde{B}_r + F_{mn} \frac{\partial F_{mr}}{\partial F_{ij}} \tilde{B}_n \tilde{B}_r - 2\mu_0 \rho_0 M_m \frac{\partial F_{mn}}{\partial F_{ij}} \tilde{B}_n \right), \\ = & \rho_0 \frac{\partial \psi_M}{\partial F_{ij}}(\mathbf{F}, \mathbf{M}) - \frac{1}{2\mu_0 J^2} \frac{\partial J}{\partial F_{ij}} \left\| \mathbf{F} \cdot \tilde{\mathbf{B}} - \mu_0 \rho_0 \mathbf{M} \right\|^2 + \\ & \frac{1}{2\mu_0 J} \left(\delta_{mi} \delta_{nj} \tilde{B}_n F_{mr} \tilde{B}_r + F_{mn} \delta_{mi} \delta_{rj} \tilde{B}_n \tilde{B}_r - 2\mu_0 \rho_0 M_m \delta_{mi} \delta_{nj} \tilde{B}_n \right), \end{aligned} \quad (\text{III.A.23})$$

where δ is the Kronecker delta

$$\delta_{ij} = \begin{cases} 0 & , \text{ if } i \neq j, \\ 1 & , \text{ if } i = j, \end{cases} \quad (\text{III.A.24})$$

and based on the kinematic relation (III.3.1),

$$\frac{\partial J}{\partial F_{ij}} = J F_{ji}^{-1}. \quad (\text{III.A.25})$$

At this stage, if we substitute Eq. (III.A.24) and Eq. (III.A.25) into Eq. (III.A.23), we obtain

$$\begin{aligned} \frac{\partial \tilde{W}_M}{\partial F_{ij}}(\mathbf{F}, \mathbf{M}, \tilde{\mathbf{B}}) = & \rho_0 \frac{\partial \psi_M}{\partial F_{ij}}(\mathbf{F}, \mathbf{M}) - \frac{1}{2\mu_0 J} F_{ji}^{-1} \left\| \mathbf{F} \cdot \tilde{\mathbf{B}} - \mu_0 \rho_0 \mathbf{M} \right\|^2 + \\ & \frac{1}{2\mu_0 J} \left[\left(F_{ir} \tilde{B}_r \right) \tilde{B}_j + \left(F_{in} \tilde{B}_n \right) \tilde{B}_j - 2\mu_0 \rho_0 M_i \tilde{B}_j \right]. \end{aligned} \quad (\text{III.A.26})$$

Finally, we can rewrite this last expression in a tensorial form

$$\frac{\partial \widetilde{W}_M}{\partial \mathbf{F}}(\mathbf{F}, \mathbf{M}, \widetilde{\mathbf{B}}) = \rho_0 \frac{\partial \psi_M}{\partial \mathbf{F}}(\mathbf{F}, \mathbf{M}) - \frac{1}{2\mu_0 J} \left\| \mathbf{F} \cdot \widetilde{\mathbf{B}} - \mu_0 \rho_0 \mathbf{M} \right\|^2 \mathbf{F}^{-T} + \frac{1}{\mu_0 J} \left(\mathbf{F} \cdot \widetilde{\mathbf{B}} - \mu_0 \rho_0 \mathbf{M} \right) \widetilde{\mathbf{B}}. \quad (\text{III.A.27})$$

III.A.4 Calculation of the total stress tensor $\mathbf{\Pi}$

In this section, we show how the total first-Piola stress tensor $\mathbf{\Pi}$ can be related to the perturbed stress $\widetilde{\mathbf{\Pi}}$.

Instead of choosing \mathbf{F} and $\widetilde{\mathbf{B}}$ as independent variables as in Section III.3.2.a, we can choose to work with \mathbf{F} and \mathbf{B} as independent variables and hence we obtain the following energy density (which shouldn't be confused with $\widetilde{W}_B(\mathbf{F}, \widetilde{\mathbf{B}})$)

$$W_B(\mathbf{F}, \mathbf{B}) = \begin{cases} \rho_0 \psi_B(\mathbf{F}, \mathbf{B}) + \frac{1}{2\mu_0 J} \mathbf{B} \cdot \mathbf{C} \cdot \mathbf{B}; & \forall \mathbf{X} \in V, \\ \frac{1}{2\mu_0 J} \mathbf{B} \cdot \mathbf{C} \cdot \mathbf{B}; & \forall \mathbf{X} \in \mathbb{R}^3 \setminus V, \end{cases} \quad (\text{III.A.28})$$

where ψ_B is the Helmholtz free energy used in Section III.3.2.a. Then we can show (see Dorfmann and Ogden [48]) that the governing equations read

$$\begin{cases} \mathbf{m} = -\rho_0 \mathbf{F}^{-T} \cdot \frac{\partial \psi_B}{\partial \mathbf{B}} \Big|_{\mathbf{F}}, \\ \mathbf{\Pi}^T = \frac{\partial W_B}{\partial \mathbf{F}} \Big|_{\mathbf{B}} = \rho_0 \frac{\partial \psi_B}{\partial \mathbf{F}} \Big|_{\mathbf{B}} + \frac{1}{\mu_0 J} (\mathbf{F} \cdot \mathbf{B}) \mathbf{B} - \frac{1}{2\mu_0 J} (\mathbf{B} \cdot \mathbf{C} \cdot \mathbf{B}) \mathbf{F}^{-T}. \end{cases} \quad (\text{III.A.29})$$

If we introduce the decomposition, $\mathbf{B} = \mathbf{B}_0 + \widetilde{\mathbf{B}}$, in the expression of the total stress $\mathbf{\Pi}$, and if we use the magnetic governing equation of Eq. (III.A.29), one obtains

$$\begin{aligned} \mathbf{\Pi}^T &= \left\{ \rho_0 \frac{\partial \psi_B}{\partial \mathbf{F}} \Big|_{\mathbf{B}} + \frac{1}{\mu_0 J} (\mathbf{F} \cdot \widetilde{\mathbf{B}}) \widetilde{\mathbf{B}} - \frac{1}{2\mu_0 J} (\widetilde{\mathbf{B}} \cdot \mathbf{C} \cdot \widetilde{\mathbf{B}}) \mathbf{F}^{-T} + \left(\rho_0 \frac{\partial \psi_B}{\partial \mathbf{B}} \Big|_{\mathbf{F} \cdot \mathbf{B}_0} \right) \mathbf{F}^{-T} - \right. \\ &\quad \left. \left(\rho_0 \frac{\partial \psi_B}{\partial \mathbf{B}} \Big|_{\mathbf{F} \cdot \mathbf{F}^{-1}} \right) \mathbf{B}_0 \right\} + \frac{1}{\mu_0 J} (\mathbf{F} \cdot \mathbf{B}_0) \mathbf{B} - \frac{1}{2\mu_0 J} (\mathbf{B}_0 \cdot \mathbf{C} \cdot \mathbf{B}_0) \mathbf{F}^{-T} - \\ &\quad \left[\left(\frac{1}{\mu_0 J} \widetilde{\mathbf{B}} \cdot \mathbf{C} + \rho_0 \frac{\partial \psi_B}{\partial \mathbf{B}} \Big|_{\mathbf{F}} \right) \cdot \mathbf{B}_0 \right] \mathbf{F}^{-T} + \left[\frac{1}{\mu_0 J} \mathbf{F} \cdot \widetilde{\mathbf{B}} - \rho_0 \frac{\partial \psi_B}{\partial \mathbf{B}} \Big|_{\mathbf{F} \cdot \mathbf{F}^{-1}} \right] \mathbf{B}_0, \\ &= \widetilde{\mathbf{\Pi}} + \frac{1}{\mu_0 J} (\mathbf{F} \cdot \mathbf{B}_0) \mathbf{B} - \frac{1}{2\mu_0 J} (\mathbf{B}_0 \cdot \mathbf{C} \cdot \mathbf{B}_0) \mathbf{F}^{-T} - \left(\widetilde{\mathbf{H}} \cdot \mathbf{B}_0 \right) \mathbf{F}^{-T} + \left(\mathbf{F}^{-T} \cdot \widetilde{\mathbf{H}} \right) \mathbf{B}_0. \end{aligned} \quad (\text{III.A.30})$$

One can give the expression of the total Cauchy stress tensor $\boldsymbol{\sigma}$ with respect to its perturbed counterpart $\widetilde{\boldsymbol{\sigma}}$, using the fact that, $\boldsymbol{\sigma} = \frac{1}{J} \mathbf{\Pi}^T \cdot \mathbf{F}^T$

$$\boldsymbol{\sigma} = \widetilde{\boldsymbol{\sigma}} + \frac{1}{\mu_0} \mathbf{b}_0 \mathbf{b}_0 - \frac{1}{2\mu_0} (\mathbf{b}_0 \cdot \mathbf{b}_0) \mathbf{I} - \left(\widetilde{\mathbf{h}} \cdot \mathbf{b}_0 \right) \mathbf{I} + \widetilde{\mathbf{h}} \mathbf{b}_0. \quad (\text{III.A.31})$$

At this stage, we can compute the traction \mathbf{t} in the current configuration knowing that \mathbf{b}_0 is a continuous magnetic field

$$\mathbf{t} = \llbracket \boldsymbol{\sigma} \rrbracket \cdot \mathbf{n} = \llbracket \tilde{\boldsymbol{\sigma}} \rrbracket \cdot \mathbf{n} + \frac{1}{\mu_0} (\llbracket \mathbf{b} \rrbracket \cdot \mathbf{n}) - \left(\llbracket \tilde{\mathbf{h}} \rrbracket \cdot \mathbf{b}_0 \right) \mathbf{n} + \llbracket \tilde{\mathbf{h}} \rrbracket (\mathbf{b}_0 \cdot \mathbf{n}). \quad (\text{III.A.32})$$

Moreover, from the boundary/interface conditions of Eq. (III.3.5) and (III.3.6), we can write that

$$\begin{cases} \llbracket \mathbf{b} \rrbracket \cdot \mathbf{n} = 0, \\ \llbracket \tilde{\mathbf{h}} \rrbracket = \left(\llbracket \tilde{\mathbf{h}} \rrbracket \cdot \mathbf{n} \right) \mathbf{n}. \end{cases} \quad (\text{III.A.33})$$

If we substitute Eq. (III.A.33) in Eq. (III.A.32), we get

$$\mathbf{t} = \llbracket \boldsymbol{\sigma} \rrbracket \cdot \mathbf{n} = \llbracket \tilde{\boldsymbol{\sigma}} \rrbracket \cdot \mathbf{n}. \quad (\text{III.A.34})$$

This result remains valid in current configuration, i.e. $\mathbf{T} = \mathbf{N} \cdot \llbracket \boldsymbol{\Pi} \rrbracket = \mathbf{N} \cdot \llbracket \tilde{\boldsymbol{\Pi}} \rrbracket$, which means that the mechanical traction can either be computed with $\boldsymbol{\Pi}$ or $\tilde{\boldsymbol{\Pi}}$. A similar result holds for the other two formulations.

III.B Importance of specimen geometry

Before combining the FEM numerical simulation of the coupled magneto-mechanical test in pure magnetostriction with a least square optimization algorithm¹⁵, other methods and simplifications have been tried for the fitting process.

B1. Purely analytical fitting

The first approach that one can envision to fit the coupled magneto-mechanical test in pure magnetostriction is to use the governing equations of Section III.3.2.a to solve analytically the problem of a stress free material subjected to an externally applied magnetic field. The material parameters are then computed with a least square optimization technique¹⁶ to minimize the difference between analytical solutions and experimental data.

The analytical solutions of the coupled magneto-mechanical test under pure magnetostriction obtained with the material parameters identified with this approach are presented in Fig. III.16 (where all curves are plotted against the remotely applied field b_0 along the \mathbf{e}_1 direction). As one can notice, the stretch ratio λ_1 (see Fig. III.16a) along the direction of the applied field and the magnetic response (i.e. the internal magnetic field b_1 (see Fig. III.16c) and magnetization m_1 (see Fig. III.16d)) are modeled very accurately. However, the major drawback lies in the fact that the transverse and axial stretch ratios (λ_2, λ_3) cannot be described properly (see Fig. III.16b).

¹⁵ NOTE: The cost function to minimize is

$$f(\mathbf{q}_B) = \sum_{k=0}^N \left[\sum_{i=1}^3 \left| \lambda_{i,exp}\left(\frac{k}{N}b_0\right) - \lambda_{i,num}\left(\frac{k}{N}b_0, \mathbf{q}_B\right) \right|^2 + \left| \frac{b_{1,exp}\left(\frac{k}{N}b_0\right) - b_{1,num}\left(\frac{k}{N}b_0, \mathbf{q}_B\right)}{b_0} \right|^2 + \left| \frac{m_{1,exp}\left(\frac{k}{N}b_0\right) - m_{1,num}\left(\frac{k}{N}b_0, \mathbf{q}_B\right)}{\mu_0 b_0} \right|^2 \right], \quad (\text{III.B.1})$$

where subscript ‘*exp*’ denotes experimental data, subscript ‘*num*’ denotes numerically calculated variables, N represents the number of available measurements and where $\mathbf{q}_B = (m_s, \chi^*, \beta_{1B}, \beta_{2B})$ is the vector of material parameters to be computed.

¹⁶ NOTE: The cost function to minimize is

$$g(\mathbf{q}_B) = \sum_{k=0}^N \left[\sum_{i=1}^3 \left| \lambda_{i,exp}\left(\frac{k}{N}b_0\right) - \lambda_{i,ana}\left(\frac{k}{N}b_0, \mathbf{q}_B\right) \right|^2 + \left| \frac{b_{1,exp}\left(\frac{k}{N}b_0\right) - b_{1,ana}\left(\frac{k}{N}b_0, \mathbf{q}_B\right)}{b_0} \right|^2 + \left| \frac{m_{1,exp}\left(\frac{k}{N}b_0\right) - m_{1,ana}\left(\frac{k}{N}b_0, \mathbf{q}_B\right)}{\mu_0 b_0} \right|^2 \right], \quad (\text{III.B.2})$$

where subscript ‘*exp*’ denotes experimental data, subscript ‘*ana*’ denotes analytically calculated variables, N represents the number of available measurements and where $\mathbf{q}_B = (m_s, \chi^*, \beta_{1B}, \beta_{2B})$ is the vector of material parameters to be computed.

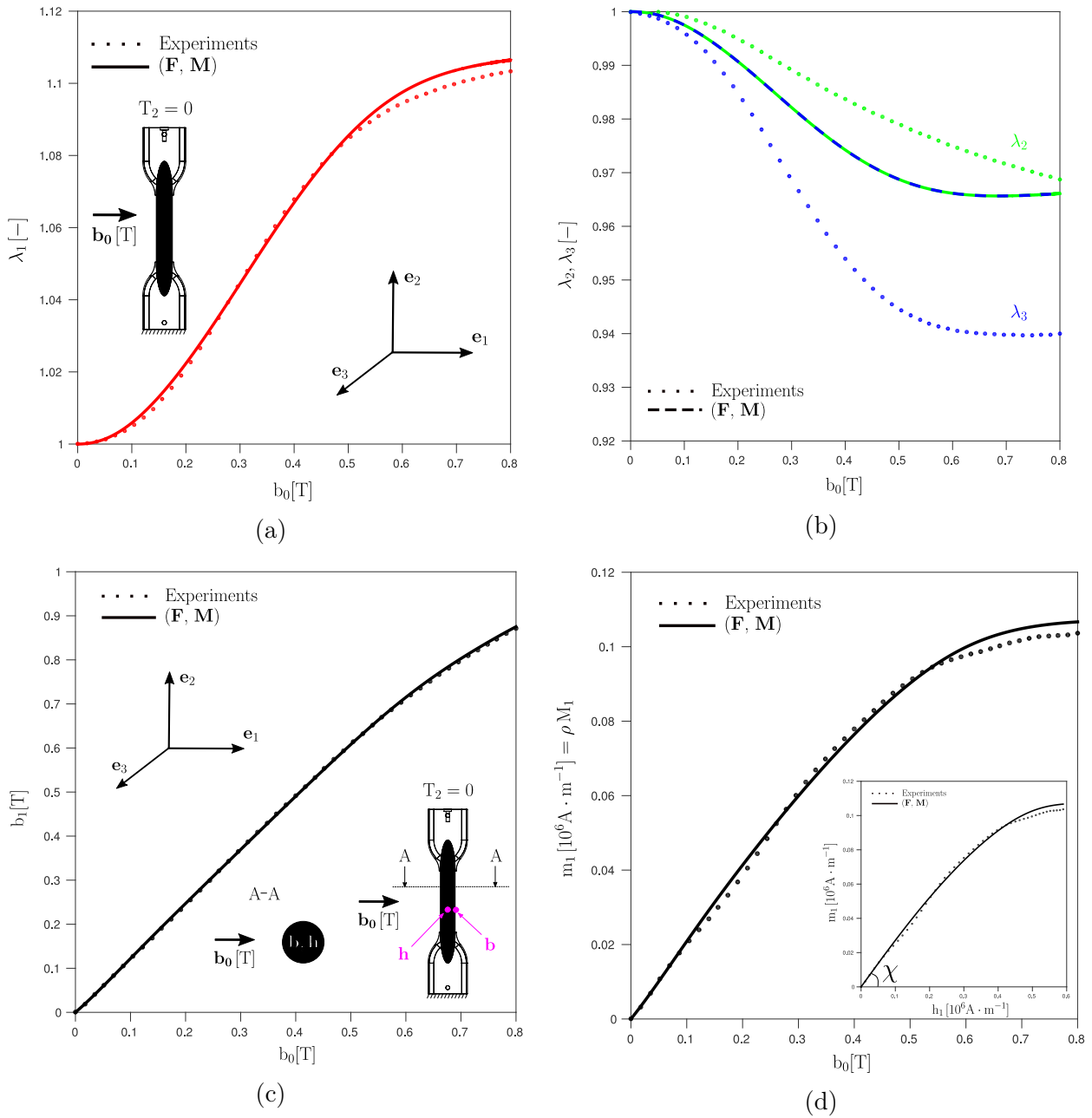


Figure III.16: Coupled magneto-mechanical (pure magnetostriction, $T_2 = 0$) test used for obtaining the energy density ψ_B for an isotropic MRE. The stretch ratio (λ_1) in the direction of the applied magnetic field is shown in (a), the transverse and axial stretch ratios (λ_2, λ_3) are shown in (b), the magnetic field (b_1) inside the MRE specimen is shown in (c) and the magnetization (m_1) is shown in (d). All curves are plotted against the remotely applied field (b_0) along the e_1 direction. Experimental curves are plotted in dotted lines while the analytical solutions are in continuous lines except in (b) where λ_2 and λ_3 are represented in dashed lines (since $\lambda_2 = \lambda_3$).

Indeed, since the analytical equations do not account for the shape of the specimens used

experimentally and since the isotropy of the material is embedded in the equations, it is obvious that such a method yields $\lambda_2 = \lambda_3$ which is not what we measure. This fact is a sign of the strong shape effect observed. The parameters computed with this approach cannot be classified as ‘material properties’ since they embed some structural effects.

Moreover, this method relies on the fact that both mechanical and magnetic internal variables are uniform within the specimen. Even if a lot of research has been devoted to the design of experimental specimens (see Chapter II) to reduce non-uniformities of the internal variables, we show numerically that such an assumption is not valid. As one can see in Fig. III.17 (which shows a cross-section of the nearly-ellipsoidal sample), the internal stretch ratio λ_1 (one the left) is much larger at the center than close to the boundary. As for the internal Eulerian magnetic field b_1 (see Fig. III.17 on the right), the assumption of uniformity appears to be valid.

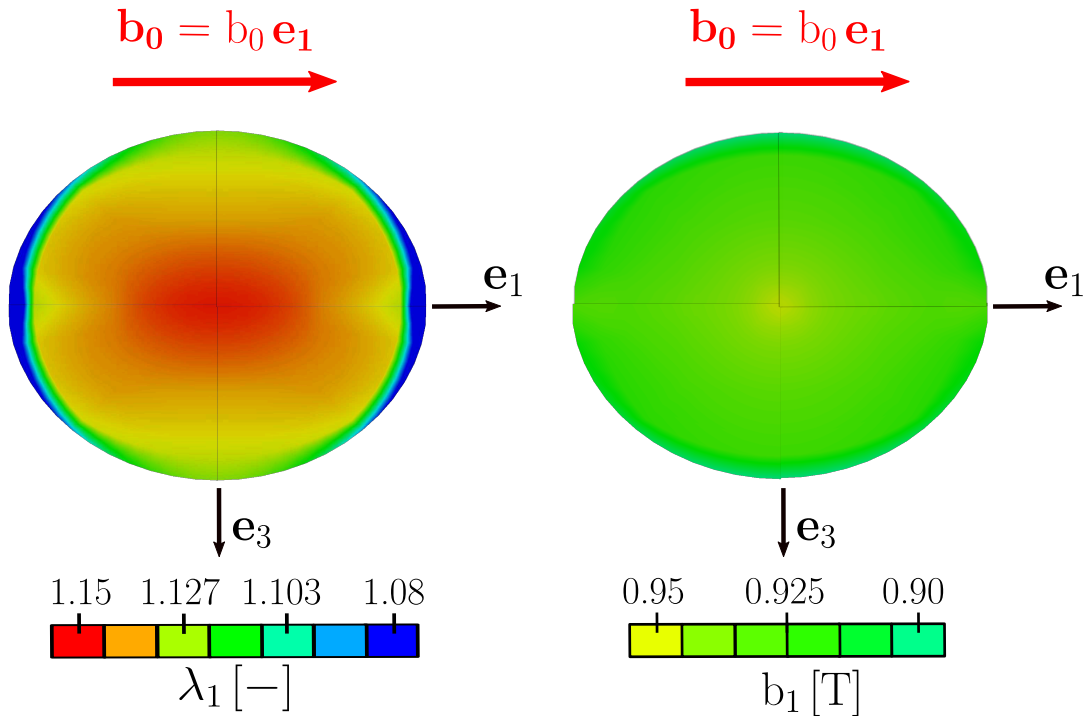


Figure III.17: Numerical results plotted in the middle cross-section of the nearly-ellipsoidal sample for the coupled magneto-mechanical test in pure magnetostriction. On the left, we notice a strong non-uniformity of the principal stretch ratio λ_1 along the direction of the applied field \mathbf{b}_0 . On the right, we see that the Eulerian magnetic field b_1 presents a small (almost negligible) non-uniformity.

B2. Numerical fitting using a 2D Mesh

As we have seen in previous section, it is necessary to correctly simulate the non-uniformity of the internal mechanical and magnetic fields using finite elements. In the fitting process, due to that non-uniformity, special attention is required to compare numerical and experimental data measured at the same location.

However, before simulating the ‘full’ ellipsoidal sample, one can think of some simplifications in the geometry of the specimen to run the numerical simulations used in the fitting process. Since all experimental measurements are made in the gage area of the specimen, one could envision to simulate an infinite cylinder subjected to an external magnetic field \mathbf{b}_0 applied in a direction perpendicular to its axis (see Fig. III.18).

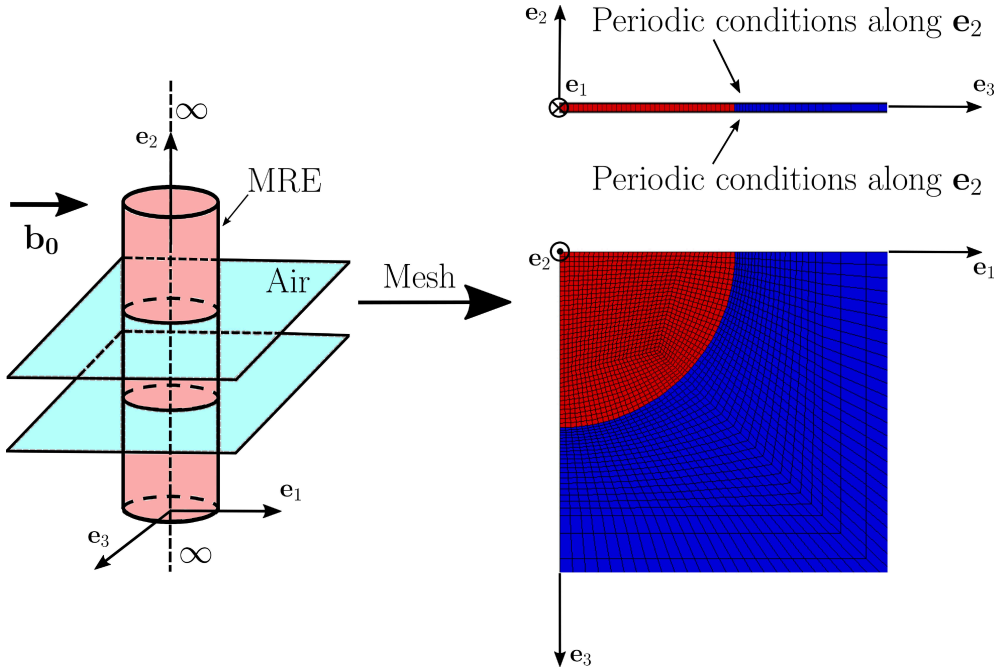


Figure III.18: Schematic of a infinite magneto-elastic cylinder used as a simplified geometry of the experimental sample. To model the pure magnetostriction experiment, the cylinder is stress free and submitted to an externally applied magnetic field \mathbf{b}_0 , perpendicular to its axis and far from its boundaries. The picture on the right shows the entire system with the surrounding air. In the picture on the left, we present the mesh used for numerical calculations and we indicate where periodicity conditions are applied.

Similarly to what is done in Section III.5.1, the material parameters are computed using a combination of FEM simulations and least square optimization. The numerical solutions of the coupled magneto-mechanical test under pure magnetostriction using the material parameters computed with the simplified geometry are plotted in Fig. III.19. The numerical solutions using the simplified mesh are plotted in continuous lines whereas the experimental data are plotted in dotted lines. As one can notice, the stretch ratio λ_1 (see Fig. III.19a) and the magnetic response (i.e. the internal magnetic field b_1 (see Fig. III.19c) and magnetization m_1 (see Fig. III.19d)) are very well modeled. In terms of the transverse and axial stretch ratios (λ_2, λ_3), even if $\lambda_2 \neq \lambda_3$, the accuracy of the numerical simulations is not satisfactory (see Fig. III.19b).

One very important thing to note on Fig. III.19 is that simulating the magnetostriction test with the exact geometry of the experimental specimen using the previous material parameters, provides a very different solution. The results of that ‘full’ simulation are plotted in dashed lines.

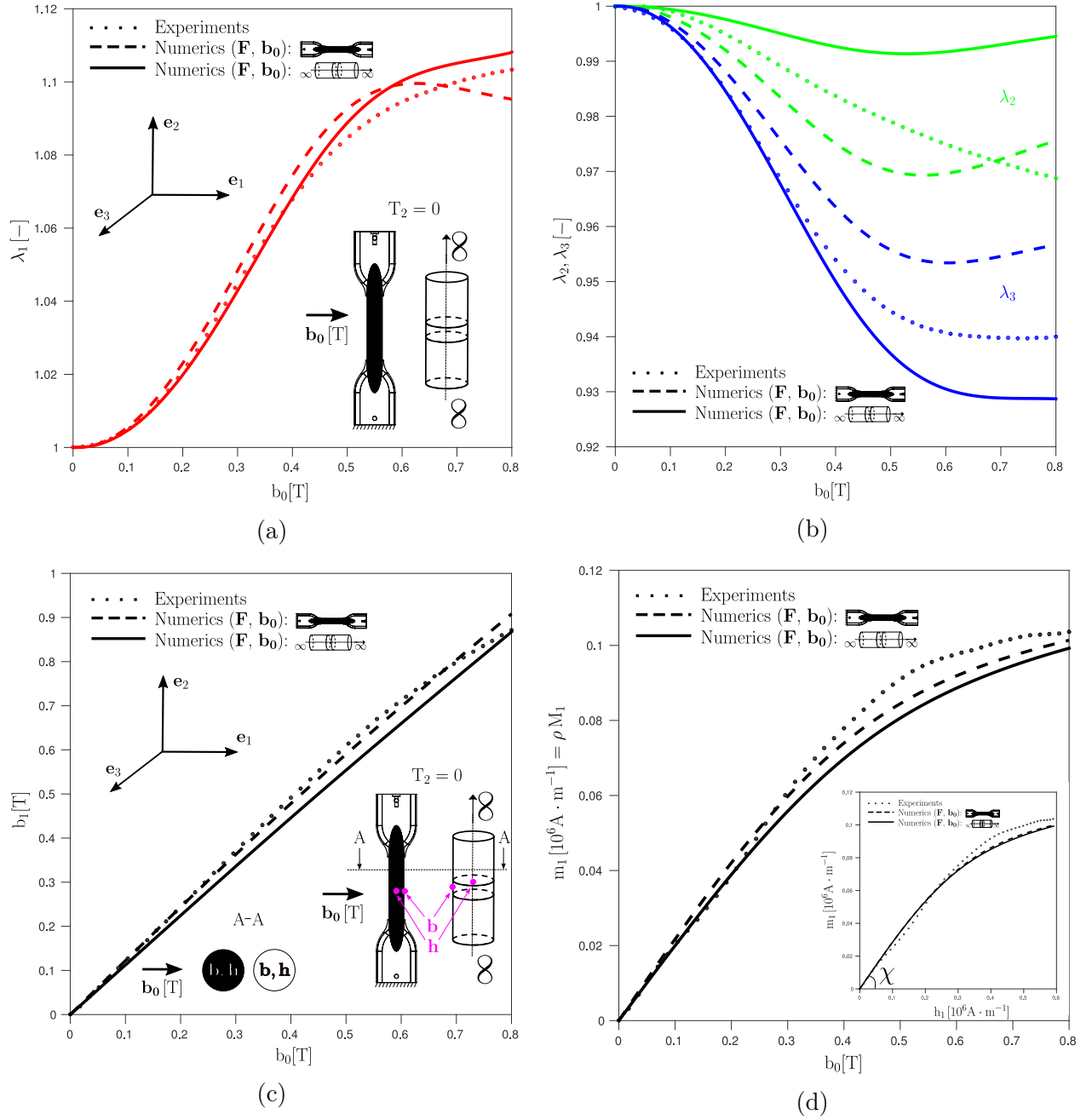


Figure III.19: Coupled magneto-mechanical (pure magnetostriction, $T_2 = 0$) test used for obtaining the energy density ψ_B for an isotropic MRE. The stretch ratio (λ_1) in the direction of the applied magnetic field is shown in (a), the transverse and axial stretch ratios (λ_2, λ_3) are shown in (b), the magnetic field (b_1) inside the MRE specimen is shown in (c) and the magnetization (m_1) is shown in (d). All curves are plotted against the remotely applied field (b_0) along the e_1 direction. Experimental curves are plotted in dotted lines while FEM calculations using the simplified geometry (i.e. the infinite magneto-elastic cylinder) are in continuous lines. The FEM calculations on the exact geometry of the nearly-ellipsoidal sample, obtained using the material parameters computed using the simplified geometry, are plotted in dashed lines.

Based on the comparison of the numerical solutions computed with the same material properties on different geometries, we show to which extent (much more than what was expected) the ‘shape effect’ influences the coupled behavior of an MRE-based structure. Such a result suggests that any simplification of the geometry to numerically simulate an MRE boundary value problem (in particular the magnetostriction test) doesn’t provide a correct solution. The only option left in the fitting procedure is to simulate the full geometry and compare the obtained solution with experimental data.

CHAPTER IV

ON 3D FEM FINITE STRAIN FORMULATIONS FOR MAGNETORHEOLOGICAL ELASTOMERS

Contents

IV.1	Introduction	120
IV.2	F-B Theory	121
IV.2.1	Variational formulation	121
IV.2.2	Form of energy density functions	122
IV.2.3	Finite element discretization	123
IV.3	F-M Theory	125
IV.3.1	Variational formulation	125
IV.3.2	Form of energy density functions	126
IV.3.3	Finite element discretization	126
IV.4	Solving a boundary value problem	129
IV.4.1	Boundary conditions	129
IV.4.2	Symmetry conditions for the perturbed magnetic vector potential $\tilde{\mathbf{A}}$	129
IV.5	Code testing	131
IV.5.1	Purely mechanical patch test	131
IV.5.2	Purely magnetic patch test	134
IV.5.3	Coupled magneto-mechanical patch test on an infinite medium (uniform field case)	137
IV.5.4	Coupled magneto-mechanical patch test on a sphere (non-uniform field case)	138
IV.6	Conclusions	144
Appendix IV.A	Complement for the F-B Theory	145

IV.A.1	First and second derivatives of the energy density, and of the invariants	145
IV.A.2	ABAQUS UEL implementation	149
IV.A.3	Shape functions and their derivatives for an 8-node isoparametric cubic element (C3D8)	159
IV.A.4	ABAQUS UEL implementation for a 10-node isoparametric tetrahedral element	160
Appendix IV.B	Complement for the F-M Theory	163
IV.B.1	First and second derivatives of the energy density, and of the invariants	163
IV.B.2	ABAQUS UEL implementation	166

IV.1 Introduction

Based on previous developments for coupled electromagnetic-mechanical processes by Brown [22], Kovetz [97], Kankanala [90], Danas [39], we proposed in Chapter III three different and equivalent fully coupled variational formulations for finite strains magneto-elasticity. By minimizing the models' generalized potential energy with respect to their independent variables, one obtains the appropriate mechanical as well as magnetic governing equations and boundary/interface conditions. Except for some trivial geometries, analytical solutions cannot generally be derived due to strong non-linearities in the governing equations and due to 'shape effects' that are caused through the interaction of the specimen with its surrounding. As a result, we propose in this work a powerful technique for generating finite element approximations. This approach, first used in Danas and Triantafyllidis [41] to develop numerical solutions for two dimensional boundary value problems (BVPs) in MREs, is extended in three dimensions for each of the three formulations presented in Chapter III.

The numerical implementation of the variational formulation based on the $\mathbf{F-H}$ theory (and thus relying on a magnetic scalar potential) won't be explained in detail in this study since it is already widely discussed in the literature. Indeed, quite a number of computational homogenization results using this formulation have been recently reported for rubber filled with periodic/hexagonal arrays (Galipeau et al. [61], Javili et al. [83], Keip and Rambauser [93]) and approximately isotropic distributions (Danas [39], Kalina et al. [87]) of circular particles in $N = 2$ space dimensions and with periodic cubic arrays of spherical particles (Javili et al. [83], Miehe et al. [114]) in $N = 3$ space dimensions. These computational results pertain to rubber matrices featuring high compressibility (presumably in order to avoid numerical complications such as volumetric locking). Moreover, Lefèvre and Lopez-Pamies [100] studied the axi-symmetric boundary problem of a magneto-elastic sphere subjected to an externally applied magnetic field far from its boundaries.

In this Chapter we will focus on the numerical implementations of the variational formulations relying on the magnetic vector potential (i.e. the $\mathbf{F-B}$ and $\mathbf{F-H}$ theory), which present several benefits such as being very useful for: numerical instability studies, simulating coupled electro-magneto-mechanical problems and avoiding the use of the arclength method

to deal with ‘softening’ phenomena (see Miehe et al. [114], Zurlo et al. [158]).

Therefore, in Section IV.2, we briefly remind the variational framework presented in Chapter III and we explain how to deal with numerical complications arising from the use of the vector potential, in particular the enforcement of the Coulomb gauge. Then, even if the numerical implementations of the **F-M** and **F-B** theories present lots of similarities, we highlight in Section IV.3 their main differences. We specifically describe the static condensation method needed to implement the **F-M** theory. Lastly, we remind in Section IV.4 the valid boundary and symmetry conditions for the vector potential to solve a boundary value problem, before presenting the different patch tests used to validate the codes in Section IV.5. For the interested reader, the practical procedure to implement the described discretizations in an ABAQUS user element (UEL) is explained in Appendix IV.A and Appendix IV.B.

IV.2 F-B Theory

This section pertains to the numerical implementation in three dimensions of the variational formulation presented in Chapter III in which the Helmholtz free energy of the different constituents of the system (magnetoelastic solid, surrounding air, etc...) depends (in addition to the deformation gradient **F**) on the Lagrangian magnetic field **B**. The first part presents the variational formulation used to solve MRE boundary value problems (see Section III.3.2.a for more details). The second part specifies which type of energy density functions will be used and the third part explains how to discretize the variational formulation using finite elements. For the interested reader, the practical procedure to implement such a discretization in an ABAQUS user element is explained in Appendix IV.A.2.

IV.2.1 Variational formulation

We assume in this section that the specific free energy is a function of the reference magnetic field **B**. Consequently, as it is explained in Chapter III, if we follow the approach introduced by Brown [22] using the perturbed magnetic field, we can prove that the relevant total potential energy \mathcal{P}_B to consider is obtained by subtracting the potential of the externally applied mechanical loads¹ \mathcal{W} (i.e. $\mathcal{W} = \int_{\mathcal{D}} \rho_0 \mathbf{f} \cdot \mathbf{u} \, dV + \int_{\partial \mathcal{D}} \mathbf{T} \cdot \mathbf{u} \, dS$) to the total energy stored in the system² \mathcal{E}_B (i.e. $\mathcal{E}_B = \int_V \widetilde{W}_B(\mathbf{u}, \widetilde{\mathbf{A}}; \mathbf{b}_0) \, dV$)

$$\mathcal{P}_B = \int_V \widetilde{W}_B(\mathbf{u}, \widetilde{\mathbf{A}}; \mathbf{b}_0) \, dV - \int_{\mathcal{D}} \rho_0 \mathbf{f} \cdot \mathbf{u} \, dV - \int_{\partial \mathcal{D}} \mathbf{T} \cdot \mathbf{u} \, dS, \quad (\text{IV.2.1})$$

where V is the volume of the entire system, \mathcal{D} (resp. $\partial \mathcal{D}$) is the volume (resp. the boundary) of the magnetoelastic solid, and where

$$\mathbf{F} = \mathbf{I} + \mathbf{u} \nabla, \quad \rho_0 = \rho J, \quad J = \det \mathbf{F}, \quad \mathbf{B} = \widetilde{\mathbf{B}} + J \mathbf{F}^{-1} \cdot \mathbf{b}_0, \quad \widetilde{\mathbf{B}} = \nabla \times \widetilde{\mathbf{A}}. \quad (\text{IV.2.2})$$

¹ NOTE: The mechanical loads are applied on a magnetoelastic solid of volume \mathcal{D} and boundary $\partial \mathcal{D}$.

² NOTE: Since this chapter is focused on the numerical implementation, the system considered has a finite volume V and a boundary ∂V . It can be composed of subsystems such as the MRE solid, the surrounding air, a coil, etc...

We introduce the energy density \widetilde{W}_B with independent variables \mathbf{u} (the displacement field) and $\widetilde{\mathbf{A}}$ (the perturbed magnetic vector potential) with respect to which the potential \mathcal{P}_B is minimized

$$\begin{aligned} \widetilde{W}_B(\mathbf{u}, \widetilde{\mathbf{A}}; \mathbf{b}_0) = & \rho_0 \psi_B(\mathbf{F}, \nabla \times \widetilde{\mathbf{A}} + J \mathbf{F}^{-1} \cdot \mathbf{b}_0, \mathbf{N}) + \frac{1}{2\mu_0 J} (\nabla \times \widetilde{\mathbf{A}}) \cdot \mathbf{C} \cdot (\nabla \times \widetilde{\mathbf{A}}) + \\ & \frac{1}{2\mu_0 \kappa} (\nabla \cdot \widetilde{\mathbf{A}})^2, \end{aligned} \quad (\text{IV.2.3})$$

where ψ_B is the Helmholtz free energy of each component of the system. For instance, $\psi_B = \psi_{\text{Mat}}(\mathbf{F}, \mathbf{B}, \mathbf{N})$ in the material and $\psi_B = \psi_{\text{Air}}(\mathbf{F})$ for the surrounding air. As it has been pointed out in Chapter II, the magnetoelastic material under investigation can either be isotropic or transversely isotropic (i.e. the iron particles form chains along a given direction) depending if the curing process is conducted under a magnetic field or not. This implies that the solid's Helmholtz free energy also depends on a unit vector \mathbf{N} which defines the initial orientation of the particle chains ($\mathbf{N} = \mathbf{0}$ in the case of an isotropic sample). The additional variable \mathbf{N} is known and chosen during the fabrication process. Hence, it is not a variable that we have to solve for and as a result the same FEM code can be used to solve boundary value problems for different microstructures (isotropic or transversely isotropic).

In addition, to ensure the uniqueness of the perturbed magnetic vector potential $\widetilde{\mathbf{A}}$, the Coulomb gauge is used. To numerically enforce it, we choose to add a penalty term in the total potential energy with penalty $\kappa \ll 1$ ³. The choice of the penalty method has been justified in Section III.4.1. The value of the penalty κ will be adjusted by running several patch tests and making sure that our numerical code can reproduce exact analytical solutions of some boundary value problems as well as numerical calculations given by an already validated finite element code based on the \mathbf{F} - \mathbf{H} theory which relies on a magnetic scalar potential. It is important to specify that the penalty term added must be under-integrated to avoid any 'locking phenomena' (similarly to what is done in purely mechanical problems to avoid volumetric locking).

IV.2.2 Form of energy density functions

In this section we specify the energy density functions that will be used in numerical calculations of MRE boundary value problems.

As mentioned Kankanala [90] and Danas [40], due to the properties of objectivity and material symmetry, the general form of the specific Helmholtz free energy for transversely isotropic MREs ($\mathbf{N} = \mathbf{0}$ for isotropic samples) is given by

$$\psi_B = \psi_B(\mathbf{C}, \mathbf{B}, \mathbf{N}) = \psi_B(\mathbf{C}, \widetilde{\mathbf{B}} + J \mathbf{F}^{-1} \cdot \mathbf{b}_0, \mathbf{N}), \quad \mathbf{N} \cdot \mathbf{N} = 1. \quad (\text{IV.2.4})$$

Using the general theory of transversely isotropic functions (see Adkins [2, 3], and Pipkin and Rivlin [123]) that depend on a rank-two tensor (the right Cauchy-Green strain tensor \mathbf{C}) and two vectors (the Lagrangian total magnetic field \mathbf{B} and the orientation vector \mathbf{N}), one obtains that ψ_B is a function of ten independent invariants, namely

$$\psi_B = \psi_B(\mathbf{C}, \mathbf{B}, \mathbf{N}) = \psi_B(I_i^B), \quad i \in 1, \dots, 10, \quad (\text{IV.2.5})$$

³ NOTE: The final solution shouldn't depend on the parameter κ .

where

Mechanical (Iso)	$I_1 = \text{tr} \mathbf{C}, \quad I_2 = \frac{1}{2} [(\text{tr} \mathbf{C})^2 - \text{tr} (\mathbf{C}^2)], \quad I_3 = \det \mathbf{C} = J^2$
Mechanical (Transversely iso)	$I_4 = \mathbf{N} \cdot \mathbf{C} \cdot \mathbf{N}, \quad I_5 = \mathbf{N} \cdot \mathbf{C}^2 \cdot \mathbf{N}$
Coupled (Iso)	$I_6^B = \mathbf{B} \cdot \mathbf{C} \cdot \mathbf{B} = J^2 \mathbf{b}_0 \cdot \mathbf{b}_0 + 2J \mathbf{b}_0 \cdot \mathbf{F} \cdot \tilde{\mathbf{B}} + \tilde{\mathbf{B}} \cdot \mathbf{C} \cdot \tilde{\mathbf{B}}$ $I_7^B = \mathbf{B} \cdot \mathbf{C}^2 \cdot \mathbf{B} = J^2 (\mathbf{F}^T \cdot \mathbf{b}_0) \cdot (\mathbf{F}^T \cdot \mathbf{b}_0) + 2J (\mathbf{F}^T \cdot \mathbf{b}_0) \cdot (\mathbf{C} \cdot \tilde{\mathbf{B}}) + \tilde{\mathbf{B}} \cdot \mathbf{C}^2 \cdot \tilde{\mathbf{B}}$ $I_8^B = \mathbf{B} \cdot \mathbf{B} = J^2 \mathbf{b}_0 \cdot \mathbf{F}^{-T} \cdot \mathbf{F}^{-1} \cdot \mathbf{b}_0 + 2J \mathbf{b}_0 \cdot \mathbf{F}^{-T} \cdot \tilde{\mathbf{B}} + \tilde{\mathbf{B}} \cdot \tilde{\mathbf{B}}$
Coupled (Transversely iso)	$I_9^B = (\mathbf{B} \cdot \mathbf{N})^2 = \left[(\tilde{\mathbf{B}} + J \mathbf{F}^{-1} \cdot \mathbf{b}_0) \cdot \mathbf{N} \right]^2$ $I_{10}^B = (\mathbf{B} \cdot \mathbf{N}) (\mathbf{B} \cdot \mathbf{C} \cdot \mathbf{N}) = \left[(\tilde{\mathbf{B}} + J \mathbf{F}^{-1} \cdot \mathbf{b}_0) \cdot \mathbf{N} \right] \left[(\tilde{\mathbf{B}} + J \mathbf{F}^{-1} \cdot \mathbf{b}_0) \cdot \mathbf{C} \cdot \mathbf{N} \right]$

(IV.2.6)

IV.2.3 Finite element discretization

The next step is to consider the variations of \mathcal{P}_B with respect to its independent variables $\mathbf{q} = [\mathbf{u}; \tilde{\mathbf{A}}]$ (column vector of unknowns). If we use this notation, the total potential energy can be written as

$$\mathcal{P}_B(\mathbf{u}, \tilde{\mathbf{A}}; \mathbf{b}_0) = \mathcal{P}_B(\mathbf{q}, \mathbf{b}_0). \quad (\text{IV.2.7})$$

Then the first variation of \mathcal{P}_B with respect to \mathbf{q} reads

$$\delta \mathcal{P}_B = \mathcal{P}_{B,\mathbf{q}} \delta \mathbf{q} = [\delta \mathbf{q}]^T \cdot [\mathbf{F}_v(\mathbf{q}, \mathbf{b}_0)]. \quad (\text{IV.2.8})$$

A more detailed expression of the global force vector \mathbf{F}_v will be given in what follows. Similarly, the second variation of the potential energy is given by

$$\Delta \delta \mathcal{P}_B = [\delta \mathbf{q}]^T \cdot [\mathbf{K}(\mathbf{q}, \mathbf{b}_0)] \cdot [\Delta \mathbf{q}], \quad (\text{IV.2.9})$$

where the global stiffness matrix \mathbf{K} is better defined later in this section.

The variational formulation written in Eq. (IV.2.1) leads to seek the vector of unknown nodal degrees of freedom \mathbf{q} by solving the non-linear equation $\delta \mathcal{P}_B = \mathcal{P}_{B,\mathbf{q}} \delta \mathbf{q} = 0$. The Newton-Raphson method which is based on the first order Taylor expansion of the global force vector about the previous iteration is used

$$\mathcal{P}_{B,\mathbf{q}}(\mathbf{q} + \Delta \mathbf{q}, \mathbf{b}_0 + \Delta \mathbf{b}_0) \delta \mathbf{q} = [\delta \mathbf{q}]^T \cdot \left[\mathcal{P}_{B,\mathbf{q}}(\mathbf{q}, \mathbf{b}_0) + \mathcal{P}_{B,\mathbf{q}\mathbf{b}_0}(\mathbf{q}, \mathbf{b}_0) \Delta \mathbf{b}_0 + \mathcal{P}_{B,\mathbf{q}\mathbf{q}}(\mathbf{q}, \mathbf{b}_0) \Delta \mathbf{q} \right] = 0. \quad (\text{IV.2.10})$$

To compute the global force vector \mathbf{F}_v and stiffness matrix \mathbf{K} , one can discretize the total potential energy \mathcal{P}_B by decomposing the total volume V of the system in N_e discrete and disjoint finite elements of volume V_e

$$V = \bigcup_{e=1}^{N_e} V_e. \quad (\text{IV.2.11})$$

The total potential energy \mathcal{P}_B is then the sum of the potential energies \mathcal{P}_B^e of all elements

$$\mathcal{P}_B = \sum_{e=1}^{N_e} \mathcal{P}_B^e = \sum_{e=1}^{N_e} \left(\int_{V_e} \widetilde{W}_B(\mathbf{u}, \widetilde{\mathbf{A}}; \mathbf{b}_0) dV - \int_{V_e \cap \mathcal{D}} \rho_0 \mathbf{f} \cdot \mathbf{u} dV - \int_{\partial V_e \cap \partial \mathcal{D}} \mathbf{T} \cdot \mathbf{u} dS \right). \quad (\text{IV.2.12})$$

In each element, we use the element vector of unknowns⁴ $\mathbf{q}_e = [\mathbf{u}; \widetilde{\mathbf{A}}]$ that leads to the definition (in a general fashion) of the discretized form of the unknown variables, i.e. $\forall \mathbf{X} \in V_e$

$$[\mathbf{u}(\mathbf{X})] = [\mathbf{N}_u(\mathbf{X})] \cdot [\mathbf{q}_e], \quad [\widetilde{\mathbf{A}}(\mathbf{X})] = [\mathbf{N}_A(\mathbf{X})] \cdot [\mathbf{q}_e], \quad (\text{IV.2.13})$$

where \mathbf{N}_u and \mathbf{N}_A are matrices associated with the element shape functions. In order to compute the gradient of \mathbf{u} , we use

$$[\mathbf{u}\nabla(\mathbf{X})] = [\mathbf{G}_u(\mathbf{X})] \cdot [\mathbf{q}_e], \quad \mathbf{F} = \mathbf{I} + \mathbf{u}\nabla = \mathbf{I} + [\mathbf{G}_u] \cdot [\mathbf{q}_e], \quad (\text{IV.2.14})$$

where \mathbf{G}_u is a rank three tensor denoting the gradient of the \mathbf{N}_u matrix. Finally, the operators Curl and Divergence of the perturbed magnetic vector potential can be evaluated using the rank two tensor \mathbf{G}_A and vector \mathbf{D}_A such that

$$[\widetilde{\mathbf{B}}(\mathbf{X})] = [\nabla \times \widetilde{\mathbf{A}}(\mathbf{X})] = [\mathbf{G}_A(\mathbf{X})] \cdot [\mathbf{q}_e], \quad \nabla \cdot \widetilde{\mathbf{A}}(\mathbf{X}) = [\mathbf{D}_A(\mathbf{X})]^T \cdot [\mathbf{q}_e]. \quad (\text{IV.2.15})$$

The global force vector \mathbf{F}_v is obtained by assembling the element force vectors \mathbf{f}_e

$$\delta \mathcal{P}_B = \mathcal{P}_{B,\mathbf{q}} \delta \mathbf{q} = [\delta \mathbf{q}]^T \cdot [\mathbf{F}_v(\mathbf{q}, \mathbf{b}_0)] = \sum_{e=1}^{N_e} \mathcal{P}_{B,\mathbf{q}_e}^e \delta \mathbf{q}_e = \sum_{e=1}^{N_e} [\delta \mathbf{q}_e]^T \cdot [\mathbf{f}_e], \quad (\text{IV.2.16})$$

where

$$\mathbf{f}_e = \int_{V_e} \left\{ \left[\frac{\partial \widetilde{W}_B}{\partial \mathbf{F}} \right] \cdot [\mathbf{G}_u] + \left[\frac{\partial \widetilde{W}_B}{\partial \widetilde{\mathbf{B}}} \right] \cdot [\mathbf{G}_A] + \frac{1}{\mu_0 \kappa} (\nabla \cdot \widetilde{\mathbf{A}}) \mathbf{D}_A^T \right\} dV - \int_{V_e \cap \mathcal{D}} \rho_0 [\mathbf{f}] \cdot [\mathbf{N}_u] dV - \int_{\partial V_e \cap \partial \mathcal{D}} [\mathbf{T}] \cdot [\mathbf{N}_u] dS. \quad (\text{IV.2.17})$$

Similarly, the global stiffness matrix \mathbf{K} is obtained by assembling the element stiffness matrices \mathbf{k}_e

$$\Delta \delta \mathcal{P}_B = [\delta \mathbf{q}]^T \cdot [\mathbf{K}(\mathbf{q}, \mathbf{b}_0)] \cdot [\Delta \mathbf{q}] = \sum_{e=1}^{N_e} [\delta \mathbf{q}_e]^T \cdot [\mathbf{k}_e] \cdot [\Delta \mathbf{q}_e], \quad (\text{IV.2.18})$$

with

$$\mathbf{k}_e = \int_{V_e} \left\{ [\mathbf{G}_u^T, \mathbf{G}_A^T] \cdot \begin{bmatrix} \frac{\partial^2 \widetilde{W}_B}{\partial \mathbf{F} \partial \mathbf{F}} & \frac{\partial^2 \widetilde{W}_B}{\partial \mathbf{F} \partial \widetilde{\mathbf{B}}} \\ \frac{\partial^2 \widetilde{W}_B}{\partial \widetilde{\mathbf{B}} \partial \mathbf{F}} & \frac{\partial^2 \widetilde{W}_B}{\partial \widetilde{\mathbf{B}} \partial \widetilde{\mathbf{B}}} \end{bmatrix} \cdot \begin{bmatrix} \mathbf{G}_u \\ \mathbf{G}_A \end{bmatrix} + \frac{1}{\mu_0 \kappa} \mathbf{D}_A \mathbf{D}_A^T \right\} dV. \quad (\text{IV.2.19})$$

⁴ NOTE: The element vector of unknowns \mathbf{q}_e is simply the restriction of the global vector of unknowns \mathbf{q} to element e .

A detailed calculation of the first⁵ and second derivatives of the energy density \widetilde{W}_B is given in Appendix IV.A.1. For the interested reader, the practical procedure to implement the described discretization in an ABAQUS user element (UEL) is explained in Appendix IV.A.2.

IV.3 F-M Theory

In this section, we detail the numerical implementation of the variational formulation based on the **F-M** theory which has been introduced in Section III.3.2.c. The objective is not to duplicate the previous section. Instead we will simply highlight the main differences in the numerical implementation of the two theories relying on a magnetic vector potential.

For that purpose, the first part presents the variational formulation based on the **F-M** theory. The second part specifies without details the form of energy density function considered. The third part focuses on the differences between the **F-B** and **F-M** theory in terms of discretization using finite elements. For the interested reader, the main differences between the **F-B** and **F-M** formulations in terms of numerical implementation in an ABAQUS user element are explained in Appendix IV.B.2.

IV.3.1 Variational formulation

The specific Helmholtz free energy ψ_M of interest here is a function of the deformation gradient **F** and the magnetization per unit mass **M** ($\mathbf{m} = \rho\mathbf{M}$ where **m** is the magnetization per unit volume and ρ is the density of the magnetoelastic solid in current configuration). As shown in Section III.3.2.c, we prove that the relevant potential energy to consider reads

$$\mathcal{P}_M = \int_V \widetilde{W}_M(\mathbf{u}, \widetilde{\mathbf{A}}, \mathbf{M}; \mathbf{b}_0) dV - \int_{\mathcal{D}} \rho_0 \mathbf{f} \cdot \mathbf{u} dV - \int_{\partial\mathcal{D}} \mathbf{T} \cdot \mathbf{u} dS, \quad (\text{IV.3.1})$$

where the energy density \widetilde{W}_M is defined as

$$\begin{aligned} \widetilde{W}_M(\mathbf{u}, \widetilde{\mathbf{A}}, \mathbf{M}; \mathbf{b}_0) = & \rho_0 [\psi_M(\mathbf{F}, \mathbf{M}, \mathbf{N}) - \mathbf{M} \cdot \mathbf{b}_0] + \frac{1}{2\mu_0 J} \left\| \mathbf{F} \cdot (\nabla \times \widetilde{\mathbf{A}}) - \mu_0 \rho_0 \mathbf{M} \right\|^2 + \\ & \frac{1}{2\mu_0 \kappa} (\nabla \cdot \widetilde{\mathbf{A}})^2. \end{aligned} \quad (\text{IV.3.2})$$

The Helmholtz free energy ψ_M depends on the unit vector **N** since the magnetoelastic material under investigation can either be isotropic ($\mathbf{N} = \mathbf{0}$) or transversely isotropic ($\mathbf{N} \neq \mathbf{0}$). Moreover, the Coulomb gauge introduced in Eq. (III.4.1) is as well numerically enforced using the penalty approach ($\kappa \ll 1$). It is interesting to notice that unlike the **F-B** theory, \mathcal{P}_M has three independent variables (instead of just two), namely the displacement vector **u**, the perturbed magnetic vector potential $\widetilde{\mathbf{A}}$ and the magnetization vector **M**.

⁵ NOTE: The standard indicial notation in Cartesian coordinates is used to compute the first and second variations of the energy density, i.e. $\frac{\partial \widetilde{W}_B}{\partial \mathbf{F}}(\mathbf{F}, \widetilde{\mathbf{B}}) = \frac{\partial \widetilde{W}_B}{\partial F_{ij}}(\mathbf{F}, \widetilde{\mathbf{B}}) \mathbf{e}_i \mathbf{e}_j$, $\frac{\partial \widetilde{W}_B}{\partial \widetilde{\mathbf{B}}}(\mathbf{F}, \widetilde{\mathbf{B}}) = \frac{\partial \widetilde{W}_B}{\partial \widetilde{B}_i}(\mathbf{F}, \widetilde{\mathbf{B}}) \mathbf{e}_i$, etc...

IV.3.2 Form of energy density functions

In terms of the solid's Helmholtz free energy, the properties used in Section IV.2.2 to justify its general form remain valid for the **F-M** theory. As a result, ψ_M is given by

$$\psi_M = \psi_M(\mathbf{F}, \mathbf{M}, \mathbf{N}) = \psi_M(I_i^M), \quad i \in 1, \dots, 10, \quad \mathbf{N} \cdot \mathbf{N} = 1, \quad (\text{IV.3.3})$$

where the mechanical invariants (I_i , $i \in [1, 5]$) remain the same as in Eq. (IV.2.6) and where the coupled invariants can be written as

Coupled (Iso)	$I_6^M = \mathbf{M} \cdot \mathbf{M}, \quad I_7^M = \mathbf{M} \cdot \mathcal{B} \cdot \mathbf{M}, \quad I_8^M = \mathbf{M} \cdot \mathcal{B}^2 \cdot \mathbf{M},$
Coupled (Transversely iso)	$I_9^M = (\mathbf{M} \cdot \mathbf{F} \cdot \mathbf{N})^2, \quad I_{10}^M = (\mathbf{M} \cdot \mathbf{F} \cdot \mathbf{N}) (\mathbf{M} \cdot \mathbf{F} \cdot \mathbf{F}^T \cdot \mathbf{F} \cdot \mathbf{N}),$

(IV.3.4)

with $\mathcal{B} = \mathbf{F} \cdot \mathbf{F}^T$ the left Cauchy-Green strain tensor.

IV.3.3 Finite element discretization

The next step is to consider the variations of \mathcal{P}_M with respect to its independent variables $\mathbf{q} = [\mathbf{u}, \tilde{\mathbf{A}}, \mathbf{M}]$ (column vector of unknowns). Since the potential energy can be written as $\mathcal{P}_M(\mathbf{u}, \tilde{\mathbf{A}}, \mathbf{M}; \mathbf{b}_0) = \mathcal{P}_M(\mathbf{q}; \mathbf{b}_0)$, its first and second variation read

$$\begin{aligned} \delta \mathcal{P}_M &= \mathcal{P}_{M, \mathbf{q}} \delta \mathbf{q} = [\delta \mathbf{q}]^T \cdot [\mathbf{F}_v(\mathbf{q}, \mathbf{b}_0)], \\ \Delta \delta \mathcal{P}_M &= [\delta \mathbf{q}]^T \cdot [\mathbf{K}(\mathbf{q}, \mathbf{b}_0)] \cdot [\Delta \mathbf{q}], \end{aligned} \quad (\text{IV.3.5})$$

where \mathbf{F}_v and \mathbf{K} are respectively the global force vector and the global stiffness matrix in the **F-M** theory.

Similarly to what has been done in Section IV.2.3, \mathbf{F}_v and \mathbf{K} are computed by first discretizing the total potential energy \mathcal{P}_M . If we decompose the total volume of the system in N_e discrete and disjoint finite elements of volume V_e (see Eq. (IV.2.11)), \mathcal{P}_M is obtained as the sum of the element potential energies \mathcal{P}_M^e

$$\mathcal{P}_M = \sum_{e=1}^{N_e} \mathcal{P}_M^e = \sum_{e=1}^{N_e} \left(\int_{V_e} \tilde{W}_M(\mathbf{u}, \tilde{\mathbf{A}}, \mathbf{M}; \mathbf{b}_0) dV - \int_{V_e \cap \mathcal{D}} \rho_0 \mathbf{f} \cdot \mathbf{u} dV - \int_{\partial V_e \cap \partial \mathcal{D}} \mathbf{T} \cdot \mathbf{u} dS \right). \quad (\text{IV.3.6})$$

If we use in each element the vector of unknowns $\mathbf{q}_e = [\mathbf{u}, \tilde{\mathbf{A}}, \mathbf{M}]$, we can define the discretized form of the unknown variables, i.e. $\forall \mathbf{X} \in V_e$

$$[\mathbf{u}(\mathbf{X})] = [\mathbf{N}_u(\mathbf{X})] \cdot [\mathbf{q}_e], \quad [\tilde{\mathbf{A}}(\mathbf{X})] = [\mathbf{N}_A(\mathbf{X})] \cdot [\mathbf{q}_e], \quad [\mathbf{M}(\mathbf{X})] = [\mathbf{N}_M(\mathbf{X})] \cdot [\mathbf{q}_e], \quad (\text{IV.3.7})$$

where \mathbf{N}_u , \mathbf{N}_A and \mathbf{N}_M are matrices associated with the element shape functions. The gradient of \mathbf{u} , the Curl and Divergence of $\tilde{\mathbf{A}}$ are calculated using the tensors \mathbf{G}_u , \mathbf{G}_A and \mathbf{D}_A (already defined in Section IV.2.3) such that

$$\begin{aligned} [\mathbf{u} \nabla(\mathbf{X})] &= [\mathbf{G}_u(\mathbf{X})] \cdot [\mathbf{q}_e], \quad [\tilde{\mathbf{B}}(\mathbf{X})] = [\nabla \times \tilde{\mathbf{A}}(\mathbf{X})] = [\mathbf{G}_A(\mathbf{X})] \cdot [\mathbf{q}_e], \\ \nabla \cdot \tilde{\mathbf{A}}(\mathbf{X}) &= [\mathbf{D}_A(\mathbf{X})]^T \cdot [\mathbf{q}_e]. \end{aligned} \quad (\text{IV.3.8})$$

The global force vector \mathbf{F}_v is obtained by assembling the element force vectors \mathbf{f}_e

$$\delta\mathcal{P}_M = \mathcal{P}_{M,\mathbf{q}} \delta\mathbf{q} = [\delta\mathbf{q}]^T \cdot [\mathbf{F}_v(\mathbf{q}, \mathbf{b}_0)] = \sum_{e=1}^{N_e} \mathcal{P}_{M,\mathbf{q}_e}^e \delta\mathbf{q}_e = \sum_{e=1}^{N_e} [\delta\mathbf{q}_e]^T \cdot [\mathbf{f}_e], \quad (\text{IV.3.9})$$

where

$$\begin{aligned} \mathbf{f}_e = \int_{V_e} \left\{ \left[\frac{\partial \widetilde{W}_M}{\partial \mathbf{F}} \right] \cdot [\mathbf{G}_u] + \left[\frac{\partial \widetilde{W}_M}{\partial \widetilde{\mathbf{B}}} \right] \cdot [\mathbf{G}_A] + \left[\frac{\partial \widetilde{W}_M}{\partial \mathbf{M}} \right] \cdot [\mathbf{N}_M] + \frac{1}{\mu_0 \kappa} (\nabla \cdot \widetilde{\mathbf{A}}) \mathbf{D}_A^T \right\} dV - \\ \int_{V_e \cap \mathcal{D}} \rho_0 [\mathbf{f}] \cdot [\mathbf{N}_u] dV - \int_{\partial V_e \cap \partial \mathcal{D}} [\mathbf{T}] \cdot [\mathbf{N}_u] dS. \end{aligned} \quad (\text{IV.3.10})$$

Similarly, the global stiffness matrix \mathbf{K} is computed by assembling the element stiffness matrices \mathbf{k}_e

$$\Delta \delta\mathcal{P}_M = [\delta\mathbf{q}]^T \cdot [\mathbf{K}(\mathbf{q}, \mathbf{b}_0)] \cdot [\Delta\mathbf{q}] = \sum_{e=1}^{N_e} [\delta\mathbf{q}_e]^T \cdot [\mathbf{k}_e] \cdot [\Delta\mathbf{q}_e], \quad (\text{IV.3.11})$$

with

$$\mathbf{k}_e = \int_{V_e} \left\{ [\mathbf{G}_u^T, \mathbf{G}_A^T, \mathbf{N}_M^T] \cdot \begin{bmatrix} \frac{\partial^2 \widetilde{W}_M}{\partial \mathbf{F} \partial \mathbf{F}} & \frac{\partial^2 \widetilde{W}_M}{\partial \mathbf{F} \partial \widetilde{\mathbf{B}}} & \frac{\partial^2 \widetilde{W}_M}{\partial \mathbf{F} \partial \mathbf{M}} \\ \frac{\partial^2 \widetilde{W}_M}{\partial \widetilde{\mathbf{B}} \partial \mathbf{F}} & \frac{\partial^2 \widetilde{W}_M}{\partial \widetilde{\mathbf{B}} \partial \widetilde{\mathbf{B}}} & \frac{\partial^2 \widetilde{W}_M}{\partial \widetilde{\mathbf{B}} \partial \mathbf{M}} \\ \frac{\partial^2 \widetilde{W}_M}{\partial \mathbf{M} \partial \mathbf{F}} & \frac{\partial^2 \widetilde{W}_M}{\partial \mathbf{M} \partial \widetilde{\mathbf{B}}} & \frac{\partial^2 \widetilde{W}_M}{\partial \mathbf{M} \partial \mathbf{M}} \end{bmatrix} \cdot \begin{bmatrix} \mathbf{G}_u \\ \mathbf{G}_A \\ \mathbf{N}_M \end{bmatrix} + \frac{1}{\mu_0 \kappa} \mathbf{D}_A \mathbf{D}_A^T \right\} dV. \quad (\text{IV.3.12})$$

A detailed calculation of the first and second derivatives of the energy density \widetilde{W}_M is given in Appendix IV.B.1.

The main difference with Section IV.2.3 lies in the fact that we need to compute \mathbf{M} in addition to \mathbf{u} and $\widetilde{\mathbf{A}}$. In the following, we set the magnetization vector \mathbf{M} constant per element. Furthermore, the magnetization does not need to satisfy any continuity condition between connecting elements and thus a static condensation argument can be used to eliminate all degrees of freedom associated with \mathbf{M} (i.e. the magnetization in each element is not coupled

to the magnetization in neighboring elements). It implies that, $\forall \mathbf{X} \in V_e$

$$\begin{aligned} \delta \widetilde{W}_M|_M &= \frac{\partial \widetilde{W}_M}{\partial \mathbf{M}} \cdot [\delta \mathbf{M}] + [\Delta \mathbf{q}_e]^T \cdot \begin{bmatrix} \frac{\partial^2 \widetilde{W}_M}{\partial \mathbf{F} \partial \mathbf{M}} \\ \frac{\partial^2 \widetilde{W}_M}{\partial \widetilde{\mathbf{B}} \partial \mathbf{M}} \\ \frac{\partial^2 \widetilde{W}_M}{\partial \mathbf{M} \partial \mathbf{M}} \end{bmatrix} \cdot [\delta \mathbf{M}] \\ &= \left(\frac{\partial \widetilde{W}_M}{\partial \mathbf{M}} + \Delta \mathbf{F} \cdot \frac{\partial^2 \widetilde{W}_M}{\partial \mathbf{F} \partial \mathbf{M}} + \Delta \widetilde{\mathbf{B}} \cdot \frac{\partial^2 \widetilde{W}_M}{\partial \widetilde{\mathbf{B}} \partial \mathbf{M}} + \Delta \mathbf{M} \cdot \frac{\partial^2 \widetilde{W}_M}{\partial \mathbf{M} \partial \mathbf{M}} \right) \cdot \delta \mathbf{M} = 0. \end{aligned} \quad (\text{IV.3.13})$$

In view of the arbitrariness of $\delta \mathbf{M}$, we can conclude that

$$\Delta \mathbf{M} = - \left\{ \frac{\partial \widetilde{W}_M}{\partial \mathbf{M}} + \Delta \mathbf{F} \cdot \frac{\partial^2 \widetilde{W}_M}{\partial \mathbf{F} \partial \mathbf{M}} + \Delta \widetilde{\mathbf{B}} \cdot \frac{\partial^2 \widetilde{W}_M}{\partial \widetilde{\mathbf{B}} \partial \mathbf{M}} \right\} \cdot \left(\frac{\partial^2 \widetilde{W}_M}{\partial \mathbf{M} \partial \mathbf{M}} \right)^{-1}. \quad (\text{IV.3.14})$$

At this stage by rearranging the terms, one can easily obtain the condensed form of the element force vector and the element stiffness matrix by defining first the new element vector of unknowns

$$\mathbf{q}_e = [\mathbf{u}; \widetilde{\mathbf{A}}]. \quad (\text{IV.3.15})$$

Then, using Eq. (IV.3.1) and Eq. (IV.3.10) together with Eq. (IV.3.14), one gets

$$\begin{aligned} \mathbf{f}_e &= \int_{V_e} \left\{ \left[\frac{\partial \widetilde{W}_M}{\partial \mathbf{F}}, \frac{\partial \widetilde{W}_M}{\partial \widetilde{\mathbf{B}}} \right] - \frac{\partial \widetilde{W}_M}{\partial \mathbf{M}} \cdot \left[\frac{\partial^2 \widetilde{W}_M}{\partial \mathbf{M} \partial \mathbf{M}} \right]^{-1} \cdot \left[\frac{\partial^2 \widetilde{W}_M}{\partial \mathbf{M} \partial \mathbf{F}}, \frac{\partial^2 \widetilde{W}_M}{\partial \mathbf{M} \partial \widetilde{\mathbf{B}}} \right] \right\} \cdot \begin{bmatrix} \mathbf{G}_u \\ \mathbf{G}_{\widetilde{\mathbf{A}}} \end{bmatrix} dV + \\ &\quad \frac{1}{\mu_0 \kappa} \int_{V_e} (\nabla \cdot \widetilde{\mathbf{A}}) \mathbf{D}_{\widetilde{\mathbf{A}}}^T dV - \int_{V_e \cap \mathcal{D}} \rho_0 [\mathbf{f}] \cdot [\mathbf{N}_u] dV - \int_{\partial V_e \cap \partial \mathcal{D}} [\mathbf{T}] \cdot [\mathbf{N}_u] dS, \end{aligned} \quad (\text{IV.3.16})$$

where the definition of $\mathbf{D}_{\widetilde{\mathbf{A}}}$ has been adjusted to the new definition of \mathbf{q}_e given in Eq. (IV.3.15), so that we still have

$$\nabla \cdot \delta \widetilde{\mathbf{A}} = \mathbf{D}_{\widetilde{\mathbf{A}}}^T \cdot \delta \mathbf{q}_e. \quad (\text{IV.3.17})$$

For the condensed stiffness matrix, based on Eq. (IV.3.12) we obtain

$$\begin{aligned} \mathbf{k}_e &= \int_{V_e} \begin{bmatrix} \mathbf{G}_u^T & \mathbf{G}_{\widetilde{\mathbf{A}}}^T \end{bmatrix} \cdot \left\{ \begin{bmatrix} \frac{\partial^2 \widetilde{W}_M}{\partial \mathbf{F} \partial \mathbf{F}} & \frac{\partial^2 \widetilde{W}_M}{\partial \mathbf{F} \partial \widetilde{\mathbf{B}}} \\ \frac{\partial^2 \widetilde{W}_M}{\partial \widetilde{\mathbf{B}} \partial \mathbf{F}} & \frac{\partial^2 \widetilde{W}_M}{\partial \widetilde{\mathbf{B}} \partial \widetilde{\mathbf{B}}} \end{bmatrix} - \begin{bmatrix} \frac{\partial^2 \widetilde{W}_M}{\partial \mathbf{F} \partial \mathbf{M}} \\ \frac{\partial^2 \widetilde{W}_M}{\partial \widetilde{\mathbf{B}} \partial \mathbf{M}} \end{bmatrix} \cdot \left[\frac{\partial^2 \widetilde{W}_M}{\partial \mathbf{M} \partial \mathbf{M}} \right]^{-1} \cdot \begin{bmatrix} \frac{\partial^2 \widetilde{W}_M}{\partial \mathbf{M} \partial \mathbf{F}} & \frac{\partial^2 \widetilde{W}_M}{\partial \mathbf{M} \partial \widetilde{\mathbf{B}}} \end{bmatrix} \right\} \cdot \begin{bmatrix} \mathbf{G}_u \\ \mathbf{G}_{\widetilde{\mathbf{A}}} \end{bmatrix} dV + \\ &\quad + \frac{1}{\mu_0 \kappa} \int_{V_e} \mathbf{D}_{\widetilde{\mathbf{A}}} \mathbf{D}_{\widetilde{\mathbf{A}}}^T dV. \end{aligned} \quad (\text{IV.3.18})$$

For the interested reader, the practical procedure to implement the above discretization in an ABAQUS user element (UEL) is explained in Appendix IV.B.2.

IV.4 Solving a boundary value problem

The purpose of this section is to briefly recall the main results that have been derived (in details) in Section III.4 in terms of boundary and symmetry conditions to apply when it comes to solving a MRE boundary value problem.

IV.4.1 Boundary conditions

If we consider a simulated system of volume V and boundary ∂V , in terms of boundary conditions only the components of $\tilde{\mathbf{A}}$ that are tangential to ∂V need to be prescribed to uniquely define the magnetic vector potential in the entire domain V . In practice, on the particular case of Fig. IV.1, if we simulate a region of surrounding air sufficiently large compared to the dimensions of the magnetoelastic solid, and since we know that the influence of the solid on the external magnetic field vanishes far from its boundaries, we can reasonably impose the following boundary conditions on the faces ‘Top’, ‘Right’ and ‘Front’⁶

$$\begin{cases} \mathbf{u} = \mathbf{0}, \\ \mathbf{N} \times \tilde{\mathbf{A}} = \mathbf{0}. \end{cases} \quad (\text{IV.4.1})$$

IV.4.2 Symmetry conditions for the perturbed magnetic vector potential $\tilde{\mathbf{A}}$

For some problems in which the geometry presents some symmetries and where the applied field keep these symmetries, we can reduce the size of the model (to minimize the computational resources and time needed to solve it) by applying proper symmetry conditions.

As it has been recalled in Section III.4.3, the pseudovector $\tilde{\mathbf{B}}$ is expressed as the curl of the polar vector $\tilde{\mathbf{A}}$ and hence these vectors have opposite symmetry properties. In what follows, we explain what it implies on the particular case of a magnetoelastic sphere subjected to a unidirectional external magnetic field that is applied far from its boundaries (see Fig. IV.1).

⁶ NOTE: Careful on Fig. IV.1, the boundary conditions of Eq. IV.4.1 must not be applied on the symmetry planes ‘Bottom’, ‘Left’ and ‘Back’.

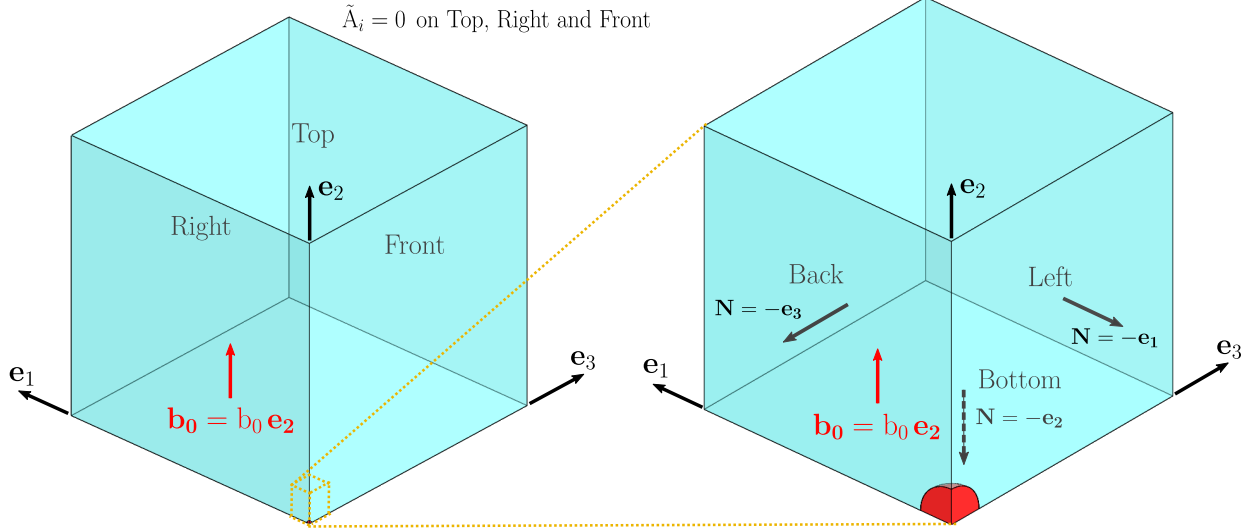


Figure IV.1: Schematic of the boundary value problem of a magnetoelastic sphere subjected to an externally applied magnetic field \mathbf{b}_0 far from its boundaries. The figure on the right shows the entire system with the surrounding air. The picture on the left is a zoom in that presents the symmetry planes of the problem.

As we can see on the schematics in Fig. IV.1, there are three remarkable planes (about which the geometry is exactly mirrored). This is the reason why only one-eighth of the problem is shown in this figure. Due to the external magnetic field \mathbf{b}_0 being applied along the vertical direction⁷ \mathbf{e}_2 , we can see that the plane of normal \mathbf{e}_2 named ‘Bottom’ (see Fig. IV.1) is a plane of anti-symmetry whereas the planes of normal \mathbf{e}_1 and \mathbf{e}_3 that are named ‘Left’ and ‘Back’ are symmetry planes of the perturbed magnetic field $\tilde{\mathbf{B}}$. Hence, the perturbed magnetic field verifies the following symmetry properties whereas the ones verified by $\tilde{\mathbf{A}}$ are opposite (anti-symmetry properties)

$$\left\{ \begin{array}{l} \tilde{B}_1(X_1, X_2, X_3) = -\tilde{B}_1(-X_1, X_2, X_3), \\ \tilde{B}_1(X_1, X_2, X_3) = -\tilde{B}_1(X_1, -X_2, X_3), \\ \tilde{B}_1(X_1, X_2, X_3) = \tilde{B}_1(X_1, X_2, -X_3), \\ \tilde{B}_2(X_1, X_2, X_3) = \tilde{B}_2(-X_1, X_2, X_3), \\ \tilde{B}_2(X_1, X_2, X_3) = \tilde{B}_2(X_1, -X_2, X_3), \\ \tilde{B}_2(X_1, X_2, X_3) = \tilde{B}_2(X_1, X_2, -X_3), \\ \tilde{B}_3(X_1, X_2, X_3) = \tilde{B}_3(-X_1, X_2, X_3), \\ \tilde{B}_3(X_1, X_2, X_3) = -\tilde{B}_3(X_1, -X_2, X_3), \\ \tilde{B}_3(X_1, X_2, X_3) = -\tilde{B}_3(X_1, X_2, -X_3), \end{array} \right. \Rightarrow \left\{ \begin{array}{l} \tilde{A}_1(X_1, X_2, X_3) = \tilde{A}_1(-X_1, X_2, X_3), \\ \tilde{A}_1(X_1, X_2, X_3) = \tilde{A}_1(X_1, -X_2, X_3), \\ \tilde{A}_1(X_1, X_2, X_3) = -\tilde{A}_1(X_1, X_2, -X_3), \\ \tilde{A}_2(X_1, X_2, X_3) = -\tilde{A}_2(-X_1, X_2, X_3), \\ \tilde{A}_2(X_1, X_2, X_3) = -\tilde{A}_2(X_1, -X_2, X_3), \\ \tilde{A}_2(X_1, X_2, X_3) = -\tilde{A}_2(X_1, X_2, -X_3), \\ \tilde{A}_3(X_1, X_2, X_3) = -\tilde{A}_3(-X_1, X_2, X_3), \\ \tilde{A}_3(X_1, X_2, X_3) = \tilde{A}_3(X_1, -X_2, X_3), \\ \tilde{A}_3(X_1, X_2, X_3) = \tilde{A}_3(X_1, X_2, -X_3). \end{array} \right. \quad (\text{IV.4.2})$$

⁷ NOTE: The direction of the externally applied magnetic field dictates the nature of the geometry’s symmetry planes.

From Eq. (IV.4.2), we can deduce the boundary conditions to apply on the symmetry planes ‘Bottom’, ‘Left’ and ‘Back’.

The Dirichlet boundary conditions read

$$\begin{cases} \tilde{A}_2 = \tilde{A}_3 = 0, & \forall \mathbf{X} = (0, X_2, X_3) \in \text{‘Left’}, \\ \tilde{A}_2 = 0, & \forall \mathbf{X} = (X_1, 0, X_3) \in \text{‘Bottom’}, \\ \tilde{A}_1 = \tilde{A}_2 = 0, & \forall \mathbf{X} = (X_1, X_2, 0) \in \text{‘Back’}. \end{cases} \quad (\text{IV.4.3})$$

As for the Neumann boundary conditions, as mentioned in Section III.4.3, they are automatically verified.

Based on the fact that only the tangential components of $\tilde{\mathbf{A}}$ need to be applied on ∂V , it is not necessary to impose the first relation of Eq. (IV.4.3) (i.e. $\tilde{A}_2(X_1, 0, X_3) = 0$).

IV.5 Code testing

As for any numerical method, a finite element code has to be tested on some problems (called ‘patch tests’) having an analytical solution, to make sure that these results can be reproduced numerically. Even if passing different patch tests is neither sufficient nor necessary to prove convergence, it is still a good indicator of the quality of a code. In the case of magneto-mechanical problems, except for some trivial situations, exact solutions cannot generally be derived due to strong non-linearities in the governing equations and non-uniformities in both mechanical and magnetic fields.

In this section, we show the patch tests chosen to validate both our numerical implementations. In the first part, we consider a purely mechanical tensile test. The second part focuses on a purely magnetic problem in which the deformation of the solid is not allowed (rigid body). In the third part, we solve the coupled magneto-mechanical problem in an infinite media. The last part presents a more complex patch test whose analytical solution is not known. However, this problem can be solved by another finite element code (that has already been checked for convergence) which relies on the **F-H** theory that uses a magnetic scalar potential instead of a magnetic vector potential.

For the sake of not showing twice the same curves for each patch test, we will in what follows only plot the numerical solutions obtained with the **F-B** code. Indeed, both numerical codes (**F-B** and **F-M**) yield the same solutions provided the fact that the energy densities $\tilde{W}_B(\mathbf{F}, \tilde{\mathbf{B}})$ and $\tilde{W}_M(\mathbf{F}, \tilde{\mathbf{B}}, \mathbf{M})$ are equal (for more details about the equivalence of the different formulations see Section III.3.3).

IV.5.1 Purely mechanical patch test

The first problem considered is a purely uniaxial tensile test on a parallelepiped in which the axial displacement is controlled (i.e λ_2 is controlled, see Fig IV.2a) and where the solid is stress free in the directions transverse to the applied load. Based on the governing equations provided in Section III.3.2.a, the analytical solution of this problem is given by

$$\mathbf{T} = \rho_0 \frac{\partial \psi_B}{\partial \mathbf{F}} \cdot \mathbf{N}, \quad (\text{IV.5.1})$$

where \mathbf{T} is the nominal traction and \mathbf{N} is the outward normal in the undeformed reference configuration. In the case of the parallelepiped, the principal axes of the deformation gradient \mathbf{F} are aligned with the principal axis of the material. Therefore, there are three independent equations of static equilibrium in the reference normal directions $\mathbf{N}_k = \mathbf{e}_k$ ($k = 1, 2, 3$), deduced from Eq. (IV.5.1)

$$\begin{cases} T_1 = 0 = \rho_0 \left(2 \lambda_1 \frac{\partial \psi_B}{\partial I_1} + \frac{J}{\lambda_1} \frac{\partial \psi_B}{\partial I_3} \right), \\ T_2 = \rho_0 \left(2 \lambda_2 \frac{\partial \psi_B}{\partial I_1} + \frac{J}{\lambda_2} \frac{\partial \psi_B}{\partial I_3} \right), \\ T_3 = 0 = \rho_0 \left(2 \lambda_3 \frac{\partial \psi_B}{\partial I_1} + \frac{J}{\lambda_3} \frac{\partial \psi_B}{\partial I_3} \right), \end{cases} \quad (\text{IV.5.2})$$

where λ_i are the principal stretch ratios. The Helmholtz free energy used takes the following form

$$\rho_0 \psi_B(\mathbf{F}) = \rho_0 \psi_{mech}(\mathbf{F}) = \sum_{i=1}^2 \frac{3^{1-\alpha_i}}{2\alpha_i} \mu_i [(I_1 - \ln I_3)^{\alpha_i} - 3^{\alpha_i}] + \frac{G'}{2} (\sqrt{I_3} - 1)^2, \quad (\text{IV.5.3})$$

where α_i , μ_i and G' are material parameters and where the invariants I_k are defined in Eq. (IV.2.6). The expression of ψ_{mech} (i.e. the mechanical part of the Helmholtz free energy) is a generalization for compressible materials of a hyperelastic model well suited for rubber materials that has been proposed by Lopez-Pamies [103].

If we solve the system of equations (IV.5.2) with the following material constants

μ_1 [MPa]	α_1 [-]	μ_2 [MPa]	α_2 [-]	G' [MPa]
$1.5954 \cdot 10^{-2}$	1	$3.688 \cdot 10^{-3}$	1	$125(\mu_1 + \mu_2)$

we end up with the plots of Fig. IV.2.

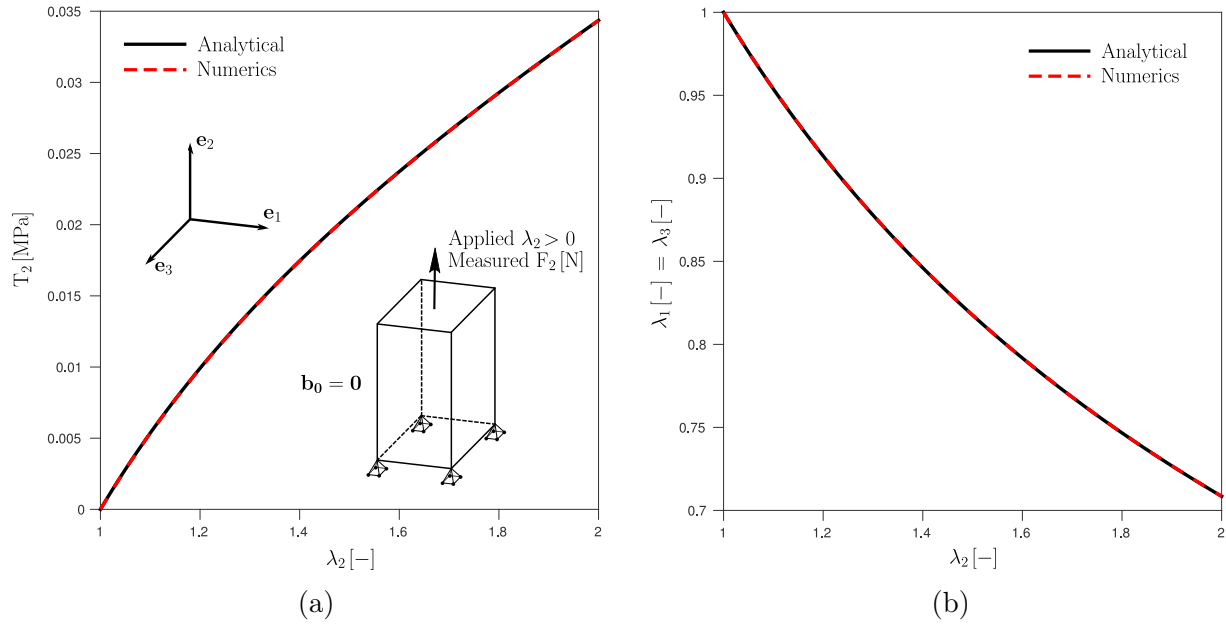


Figure IV.2: Numerical simulation of a purely mechanical test in which the axial displacement is controlled (i.e λ_2 is controlled) and where the solid is stress free in the directions transverse to the applied load. The nominal traction T_2 - stretch ratio λ_2 curve in a uniaxial test is shown in (a), and the lateral stretch ratios λ_1 , λ_3 appear in (b). Notice the excellent agreement between the numerical and analytical solutions.

We notice that there is an excellent agreement between the analytical and numerical solutions. As a result, we conclude that our code provides a valid solution to this problem.

IV.5.2 Purely magnetic patch test

The second step in testing the codes still doesn't involve any magneto-mechanical coupling. In this section, as one can see in Fig. IV.3, we consider a rigid infinite magnetic cylinder subjected to an external magnetic field \mathbf{b}_0 applied far from its boundaries in a direction perpendicular to its axis.

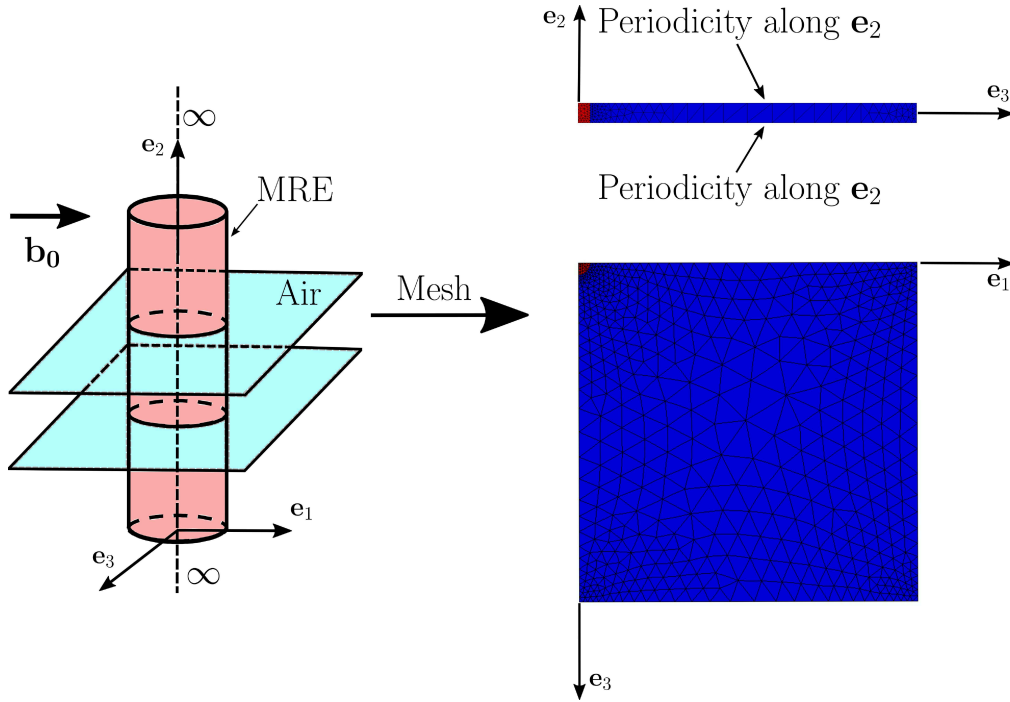


Figure IV.3: Schematic of a rigid infinite magnetic cylinder submitted to an externally applied magnetic field \mathbf{b}_0 far from its boundaries. The picture on the right shows the entire system with the surrounding air. In the picture on the left, we present the mesh used for numerical calculations and we indicate where periodicity conditions are applied.

The analytical solution to this boundary value problem doesn't depend on the coordinate along the \mathbf{e}_2 direction since the cylinder is infinite in that direction and hence it is equivalent to solving a two-dimensional magnetic disk subjected to the same loading. For the interested reader, a detailed derivation of the analytical solution based on the Laplace's equation governing the \mathbf{h} -field outside the specimen is provided in the Appendix of Bodelot [14]. Inside the specimen, the Eulerian magnetic field \mathbf{b} and the Eulerian magnetic intensity \mathbf{h} are uniform and read

$$\begin{cases} \mathbf{h}_{in} = \frac{2}{\mu_0 (2 + \chi)} \mathbf{b}_0, \\ \mathbf{b}_{in} = \mu_0 (1 + \chi) \mathbf{h}_{in} = \frac{2(1 + \chi)}{2 + \chi} \mathbf{b}_0, \end{cases} \quad (\text{IV.5.4})$$

where χ is the initial magnetic susceptibility of the material. As one can notice from Eq. (IV.5.4), we choose a linear magnetic law such that the magnetization per unit volume \mathbf{m}

(not to confuse with the magnetization per unit mass $\mathbf{M} = \mathbf{m}/\rho$) inside the material is given by $\mathbf{m} = \chi \mathbf{h}$.

Outside the specimen, for material points $\mathbf{X}(x, y, z)$ located along the principal axis \mathbf{e}_1 and \mathbf{e}_3 , \mathbf{b} and \mathbf{h} are given by

$$\left\{ \begin{array}{l} \mathbf{h}(x, y, 0) = h_1(x, y, 0)\mathbf{e}_1 = \frac{\|\mathbf{b}_0\|}{\mu_0} \left(1 + \frac{\chi}{(2+\chi)} \left(\frac{r}{x}\right)^2\right) \mathbf{e}_1, \quad \forall x > r, \\ \mathbf{b}(x, y, 0) = b_1(x, y, 0)\mathbf{e}_1 = \mu_0 \mathbf{h}(x, y, 0) = \|\mathbf{b}_0\| \left(1 + \frac{\chi}{(2+\chi)} \left(\frac{r}{x}\right)^2\right) \mathbf{e}_1, \quad \forall x > r, \\ \mathbf{h}(0, y, z) = h_1(0, y, z)\mathbf{e}_1 = \frac{\|\mathbf{b}_0\|}{\mu_0} \left(1 - \frac{\chi}{(2+\chi)} \left(\frac{r}{z}\right)^2\right) \mathbf{e}_1, \quad \forall z > r, \\ \mathbf{b}(0, y, z) = b_1(0, y, z)\mathbf{e}_1 = \mu_0 \mathbf{h}(0, y, z) = \|\mathbf{b}_0\| \left(1 - \frac{\chi}{(2+\chi)} \left(\frac{r}{z}\right)^2\right) \mathbf{e}_1, \quad \forall z > r, \end{array} \right. \quad (\text{IV.5.5})$$

where r is the radius of the cylinder. Based on Eq. (IV.5.5) and (IV.5.4), it is interesting to note that the normal component of \mathbf{b} (resp. the tangential component of \mathbf{b}) and the tangential component of \mathbf{h} (resp. the normal component of \mathbf{h}) are continuous (resp. discontinuous) at the interface between the magnetic cylinder and the surrounding air (i.e. $\|\mathbf{X}\| = r$), as impose by the interface conditions mentionned in Section III.3.1 (i.e. $\mathbf{n} \cdot \llbracket \mathbf{b} \rrbracket = 0$ and $\mathbf{n} \times \llbracket \mathbf{h} \rrbracket = \mathbf{0}$, $\forall \mathbf{X} \in \partial v$).

Numerically, as one can see in Fig. IV.3, we simulate only a small portion of the problem. Indeed, we first impose periodicity conditions along the \mathbf{e}_2 direction. Secondly, we use the symetries of the problem and as stated in Section IV.4.2, we impose symetry conditions that read in this case

$$\tilde{\mathbf{A}}_1 = \tilde{\mathbf{A}}_2 = 0, \quad \forall \mathbf{X} = (X_1, X_2, 0) \in \text{symetry plane of normal } \mathbf{e}_3. \quad (\text{IV.5.6})$$

And since the influence of the solid vanishes, we need to impose $\tilde{\mathbf{A}} = \mathbf{0}$ far from its boundaries.

In terms of the Helmholtz free energy, we consider the following form (where $I_6^B = \mathbf{B} \cdot \mathbf{C} \cdot \mathbf{B}$)

$$\rho_0 \psi_B(\mathbf{F} = \mathbf{I}, \tilde{\mathbf{B}} + J\mathbf{F}^{-1} \cdot \mathbf{b}_0) = \rho_0 \psi_B(\tilde{\mathbf{B}} + \mathbf{b}_0) = -\frac{\chi}{2\mu_0(1+\chi)} I_6^B, \quad (\text{IV.5.7})$$

which according to the governing equations (provided in Section III.3.2.a) provides a linear magnetic law

$$\begin{aligned} \mathbf{h} &= \mathbf{h}_0 + \tilde{\mathbf{h}} = \frac{1}{\mu_0} \mathbf{b}_0 + \left(\rho_0 \frac{\partial \psi_B}{\partial \tilde{\mathbf{B}}} + \frac{1}{\mu_0} \tilde{\mathbf{b}} \right) = \frac{1}{\mu_0} \mathbf{b} + \rho_0 \frac{\partial \psi_B}{\partial I_6^B} \frac{\partial I_6^B}{\partial \tilde{\mathbf{B}}} \\ &= \frac{1}{\mu_0} \mathbf{b} - \frac{\chi}{\mu_0(1+\chi)} (\tilde{\mathbf{b}} + \mathbf{b}_0) = \frac{1}{\mu_0(1+\chi)} \mathbf{b}, \\ \Rightarrow \mathbf{m} &= \frac{1}{\mu_0} \mathbf{b} - \mathbf{h} = \chi \mathbf{h}. \end{aligned} \quad (\text{IV.5.8})$$

Figure IV.4 shows the evolution of the manetic field \mathbf{b} and the magnetic intensity \mathbf{h} along the principal directions \mathbf{e}_1 and \mathbf{e}_3 for $\chi = 0.3$. As one can notice, there is an excellent agreement between the analytical and numerical solutions.

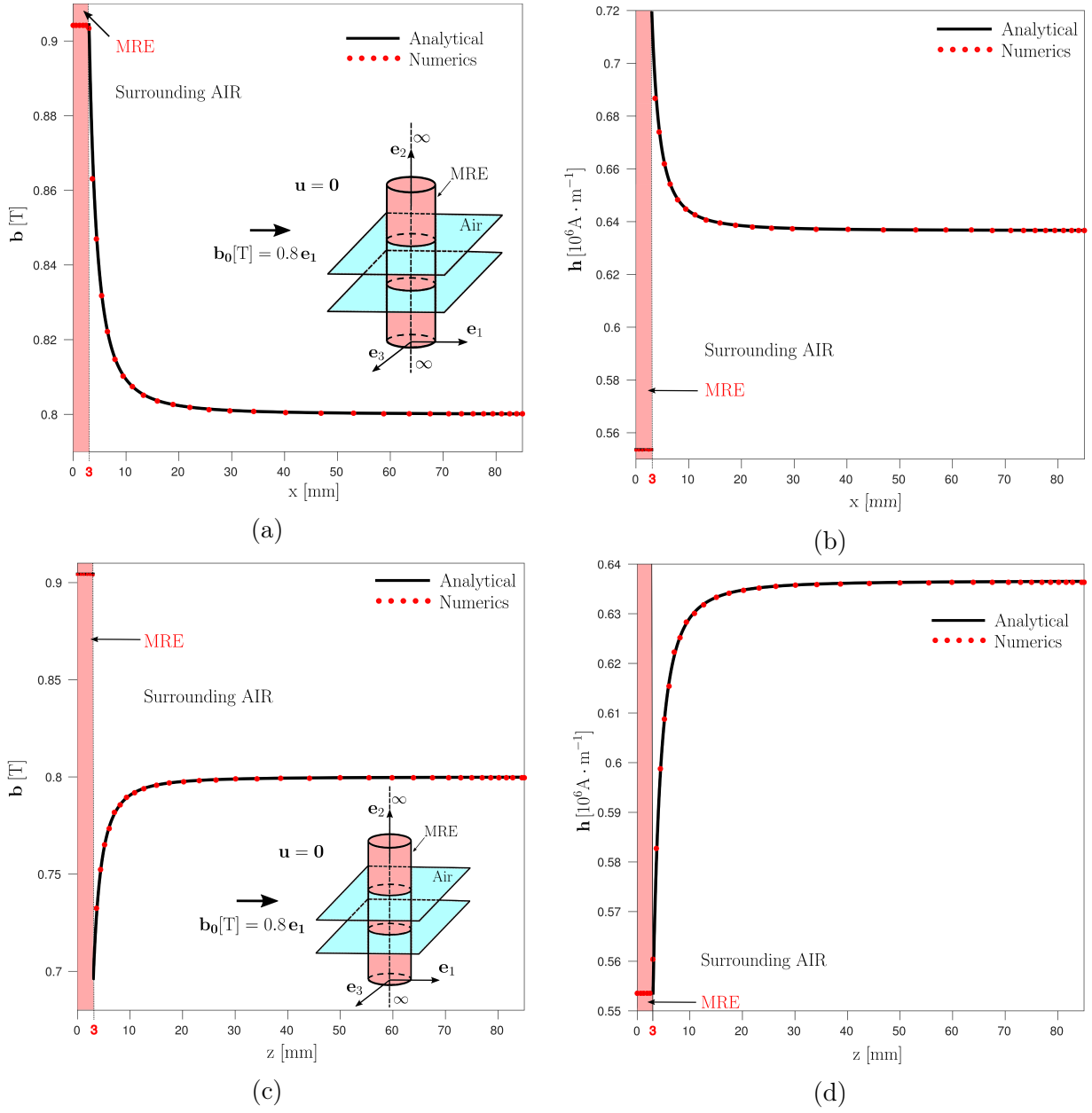


Figure IV.4: Plots of the magnetic field \mathbf{b} and magnetic intensity \mathbf{h} distributions in the case of an infinite rigid magnetic cylinder subjected to an external magnetic field \mathbf{b}_0 applied in the \mathbf{e}_1 direction (perpendicular to its axis). The spatial distribution of \mathbf{b} along a line passing through the axis of the cylinder and of direction \mathbf{e}_1 is presented in (a), and the distribution of the \mathbf{h} -field along that same path is shown in (b). The spatial distributions of \mathbf{b} and \mathbf{h} along direction \mathbf{e}_3 are shown in (c) and (d).

The finite element code relying on the \mathbf{F} - \mathbf{M} theory provides the same solution if the energy densities of the two formulations are equal (i.e. $\widetilde{W}_B(\mathbf{F}, \widetilde{\mathbf{B}}) = \widetilde{W}_M(\mathbf{F}, \widetilde{\mathbf{B}}, \mathbf{M})$) as suggested in

Section III.3.3. We obtain

$$\widetilde{W}_M(\mathbf{F} = \mathbf{I}, \widetilde{\mathbf{B}}, \mathbf{M}) = \frac{\mu_0 \rho_0^2}{2\chi} \mathbf{M} \cdot \mathbf{M} - \rho_0 \mathbf{M} \cdot \mathbf{b}_0 + \frac{1}{2\mu_0} \left\| \widetilde{\mathbf{B}} - \mu_0 \rho_0 \mathbf{M} \right\|^2. \quad (\text{IV.5.9})$$

According to Eq. (IV.3.2), we end up for the Helmholtz free energy with

$$\psi_M(\mathbf{F} = \mathbf{I}, \mathbf{M}) = \frac{\mu_0 \rho_0}{2\chi} \mathbf{M} \cdot \mathbf{M}. \quad (\text{IV.5.10})$$

IV.5.3 Coupled magneto-mechanical patch test on an infinite medium (uniform field case)

As a step further in testing the numerical implementations, we consider a coupled magneto-mechanical problem. We compute the magnetization and the principal stretch ratios of an infinite magnetoelastic media that is stress free and subjected to a uniform magnetic field \mathbf{b}_0 along the \mathbf{e}_2 direction.

According to Danas [39] (see precisely Eq. 3.11 and Eq. 3.21 of the paper), the governing equations that apply take the following form,

$$\begin{cases} \mathbf{m} = -\rho_0 \mathbf{F}^{-T} \cdot \frac{\partial \psi_B}{\partial \widetilde{\mathbf{B}}}(\mathbf{F}, \widetilde{\mathbf{B}} + J \mathbf{F}^{-1} \cdot \mathbf{b}_0), \\ \mathbf{T} = \rho_0 \left[\frac{\partial \psi_B}{\partial \mathbf{F}}(\mathbf{F}, \widetilde{\mathbf{B}} + J \mathbf{F}^{-1} \cdot \mathbf{b}_0) \right] \cdot \mathbf{N} - J \left(\mathbf{m} \cdot \widetilde{\mathbf{b}} \right) \mathbf{F}^{-T} \cdot \mathbf{N} + \\ J \left(\mathbf{m} \widetilde{\mathbf{b}} \right) \cdot \left(\mathbf{F}^{-T} \cdot \mathbf{N} \right). \end{cases} \quad (\text{IV.5.11})$$

In the present case, we impose a uniform magnetic field \mathbf{b}_0 (i.e. $\widetilde{\mathbf{b}} = \mathbf{0}$, $\mathbf{b} = \mathbf{b}_0$, $\forall \mathbf{X} \in V$) and the material is stress free in each principal directions. Hence the analytical solution to this problem is obtained by solving a system of equations composed of the magnetic equation (Eq. (IV.5.11a)) and three independent equations of static equilibrium in the reference normal directions $\mathbf{N}_k = \mathbf{e}_k$, $k = 1, 2, 3$, deduced from Eq. (IV.5.11b).

$$\begin{cases} \mathbf{m} = -2J\rho_0 \left[\frac{\partial \psi_B}{\partial I_6^B} + \lambda_2^2 \frac{\partial \psi_B}{\partial I_7^B} \right] \mathbf{b}_0, \\ \mathbf{T}_1 = 0 = \rho_0 \left[2\lambda_1 \frac{\partial \psi_B}{\partial I_1} + \frac{J}{\lambda_1} \frac{\partial \psi_B}{\partial I_3} + \frac{2J^2}{\lambda_1} \mathbf{b}_0^2 \left(\frac{\partial \psi_B}{\partial I_6^B} + \lambda_2^2 \frac{\partial \psi_B}{\partial I_7^B} \right) \right], \\ \mathbf{T}_2 = 0 = \rho_0 \left[2\lambda_2 \frac{\partial \psi_B}{\partial I_1} + \frac{J}{\lambda_2} \frac{\partial \psi_B}{\partial I_3} + \frac{2J^2}{\lambda_2} \mathbf{b}_0^2 \frac{\partial \psi_B}{\partial I_6^B} + 4J^2 \lambda_2 \mathbf{b}_0^2 \frac{\partial \psi_B}{\partial I_7^B} \right], \\ \mathbf{T}_3 = 0 = \rho_0 \left[2\lambda_3 \frac{\partial \psi_B}{\partial I_1} + \frac{J}{\lambda_3} \frac{\partial \psi_B}{\partial I_3} + \frac{2J^2}{\lambda_3} \mathbf{b}_0^2 \left(\frac{\partial \psi_B}{\partial I_6^B} + \lambda_2^2 \frac{\partial \psi_B}{\partial I_7^B} \right) \right]. \end{cases} \quad (\text{IV.5.12})$$

Numerically, we don't apply any traction and we simply set $\widetilde{\mathbf{A}} = \mathbf{0}$ everywhere in the material since we impose a uniform magnetic field $\mathbf{b} = \mathbf{b}_0$. Periodicity conditions are used in each principal directions to simulate an infinite media.

In terms of the Helmholtz free energy, we add the I_7^B invariant compared to the free energy that we used in the previous patch test

$$\begin{aligned} \rho_0 \psi_B(\mathbf{F}, \tilde{\mathbf{B}}) = & \sum_{i=1}^2 \frac{3^{1-\alpha_i}}{2\alpha_i} \mu_i [(I_1 - \ln I_3)^{\alpha_i} - 3^{\alpha_i}] + \frac{G'}{2} (\sqrt{I_3} - 1)^2 \\ & - C_6 \frac{\chi}{2\mu_0 J (1 + \chi)} I_6^B - (1 - C_6) \frac{\chi}{2\mu_0 J (1 + \chi)} I_7^B, \end{aligned} \quad (\text{IV.5.13})$$

where we choose $\chi = 0.3$ and $C_6 = 1.02$.

As one can notice in Fig. IV.5, there is an excellent agreement between the analytical and numerical solutions which indicates that the finite element code captures correctly the magneto-mechanical coupling.

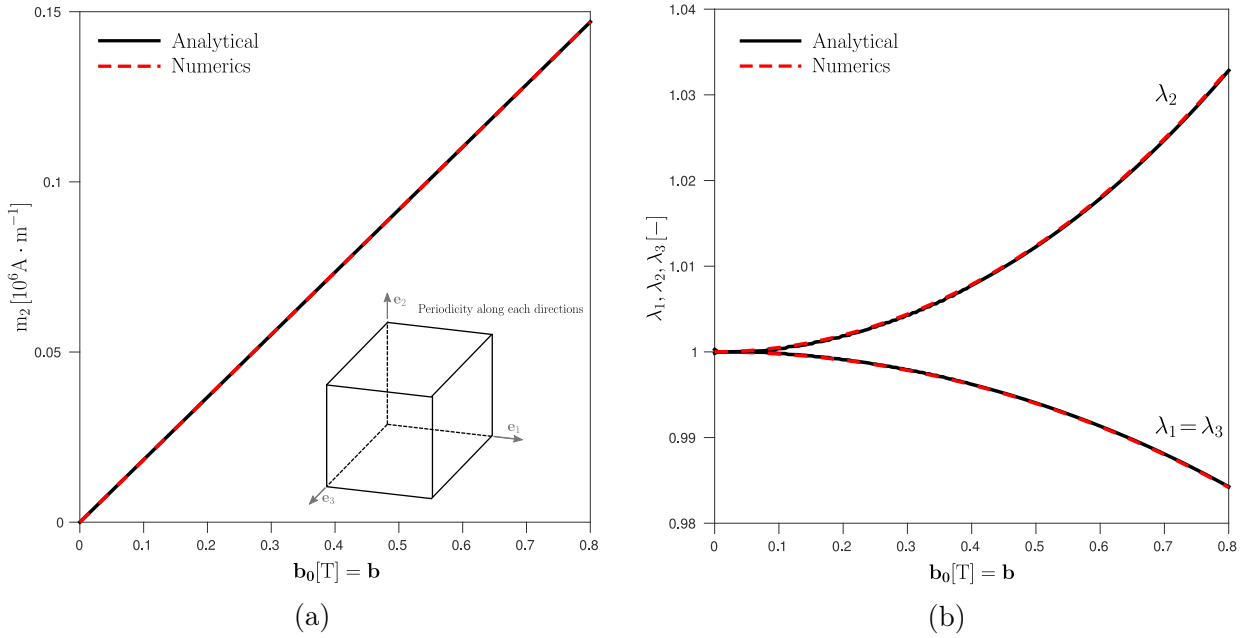


Figure IV.5: Numerical simulation of a coupled magneto-mechanical test in an infinite media. The magnetic response m_2 - b_0 is shown in (a) and the evolution of the principal stretch ratios λ_i is plotted in (b). Notice the very good agreement between the numerical and analytical solutions.

The code relying on the **F-M** theory can as well reproduce the analytical solution of that problem.

IV.5.4 Coupled magneto-mechanical patch test on a sphere (non-uniform field case)

The last boundary value problem chosen as a patch test is the case of a mechanically stress free magnetoelastic sphere subjected to an external magnetic field \mathbf{b}_0 applied far from its

boundaries that has been described in Section IV.4.2 (see Fig. IV.1). A part of the mesh used to simulate this problem is shown in Fig. IV.6.

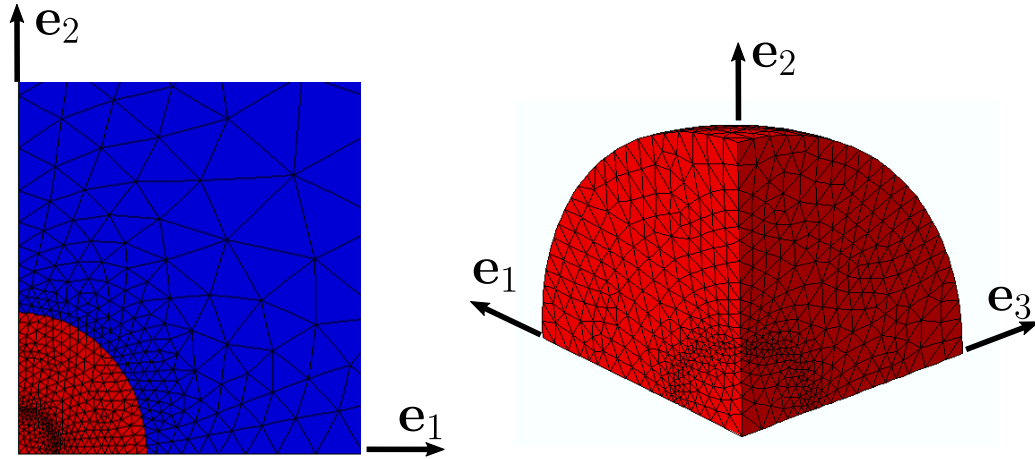


Figure IV.6: Mesh used to numerically solve the problem of a magneto-elastic sphere subjected to an externally applied magnetic field \mathbf{b}_0 far from its boundaries.

Such a boundary value problem doesn't have an explicit analytical solution and one can notice in Fig. IV.7 that neither the mechanical nor the magnetic quantities are uniform in the solid.

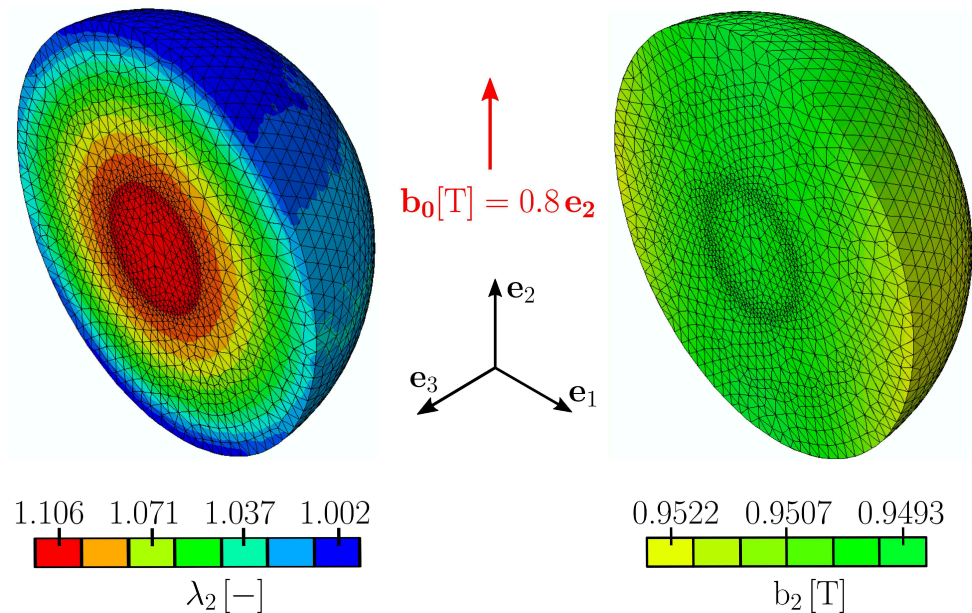


Figure IV.7: Numerical results for the magneto-elastic sphere. On the left, we notice a strong non-uniformity of the principal stretch ratio λ_2 along the direction of the applied field \mathbf{b}_0 . On the right, we see that the Eulerian magnetic field b_2 presents a small (almost negligible) non-uniformity.

To validate our code on such a complex problem, we use an existing finite element code relying on the \mathbf{F} - \mathbf{H} theory (which uses a magnetic scalar potential as explained in Section III.3.2.b). In order to compare the solutions given by the \mathbf{F} - \mathbf{B} and \mathbf{F} - \mathbf{H} codes, the energy densities used in both codes need to be linked by a partial Legendre's transform (i.e. $\widetilde{W}_H(\mathbf{F}, \widetilde{\mathbf{H}}) = \widetilde{W}_B(\mathbf{F}, \widetilde{\mathbf{B}}) - \widetilde{\mathbf{B}} \cdot \widetilde{\mathbf{H}}$) as it is explained in Section III.3.3. In the present case, we use $\widetilde{W}_B(\mathbf{F}, \widetilde{\mathbf{B}}) = \rho_0 \psi_B + 1/(2\mu_0 J) \widetilde{\mathbf{B}} \cdot \mathbf{C} \cdot \widetilde{\mathbf{B}}$ where

$$\rho_0 \psi_B(\mathbf{F}, \widetilde{\mathbf{B}} + J\mathbf{F}^{-1} \cdot \mathbf{b}_0) = \sum_{i=1}^2 \frac{3^{1-\alpha_i}}{2\alpha_i} \mu_i [(I_1 - \ln I_3)^{\alpha_i} - 3^{\alpha_i}] + \frac{G'}{2} (\sqrt{I_3} - 1)^2 - \frac{\chi}{2\mu_0 J (1 + \chi)} I_6^B, \quad (\text{IV.5.14})$$

which leads to $\widetilde{W}_H(\mathbf{F}, \widetilde{\mathbf{H}}) = \rho_0 \psi_H - (J\mu_0/2) \widetilde{\mathbf{H}} \cdot \mathbf{C}^{-1} \cdot \widetilde{\mathbf{H}}$ where

$$\rho_0 \psi_H(\mathbf{F}, \widetilde{\mathbf{H}} + \mathbf{F}^T \cdot \mathbf{h}_0) = \sum_{i=1}^2 \frac{3^{1-\alpha_i}}{2\alpha_i} \mu_i [(I_1 - \ln I_3)^{\alpha_i} - 3^{\alpha_i}] + \frac{G'}{2} (\sqrt{I_3} - 1)^2 - \frac{\mu_0 J \chi}{2} I_6^H, \quad (\text{IV.5.15})$$

with $I_6^H = \mathbf{h} \cdot \mathbf{h} = \mathbf{H} \cdot \mathbf{C}^{-1} \cdot \mathbf{H} = \mathbf{h}_0 \cdot \mathbf{h}_0 + 2\mathbf{h}_0 \cdot \mathbf{F}^{-T} \cdot \widetilde{\mathbf{H}} + \widetilde{\mathbf{H}} \cdot \mathbf{C}^{-1} \cdot \widetilde{\mathbf{H}}$.

Multiple figures are presented in this section to show that both codes provide the same solution. Figure IV.8 provides the deformed principal cross-sections of the sphere when we cut it with planes passing through the origin and of normal \mathbf{e}_k ($k = 1, 2, 3$).

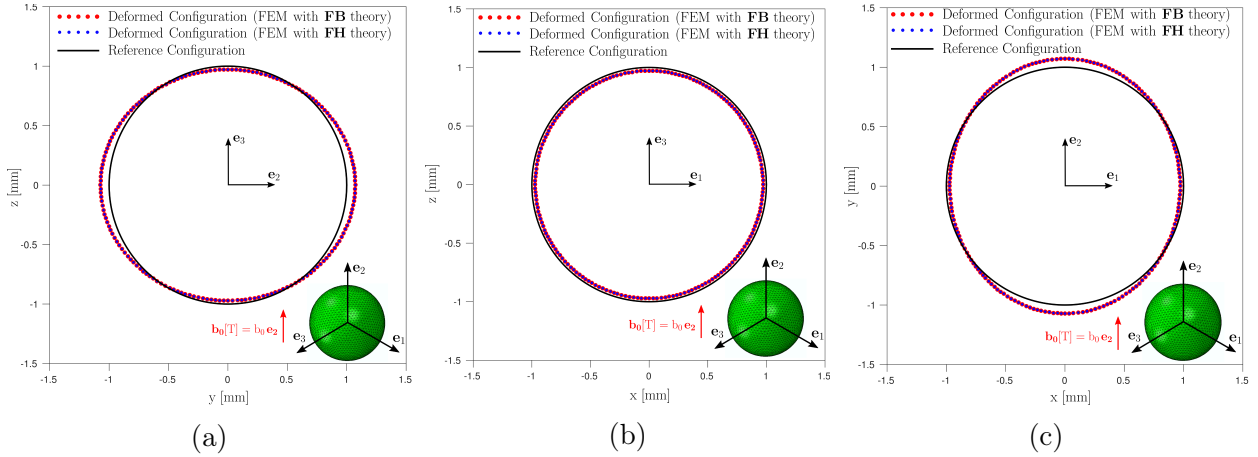


Figure IV.8: Deformed principal cross-sections of the sphere when we cut it with planes passing through the origin and of normal \mathbf{e}_k . The cross-section in (a) is obtained by cutting the sphere with a plane of normal \mathbf{e}_1 , the one in (b) by a plane of normal \mathbf{e}_2 and the one in (c) by a plane of normal \mathbf{e}_3 .

Figure IV.9 shows the evolution of the average (in the sphere) of the second component of the magnetic field b_2 and magnetization vector m_2 as well as the average of the principal stretch ratios λ_i with respect to the loading parameter b_0 .

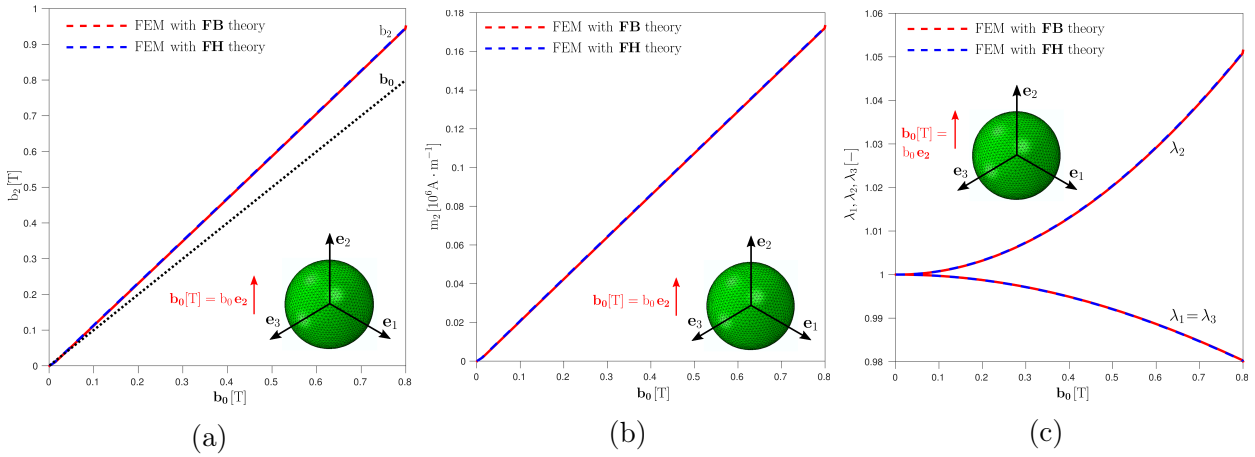


Figure IV.9: Averaged quantities computed based on the numerical simulation of the sphere. The evolution of the averaged magnetic field b_2 with respect to the applied field b_0 is shown in (a) and the magnetic response m_2 - b_0 is presented in (b). The evolution of the averaged principal stretch ratios λ_i is plotted in (c). We notice an excellent agreement between the numerical results of the **F-B** and **F-H** codes.

Figures IV.10 and IV.11 present the spatial evolution of the magnetic variables b_2 and m_2 , and the spatial evolution of the principal stretch ratios λ_i and principal components of the first Piola-Kirchhoff stress tensor \mathbf{S} , in the \mathbf{e}_2 direction (the path is parallel to the applied magnetic field \mathbf{b}_0).

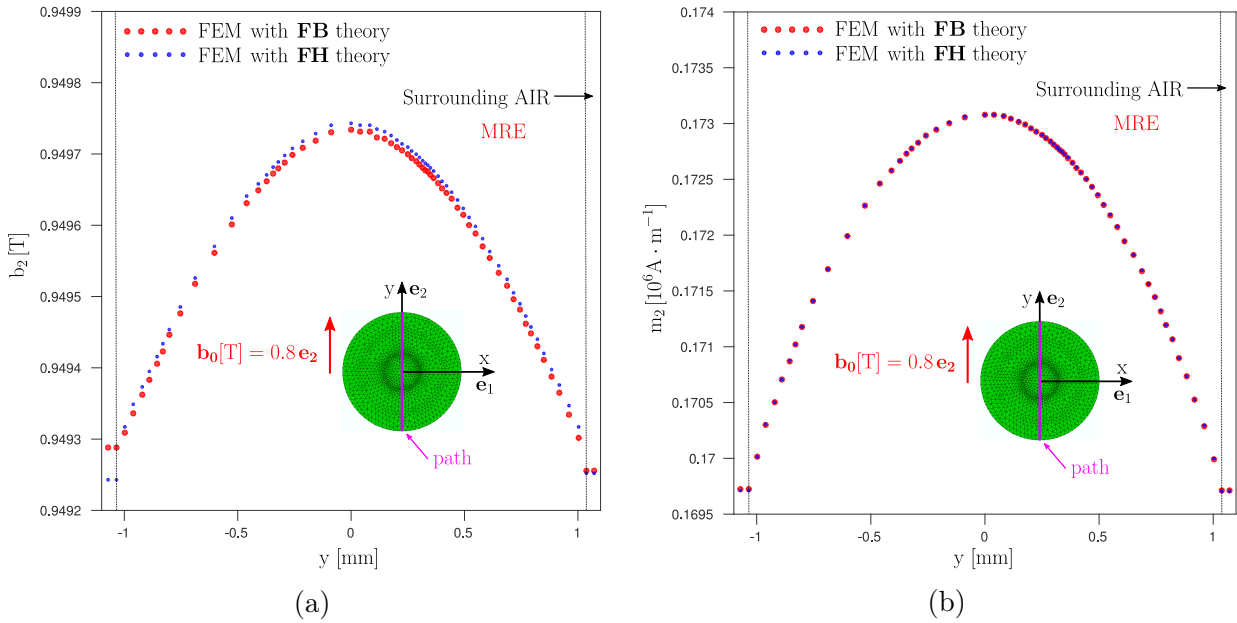


Figure IV.10: Spatial distribution of the magnetic field b_2 in (a) and the magnetization m_2 in (b), along a path passing through the origin and of direction \mathbf{e}_2 (parallel to the applied field \mathbf{b}_0).

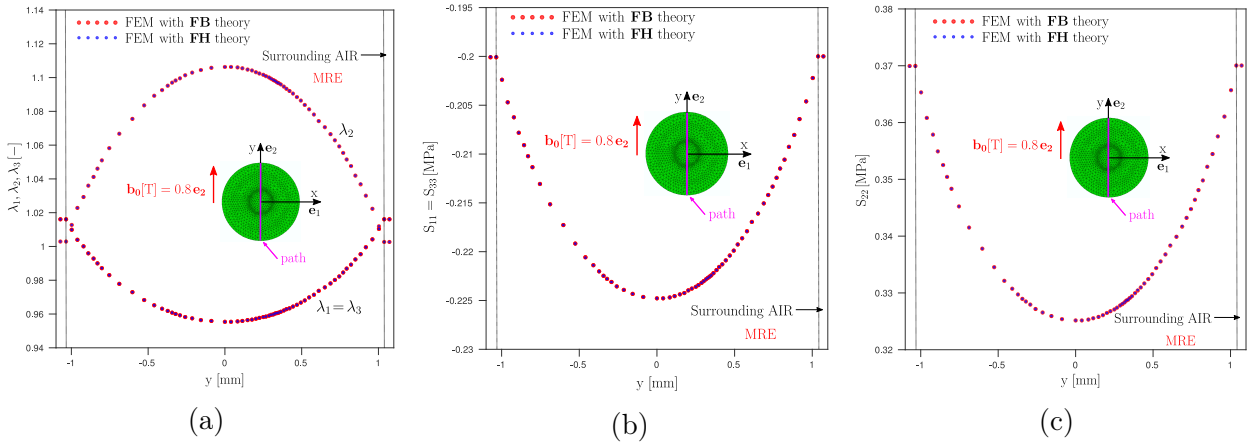


Figure IV.11: Spatial distribution of the principal stretch ratios λ_i in (a), of the components S_{11} and S_{33} of the first Piola-Kirchhoff stress tensor in (b), and of S_{22} in (c), along a path passing through the origin of the sphere and of direction \mathbf{e}_2 (parallel to the applied field \mathbf{b}_0).

As for Fig. IV.12 and IV.13, they provide the same type of results as Fig. IV.10 and IV.11 for material points located on the \mathbf{e}_1 axis (the path is perpendicular to \mathbf{b}_0).

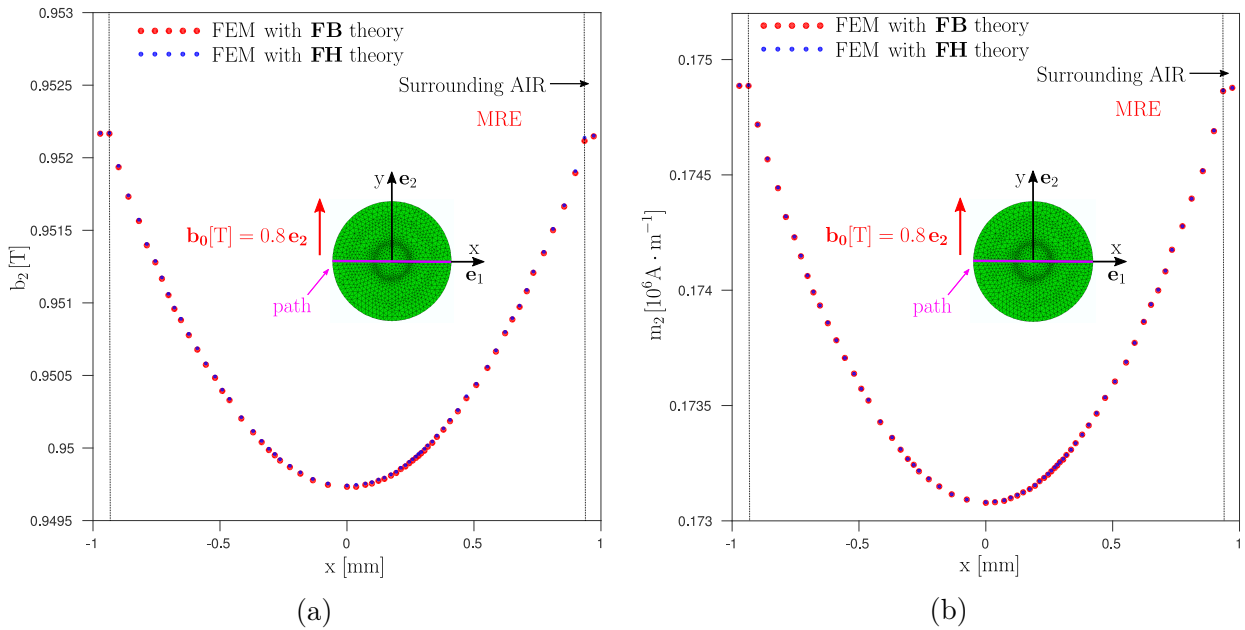


Figure IV.12: Spatial distribution of the magnetic field b_2 in (a) and the magnetization m_2 in (b), along a path passing through the origin and of direction \mathbf{e}_1 (perpendicular to the applied field \mathbf{b}_0).

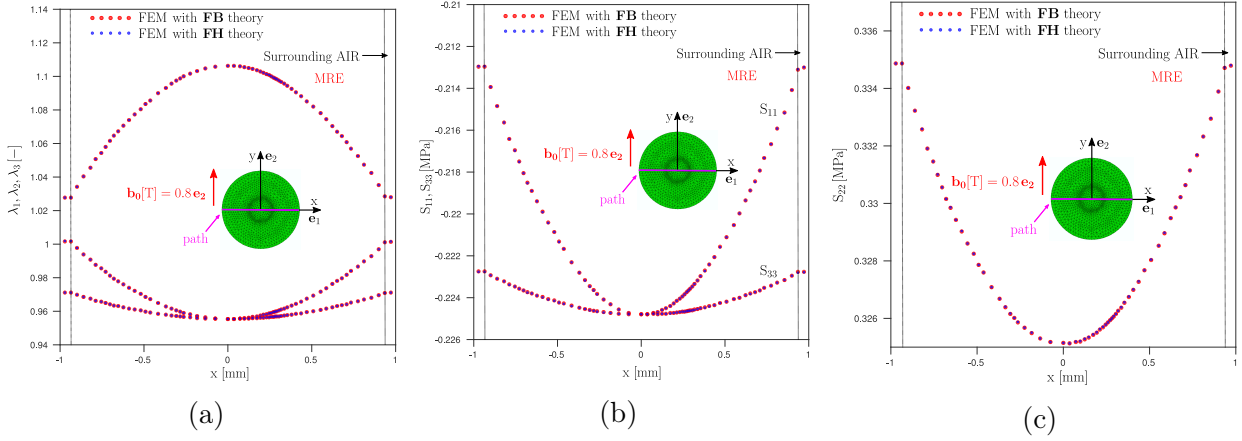


Figure IV.13: Spatial distribution of the principal stretch ratios λ_i in (a), of the components S_{11} and S_{33} of the first Piola-Kirchhoff stress tensor in (b), and of S_{22} in (c), along a path passing through the origin of the sphere and of direction \mathbf{e}_1 (perpendicular to the applied field \mathbf{b}_0).

As we can notice, for each of these plots, the **F-B** and **F-H** codes present a very good agreement. We can conclude that the **F-B** code passes this last patch test.

Once again, the **F-M** code provides the same solution if and only if the Helmholtz free energies ψ_M and ψ_H are linked by a partial Legendre's transform (i.e $\psi_H(\mathbf{F}, \tilde{\mathbf{H}} + \mathbf{F}^T \cdot \mathbf{h}_0) = \psi_M(\mathbf{F}, \mathbf{M}) - \mu_0 \mathbf{M} \cdot \mathbf{h}$) as explained in Section III.3.3. In the present case, to correspond to the energy density used in Eq. (IV.5.15), \tilde{W}_M is given by

$$\tilde{W}_M(\mathbf{F}, \tilde{\mathbf{B}}, \mathbf{M}) = \rho_0 [\psi_M(\mathbf{F}, \mathbf{M}) - \mathbf{M} \cdot \mathbf{b}_0] + \frac{1}{2\mu_0 J} \left\| \mathbf{F} \cdot \tilde{\mathbf{B}} - \mu_0 \rho_0 \mathbf{M} \right\|^2, \quad (\text{IV.5.16})$$

where

$$\begin{aligned} \rho_0 \psi_M(\mathbf{F}, \mathbf{M}) &= \sum_{i=1}^2 \frac{3^{1-\alpha_i}}{2\alpha_i} \mu_i [(I_1 - \ln I_3)^{\alpha_i} - 3^{\alpha_i}] + \frac{G'}{2} (\sqrt{I_3} - 1)^2 + \frac{\mu_0 \rho_0^2}{2J\chi} \mathbf{M} \cdot \mathbf{M} \\ &= \rho_0 \psi_{mech}(\mathbf{F}) + \frac{\mu_0 \rho_0^2}{2J\chi} I_6^M, \end{aligned} \quad (\text{IV.5.17})$$

with $I_6^M = \mathbf{M} \cdot \mathbf{M}$ (see Eq. (IV.3.4)).

IV.6 Conclusions

In this Chapter, all aspects pertaining to the numerical implementation of the material model to solve MRE boundary value problems are presented. Novel formulations of the coupled magneto-mechanical variational principle for a non-uniform applied magnetic field, using the displacement vector and the magnetic vector potential as independent variables are discussed.

First, we explain how to numerically enforce the Coulomb gauge needed to ensure the uniqueness of the vector potential. For that purpose, the penalty method is used to impose this additional constraint ($\nabla \cdot \mathbf{A} = 0$) which leads to numerical complications similar to the well known volumetric locking phenomenon observed when simulating incompressible materials. Under-integration of the penalty term is then necessary to avoid this phenomenon.

In a second time, we discuss the main differences in the numerical implementations of the \mathbf{F} - \mathbf{B} and \mathbf{F} - \mathbf{M} theories. The implementation of the latter requires the use of the static condensation method since the sharp discontinuity of the extra independent variable \mathbf{M} (the magnetization vector) at the boundary solid/air prevents its calculation at the nodes. Hence, \mathbf{M} has to be calculated inside each elements. The corresponding FEM discretizations are derived in details.

Then, before showing some usage of the codes, we present which are the valid boundary conditions to use for the vector potential. In particular, we prove that only its tangential components need to be applied on the boundary of the simulated domain. Moreover, based on the mathematical properties of the magnetic pseudo-vector \mathbf{B} and polar-vector \mathbf{A} , we explain how to use the geometrical and loading symmetries of a problem to reduce the number of degrees of freedom needed to solve it.

Lastly, the patch tests used to validate the numerical implementations are discussed. As one can notice, analytical solutions of purely mechanical, purely magnetic and coupled magneto-mechanical (in an infinite medium) problems can be retrieved numerically. Moreover, the complex and highly coupled problem of a magneto-elastic sphere subjected to an externally applied field far from its boundaries (studied by Lefèvre and Lopez-Pamies [100]) is properly solved with both numerical implementations.

For each of the three formulations presented in Chapter III, both the MRE material model and the associated 3D FEM numerical code are now available, thus opening the possibility of improving the design of MRE-based devices.

IV.A Complement for the F-B Theory

IV.A.1 First and second derivatives of the energy density, and of the invariants

In this section, based on the definition provided in Eq. (IV.2.1), we compute the first and second partial derivatives of the energy density \widetilde{W}_B with respect to its independent variables \mathbf{F} and $\widetilde{\mathbf{B}}$. These derivatives are used for the calculation of both the element force vectors \mathbf{f}_e (see Eq. (IV.2.17)) and the element stiffness matrices \mathbf{k}_e (see Eq. (IV.2.19)). The first partial derivatives of the energy density read (note that the Einstein summation convention is used)

$$\begin{aligned}\frac{\partial \widetilde{W}_B}{\partial \mathbf{F}_{ij}}(\mathbf{F}, \widetilde{\mathbf{B}}) &= \rho_0 \frac{\partial \psi_B}{\partial \mathbf{F}_{ij}}(\mathbf{F}, \widetilde{\mathbf{B}} + J\mathbf{F}^{-1} \cdot \mathbf{b}_0) - \frac{1}{2\mu_0 J} \left\| \mathbf{F} \cdot \widetilde{\mathbf{B}} \right\|^2 F_{ji}^{-1} + \frac{1}{\mu_0 J} \left(F_{ir} \widetilde{B}_r \right) \widetilde{B}_j, \\ \frac{\partial \widetilde{W}_B}{\partial \widetilde{B}_i}(\mathbf{F}, \widetilde{\mathbf{B}}) &= \rho_0 \frac{\partial \psi_B}{\partial \widetilde{B}_i}(\mathbf{F}, \widetilde{\mathbf{B}} + J\mathbf{F}^{-1} \cdot \mathbf{b}_0) + \frac{1}{\mu_0 J} C_{ir} \widetilde{B}_r,\end{aligned}\tag{IV.A.1}$$

while the second partial derivatives are given by

$$\begin{aligned}\frac{\partial^2 \widetilde{W}_B}{\partial \mathbf{F}_{ij} \partial \mathbf{F}_{kl}}(\mathbf{F}, \widetilde{\mathbf{B}}) &= \rho_0 \frac{\partial^2 \psi_B}{\partial \mathbf{F}_{ij} \partial \mathbf{F}_{kl}}(\mathbf{F}, \widetilde{\mathbf{B}} + J\mathbf{F}^{-1} \cdot \mathbf{b}_0) + \frac{1}{2\mu_0 J} \left\| \mathbf{F} \cdot \widetilde{\mathbf{B}} \right\|^2 [F_{lk}^{-1} F_{ji}^{-1} + F_{jk}^{-1} F_{li}^{-1}] - \\ &\quad \frac{1}{\mu_0 J} \left(F_{kr} \widetilde{B}_r \right) \widetilde{B}_l F_{ji}^{-1} - \frac{1}{\mu_0 J} \left(F_{ir} \widetilde{B}_r \right) \widetilde{B}_j F_{lk}^{-1} + \frac{1}{\mu_0 J} \delta_{ik} \widetilde{B}_l \widetilde{B}_j, \\ \frac{\partial^2 \widetilde{W}_B}{\partial \mathbf{F}_{ij} \partial \widetilde{B}_k}(\mathbf{F}, \widetilde{\mathbf{B}}) &= \rho_0 \frac{\partial^2 \psi_B}{\partial \mathbf{F}_{ij} \partial \widetilde{B}_k}(\mathbf{F}, \widetilde{\mathbf{B}} + J\mathbf{F}^{-1} \cdot \mathbf{b}_0) + \frac{1}{\mu_0 J} F_{ik} \widetilde{B}_j + \frac{\delta_{jk}}{\mu_0 J} \left(F_{ir} \widetilde{B}_r \right) - \frac{1}{\mu_0 J} C_{kr} \widetilde{B}_r F_{ji}^{-1}, \\ \frac{\partial^2 \widetilde{W}_B}{\partial \widetilde{B}_i \partial \widetilde{B}_j}(\mathbf{F}, \widetilde{\mathbf{B}}) &= \rho_0 \frac{\partial^2 \psi_B}{\partial \widetilde{B}_i \partial \widetilde{B}_j}(\mathbf{F}, \widetilde{\mathbf{B}} + J\mathbf{F}^{-1} \cdot \mathbf{b}_0) + \frac{C_{ij}}{\mu_0 J}.\end{aligned}\tag{IV.A.2}$$

To compute the first and second derivatives of the solid's Helmholtz free energy ψ_B , we apply the chain rule knowing that ψ_B is a function of ten independent invariants (see Eq. (IV.2.5))

$$\begin{aligned}\rho_0 \frac{\partial \psi_B}{\partial \mathbf{F}_{ij}} &= \rho_0 \frac{\partial \psi_B}{\partial I_p^B} \frac{\partial I_p^B}{\partial \mathbf{F}_{ij}}, \\ \rho_0 \frac{\partial \psi_B}{\partial \widetilde{B}_i} &= \rho_0 \frac{\partial \psi_B}{\partial I_p^B} \frac{\partial I_p^B}{\partial \widetilde{B}_i}, \\ \rho_0 \frac{\partial^2 \psi_B}{\partial \mathbf{F}_{ij} \partial \mathbf{F}_{kl}} &= \rho_0 \frac{\partial^2 \psi_B}{\partial I_p^B \partial I_q^B} \frac{\partial I_p^B}{\partial \mathbf{F}_{ij}} \frac{\partial I_q^B}{\partial \mathbf{F}_{kl}} + \rho_0 \frac{\partial \psi_B}{\partial I_p^B} \frac{\partial^2 I_p^B}{\partial \mathbf{F}_{ij} \partial \mathbf{F}_{kl}}, \\ \rho_0 \frac{\partial^2 \psi_B}{\partial \mathbf{F}_{ij} \partial \widetilde{B}_k} &= \rho_0 \frac{\partial^2 \psi_B}{\partial I_p^B \partial I_q^B} \frac{\partial I_p^B}{\partial \mathbf{F}_{ij}} \frac{\partial I_q^B}{\partial \widetilde{B}_k} + \rho_0 \frac{\partial \psi_B}{\partial I_p^B} \frac{\partial^2 I_p^B}{\partial \mathbf{F}_{ij} \partial \widetilde{B}_k}, \\ \rho_0 \frac{\partial^2 \psi_B}{\partial \widetilde{B}_i \partial \widetilde{B}_j} &= \rho_0 \frac{\partial^2 \psi_B}{\partial I_p^B \partial I_q^B} \frac{\partial I_p^B}{\partial \widetilde{B}_i} \frac{\partial I_q^B}{\partial \widetilde{B}_j} + \rho_0 \frac{\partial \psi_B}{\partial I_p^B} \frac{\partial^2 I_p^B}{\partial \widetilde{B}_i \partial \widetilde{B}_j}.\end{aligned}\tag{IV.A.3}$$

At this stage, we provide the first and second derivatives of the invariants used in the \mathbf{F} - \mathbf{B} theory, with respect to the independent variables \mathbf{F} and $\tilde{\mathbf{B}}$. For the coupled invariants (i.e, I_i^B , $i \geq 6$), the expression of these derivatives cannot be written concisely and thus we restrict ourselves to the invariants used in Section IV.5 in the expression of the free energy ψ_B , namely I_6^B and I_7^B .

Remark: In what follows we will use the Einstein summation convention. In addition, we will use the notation b_i^0 for the component of \mathbf{b}_0 along \mathbf{e}_i (i.e $\mathbf{b}_0 = b_i^0 \mathbf{e}_i$) and the following decomposition for the Eulerian magnetic field

$$\mathbf{b} = \mathbf{b}_0 + \frac{1}{J} \mathbf{F} \cdot \tilde{\mathbf{B}}. \quad (\text{IV.A.4})$$

** First order derivatives

***** $(\partial I_P / \partial \mathbf{F})$ *****

$$\frac{\partial I_1}{\partial F_{ij}} = 2 F_{ij}, \quad \frac{\partial I_2}{\partial F_{ij}} = 2 (I_1 F_{ij} - F_{ir} F_{sr} F_{sj}), \quad \frac{\partial I_3}{\partial F_{ij}} = 2 I_3 F_{ji}^{-1}$$

$$\frac{\partial I_4}{\partial F_{ij}} = 2 N_j F_{ip} N_p, \quad \frac{\partial I_5}{\partial F_{ij}} = 2 F_{ir} N_s F_{ns} (N_j F_{nr} + N_r F_{nj})$$

$$\frac{\partial I_6^B}{\partial F_{ij}} = 2 \left[J^2 F_{ji}^{-1} b_s^0 b_s^0 + J F_{ji}^{-1} b_s^0 F_{sl} \tilde{B}_l + J b_i^0 \tilde{B}_j + F_{is} \tilde{B}_s \tilde{B}_j \right]$$

$$\begin{aligned} \frac{\partial I_7^B}{\partial F_{ij}} = & 2 J^2 F_{ji}^{-1} (F_{sr} b_s^0) (F_{nr} b_n^0) + 2 J F_{ji}^{-1} (F_{sr} b_s^0) (C_{rn} \tilde{B}_n) + 2 J^2 b_i^0 b_r^0 F_{rj} + 2 J b_i^0 C_{jr} \tilde{B}_r + \\ & 2 J (F_{ir} \tilde{B}_r) (F_{sj} b_s^0) + 2 J (F_{ir} F_{rs} b_s^0) \tilde{B}_j + 2 (F_{ir} \tilde{B}_r) (C_{js} \tilde{B}_s) + 2 (F_{ir} F_{sr} F_{sn} \tilde{B}_n) \tilde{B}_j \end{aligned} \quad (\text{IV.A.5})$$

***** $(\partial I_P / \partial \tilde{\mathbf{B}})$ *****

$$\frac{\partial I_1}{\partial \tilde{B}_i} = \frac{\partial I_2}{\partial \tilde{B}_i} = \frac{\partial I_3}{\partial \tilde{B}_i} = \frac{\partial I_4}{\partial \tilde{B}_i} = \frac{\partial I_5}{\partial \tilde{B}_i} = 0$$

$$\frac{\partial I_6^B}{\partial \tilde{B}_i} = 2 J F_{ri} b_r^0 + 2 C_{is} \tilde{B}_s, \quad \frac{\partial I_7^B}{\partial \tilde{B}_i} = 2 J C_{ir} F_{sr} b_s^0 + 2 C_{ip} C_{pq} \tilde{B}_q$$

(IV.A.6)

** Second order derivatives

***** $(\partial^2 I_P / \partial \mathbf{B} \partial \mathbf{B})$ *****

$$\frac{\partial^2 I_1}{\partial \tilde{\mathbf{B}}_i \partial \tilde{\mathbf{B}}_j} = \frac{\partial^2 I_2}{\partial \tilde{\mathbf{B}}_i \partial \tilde{\mathbf{B}}_j} = \frac{\partial^2 I_3}{\partial \tilde{\mathbf{B}}_i \partial \tilde{\mathbf{B}}_j} = \frac{\partial^2 I_4}{\partial \tilde{\mathbf{B}}_i \partial \tilde{\mathbf{B}}_j} = \frac{\partial^2 I_5}{\partial \tilde{\mathbf{B}}_i \partial \tilde{\mathbf{B}}_j} = 0$$

$$\frac{\partial^2 I_6^B}{\partial \tilde{\mathbf{B}}_i \partial \tilde{\mathbf{B}}_j} = 2 C_{ij}, \quad \frac{\partial^2 I_7^B}{\partial \tilde{\mathbf{B}}_i \partial \tilde{\mathbf{B}}_j} = 2 C_{ir} C_{rj}$$
(IV.A.7)

***** $(\partial^2 I_P / \partial \mathbf{F} \partial \mathbf{B})$ *****

$$\frac{\partial^2 I_1}{\partial F_{ij} \partial \tilde{\mathbf{B}}_k} = \frac{\partial^2 I_2}{\partial F_{ij} \partial \tilde{\mathbf{B}}_k} = \frac{\partial^2 I_3}{\partial F_{ij} \partial \tilde{\mathbf{B}}_k} = \frac{\partial^2 I_4}{\partial F_{ij} \partial \tilde{\mathbf{B}}_k} = \frac{\partial^2 I_5}{\partial F_{ij} \partial \tilde{\mathbf{B}}_k}$$

$$\frac{\partial^2 I_6^B}{\partial F_{ij} \partial \tilde{\mathbf{B}}_k} = 2 \left[J F_{ji}^{-1} F_{sk} b_s^0 + J b_i^0 \delta_{jk} + F_{ir} \tilde{\mathbf{B}}_r \delta_{jk} + F_{ik} \tilde{\mathbf{B}}_j \right]$$

$$\frac{\partial^2 I_7^B}{\partial F_{ij} \partial \tilde{\mathbf{B}}_k} = 2 J F_{ji}^{-1} (C_{kr} F_{sr} b_s^0) + 2 J b_i^0 C_{jk} + 2 J F_{ik} F_{sj} b_s^0 + 2 J (F_{ir} F_{sr} b_s^0) \delta_{jk} +$$

$$2 F_{ik} (C_{jr} \tilde{\mathbf{B}}_r) + 2 (F_{ir} \tilde{\mathbf{B}}_r) C_{jk} + 2 (F_{ir} F_{sr} F_{sk}) \tilde{\mathbf{B}}_j + 2 (F_{ir} F_{sr} F_{sp} \tilde{\mathbf{B}}_p) \delta_{jk}$$
(IV.A.8)

***** $(\partial^2 I_P / \partial \mathbf{F} \partial \mathbf{F})$ *****

$$\frac{\partial^2 I_1}{\partial F_{ij} \partial F_{kl}} = 2 \delta_{ik} \delta_{jl}, \quad \frac{\partial^2 I_2}{\partial F_{ij} \partial F_{kl}} = 2 (2 F_{ij} F_{kl} + I_1 \delta_{ik} \delta_{jl} - F_{il} F_{kj} - \delta_{ik} F_{rj} F_{rl} - \delta_{jl} F_{is} F_{ks})$$

$$\frac{\partial^2 I_3}{\partial F_{ij} \partial F_{kl}} = 2 I_3 (2 F_{lk}^{-1} F_{ji}^{-1} - F_{jk}^{-1} F_{li}^{-1}), \quad \frac{\partial^2 I_4}{\partial F_{ij} \partial F_{kl}} = 2 \delta_{ik} N_j N_l$$

$$\begin{aligned} \frac{\partial^2 I_5}{\partial F_{ij} \partial F_{kl}} = & 2 \left(N_j N_s \delta_{ik} F_{rl} F_{rs} + N_j N_r F_{il} F_{kr} + N_l N_s \delta_{ik} F_{rj} F_{rs} + N_r N_s \delta_{jl} F_{ir} F_{ks} + \right. \\ & \left. N_j N_l F_{ir} F_{kr} + N_l N_r F_{ir} F_{kj} \right) \end{aligned}$$

$$\begin{aligned} \frac{\partial^2 I_6^B}{\partial F_{ij} \partial F_{kl}} = & 2 \left[J^2 (b_r^0 b_r^0) (2 F_{ji}^{-1} F_{lk}^{-1} - F_{jk}^{-1} F_{li}^{-1}) + J (b_r^0 F_{rs} \tilde{B}_s) (F_{ji}^{-1} F_{lk}^{-1} - F_{jk}^{-1} F_{li}^{-1}) + \right. \\ & \left. J F_{ji}^{-1} b_k^0 \tilde{B}_l + J F_{lk}^{-1} b_i^0 \tilde{B}_j + \tilde{B}_j \tilde{B}_l \delta_{ik} \right] \end{aligned}$$

$$\begin{aligned} \frac{\partial^2 I_7^B}{\partial F_{ij} \partial F_{kl}} = & 4 J^2 F_{lk}^{-1} F_{ji}^{-1} (F_{rs} b_r) (F_{ns} b_n) - 2 J^2 F_{jk}^{-1} F_{li}^{-1} (F_{rs} b_r) (F_{ns} b_n) + 4 J^2 F_{ji}^{-1} (F_{rl} b_r) b_k - \\ & 2 J F_{ji}^{-1} F_{lk}^{-1} (F_{sr} F_{nr} b_n) (F_{sp} \tilde{B}_p) + 2 J F_{ji}^{-1} (F_{kr} F_{nr} b_n) \tilde{B}_l + 4 J^2 F_{lk}^{-1} (F_{rj} b_r) b_i + \\ & 2 J^2 b_k b_i \delta_{jl} - 2 J b_i F_{lk}^{-1} (C_{jr} \tilde{B}_r) + 2 J F_{kj} \tilde{B}_l b_i - 2 J (F_{ir} \tilde{B}_r) (F_{sj} b_s) F_{lk}^{-1} + \\ & 2 J (F_{rj} b_r) \tilde{B}_l \delta_{ik} - 4 J F_{lk}^{-1} F_{ji}^{-1} (F_{rs} b_r) (C_{sn} \tilde{B}_n) + 2 J F_{jk}^{-1} F_{li}^{-1} (F_{rs} b_r) (C_{sn} \tilde{B}_n) - \\ & 2 J F_{ji}^{-1} (F_{rl} b_r) (F_{kn} \tilde{B}_n) - 2 J F_{ji}^{-1} b_k (C_{lr} \tilde{B}_r) + \\ & 2 F_{ji}^{-1} F_{lk}^{-1} (F_{sr} F_{nr} F_{np} \tilde{B}_p) (F_{sq} \tilde{B}_q) - 2 F_{ji}^{-1} (F_{kr} F_{nr} F_{np} \tilde{B}_p) \tilde{B}_l + \\ & 2 J F_{lk}^{-1} (F_{ir} F_{nr} b_n) \tilde{B}_j + 2 J \delta_{ik} (F_{rl} b_r) \tilde{B}_j + 2 J F_{il} b_k \tilde{B}_j - \\ & 2 F_{lk}^{-1} (F_{ir} F_{nr} F_{np} \tilde{B}_p) \tilde{B}_j + 2 (F_{ir} F_{kr}) \tilde{B}_l \tilde{B}_j \end{aligned}$$

(IV.A.9)

IV.A.2 ABAQUS UEL implementation

To numerically implement the variational formulation presented in Section IV.2, an ABAQUS user element (UEL) is developed. In the ABAQUS environment, we are required to give the expression of the element force vector \mathbf{f}_e and the element stiffness matrix \mathbf{k}_e . The purpose of this section is to give some practical details on how the user element is written.

It is convenient to define the following scalar quantities which are directly used in the UEL code

- n_{dm} : dimension of the problem ($n_{dm} = 3$ in three dimensions),
- n_{el} : number of elements in the mesh,
- n_{ne} : number of nodes per element ($n_{ne} = 8$ in this section since we choose a linear cubic element, see Fig. IV.14),
- n_{dof} : number of degrees of freedom (d.o.f) per node ($n_{dof} = 6$ in the case of the **F-B** theory. The d.o.f are $(u_1, u_2, u_3, \tilde{A}_1, \tilde{A}_2, \tilde{A}_3)$. It is interesting to note that the **F-H** theory that is mathematically equivalent requires only 4 degrees of freedom since a magnetic scalar potential is used in place of the magnetic vector potential),
- $n_{dofel} = n_{dof} \times n_{ne}$: total number of d.o.f per element ($n_{dofel} = 6 \times 8 = 48$ in our case. As we will see the size of the force vector \mathbf{f}_e is n_{dofel} , while the size of the stiffness matrix \mathbf{k}_e is $n_{dofel} \times n_{dofel}$),
- $ntens$: total number of entries in the vector of the ‘stress-like’ quantities (i.e., the number of components of $[\mathbf{d}q\mathbf{d}x]$ defined later on. In this context, $ntens = 12$).

From now on, we consider standard eight node isoparametric cubic elements (C3D8) as shown in Fig. IV.14. The same derivation for a standard ten node isoparametric tetrahedral element is given in Appendix IV.A.4.

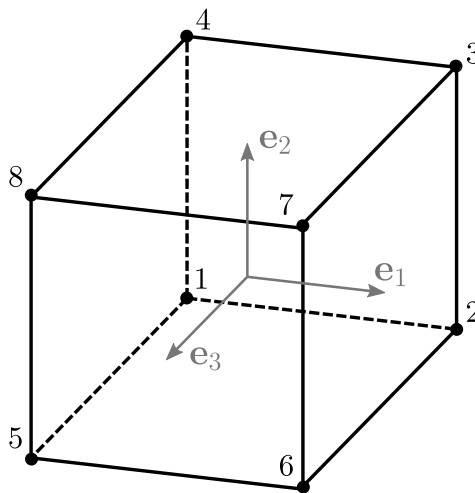


Figure IV.14: Schematic of a standard eight node cubic element (C3D8)

At this stage, we define the notation for the n_{dofel} components vector of unknowns by

$$\mathbf{q}_e = \{u_1^{(1)}, u_2^{(1)}, u_3^{(1)}, \tilde{A}_1^{(1)}, \tilde{A}_2^{(1)}, \tilde{A}_3^{(1)}, \dots, u_1^{(n_{ne})}, u_2^{(n_{ne})}, u_3^{(n_{ne})}, \tilde{A}_1^{(n_{ne})}, \tilde{A}_2^{(n_{ne})}, \tilde{A}_3^{(n_{ne})}\}, \quad (\text{IV.A.10})$$

where the subscript denotes the spatial component of each unknown and the superscript denotes the node (using the local numbering shown in Fig. IV.14) associated with the unknown under consideration.

IV.A.2.a Element jacobian and coordinate transformations

Then, we have to define the shape functions and the associated Jacobian matrix, denoted as $[\mathcal{J}]$, which serves to write quantities, which are evaluated at the local coordinate system of the element, with respect to the global coordinate system. In the present analysis, we consider isoparametric elements and hence the same shape functions will be used to interpolate all nodal unknowns. The definition of the shape functions ($N_i, i \in [1, n_{ne}]$) and the definition of the matrix \mathbf{G} which represents the derivatives of these shape functions with respect to the local coordinate system ($\mathcal{G}_{ij} = \partial N_i / \partial \xi_j, (i, j) \in [1, n_{ne}]^2$) are given in Appendix IV.A.3.

We can then define the following local to global coordinate transformation ⁸

$$\begin{aligned} [\mathcal{J}] &= \begin{bmatrix} \mathcal{J}_{11} & \mathcal{J}_{12} & \mathcal{J}_{13} \\ \mathcal{J}_{21} & \mathcal{J}_{22} & \mathcal{J}_{23} \\ \mathcal{J}_{31} & \mathcal{J}_{32} & \mathcal{J}_{33} \end{bmatrix} = \begin{bmatrix} \partial X_1 / \partial \xi_1 & \partial X_2 / \partial \xi_1 & \partial X_3 / \partial \xi_1 \\ \partial X_1 / \partial \xi_2 & \partial X_2 / \partial \xi_2 & \partial X_3 / \partial \xi_2 \\ \partial X_1 / \partial \xi_3 & \partial X_2 / \partial \xi_3 & \partial X_3 / \partial \xi_3 \end{bmatrix} \\ &= \begin{bmatrix} \sum_{I=1}^{nen} (\partial N_I / \partial \xi_1) X_1^I & \sum_{I=1}^{nen} (\partial N_I / \partial \xi_1) X_2^I & \sum_{I=1}^{nen} (\partial N_I / \partial \xi_1) X_3^I \\ \sum_{I=1}^{nen} (\partial N_I / \partial \xi_2) X_1^I & \sum_{I=1}^{nen} (\partial N_I / \partial \xi_2) X_2^I & \sum_{I=1}^{nen} (\partial N_I / \partial \xi_2) X_3^I \\ \sum_{I=1}^{nen} (\partial N_I / \partial \xi_3) X_1^I & \sum_{I=1}^{nen} (\partial N_I / \partial \xi_3) X_2^I & \sum_{I=1}^{nen} (\partial N_I / \partial \xi_3) X_3^I \end{bmatrix}, \quad (\text{IV.A.11}) \end{aligned}$$

which implies that the inverse Jacobian matrix $[\mathcal{J}]^{-1}$ can be written in the following way (we use the Sarrus' rule here)

$$\begin{aligned} [\mathcal{J}]^{-1} &= \begin{bmatrix} \mathcal{J}_{11}^{-1} & \mathcal{J}_{12}^{-1} & \mathcal{J}_{13}^{-1} \\ \mathcal{J}_{21}^{-1} & \mathcal{J}_{22}^{-1} & \mathcal{J}_{23}^{-1} \\ \mathcal{J}_{31}^{-1} & \mathcal{J}_{32}^{-1} & \mathcal{J}_{33}^{-1} \end{bmatrix} \\ &= \frac{1}{\det \mathcal{J}} \begin{bmatrix} \mathcal{J}_{22}\mathcal{J}_{33} - \mathcal{J}_{23}\mathcal{J}_{32} & \mathcal{J}_{13}\mathcal{J}_{32} - \mathcal{J}_{12}\mathcal{J}_{33} & \mathcal{J}_{12}\mathcal{J}_{23} - \mathcal{J}_{13}\mathcal{J}_{22} \\ \mathcal{J}_{23}\mathcal{J}_{31} - \mathcal{J}_{21}\mathcal{J}_{33} & \mathcal{J}_{11}\mathcal{J}_{33} - \mathcal{J}_{13}\mathcal{J}_{31} & \mathcal{J}_{13}\mathcal{J}_{21} - \mathcal{J}_{11}\mathcal{J}_{23} \\ \mathcal{J}_{21}\mathcal{J}_{32} - \mathcal{J}_{22}\mathcal{J}_{31} & \mathcal{J}_{12}\mathcal{J}_{31} - \mathcal{J}_{11}\mathcal{J}_{32} & \mathcal{J}_{11}\mathcal{J}_{22} - \mathcal{J}_{12}\mathcal{J}_{21} \end{bmatrix}, \quad (\text{IV.A.12}) \end{aligned}$$

with $\det \mathcal{J} = \mathcal{J}_{11}\mathcal{J}_{22}\mathcal{J}_{33} - \mathcal{J}_{11}\mathcal{J}_{23}\mathcal{J}_{32} - \mathcal{J}_{12}\mathcal{J}_{21}\mathcal{J}_{33} + \mathcal{J}_{12}\mathcal{J}_{23}\mathcal{J}_{31} + \mathcal{J}_{13}\mathcal{J}_{21}\mathcal{J}_{32} - \mathcal{J}_{13}\mathcal{J}_{22}\mathcal{J}_{31}$.

⁸ Careful: the convention for the definition of the Jacobian is $\mathcal{J}_{ij} = \partial X_j / \partial \xi_i$ and not $\mathcal{J}_{ij} = \partial X_i / \partial \xi_j$.

IV.A.2.b Derivative of matrices

In order to proceed further, we need to write any second order tensor T_{ij} in a vector format denoted as

$$[\mathbf{T}] = [T_{11}, T_{12}, T_{13}, T_{21}, T_{22}, T_{23}, T_{31}, T_{32}, T_{33}]. \quad (\text{IV.A.13})$$

Subsequently, we evaluate the quantities $\mathbf{u}\nabla$ and $\nabla \times \tilde{\mathbf{A}}$ in three dimensions noting that

$$\begin{aligned} \mathbf{u} &= \{u_1(X_1, X_2, X_3), u_2(X_1, X_2, X_3), u_3(X_1, X_2, X_3)\}, \\ \tilde{\mathbf{A}} &= \{\tilde{A}_1(X_1, X_2, X_3), \tilde{A}_2(X_1, X_2, X_3), \tilde{A}_3(X_1, X_2, X_3)\}, \end{aligned} \quad (\text{IV.A.14})$$

with capital X_i denoting the reference coordinates. Using the notation introduced in Eq. (IV.A.13), we have

$$\underbrace{\begin{bmatrix} \mathbf{e}_1 \cdot \mathbf{u}\nabla \cdot \mathbf{e}_1 = \partial u_1 / \partial X_1 \\ \mathbf{e}_1 \cdot \mathbf{u}\nabla \cdot \mathbf{e}_2 = \partial u_1 / \partial X_2 \\ \mathbf{e}_1 \cdot \mathbf{u}\nabla \cdot \mathbf{e}_3 = \partial u_1 / \partial X_3 \\ \mathbf{e}_2 \cdot \mathbf{u}\nabla \cdot \mathbf{e}_1 = \partial u_2 / \partial X_1 \\ \mathbf{e}_2 \cdot \mathbf{u}\nabla \cdot \mathbf{e}_2 = \partial u_2 / \partial X_2 \\ \mathbf{e}_2 \cdot \mathbf{u}\nabla \cdot \mathbf{e}_3 = \partial u_2 / \partial X_3 \\ \mathbf{e}_3 \cdot \mathbf{u}\nabla \cdot \mathbf{e}_1 = \partial u_3 / \partial X_1 \\ \mathbf{e}_3 \cdot \mathbf{u}\nabla \cdot \mathbf{e}_2 = \partial u_3 / \partial X_2 \\ \mathbf{e}_3 \cdot \mathbf{u}\nabla \cdot \mathbf{e}_3 = \partial u_3 / \partial X_3 \\ (\nabla \times \tilde{\mathbf{A}}) \cdot \mathbf{e}_1 = \tilde{B}_1 \\ (\nabla \times \tilde{\mathbf{A}}) \cdot \mathbf{e}_2 = \tilde{B}_2 \\ (\nabla \times \tilde{\mathbf{A}}) \cdot \mathbf{e}_3 = \tilde{B}_3 \end{bmatrix}}_{[\mathbf{dqdx}]} = [\mathbf{JI}] \underbrace{\begin{bmatrix} \partial u_1 / \partial \xi_1 \\ \partial u_1 / \partial \xi_2 \\ \partial u_1 / \partial \xi_3 \\ \partial u_2 / \partial \xi_1 \\ \partial u_2 / \partial \xi_2 \\ \partial u_2 / \partial \xi_3 \\ \partial u_3 / \partial \xi_1 \\ \partial u_3 / \partial \xi_2 \\ \partial u_3 / \partial \xi_3 \\ \partial \tilde{A}_1 / \partial \xi_1 \\ \partial \tilde{A}_1 / \partial \xi_2 \\ \partial \tilde{A}_1 / \partial \xi_3 \\ \partial \tilde{A}_2 / \partial \xi_1 \\ \partial \tilde{A}_2 / \partial \xi_2 \\ \partial \tilde{A}_2 / \partial \xi_3 \\ \partial \tilde{A}_3 / \partial \xi_1 \\ \partial \tilde{A}_3 / \partial \xi_2 \\ \partial \tilde{A}_3 / \partial \xi_3 \end{bmatrix}}_{[\mathbf{dqdxi}]} \quad (\text{IV.A.15})$$

with the perturbed Lagrangian magnetic field $\tilde{\mathbf{B}}$ being defined as

$$\tilde{\mathbf{B}} = \{\tilde{B}_1, \tilde{B}_2, \tilde{B}_3\} = \left\{ \frac{\partial \tilde{A}_3}{\partial X_2} - \frac{\partial \tilde{A}_2}{\partial X_3}, \frac{\partial \tilde{A}_1}{\partial X_3} - \frac{\partial \tilde{A}_3}{\partial X_1}, \frac{\partial \tilde{A}_2}{\partial X_1} - \frac{\partial \tilde{A}_1}{\partial X_2} \right\}. \quad (\text{IV.A.16})$$

Then the matrix $[\mathbf{JI}]$ can be written as

$$[\mathbf{JI}] = \overbrace{\begin{bmatrix} \mathcal{J}^{-1} & \mathbf{0} \\ \mathbf{0} & \mathcal{J}^{-1} & \mathbf{0} \\ \mathbf{0} & \mathbf{0} & \mathcal{J}^{-1} & \mathbf{0} \\ \mathbf{0} & \mathbf{0} & \mathbf{0} & 0 & 0 & 0 & -\mathcal{J}_{31}^{-1} & -\mathcal{J}_{32}^{-1} & -\mathcal{J}_{33}^{-1} & \mathcal{J}_{21}^{-1} & \mathcal{J}_{22}^{-1} & \mathcal{J}_{23}^{-1} \\ \mathbf{0} & \mathbf{0} & \mathbf{0} & \mathcal{J}_{31}^{-1} & \mathcal{J}_{32}^{-1} & \mathcal{J}_{33}^{-1} & 0 & 0 & 0 & -\mathcal{J}_{11}^{-1} & -\mathcal{J}_{12}^{-1} & -\mathcal{J}_{13}^{-1} \\ & & & -\mathcal{J}_{21}^{-1} & -\mathcal{J}_{22}^{-1} & -\mathcal{J}_{23}^{-1} & \mathcal{J}_{11}^{-1} & \mathcal{J}_{12}^{-1} & \mathcal{J}_{13}^{-1} & 0 & 0 & 0 \end{bmatrix}}^{\text{matrix of size } n_{tens} \times (n_{dm} \times n_{dof})}, \quad (\text{IV.A.17})$$

where \mathcal{J}^{-1} stands for the 3×3 inverse Jacobian matrix given in Eq. (IV.A.12) and $\mathbf{0}$ is the 3×3 zero matrix.

Next, one computes the vector \mathbf{dqdx}_i by

$$\begin{aligned}
 & \overbrace{\left[\begin{array}{l}
 \partial u_1 / \partial \xi_1 = \sum_{K=1}^{n_{ne}} \left(\frac{\partial N_K}{\partial \xi_1} \right) u_1^{(K)} \\
 \partial u_1 / \partial \xi_2 = \sum_{K=1}^{n_{ne}} \left(\frac{\partial N_K}{\partial \xi_2} \right) u_1^{(K)} \\
 \partial u_1 / \partial \xi_3 = \sum_{K=1}^{n_{ne}} \left(\frac{\partial N_K}{\partial \xi_3} \right) u_1^{(K)} \\
 \partial u_2 / \partial \xi_1 = \sum_{K=1}^{n_{ne}} \left(\frac{\partial N_K}{\partial \xi_1} \right) u_2^{(K)} \\
 \partial u_2 / \partial \xi_2 = \sum_{K=1}^{n_{ne}} \left(\frac{\partial N_K}{\partial \xi_2} \right) u_2^{(K)} \\
 \partial u_2 / \partial \xi_3 = \sum_{K=1}^{n_{ne}} \left(\frac{\partial N_K}{\partial \xi_3} \right) u_2^{(K)} \\
 \partial u_3 / \partial \xi_1 = \sum_{K=1}^{n_{ne}} \left(\frac{\partial N_K}{\partial \xi_1} \right) u_3^{(K)} \\
 \partial u_3 / \partial \xi_2 = \sum_{K=1}^{n_{ne}} \left(\frac{\partial N_K}{\partial \xi_2} \right) u_3^{(K)} \\
 \partial u_3 / \partial \xi_3 = \sum_{K=1}^{n_{ne}} \left(\frac{\partial N_K}{\partial \xi_3} \right) u_3^{(K)} \\
 \partial \tilde{A}_1 / \partial \xi_1 = \sum_{K=1}^{n_{ne}} \left(\frac{\partial N_K}{\partial \xi_1} \right) \tilde{A}_1^{(K)} \\
 \partial \tilde{A}_1 / \partial \xi_2 = \sum_{K=1}^{n_{ne}} \left(\frac{\partial N_K}{\partial \xi_2} \right) \tilde{A}_1^{(K)} \\
 \partial \tilde{A}_1 / \partial \xi_3 = \sum_{K=1}^{n_{ne}} \left(\frac{\partial N_K}{\partial \xi_3} \right) \tilde{A}_1^{(K)} \\
 \partial \tilde{A}_2 / \partial \xi_1 = \sum_{K=1}^{n_{ne}} \left(\frac{\partial N_K}{\partial \xi_1} \right) \tilde{A}_2^{(K)} \\
 \partial \tilde{A}_2 / \partial \xi_2 = \sum_{K=1}^{n_{ne}} \left(\frac{\partial N_K}{\partial \xi_2} \right) \tilde{A}_2^{(K)} \\
 \partial \tilde{A}_2 / \partial \xi_3 = \sum_{K=1}^{n_{ne}} \left(\frac{\partial N_K}{\partial \xi_3} \right) \tilde{A}_2^{(K)} \\
 \partial \tilde{A}_3 / \partial \xi_1 = \sum_{K=1}^{n_{ne}} \left(\frac{\partial N_K}{\partial \xi_1} \right) \tilde{A}_3^{(K)} \\
 \partial \tilde{A}_3 / \partial \xi_2 = \sum_{K=1}^{n_{ne}} \left(\frac{\partial N_K}{\partial \xi_2} \right) \tilde{A}_3^{(K)} \\
 \partial \tilde{A}_3 / \partial \xi_3 = \sum_{K=1}^{n_{ne}} \left(\frac{\partial N_K}{\partial \xi_3} \right) \tilde{A}_3^{(K)}
 \end{array} \right]}^{\text{vector of size } (n_{dm} \times n_{dof}) \times 1} = [\mathbf{NG}] \underbrace{\left[\begin{array}{l}
 u_1^{(1)} \\
 u_2^{(1)} \\
 u_3^{(1)} \\
 \tilde{A}_1^{(1)} \\
 \tilde{A}_2^{(1)} \\
 \tilde{A}_3^{(1)} \\
 \vdots \\
 u_1^{(n_{ne})} \\
 u_2^{(n_{ne})} \\
 u_3^{(n_{ne})} \\
 \tilde{A}_1^{(n_{ne})} \\
 \tilde{A}_2^{(n_{ne})} \\
 \tilde{A}_3^{(n_{ne})}
 \end{array} \right]}_{\mathbf{q}_e}, \quad (\text{IV.A.18})
 \end{aligned}$$

$[\mathbf{dqdx}_i]$

with

$$\begin{aligned}
 & \text{matrix of size } (n_{dm} \times n_{dof}) \times n_{dofel} \\
 [\mathbf{NG}] = & \begin{bmatrix}
 \mathcal{G}_{11} & 0 & 0 & 0 & 0 & 0 & \cdots & \mathcal{G}_{n_{ne}1} & 0 & 0 & 0 & 0 & 0 \\
 \mathcal{G}_{12} & 0 & 0 & 0 & 0 & 0 & \cdots & \mathcal{G}_{n_{ne}2} & 0 & 0 & 0 & 0 & 0 \\
 \mathcal{G}_{13} & 0 & 0 & 0 & 0 & 0 & \cdots & \mathcal{G}_{n_{ne}3} & 0 & 0 & 0 & 0 & 0 \\
 0 & \mathcal{G}_{11} & 0 & 0 & 0 & 0 & \cdots & 0 & \mathcal{G}_{n_{ne}1} & 0 & 0 & 0 & 0 \\
 0 & \mathcal{G}_{12} & 0 & 0 & 0 & 0 & \cdots & 0 & \mathcal{G}_{n_{ne}2} & 0 & 0 & 0 & 0 \\
 0 & \mathcal{G}_{13} & 0 & 0 & 0 & 0 & \cdots & 0 & \mathcal{G}_{n_{ne}3} & 0 & 0 & 0 & 0 \\
 0 & 0 & \mathcal{G}_{11} & 0 & 0 & 0 & \cdots & 0 & 0 & \mathcal{G}_{n_{ne}1} & 0 & 0 & 0 \\
 0 & 0 & \mathcal{G}_{12} & 0 & 0 & 0 & \cdots & 0 & 0 & \mathcal{G}_{n_{ne}2} & 0 & 0 & 0 \\
 0 & 0 & \mathcal{G}_{13} & 0 & 0 & 0 & \cdots & 0 & 0 & \mathcal{G}_{n_{ne}3} & 0 & 0 & 0 \\
 0 & 0 & 0 & \mathcal{G}_{11} & 0 & 0 & \cdots & 0 & 0 & 0 & \mathcal{G}_{n_{ne}1} & 0 & 0 \\
 0 & 0 & 0 & \mathcal{G}_{12} & 0 & 0 & \cdots & 0 & 0 & 0 & \mathcal{G}_{n_{ne}2} & 0 & 0 \\
 0 & 0 & 0 & \mathcal{G}_{13} & 0 & 0 & \cdots & 0 & 0 & 0 & \mathcal{G}_{n_{ne}3} & 0 & 0 \\
 0 & 0 & 0 & 0 & \mathcal{G}_{11} & 0 & \cdots & 0 & 0 & 0 & 0 & \mathcal{G}_{n_{ne}1} & 0 \\
 0 & 0 & 0 & 0 & \mathcal{G}_{12} & 0 & \cdots & 0 & 0 & 0 & 0 & \mathcal{G}_{n_{ne}2} & 0 \\
 0 & 0 & 0 & 0 & \mathcal{G}_{13} & 0 & \cdots & 0 & 0 & 0 & 0 & \mathcal{G}_{n_{ne}3} & 0 \\
 0 & 0 & 0 & 0 & 0 & \mathcal{G}_{11} & \cdots & 0 & 0 & 0 & 0 & 0 & \mathcal{G}_{n_{ne}1} \\
 0 & 0 & 0 & 0 & 0 & \mathcal{G}_{12} & \cdots & 0 & 0 & 0 & 0 & 0 & \mathcal{G}_{n_{ne}2} \\
 0 & 0 & 0 & 0 & 0 & \mathcal{G}_{13} & \cdots & 0 & 0 & 0 & 0 & 0 & \mathcal{G}_{n_{ne}3}
 \end{bmatrix}.
 \end{aligned}
 \tag{IV.A.19}$$

Then the derivative matrix $[\mathbf{G}]$ used in Eq. (IV.2.19) such that $\mathbf{dqdx} = [\mathbf{G}] \cdot \mathbf{q}_e$ is given by

$$\begin{aligned}
 \underbrace{[\mathbf{G}]}_{\text{matrix } n_{tens} \times n_{dofel}} &= \begin{bmatrix} \text{matrix } 9 \times n_{dofel} \\ \underbrace{\mathbf{G}_u}_{\text{matrix } 3 \times n_{dofel}} \\ \underbrace{\mathbf{G}_{\tilde{\mathbf{A}}}}_{\text{matrix } 3 \times n_{dofel}} \end{bmatrix} = \underbrace{\mathbf{JI}}_{\text{matrix } n_{tens} \times (n_{dm} \times n_{dof})} \underbrace{[\mathbf{NG}]}_{\text{matrix } (n_{dm} \times n_{dof}) \times n_{dofel}}.
 \end{aligned}
 \tag{IV.A.20}$$

Similarly, the divergence of $\tilde{\mathbf{A}}$ is computed by

$$\nabla \cdot \tilde{\mathbf{A}} = \sum_{i=1}^{n_{dm}} \frac{\partial \tilde{A}_i}{\partial X_i} = \underbrace{\left[\hat{\mathbf{0}} \quad \mathcal{J}_{11}^{-1} \quad \mathcal{J}_{12}^{-1} \quad \mathcal{J}_{13}^{-1} \quad \mathcal{J}_{21}^{-1} \quad \mathcal{J}_{22}^{-1} \quad \mathcal{J}_{23}^{-1} \quad \mathcal{J}_{31}^{-1} \quad \mathcal{J}_{32}^{-1} \quad \mathcal{J}_{33}^{-1} \right]}_{\text{vector } 1 \times (n_{dm} \times n_{dof})} \underbrace{\left[\begin{array}{c} \partial u_1 / \partial \xi_1 \\ \partial u_1 / \partial \xi_2 \\ \partial u_1 / \partial \xi_3 \\ \partial u_2 / \partial \xi_1 \\ \partial u_2 / \partial \xi_2 \\ \partial u_2 / \partial \xi_3 \\ \partial u_3 / \partial \xi_1 \\ \partial u_3 / \partial \xi_2 \\ \partial u_3 / \partial \xi_3 \\ \partial \tilde{A}_1 / \partial \xi_1 \\ \partial \tilde{A}_1 / \partial \xi_2 \\ \partial \tilde{A}_1 / \partial \xi_3 \\ \partial \tilde{A}_2 / \partial \xi_1 \\ \partial \tilde{A}_2 / \partial \xi_2 \\ \partial \tilde{A}_2 / \partial \xi_3 \\ \partial \tilde{A}_3 / \partial \xi_1 \\ \partial \tilde{A}_3 / \partial \xi_2 \\ \partial \tilde{A}_3 / \partial \xi_3 \end{array} \right]}_{\text{vector } (n_{dm} \times n_{dof}) \times 1}, \quad (IV.A.21)$$

with $\hat{\mathbf{0}}$ being a $1 \times \left(\frac{n_{dm} \times n_{dof}}{2} \right)$ zero line vector, so that the divergence vector $\mathbf{D}_{\tilde{\mathbf{A}}}$ defined in Eq. (IV.2.15) such that $\nabla \cdot \tilde{\mathbf{A}} = \mathbf{D}_{\tilde{\mathbf{A}}}^T \cdot \mathbf{q}_e$ is given by

$$\underbrace{\left[\mathbf{D}_{\tilde{\mathbf{A}}} \right]^T}_{\text{vector of size } 1 \times n_{dofel}} = \underbrace{\left[\text{divJI} \right]}_{\text{vector of size } 1 \times (n_{dm} \times n_{dof})} \underbrace{\left[\mathbf{NG} \right]}_{\text{matrix of size } (n_{dm} \times n_{dof}) \times n_{dofel}}. \quad (IV.A.22)$$

IV.A.2.c Expression of the force vector

At this stage, if we substitute Eq. (IV.A.20) and Eq. (IV.A.22) in Eq. (IV.2.17), we can rewrite the element force vector \mathbf{f}_e as

$$\underbrace{\mathbf{f}_e}_{\text{vector } 1 \times n_{dofel}} = \int_{V_e} \underbrace{\left[\mathbf{f}_e^{FB} \right]}_{1 \times n_{tens}} \underbrace{\left[\mathbf{G} \right]}_{n_{tens} \times n_{dofel}} dV + \frac{1}{\mu_0 k} \int_{V_e} (\nabla \cdot \tilde{\mathbf{A}}) \underbrace{\left[\mathbf{D}_{\tilde{\mathbf{A}}} \right]^T}_{1 \times n_{dofel}} dV, \quad (IV.A.23)$$

where based on the convention introduced in (IV.A.13), the vector $[\mathbf{f}_e^{FB}]$ is given by

$$\mathbf{f}_e^{FB} = \underbrace{\left[\frac{\partial \widetilde{W}_B}{\partial F_{11}}, \frac{\partial \widetilde{W}_B}{\partial F_{12}}, \frac{\partial \widetilde{W}_B}{\partial F_{13}}, \frac{\partial \widetilde{W}_B}{\partial F_{21}}, \frac{\partial \widetilde{W}_B}{\partial F_{22}}, \frac{\partial \widetilde{W}_B}{\partial F_{23}}, \frac{\partial \widetilde{W}_B}{\partial F_{31}}, \frac{\partial \widetilde{W}_B}{\partial F_{32}}, \frac{\partial \widetilde{W}_B}{\partial F_{33}}, \frac{\partial \widetilde{W}_B}{\partial \widetilde{B}_1}, \frac{\partial \widetilde{W}_B}{\partial \widetilde{B}_2}, \frac{\partial \widetilde{W}_B}{\partial \widetilde{B}_3} \right]}_{\text{vector of size } 1 \times n_{tens}}. \quad (\text{IV.A.24})$$

As one can notice, the potential of the externally applied mechanical loads, i.e. $\mathcal{W} = \int_{\mathcal{D}} \rho_0 \mathbf{f} \cdot \mathbf{u} dV + \int_{\partial \mathcal{D}} \mathbf{T} \cdot \mathbf{u} dS$ (where \mathbf{f} is the mechanical body force per unit mass in the reference configuration and \mathbf{T} is the nominal traction per unit reference area), is omitted in the expression of the element force vector \mathbf{f}_e since this term is already implemented in the ABAQUS environment.

IV.A.2.d Expression of the stiffness matrix

Then as well we can express the element stiffness matrix \mathbf{k}_e used in Eq. (IV.2.19)

$$\underbrace{\mathbf{k}_e}_{n_{dofel} \times n_{dofel}} = \int_{V_e} \underbrace{[\mathbf{G}]^T}_{n_{dofel} \times n_{tens}} \underbrace{[\mathbf{k}_e^{FB}]}_{n_{tens} \times n_{tens}} \underbrace{[\mathbf{G}]}_{n_{tens} \times n_{dofel}} dV + \frac{1}{\mu_0 K} \int_{V_e} \underbrace{[\mathbf{D}_{\tilde{\mathbf{A}}}]_{n_{dofel} \times 1}}_{1 \times n_{dofel}} \underbrace{[\mathbf{D}_{\tilde{\mathbf{A}}}]^T}_{1 \times n_{dofel}} dV, \quad (\text{IV.A.25})$$

where $[\mathbf{k}_e^{FB}]$ can be written

Then, based on the choice of elements that we made (8-node cubic element C3D8), we choose to approximate each integral by a numerical eight point Gaussian quadrature rule ¹⁰

$$\begin{aligned} \int_{\xi_1=-1}^1 \int_{\xi_2=-1}^1 \int_{\xi_3=-1}^1 f(\boldsymbol{\xi}) (\det \mathcal{J}) \, d\xi_1 \, d\xi_2 \, d\xi_3 &= \int_{\xi_1=-1}^1 \int_{\xi_2=-1}^1 \int_{\xi_3=-1}^1 g(\boldsymbol{\xi}) \, d\xi_1 \, d\xi_2 \, d\xi_3 \\ &\approx \sum_{I=1}^{n_{gp}=8} w_{gp}^{(I)} g(\boldsymbol{\xi}_{gp}^{(I)}), \end{aligned} \quad (\text{IV.A.29})$$

where $g = (\det \mathcal{J}) f$, and $\boldsymbol{\xi}_{gp}^{(I)}$ and $w_{gp}^{(I)}$ represent respectively the coordinates of the chosen Gauss points and their associated weight. In our case, we choose the following Gauss points and weights

$$\begin{aligned} \boldsymbol{\xi}_{gp}^{(1)} &= \frac{1}{\sqrt{3}} (-1, -1, -1), & w_{gp}^{(1)} &= 1, \\ \boldsymbol{\xi}_{gp}^{(2)} &= \frac{1}{\sqrt{3}} (-1, -1, -1), & w_{gp}^{(2)} &= 1, \\ \boldsymbol{\xi}_{gp}^{(3)} &= \frac{1}{\sqrt{3}} (-1, -1, -1), & w_{gp}^{(3)} &= 1, \\ \boldsymbol{\xi}_{gp}^{(4)} &= \frac{1}{\sqrt{3}} (-1, -1, -1), & w_{gp}^{(4)} &= 1, \\ \boldsymbol{\xi}_{gp}^{(5)} &= \frac{1}{\sqrt{3}} (-1, -1, -1), & w_{gp}^{(5)} &= 1, \\ \boldsymbol{\xi}_{gp}^{(6)} &= \frac{1}{\sqrt{3}} (-1, -1, -1), & w_{gp}^{(6)} &= 1, \\ \boldsymbol{\xi}_{gp}^{(7)} &= \frac{1}{\sqrt{3}} (-1, -1, -1), & w_{gp}^{(7)} &= 1, \\ \boldsymbol{\xi}_{gp}^{(8)} &= \frac{1}{\sqrt{3}} (-1, -1, -1), & w_{gp}^{(8)} &= 1. \end{aligned} \quad (\text{IV.A.30})$$

Here, it is important to specify that the penalty term added to numerically enforce the Coulomb gauge must be under-integrated to avoid any ‘locking phenomena’. For that purpose, to compute the second term of the element force vector \mathbf{f}_e in Eq. (IV.A.23) and the second term of the stiffness matrix \mathbf{k}_e in Eq. (IV.A.25), we will use only one Gauss point that has the following characteristics

$$\boldsymbol{\xi}_{gp}^{(0)} = (0, 0, 0), \quad w_{gp}^{(0)} = 2. \quad (\text{IV.A.31})$$

After computing the force vector \mathbf{f}_e and the stiffness matrix \mathbf{k}_e for each element in the user element subroutine, ABAQUS assembles the global force vector \mathbf{f} and the global stiffness matrix \mathbf{k} of the system.

The variational formulation written in Eq. (IV.2.1) leads (after a finite element discretization) to seek the vector of unknown nodal degrees of freedom \mathbf{q} by solving the (non-linear)

¹⁰ NOTE: A n -point Gaussian quadrature rule yields an exact result for polynomials of degree $2n - 1$ or less if a suitable choice of gauss points and associated weights is made.

equilibrium equation that takes the following form

$$\mathbf{f}(\mathbf{q}) = \mathbf{0}. \quad (\text{IV.A.32})$$

The Newton-Raphson method, based on the first order Taylor expansion of the global force vector about the previous iteration i is used

$$\mathbf{f}^{[i+1]} \approx \mathbf{f}^{[i]} + \Delta\mathbf{q}^{[i]} \cdot \mathbf{k}^{[i]} = \mathbf{0}. \quad (\text{IV.A.33})$$

The correction $\Delta\mathbf{q}^{[i]}$ that defines the current approximation $\mathbf{q}^{[i+1]}$ is

$$\Delta\mathbf{q}^{[i]} = \mathbf{q}^{[i+1]} - \mathbf{q}^{[i]}, \quad (\text{IV.A.34})$$

and the so called tangent stiffness matrix $\mathbf{k}^{[i]}$ at the previous iteration i is

$$\mathbf{k}^{[i]} = \left. \frac{\partial \mathbf{f}}{\partial \mathbf{q}} \right|_{\mathbf{q}^{[i]}}. \quad (\text{IV.A.35})$$

IV.A.3 Shape functions and their derivatives for an 8-node isoparametric cubic element (C3D8)

In this section, we give the shape functions corresponding to an eight node isoparametric cubic element (C3D8) as well as their derivatives.

In the local coordinate system of the element (see Fig. IV.14), the shape functions are defined via

$$\begin{aligned} N_1 &= \frac{1}{8}(1 - \xi_1)(1 - \xi_2)(1 - \xi_3), & N_2 &= \frac{1}{8}(1 + \xi_1)(1 - \xi_2)(1 - \xi_3), \\ N_3 &= \frac{1}{8}(1 + \xi_1)(1 + \xi_2)(1 - \xi_3), & N_4 &= \frac{1}{8}(1 - \xi_1)(1 + \xi_2)(1 - \xi_3), \\ N_5 &= \frac{1}{8}(1 - \xi_1)(1 - \xi_2)(1 + \xi_3), & N_6 &= \frac{1}{8}(1 + \xi_1)(1 - \xi_2)(1 + \xi_3), \\ N_7 &= \frac{1}{8}(1 + \xi_1)(1 + \xi_2)(1 + \xi_3), & N_8 &= \frac{1}{8}(1 - \xi_1)(1 + \xi_2)(1 + \xi_3). \end{aligned} \quad (\text{IV.A.36})$$

These shape functions verify the following conditions:

- $N_I(\boldsymbol{\xi}^{(J)}) = \delta_{IJ}$, where $\boldsymbol{\xi}^{(J)}$ is the coordinate vector of node J in the local coordinate system (Fig. IV.14)
- $\sum_{K=1}^{n_{ne}} N_K(\boldsymbol{\xi}) = 1$, for all $\boldsymbol{\xi}$ in the local coordinate system.

Then the derivatives of these shape functions in the local coordinate system read

$$\begin{aligned} \mathcal{G}_{11} &= \partial N_1 / \partial \xi_1 = -\frac{1}{8}(1 - \xi_2)(1 - \xi_3), & \mathcal{G}_{21} &= \partial N_2 / \partial \xi_1 = \frac{1}{8}(1 - \xi_2)(1 - \xi_3), \\ \mathcal{G}_{31} &= \partial N_3 / \partial \xi_1 = \frac{1}{8}(1 + \xi_2)(1 - \xi_3), & \mathcal{G}_{41} &= \partial N_4 / \partial \xi_1 = -\frac{1}{8}(1 + \xi_2)(1 - \xi_3), \\ \mathcal{G}_{51} &= \partial N_5 / \partial \xi_1 = -\frac{1}{8}(1 - \xi_2)(1 + \xi_3), & \mathcal{G}_{61} &= \partial N_6 / \partial \xi_1 = \frac{1}{8}(1 - \xi_2)(1 + \xi_3), \\ \mathcal{G}_{71} &= \partial N_7 / \partial \xi_1 = \frac{1}{8}(1 + \xi_2)(1 + \xi_3), & \mathcal{G}_{81} &= \partial N_8 / \partial \xi_1 = -\frac{1}{8}(1 + \xi_2)(1 + \xi_3), \end{aligned} \quad (\text{IV.A.37})$$

$$\begin{aligned}
\mathcal{G}_{12} = \partial N_1 / \partial \xi_2 &= -\frac{1}{8} (1 - \xi_1) (1 - \xi_3), & \mathcal{G}_{22} = \partial N_2 / \partial \xi_2 &= -\frac{1}{8} (1 + \xi_1) (1 - \xi_3), \\
\mathcal{G}_{32} = \partial N_3 / \partial \xi_2 &= \frac{1}{8} (1 + \xi_1) (1 - \xi_3), & \mathcal{G}_{42} = \partial N_4 / \partial \xi_2 &= \frac{1}{8} (1 - \xi_1) (1 - \xi_3), \\
\mathcal{G}_{52} = \partial N_5 / \partial \xi_2 &= -\frac{1}{8} (1 - \xi_1) (1 + \xi_3), & \mathcal{G}_{62} = \partial N_6 / \partial \xi_2 &= -\frac{1}{8} (1 + \xi_1) (1 + \xi_3), \\
\mathcal{G}_{72} = \partial N_7 / \partial \xi_2 &= \frac{1}{8} (1 + \xi_1) (1 + \xi_3), & \mathcal{G}_{82} = \partial N_8 / \partial \xi_2 &= \frac{1}{8} (1 - \xi_1) (1 + \xi_3),
\end{aligned} \tag{IV.A.38}$$

$$\begin{aligned}
\mathcal{G}_{13} = \partial N_1 / \partial \xi_3 &= -\frac{1}{8} (1 - \xi_1) (1 - \xi_2), & \mathcal{G}_{23} = \partial N_2 / \partial \xi_3 &= -\frac{1}{8} (1 + \xi_1) (1 - \xi_2), \\
\mathcal{G}_{33} = \partial N_3 / \partial \xi_3 &= -\frac{1}{8} (1 + \xi_1) (1 + \xi_2), & \mathcal{G}_{43} = \partial N_4 / \partial \xi_3 &= -\frac{1}{8} (1 - \xi_1) (1 + \xi_2), \\
\mathcal{G}_{53} = \partial N_5 / \partial \xi_3 &= \frac{1}{8} (1 - \xi_1) (1 - \xi_2), & \mathcal{G}_{63} = \partial N_6 / \partial \xi_3 &= \frac{1}{8} (1 + \xi_1) (1 - \xi_2), \\
\mathcal{G}_{73} = \partial N_7 / \partial \xi_3 &= \frac{1}{8} (1 + \xi_1) (1 + \xi_2), & \mathcal{G}_{83} = \partial N_8 / \partial \xi_3 &= \frac{1}{8} (1 - \xi_1) (1 + \xi_2).
\end{aligned} \tag{IV.A.39}$$

IV.A.4 ABAQUS UEL implementation for a 10-node isoparametric tetrahedral element

The choice of element type doesn't deeply modify the numerical implementation of the variational formulations presented in Sections IV.2.1 and IV.3.1. In this appendix we present the slight changes that need to be made in the code to use a quadratic ten node isoparametric tetrahedral element (C3D10) instead of a linear eight node isoparametric cubic element (C3D8). The element considered is shown in Fig. IV.15.

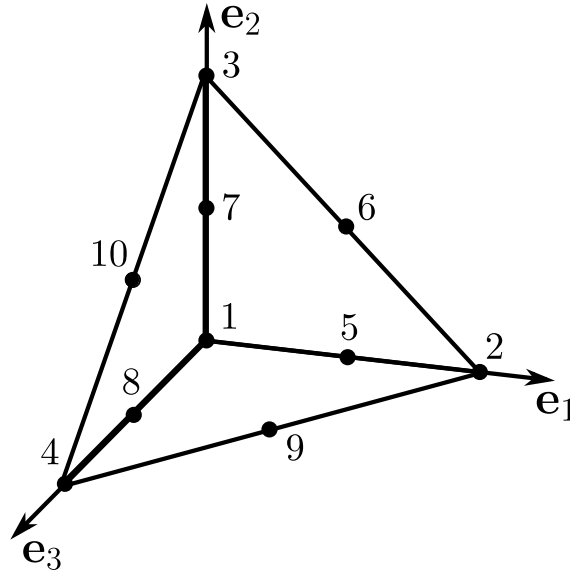


Figure IV.15: Schematic of a standard 10-node tetrahedral element

Appendix IV.A.2 remains entirely valid for such a tetrahedral element if we make the modifications that are presented in what follows. First, the number of nodes per element is modified since we have ten nodes instead of eight ($n_{ne} = 10$). Secondly, the shape functions and their derivatives with respect to the local coordinate system need to be changed as well and read

$$\begin{aligned}
N_1 &= (1 - \xi_1 - \xi_2 - \xi_3)(1 - 2\xi_1 - 2\xi_2 - 2\xi_3), \\
N_2 &= \xi_1(2\xi_1 - 1), \quad N_3 = \xi_2(2\xi_2 - 1), \quad N_4 = \xi_3(2\xi_3 - 1), \\
N_5 &= 4\xi_1(1 - \xi_1 - \xi_2 - \xi_3), \quad N_6 = 4\xi_1\xi_2, \quad N_7 = 4\xi_2(1 - \xi_1 - \xi_2 - \xi_3), \\
N_8 &= 4\xi_3(1 - \xi_1 - \xi_2 - \xi_3), \quad N_9 = 4\xi_1\xi_3, \quad N_{10} = 4\xi_2\xi_3.
\end{aligned} \tag{IV.A.40}$$

These shape functions verify the following conditions:

- $N_I(\boldsymbol{\xi}^{(J)}) = \delta_{IJ}$, where $\boldsymbol{\xi}^{(J)}$ is the coordinate vector of node J in the local coordinate system (Fig. IV.15)
- $\sum_{K=1}^{n_{ne}} N_K(\boldsymbol{\xi}) = 1$, for all $\boldsymbol{\xi}$ in the local coordinate system.

Then their derivatives in the local coordinate system is given by

$$\begin{aligned}
\mathcal{G}_{11} &= \partial N_1 / \partial \xi_1 = 4\xi_1 + 4\xi_2 + 4\xi_3 - 3, \quad \mathcal{G}_{21} = \partial N_2 / \partial \xi_1 = 4\xi_1 - 1, \\
\mathcal{G}_{31} &= \partial N_3 / \partial \xi_1 = 0, \quad \mathcal{G}_{41} = \partial N_4 / \partial \xi_1 = 0, \\
\mathcal{G}_{51} &= \partial N_5 / \partial \xi_1 = 4(1 - 2\xi_1 - \xi_2 - \xi_3), \quad \mathcal{G}_{61} = \partial N_6 / \partial \xi_1 = 4\xi_2, \\
\mathcal{G}_{71} &= \partial N_7 / \partial \xi_1 = -4\xi_2, \quad \mathcal{G}_{81} = \partial N_8 / \partial \xi_1 = -4\xi_3, \\
\mathcal{G}_{91} &= \partial N_9 / \partial \xi_1 = 4\xi_3, \quad \mathcal{G}_{101} = \partial N_{10} / \partial \xi_1 = 0,
\end{aligned} \tag{IV.A.41}$$

$$\begin{aligned}
\mathcal{G}_{12} &= \partial N_1 / \partial \xi_2 = 4\xi_1 + 4\xi_2 + 4\xi_3 - 3, \quad \mathcal{G}_{22} = \partial N_2 / \partial \xi_2 = 0, \\
\mathcal{G}_{32} &= \partial N_3 / \partial \xi_2 = 4\xi_2 - 1, \quad \mathcal{G}_{42} = \partial N_4 / \partial \xi_2 = 0, \\
\mathcal{G}_{52} &= \partial N_5 / \partial \xi_2 = -4\xi_1, \quad \mathcal{G}_{62} = \partial N_6 / \partial \xi_2 = 4\xi_1, \\
\mathcal{G}_{72} &= \partial N_7 / \partial \xi_2 = 4(1 - \xi_1 - 2\xi_2 - \xi_3), \quad \mathcal{G}_{82} = \partial N_8 / \partial \xi_2 = -4\xi_3, \\
\mathcal{G}_{92} &= \partial N_9 / \partial \xi_2 = 0, \quad \mathcal{G}_{102} = \partial N_{10} / \partial \xi_2 = 4\xi_3,
\end{aligned} \tag{IV.A.42}$$

$$\begin{aligned}
\mathcal{G}_{13} &= \partial N_1 / \partial \xi_3 = 4\xi_1 + 4\xi_2 + 4\xi_3 - 3, \quad \mathcal{G}_{23} = \partial N_2 / \partial \xi_3 = 0, \\
\mathcal{G}_{33} &= \partial N_3 / \partial \xi_3 = 0, \quad \mathcal{G}_{43} = \partial N_4 / \partial \xi_3 = 4\xi_3 - 1, \\
\mathcal{G}_{53} &= \partial N_5 / \partial \xi_3 = -4\xi_1, \quad \mathcal{G}_{63} = \partial N_6 / \partial \xi_3 = 0, \\
\mathcal{G}_{73} &= \partial N_7 / \partial \xi_3 = -4\xi_2, \quad \mathcal{G}_{83} = \partial N_8 / \partial \xi_3 = 4(1 - \xi_1 - \xi_2 - 2\xi_3), \\
\mathcal{G}_{93} &= \partial N_9 / \partial \xi_3 = 4\xi_1, \quad \mathcal{G}_{103} = \partial N_{10} / \partial \xi_3 = 4\xi_2.
\end{aligned} \tag{IV.A.43}$$

Lastly, in terms of calculation of the element volume integrals, we choose to approximate each integrals by a numerical four point Gaussian quadrature rule. The coordinates and weight of

the chosen Gauss integration points in the local coordinate system are given by

$$\begin{aligned}
 \boldsymbol{\xi}_{gp}^{(1)} &= (a, b, b), & w_{gp}^{(1)} &= \frac{1}{24}, \\
 \boldsymbol{\xi}_{gp}^{(2)} &= (b, a, b), & w_{gp}^{(2)} &= \frac{1}{24}, \\
 \boldsymbol{\xi}_{gp}^{(3)} &= (b, b, a), & w_{gp}^{(3)} &= \frac{1}{24}, \\
 \boldsymbol{\xi}_{gp}^{(4)} &= (b, b, b), & w_{gp}^{(4)} &= \frac{1}{24},
 \end{aligned} \tag{IV.A.44}$$

where $a = \frac{5 + 3\sqrt{5}}{20}$ and $b = \frac{5 - \sqrt{5}}{20}$.

The penalty term that numerically enforces the Coulomb gauge is still under-integrated to avoid any ‘locking phenomena’. For that purpose, the second term of the force vector \mathbf{f}_e and the second term of the stiffness matrix \mathbf{k}_e are computed using one Gauss integration point

$$\boldsymbol{\xi}_{gp}^{(0)} = \left(\frac{1}{4}, \frac{1}{4}, \frac{1}{4} \right), \quad w_{gp}^{(1)} = \frac{1}{6}. \tag{IV.A.45}$$

IV.B Complement for the F-M Theory

IV.B.1 First and second derivatives of the energy density, and of the invariants

In this section we provide the first and second derivatives of the total energy \widetilde{W}_M (see Eq. (IV.3.2)) with respect to \mathbf{F} , $\widetilde{\mathbf{B}}$ and \mathbf{M} .

$$\begin{aligned}
\frac{\partial \widetilde{W}_M}{\partial \mathbf{F}_{ij}}(\mathbf{F}, \widetilde{\mathbf{B}}, \mathbf{M}) &= \rho_0 \frac{\partial \psi_M}{\partial \mathbf{F}_{ij}}(\mathbf{F}, \mathbf{M}) - \frac{1}{2\mu_0 J} F_{ji}^{-1} \left\| \mathbf{F} \cdot \widetilde{\mathbf{B}} - \mu_0 \rho_0 \mathbf{M} \right\|^2 + \frac{1}{\mu_0 J} \left(F_{ir} \widetilde{B}_r - \mu_0 \rho_0 M_i \right) \widetilde{B}_j \\
\frac{\partial \widetilde{W}_M}{\partial \widetilde{B}_i}(\mathbf{F}, \widetilde{\mathbf{B}}, \mathbf{M}) &= \frac{1}{\mu_0 J} \left(F_{sr} \widetilde{B}_r - \mu_0 \rho_0 M_s \right) F_{si} \\
\frac{\partial \widetilde{W}_M}{\partial M_i}(\mathbf{F}, \widetilde{\mathbf{B}}, \mathbf{M}) &= \rho_0 \frac{\partial \psi_M}{\partial M_i}(\mathbf{F}, \mathbf{M}) - \rho_0 b_i^0 - \frac{\rho_0}{J} \left(F_{ir} \widetilde{B}_r - \mu_0 \rho_0 M_i \right) \\
\frac{\partial^2 \widetilde{W}_M}{\partial \mathbf{F}_{ij} \partial \mathbf{F}_{kl}}(\mathbf{F}, \widetilde{\mathbf{B}}, \mathbf{M}) &= \rho_0 \frac{\partial^2 \psi_M}{\partial \mathbf{F}_{ij} \partial \mathbf{F}_{kl}}(\mathbf{F}, \mathbf{M}) + \frac{1}{2\mu_0 J} \left(F_{lk}^{-1} F_{ji}^{-1} + F_{jk}^{-1} F_{li}^{-1} \right) \left\| \mathbf{F} \cdot \widetilde{\mathbf{B}} - \mu_0 \rho_0 \mathbf{M} \right\|^2 - \\
&\quad \frac{1}{\mu_0 J} \left[\left(F_{kr} \widetilde{B}_r - \mu_0 \rho_0 M_k \right) \widetilde{B}_l F_{ji}^{-1} + \left(F_{ir} \widetilde{B}_r - \mu_0 \rho_0 M_i \right) \widetilde{B}_j F_{lk}^{-1} \right] + \frac{1}{\mu_0 J} \delta_{ik} \widetilde{B}_l \widetilde{B}_j \\
\frac{\partial^2 \widetilde{W}_M}{\partial \mathbf{F}_{ij} \partial \widetilde{B}_k}(\mathbf{F}, \widetilde{\mathbf{B}}, \mathbf{M}) &= \frac{1}{\mu_0 J} \left[F_{ik} \widetilde{B}_j + \left(F_{ir} \widetilde{B}_r - \mu_0 \rho_0 M_i \right) \delta_{jk} - F_{ji}^{-1} F_{sk} \left(F_{sr} \widetilde{B}_r - \mu_0 \rho_0 M_s \right) \right] \\
\frac{\partial^2 \widetilde{W}_M}{\partial \mathbf{F}_{ij} \partial M_k}(\mathbf{F}, \widetilde{\mathbf{B}}, \mathbf{M}) &= \rho_0 \frac{\partial^2 \psi_M}{\partial \mathbf{F}_{ij} \partial M_k}(\mathbf{F}, \mathbf{M}) + \frac{\rho_0}{J} F_{ji}^{-1} \left(F_{kr} \widetilde{B}_r - \mu_0 \rho_0 M_k \right) - \frac{\rho_0}{J} \delta_{ik} \widetilde{B}_j \\
\frac{\partial^2 \widetilde{W}_M}{\partial \widetilde{B}_i \partial \widetilde{B}_j}(\mathbf{F}, \widetilde{\mathbf{B}}, \mathbf{M}) &= \frac{1}{\mu_0 J} C_{ij} \\
\frac{\partial^2 \widetilde{W}_M}{\partial \widetilde{B}_i \partial M_j}(\mathbf{F}, \widetilde{\mathbf{B}}, \mathbf{M}) &= -\frac{\rho_0}{J} F_{ji} \\
\frac{\partial^2 \widetilde{W}_M}{\partial M_i \partial M_j}(\mathbf{F}, \widetilde{\mathbf{B}}, \mathbf{M}) &= \rho_0 \frac{\partial^2 \psi_M}{\partial M_i \partial M_j}(\mathbf{F}, \mathbf{M}) + \frac{\mu_0 \rho_0^2}{J} \delta_{ij}
\end{aligned} \tag{IV.B.1}$$

To give the expression of the first and second derivatives of the solid's Helmholtz free energy, we apply the chain rule to ψ_M knowing that it is a function of ten independent invariants

(see Eq. (IV.3.3))

$$\begin{aligned}
\rho_0 \frac{\partial \psi_M}{\partial \mathbf{F}_{ij}}(\mathbf{F}, \mathbf{M}) &= \rho_0 \frac{\partial \psi_M}{\partial I_p^M} \frac{\partial I_p^M}{\partial \mathbf{F}_{ij}} \\
\rho_0 \frac{\partial \psi_M}{\partial M_i}(\mathbf{F}, \mathbf{M}) &= \rho_0 \frac{\partial \psi_M}{\partial I_p^M} \frac{\partial I_p^M}{\partial M_i} \\
\rho_0 \frac{\partial^2 \psi_M}{\partial \mathbf{F}_{ij} \partial \mathbf{F}_{kl}}(\mathbf{F}, \mathbf{M}) &= \rho_0 \frac{\partial^2 \psi_M}{\partial I_p^M \partial I_q^M} \frac{\partial I_p^M}{\partial \mathbf{F}_{ij}} \frac{\partial I_q^M}{\partial \mathbf{F}_{kl}} + \rho_0 \frac{\partial \psi_M}{\partial I_p^M} \frac{\partial^2 I_p^M}{\partial \mathbf{F}_{ij} \partial \mathbf{F}_{kl}} \\
\rho_0 \frac{\partial^2 \psi_M}{\partial \mathbf{F}_{ij} \partial M_k}(\mathbf{F}, \mathbf{M}) &= \rho_0 \frac{\partial^2 \psi_M}{\partial I_p^M \partial I_q^M} \frac{\partial I_p^M}{\partial \mathbf{F}_{ij}} \frac{\partial I_q^M}{\partial M_k} + \rho_0 \frac{\partial \psi_M}{\partial I_p^M} \frac{\partial^2 I_p^M}{\partial \mathbf{F}_{ij} \partial M_k} \\
\rho_0 \frac{\partial^2 \psi_M}{\partial M_i \partial M_j}(\mathbf{F}, \mathbf{M}) &= \rho_0 \frac{\partial^2 \psi_M}{\partial I_p^M \partial I_q^M} \frac{\partial I_p^M}{\partial M_i} \frac{\partial I_q^M}{\partial M_j} + \rho_0 \frac{\partial \psi_M}{\partial I_p^M} \frac{\partial^2 I_p^M}{\partial M_i \partial M_j}
\end{aligned} \tag{IV.B.2}$$

At this stage, it is helpful to compute the first and second derivatives of the invariants with respect to \mathbf{F} and \mathbf{M} . The derivatives of the mechanical invariants (I_i^M , $i \in [1, 5]$) are given in Appendix IV.A.1. For the coupled magneto-mechanical invariants, their derivatives are given in what follows.

** First order derivatives

***** ($\partial I_P / \partial \mathbf{F}$) *****

$$\begin{aligned}
\frac{\partial I_6^M}{\partial \mathbf{F}_{ij}} &= 0, & \frac{\partial I_7^M}{\partial \mathbf{F}_{ij}} &= 2 M_i M_r F_{rj}, \\
\frac{\partial I_8^M}{\partial \mathbf{F}_{ij}} &= 2 (M_i F_{sr} F_{qr} M_q F_{sj} + M_s F_{sr} F_{ir} M_q F_{qj}), & \frac{\partial I_9^M}{\partial \mathbf{F}_{ij}} &= 2 M_i N_j (M_s F_{sr} N_r), \\
\frac{\partial I_{10}^M}{\partial \mathbf{F}_{ij}} &= (M_s F_{sn} N_n) [M_i F_{rj} F_{rp} N_p + F_{ir} N_r M_p F_{pj} + M_r F_{rp} F_{ip} N_j] + (M_s F_{sn} F_{pn} F_{pr} N_r) M_i N_j,
\end{aligned} \tag{IV.B.3}$$

***** ($\partial I_P / \partial \mathbf{M}$) *****

$$\begin{aligned}
\frac{\partial I_6^M}{\partial M_i} &= 2 M_i, & \frac{\partial I_7^M}{\partial M_i} &= 2 F_{ir} F_{sr} M_s, & \frac{\partial I_8^M}{\partial M_i} &= 2 F_{in} F_{sn} F_{sp} F_{rp} M_r, \\
\frac{\partial I_9^M}{\partial M_i} &= 2 F_{ip} N_p (M_s F_{sr} N_r), & \frac{\partial I_{10}^M}{\partial M_i} &= (M_s F_{sn} N_n) [F_{ip} F_{rp} F_{rq} N_q] + (M_s F_{sn} F_{pn} F_{pr} N_r) F_{iq} N_q,
\end{aligned} \tag{IV.B.4}$$

** Second order derivatives

$$\begin{aligned}
 & \text{***** } (\partial^2 I_P / \partial \mathbf{M} \partial \mathbf{M}) \text{ *****} \\
 & \frac{\partial^2 I_6^M}{\partial M_i \partial M_j} = 2 \delta_{ij}, \quad \frac{\partial^2 I_7^M}{\partial M_i \partial M_j} = 2 F_{ir} F_{jr}, \quad \frac{\partial^2 I_8^M}{\partial M_i \partial M_j} = 2 F_{ir} F_{sr} F_{sp} F_{jp}, \\
 & \frac{\partial^2 I_9^M}{\partial M_i \partial M_j} = 2 F_{is} N_s F_{jr} N_r, \quad \frac{\partial^2 I_{10}^M}{\partial M_i \partial M_j} = F_{jn} N_n F_{ip} F_{rp} F_{rq} N_q + F_{jn} F_{pn} F_{pr} N_r F_{iq} N_q,
 \end{aligned} \tag{IV.B.5}$$

$$\begin{aligned}
 & \text{***** } (\partial^2 I_P / \partial \mathbf{F} \partial \mathbf{M}) \text{ *****} \\
 & \frac{\partial^2 I_6^M}{\partial F_{ij} \partial M_k} = 0, \quad \frac{\partial^2 I_7^M}{\partial F_{ij} \partial M_k} = 2 (\delta_{ik} F_{rj} M_r + M_i F_{kj}), \\
 & \frac{\partial^2 I_8^M}{\partial F_{ij} \partial M_k} = 2 (\delta_{ik} F_{sr} F_{qr} M_q F_{sj} + M_i F_{sr} F_{kr} F_{sj} + F_{kr} F_{ir} M_q F_{qj} + M_s F_{sr} F_{ir} F_{kj}), \\
 & \frac{\partial^2 I_9^M}{\partial F_{ij} \partial M_k} = 2 [\delta_{ik} N_j (M_s F_{sr} N_r) + M_i N_j F_{kr} N_r], \\
 & \frac{\partial^2 I_{10}^M}{\partial F_{ij} \partial M_k} = (F_{kn} N_n) [M_i F_{rj} F_{rp} N_p + F_{ir} N_r M_p F_{pj} + M_r F_{rp} F_{ip} N_j] + \\
 & \quad (M_s F_{sn} N_n) [\delta_{ik} F_{rj} F_{rp} N_p + F_{ir} N_r F_{kj} + F_{kp} F_{ip} N_j] + \\
 & \quad (F_{kn} F_{pn} F_{pr} N_r) M_i N_j + (M_s F_{sn} F_{pn} F_{pr} N_r) \delta_{ik} N_j,
 \end{aligned} \tag{IV.B.6}$$

$$\begin{aligned}
 & \text{***** } (\partial^2 I_P / \partial \mathbf{F} \partial \mathbf{F}) \text{ *****} \\
 & \frac{\partial^2 I_6^M}{\partial F_{ij} \partial F_{kl}} = 0, \quad \frac{\partial^2 I_7^M}{\partial F_{ij} \partial F_{kl}} = 2 M_i M_k \delta_{jl}, \\
 & \frac{\partial^2 I_8^M}{\partial F_{ij} \partial F_{kl}} = 2 \left(M_i F_{ql} M_q F_{kj} + M_i F_{sl} M_k F_{sj} + M_i F_{kr} F_{qr} M_q \delta_{jl} + \right. \\
 & \quad \left. M_k F_{il} M_q F_{qj} + M_s F_{sl} M_q F_{qj} \delta_{ik} + M_s F_{sr} F_{ir} M_k \delta_{jl} \right), \\
 & \frac{\partial^2 I_9^M}{\partial F_{ij} \partial F_{kl}} = 2 M_i N_j M_k N_l, \\
 & \frac{\partial^2 I_{10}^M}{\partial F_{ij} \partial F_{kl}} = (M_k N_l) [M_i F_{rj} F_{rp} N_p + F_{ir} N_r M_p F_{pj} + M_r F_{rp} F_{ip} N_j] + \\
 & \quad (M_s F_{sn} N_n) \left[M_i F_{kp} N_p \delta_{jl} + M_i F_{kj} N_l + \delta_{ik} N_l M_p F_{pj} + F_{ir} N_r M_k \delta_{jl} + \right. \\
 & \quad \left. M_k F_{il} N_j + M_r F_{rl} \delta_{ik} N_j \right] + (M_k F_{pl} F_{pr} N_r + M_s F_{sn} F_{kr} N_r \delta_{ln} + M_s F_{sn} F_{kn} N_l) M_i N_j.
 \end{aligned} \tag{IV.B.7}$$

IV.B.2 ABAQUS UEL implementation

In this section, we consider the same element (shown in Fig. IV.14) and we use the same notations as in Section IV.A.2.

This implies that all the derivations (from Eq. IV.A.10 to Eq. IV.A.22) made in Appendix IV.A.2 remain valid for the **F-M** theory. Hence, here we will simply give the final expressions of the element force vector \mathbf{f}_e and the element stiffness matrix \mathbf{k}_e .

Base on Eq. (IV.3.16), we can rewrite the force vector as

$$\mathbf{f}_e = \int_{V_e} [\mathbf{f}_e^{FM} - \mathbf{f}_e^M] [\mathbf{G}] dV + \frac{1}{\mu_0 \kappa} \int_{V_e} (\nabla \cdot \tilde{\mathbf{A}}) [\mathbf{D}_{\tilde{\mathbf{A}}}]^T dV, \quad (\text{IV.B.8})$$

where

$$\mathbf{f}_e^{FM} = \left[\frac{\partial \tilde{W}_M}{\partial F_{11}}, \frac{\partial \tilde{W}_M}{\partial F_{12}}, \frac{\partial \tilde{W}_M}{\partial F_{13}}, \frac{\partial \tilde{W}_M}{\partial F_{21}}, \frac{\partial \tilde{W}_M}{\partial F_{22}}, \frac{\partial \tilde{W}_M}{\partial F_{23}}, \frac{\partial \tilde{W}_M}{\partial F_{31}}, \frac{\partial \tilde{W}_M}{\partial F_{32}}, \frac{\partial \tilde{W}_M}{\partial F_{33}}, \frac{\partial \tilde{W}_M}{\partial \tilde{B}_1}, \frac{\partial \tilde{W}_M}{\partial \tilde{B}_2}, \frac{\partial \tilde{W}_M}{\partial \tilde{B}_3} \right], \quad (\text{IV.B.9})$$

and

$$\mathbf{f}_e^M = \left[D\tilde{W}_{F_{11}}^M, D\tilde{W}_{F_{12}}^M, D\tilde{W}_{F_{13}}^M, D\tilde{W}_{F_{21}}^M, D\tilde{W}_{F_{22}}^M, D\tilde{W}_{F_{23}}^M, D\tilde{W}_{F_{31}}^M, D\tilde{W}_{F_{32}}^M, D\tilde{W}_{F_{33}}^M, D\tilde{W}_{\tilde{B}_1}^M, D\tilde{W}_{\tilde{B}_2}^M, D\tilde{W}_{\tilde{B}_3}^M \right], \quad (\text{IV.B.10})$$

with

$$\begin{cases} D\tilde{W}_{F_{ij}}^M = \frac{\partial \tilde{W}_M}{\partial M_s} \left(\frac{\partial^2 \tilde{W}_M}{\partial M_s \partial M_r} \right)^{-1} \frac{\partial^2 \tilde{W}_M}{\partial M_r \partial F_{ij}}, \\ D\tilde{W}_{\tilde{B}_i}^M = \frac{\partial \tilde{W}_M}{\partial M_s} \left(\frac{\partial^2 \tilde{W}_M}{\partial M_s \partial M_r} \right)^{-1} \frac{\partial^2 \tilde{W}_M}{\partial M_r \partial \tilde{B}_i}. \end{cases} \quad (\text{IV.B.11})$$

Then, based on Eq. (IV.3.18), the stiffness matrix \mathbf{k}_e is expressed as

$$\mathbf{k}_e = \int_{V_e} [\mathbf{G}]^T [\mathbf{k}_e^{FM} - \mathbf{k}_e^M] [\mathbf{G}] dV + \frac{1}{\mu_0 \kappa} \int_{V_e} [\mathbf{D}_{\tilde{\mathbf{A}}}] [\mathbf{D}_{\tilde{\mathbf{A}}}]^T dV \quad (\text{IV.B.12})$$

The matrix \mathbf{k}_e^M is defined by

$$\mathbf{k}_e^M = \begin{bmatrix} D\tilde{W}_{FF1111}^M & \dots & \dots & \dots & \dots & \dots & D\tilde{W}_{FF1133}^M & D\tilde{W}_{F\tilde{B}111}^M & D\tilde{W}_{F\tilde{B}112}^M & D\tilde{W}_{F\tilde{B}113}^M \\ & \ddots & \dots & \dots & \dots & \dots & D\tilde{W}_{FF1233}^M & D\tilde{W}_{F\tilde{B}121}^M & D\tilde{W}_{F\tilde{B}122}^M & D\tilde{W}_{F\tilde{B}123}^M \\ & & \ddots & \dots & \dots & \dots & D\tilde{W}_{FF1333}^M & D\tilde{W}_{F\tilde{B}131}^M & D\tilde{W}_{F\tilde{B}132}^M & D\tilde{W}_{F\tilde{B}133}^M \\ & & & \ddots & \dots & \dots & D\tilde{W}_{FF2133}^M & D\tilde{W}_{F\tilde{B}211}^M & D\tilde{W}_{F\tilde{B}212}^M & D\tilde{W}_{F\tilde{B}213}^M \\ & & & & \ddots & \dots & D\tilde{W}_{FF2233}^M & D\tilde{W}_{F\tilde{B}221}^M & D\tilde{W}_{F\tilde{B}222}^M & D\tilde{W}_{F\tilde{B}223}^M \\ & & & & & \ddots & D\tilde{W}_{FF2333}^M & D\tilde{W}_{F\tilde{B}231}^M & D\tilde{W}_{F\tilde{B}232}^M & D\tilde{W}_{F\tilde{B}233}^M \\ & & & & & & \ddots & \dots & D\tilde{W}_{F\tilde{B}311}^M & D\tilde{W}_{F\tilde{B}312}^M & D\tilde{W}_{F\tilde{B}313}^M \\ & & & & & & & \ddots & D\tilde{W}_{F\tilde{B}321}^M & D\tilde{W}_{F\tilde{B}322}^M & D\tilde{W}_{F\tilde{B}323}^M \\ & & & & & & & & D\tilde{W}_{F\tilde{B}331}^M & D\tilde{W}_{F\tilde{B}332}^M & D\tilde{W}_{F\tilde{B}333}^M \\ & & & & & & & & & D\tilde{W}_{\tilde{B}\tilde{B}11}^M & D\tilde{W}_{\tilde{B}\tilde{B}12}^M & D\tilde{W}_{\tilde{B}\tilde{B}13}^M \\ & & & & & & & & & & D\tilde{W}_{\tilde{B}\tilde{B}22}^M & D\tilde{W}_{\tilde{B}\tilde{B}23}^M \\ & & & & & & & & & & & D\tilde{W}_{\tilde{B}\tilde{B}33}^M \end{bmatrix}, \quad (\text{IV.B.14})$$

with

$$\begin{cases} D\tilde{W}_{FFijkl}^M = \frac{\partial^2 \tilde{W}_M}{\partial F_{ij} \partial M_s} \left(\frac{\partial^2 \tilde{W}_M}{\partial M_s \partial M_r} \right)^{-1} \frac{\partial^2 \tilde{W}_M}{\partial M_r \partial F_{kl}}, \\ D\tilde{W}_{F\tilde{B}ijk}^M = \frac{\partial^2 \tilde{W}_M}{\partial F_{ij} \partial M_s} \left(\frac{\partial^2 \tilde{W}_M}{\partial M_s \partial M_r} \right)^{-1} \frac{\partial^2 \tilde{W}_M}{\partial M_r \partial \tilde{B}_k}, \\ D\tilde{W}_{\tilde{B}\tilde{B}ij}^M = \frac{\partial^2 \tilde{W}_M}{\partial \tilde{B}_i \partial M_s} \left(\frac{\partial^2 \tilde{W}_M}{\partial M_s \partial M_r} \right)^{-1} \frac{\partial^2 \tilde{W}_M}{\partial M_r \partial \tilde{B}_j}. \end{cases} \quad (\text{IV.B.15})$$

Finally, the calculation of the integrals and the method used to solve for the equilibrium equation remain the same as in Appendix IV.A.2.

Contents

V.1 Conclusion	169
V.2 Future work	171

V.1 Conclusion

This doctoral thesis brings a completely novel experimental, theoretical and numerical approach to study the macroscopic response of MREs.

After presenting an extensive literature survey in Chapter I, we introduce the motivation of the present study which is to cope with the lack of characterization of the coupled magneto-mechanical behavior of MREs up to large strains and high magnetic fields. Obtaining a phenomenological material model to be implemented in numerical analysis is necessary to improve the design of MRE-based devices.

The thesis continues with Chapter II that focuses on an experimental investigation of MREs. For the sake of capturing the coupled behavior, sample testing occurs under combined mechanical and magnetic fields. A new sample's design is envisioned in order to increase the uniformity of internal fields. For that purpose, an almost ellipsoidal MRE core terminated at both ends by 3D printed non-magnetic plastic heads is proposed. The fabrication of both isotropic and transversely isotropic samples, the influence of curing conditions and the surface treatment of iron particles are also discussed. It is shown that a chemical particle surface treatment prior to sample fabrication is necessary to prevent debonding of the particles from the matrix. This debonding phenomena (that can be neglected for purely mechanical experiments) has been highlighted during coupled magneto-mechanical tests.

In addition, we present in Chapter II, the novel magneto-mechanical testing setup where a uniaxial tensile machine can slide in place between the poles of a powerful electromagnet.

This setup allows simultaneous 3D mechanical and magnetic field measurements using optical techniques for strain measurements and Hall probes for magnetic ones. In particular, we detail a way to measure the internal magnetic field variables (i.e. the \mathbf{h} -field, the magnetization \mathbf{m} and the magnetic field \mathbf{b}) during deformation without displacing the Hall probes by using analytical expressions describing the decay of magnetic fields outside elliptical samples (and by measuring in-situ the distances between the probes and the sample).

In the last part of Chapter II, the results for both purely mechanical and coupled experiments for various volume fraction of particles and different microstructures are discussed. It is found that instabilities are ubiquitous in MREs. In the case of isotropic samples, Maxwell stresses at the solid/air interface lead to an expansion in the applied field direction and deformations up to 28% (for the highest volume fraction considered: 22%) have been observed for a magnetic field $\mathbf{b}_0 = 0.65$ T. Lots of experimental data are collected and will be used in Chapter III to propose a constitutive model for isotropic MREs.

In Chapter III, a continuum description to derive constitutive laws that accounts for finite strains and anisotropy is proposed. The energetic approach is used and requires an energy density function for the MRE solid. Multiple variational formulation alternatives are given based on different choices of the independent magnetic variable (\mathbf{B} , \mathbf{H} or \mathbf{M}) used in the energy function. We prove that all these admissible formulations are equivalent provided the fact that the different energy densities are linked by proper transformations (for instance, the \mathbf{F} - \mathbf{B} and \mathbf{F} - \mathbf{H} energy densities are linked by a partial Legendre's transform). A method to numerically implement these three formulations into finite elements codes is also presented. In the last part of Chapter III, we use these numerical codes to compute the material parameters based on experimental data obtained in Chapter II. In particular, by combining FEM simulation and least squares optimization algorithms, a fitting of all three formulations ψ_B , ψ_H and ψ_M is given. The proposed energy functions show excellent predictive capabilities.

Finally, Chapter IV details the numerical implementation of the different variational formulations proposed in Chapter III. For all three formulations, we show that isoparametric elements are well suited for coupled magneto-mechanical problems, and there is no need to use Nedelec elements. Then, unlike the numerical implementation of the \mathbf{F} - \mathbf{H} theory that doesn't create any particular issue due to the uniqueness of the scalar potential ϕ , we show that special attention is needed for the variational formulations based on the vector potential (i.e. the \mathbf{F} - \mathbf{B} and \mathbf{F} - \mathbf{M} theories). Indeed, the uniqueness of the vector potential requires an additional constraint, namely the Coulomb gauge, to be numerically enforced. For that purpose, the penalty method is chosen, and under-integration of that penalty term is necessary to avoid any locking phenomenon. In terms of the numerical implementation of the \mathbf{F} - \mathbf{M} theory, even though it is very similar to the numerical implementation of the \mathbf{F} - \mathbf{B} theory, the static condensation technique is needed to compute the magnetization vector \mathbf{M} inside each elements. Finally, before the presentation of the different patch tests used to validate the codes, we show which are the valid boundary conditions to use for the vector potential \mathbf{A} . Furthermore, we explain how to use the symmetry properties of a problem to reduce the computational resources needed to solve it.

To sum up, this thesis provides a complete roadmap (involving fabrication, experimental testing, modeling and numerical implementation) to study the highly coupled behavior of magneto-rheological elastomers. The tools developed can then be used to improve the design of MRE-based devices.

V.2 Future work

This work brought new answers but also paved the way for numerous new research to be conducted.

In terms of fabrication, a variety of different matrix (softer and harder, as well as various material formulations) and particle materials (size and geometry, hard magnetic particles) could be tested to characterize their aptitude for novel MRE applications.

In terms of experiments, obtaining extra experimental data for various deformation modes such as uni-axial compression, shear, bi-axial tension, etc..., could be helpful to further check the predictive capabilities of the proposed constitutive model. However, this task seems very complicated and it can be questioned if it is even possible to achieve uniform field distributions in strain and magnetization space for such loadings. The use of 3D finite element codes provided in this thesis might be key to conduct such a study. Additionally, the testing configuration in uni-axial tension with the applied field along the longest axis of the proposed specimen could give interesting results but further major developments of the testing apparatus would be needed.

In terms of modeling, more complex free energy density functions taking into account higher order invariants would further improve the prediction capabilities of the constitutive model. Moreover, the time-dependent material behavior (and thus relaxation, creep, stress recovery and fatigue experiments) as well as the temperature-dependent behavior (and thus the integration of heating/cooling systems into the experimental setup) would be important extensions of our existing model.

In a less distant future, all the immediately available tools developed in this thesis can be used to solve boundary value problems involving MRE-based devices. For instance, one could numerically study the different instabilities highlighted in experiments for both isotropic and transversely isotropic MREs (see Section II.5.2). Regarding the development of haptic devices such as tactile MRE interface, we recommend to numerically simulate the problem of a simple MRE disk subjected to a spatially localized magnetic field generated by an electromagnetic coil. Such a device has already been prototyped (see Fig. V.1) and experimentally tested (see Fig. V.2).

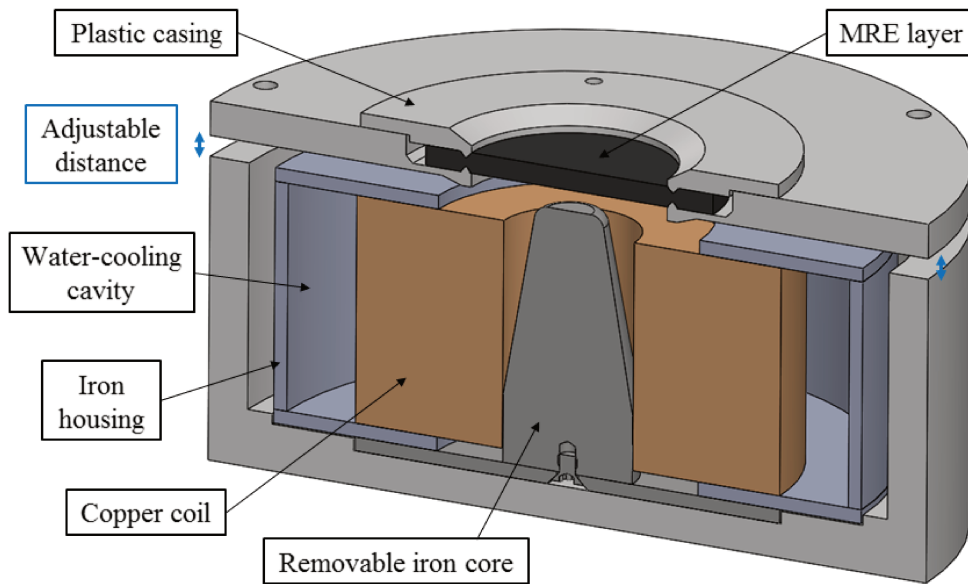


Figure V.1: Schematic (cross-section view along a symmetry plane) of the prototype of a simple MRE layer placed on top of an electromagnetic coil.

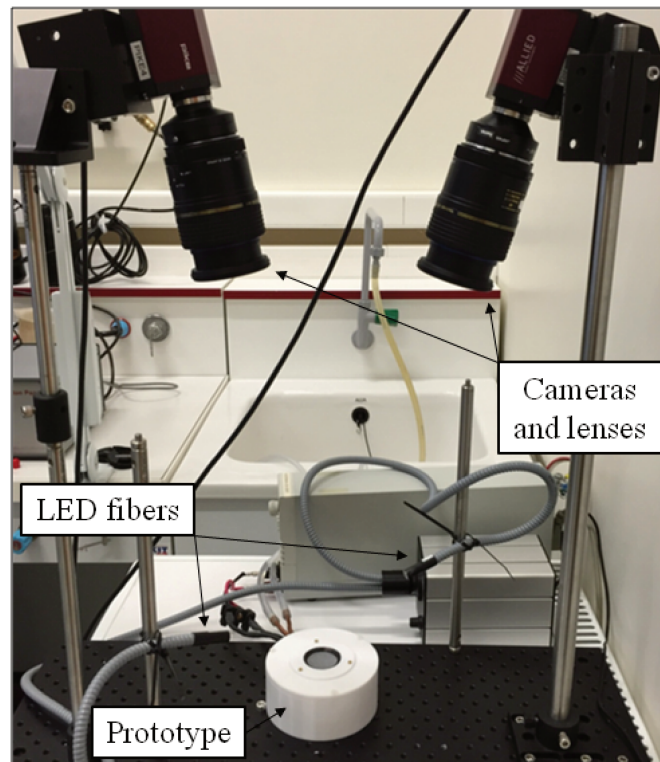


Figure V.2: 3D-DIC experimental setup used to access the full displacement field of the MRE disk under increasing value of the magnetic field generated within the prototype.

It would be very interesting to see if our constitutive model for isotropic materials can predict the measured experimental data (multiple configurations have been tested: with or without a tapered iron core placed at the center of the coil). In particular, we could try to obtain numerically the curve representing the vertical position of the center of the upper surface of the disk as a function of the applied current intensity (see the experimental data in Fig. V.3), or the curve representing the vertical displacement profile of the upper surface along the cross-section of a symmetry plane (see the experimental data in Fig. V.4). We could also envision to compare the result of a numerical simulation with experimental data on the full displacement field of the upper MRE-surface.

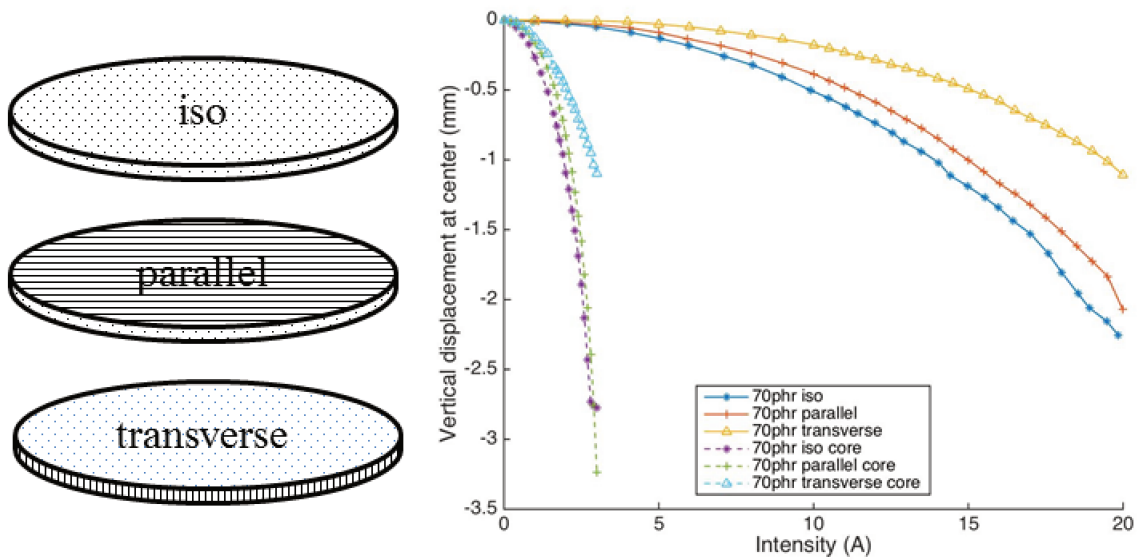


Figure V.3: Vertical displacement of the center of the upper surface of the MRE disk as a function of the current intensity for different tested configurations (with or without an iron core, with isotropic or transversely isotropic MREs).

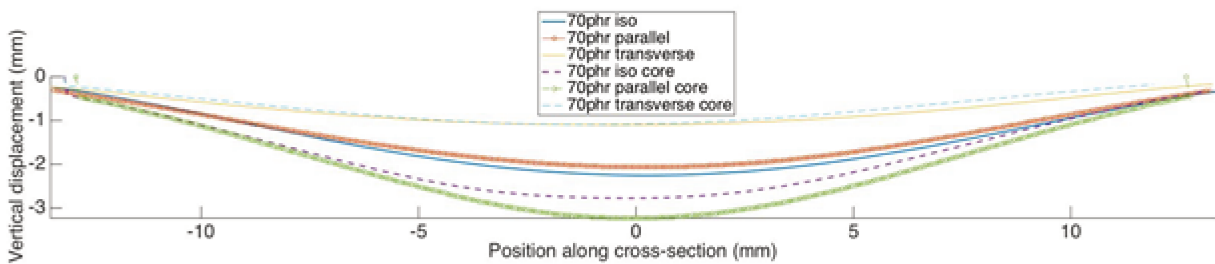


Figure V.4: Vertical displacement profiles along the cross-section of a symmetry plane for different tested configurations (with or without an iron core, with isotropic or transversely isotropic MREs).

BIBLIOGRAPHY

- [1] ISO 6892-1:2016. Metallic materials Tensile testing Part 1: Method of test at room temperature. International Organization for Standardization, Geneva, Switzerland, 2016. (Cited on page [31](#).)
- [2] J.E. Adkins. Symmetry relations for orthotropic and transversely isotropic materials. Archive for Rational Mechanics and Analysis, 4(1):193–213, 1959. (Cited on page [122](#).)
- [3] J.E. Adkins. Further symmetry relations for transversely isotropic materials. Archive for Rational Mechanics and Analysis, 5(1):263–274, 1960. (Cited on page [122](#).)
- [4] Th. Alshuth, M. Ramspeck, R.H. Schuster, B. Halbedel, and F. Zschunke. Magnetorheologische elastomere: Einfluss der partikelausrichtung auf die schaltbarkeit. Kautschuk Gummi Kunststoffe, (September 2007):448–455, 2007. (Cited on page [12](#).)
- [5] P.S. Antonel, G. Jorge, O.E. Perez, A. Butera, and A.G. Leyva. Magnetic and elastic properties of CoFe_2O_4 -polydimethylsiloxane magnetically oriented elastomer nanocomposites. Journal of Applied Physics, 110(043920):1–8, 2011. (Cited on page [12](#).)
- [6] G. Ausanio, C.L. Hison, V. Iannotti, L. Lanotte, and L. Lanotte. Magneto-piezoresistance in elastomagnetic composites. Journal of Applied Physics, 110(063903):1–5, 2011. (Cited on page [12](#).)
- [7] G. Ausanio, V. Iannotti, E. Ricciardi, L. Lanotte, and L. Lanotte. Magneto-piezoresistance in magnetorheological elastomers for magnetic induction gradient or position sensors. Sensors and Actuators A, 205:235–239, 2014. (Cited on page [11](#).)
- [8] Y. Bar-Cohen. Electroactive Polymer (EAP) Actuators as Artificial Muscles: Reality, Potential, and Challenges. SPIE, the International society for Optical Engineering, Bellingham, Washington, USA, 2004. (Cited on page [10](#).)
- [9] C. Bellan and G. Bossis. Field dependence of viscoelastic properties of mr elastomers. Journal of Modern Physics B, 16(17 & 18):2447–2453, 2002. (Cited on pages [18](#), [25](#), [30](#), and [53](#).)

-
- [10] A. Bergander, J. Lozada, T. Pössinger, and S. Roselier. EP 2504607 A2. Translatably and rotably semi-active device, 2012. (Cited on page 24.)
- [11] I. Bica. Magnetoresistor sensor with magnetorheological elastomers. Journal of Industrial and Engineering Chemistry, 17:83–89, 2011. (Cited on page 11.)
- [12] O. Biro and K. Preis. On the use of the magnetic vector potential in the finite-element analysis of three-dimensional eddy currents. IEEE Transactions on Magnetics, 25(4):3145–3159, 1989. (Cited on page 91.)
- [13] A. Boczkowska and S. Awietjan. Microstructure and properties of magnetorheological elastomers, chapter 6, pages 147–180. InTech, 2012. (Cited on pages 11 and 29.)
- [14] L. Bodelot, J-P. Voropaieff, and T. Pössinger. Experimental investigation of the coupled magneto-mechanical response in magnetorheological elastomers. Experimental Mechanics, 58(2):207 – 221, 2017. (Cited on pages 64, 65, 66, 68, and 134.)
- [15] C. Bolzmacher, G. Changeon, V. Plaud, S. Roselier, J. Lozada, and M. Hafez. Tactile refreshable screen based on magneto-rheological fluids for map exploration and navigation tasks. SPIE Proceedings, 8066, 2011. (Cited on page 13.)
- [16] T. Borbath, S. Günther, D.Y. Borin, Th. Gundermann, and S. Odenbach. X-ray microtomographic analysis of magnetic field-induced phase transitions in magnetorheological elastomers. Smart Materials and Structures, 21(105018):1–7, 2012. (Cited on page 12.)
- [17] L. Borcea and O. Bruno. On the magneto-elastic properties of elastomer-ferromagnet composites. Journal of the Mechanics and Physics of Solids, 49:2877–2919, 2001. (Cited on pages 16, 25, and 28.)
- [18] H. Böse. Viscoelastic properties of silicone-based magnetorheological elastomers. Journal of Modern Physics B, 21(29):4790–4797, 2007. (Cited on page 12.)
- [19] H. Böse, R. Rabindranath, and J. Ehrlich. Soft magnetorheological elastomers as new actuators for valves. Journal of Intelligent Material Systems and Structures, 23(9):989–994, 2012. (Cited on page 14.)
- [20] G. Bossis, C. Abbo, S. Cutillas, S. Lacis, and C. Metayer. Electroactive and electrostructured elastomers. Journal of Modern Physics B, 15(6 & 7):564–573, 2001. (Cited on pages 18 and 25.)
- [21] W.F. Brown. Magnetostatic Principles. North-Holland Publishing Company, Amsterdam, 1962. (Cited on page 31.)
- [22] W.F. Brown. Magnetoelastic Interactions. Springer New York, 1966. (Cited on pages 65, 74, 120, and 121.)
- [23] A.L. Browne and N.L. Johnson. US 0266417 A1. Active material based fasteners including cable ties and twist ties, 2012. (Cited on page 14.)

-
- [24] R. Bustamante. Mathematical modelling of non-linear magneto- and electro-active rubber-like materials. PhD thesis, University of Glasgow, 2007. (Cited on pages 9, 24, and 25.)
- [25] R. Bustamante. Transversely isotropic nonlinear magneto-active elastomers. Acta Mechanica, 210:183–214, 2010. (Cited on page 17.)
- [26] R. Bustamante, A. Dorfmann, and R.W. Ogden. On variational formulations in non-linear magnetoelastostatics. Mathematics and Mechanics of Solids, 13:725–745, 2008. (Cited on pages 16, 71, 72, 73, and 75.)
- [27] R. Bustamante, A. Dorfmann, and R.W. Ogden. Nonlinear electroelastostatics: a variational framework. Journal of Applied Mathematics and Physics, 60(1):154–177, 2009. (Cited on pages 77 and 83.)
- [28] J.D. Carlson. US 6296088 B1. Magnetorheological fluid seismic damper, 2001. (Cited on page 24.)
- [29] J.D. Carlson and M.R. Jolly. MR fluid, foam and elastomer devices. Mechatronics, 10:555–569, 2000. (Cited on pages 10, 12, and 25.)
- [30] D.J. Charlton, J. Yang, and K.K. Teh. A review of methods to characterize rubber elastic behavior for use in finite element analysis. Rubber Chemistry and Technology, 67(3):481–503, 1994. (Cited on page 17.)
- [31] L. Chen, X.L. Gong, W.Q. Jiang, J.J. Yao, H.X. Deng, and W.H. Li. Investigation on magnetorheological elastomers based on natural rubber. Journal of Materials Science, 42:5483–5489, 2007. (Cited on pages 11 and 25.)
- [32] L. Chen, X.L. Gong, and W.H. Li. Microstructures and viscoelastic properties of anisotropic magnetorheological elastomers. Smart Materials and Structures, 16, 2007. (Cited on page 12.)
- [33] A. Ciesielski. An introduction to rubber technology. iSmithers Rapra Publishing, Shawbury, 1999. (Cited on page 35.)
- [34] E. Coquelle. Propriétés élastiques et viscoélastiques de matériaux composites adaptifs. PhD thesis, University of Nice Sophia-Antipolis, 2004. (Cited on pages 18 and 19.)
- [35] E. Coquelle and G. Bossis. Magnetostriction and piezoresistivity in elastomers filled with magnetic particles. Journal of Advanced Science, 17:132–138, 2005. (Cited on pages 25 and 29.)
- [36] E. Coquelle and G. Bossis. Mullins effect in elastomers filled with particles aligned by a magnetic field. International Journal of Solids and Structures, 43:7659–7672, 2006. (Cited on page 26.)

- [37] R. Corcolle, L. Daniel, and F. Bouillault. Optimal design of magnetostrictive composites: An analytical approach. IEEE Transactions on Magnetics, 44(1):17–23, 2008. (Cited on pages 16 and 65.)
- [38] R.J. Crist. US 7584685 B2. Active vibrational damper, 2009. (Cited on pages 13, 17, and 25.)
- [39] K. Danas. Effective response of classical, auxetic and chiral magnetoelastic materials by use of a new variational principle. Journal of the Mechanics and Physics of Solids, 105:25–53, 2017. (Cited on pages 16, 65, 67, 71, 72, 73, 74, 75, 77, 86, 101, 120, and 137.)
- [40] K. Danas, S.V. Kankanala, and N. Triantafyllidis. Experiments and modeling of iron-particle-filled magnetorheological elastomers. Journal of the Mechanics and Physics of Solids, 60:120–138, 2012. (Cited on pages 5, 6, 17, 21, 25, 27, 28, 29, 64, 65, 71, 72, 85, 97, and 122.)
- [41] K. Danas and N. Triantafyllidis. Instability of a magnetoelastic layer resting on a non-magnetic substrate. Journal of the Mechanics and Physics of Solids, 69:67–83, 2014. (Cited on pages 5, 6, 17, 21, and 120.)
- [42] L.C. Davis. Model of magnetorheological elastomers. Journal of Applied Physics, 85(6):3348–3351, 1999. (Cited on pages 16, 25, and 30.)
- [43] M.E.J. Dekkers and D. Heikens. The effect of interfacial adhesion on the tensile behavior of polystyrene-glass-bead composites. Journal of Applied Polymer Science, 28:3809–3815, 1983. (Cited on page 26.)
- [44] G. Diguët. Huge magnetostriction of magneto-rheological composite. PhD thesis, University of Grenoble, 2010. (Cited on pages 11, 12, and 20.)
- [45] G. Diguët, E. Beaunon, and J.Y. Cavallé. From dipolar interactions of a random distribution of ferromagnetic particles to magnetostriction. Journal of Magnetism and Magnetic Materials, 321:396–401, 2008. (Cited on pages 16, 25, and 28.)
- [46] G. Diguët, E. Beaunon, and J.Y. Cavallé. Shape effect in the magnetostriction of ferromagnetic composite. Journal of Magnetism and Magnetic Materials, 322:3337–3341, 2010. (Cited on pages 25, 27, 28, 30, 50, and 64.)
- [47] A. Dorfmann and R.W. Ogden. Magnetoelastic modelling of elastomers. European Journal of Mechanics - A/Solids, 22(4):497–507, 2003. (Cited on pages 16, 25, 65, 71, 72, 73, 75, and 77.)
- [48] A. Dorfmann and R.W. Ogden. A constitutive model for the Mullins effect with permanent set in particle-reinforced rubber. International Journal of Solids and Structures, 41:1855–1878, 2004. (Cited on page 111.)

-
- [49] A. Dorfmann and R.W. Ogden. Some problems in nonlinear magnetoelasticity. Zeitschrift für angewandte Mathematik und Physik ZAMP, 56(4):718–745, 2005. (Cited on pages [17](#), [71](#), [73](#), and [77](#).)
- [50] T.A. Duenas and G.P. Carman. Large magnetostrictive response of Terfenol-D resin composites. Journal of Applied Physics, 87(9):4696–4701, 2000. (Cited on page [12](#).)
- [51] ASTM E8-01. Standard test methods for tension testing of metallic materials. ASTM International, West Conshohocken, 2001. (Cited on page [31](#).)
- [52] L.D. Elie and J.M. Ginder. EP 0784163 B1. Variable stiffness bushing using magnetorheological elastomers, 2002. (Cited on pages [13](#) and [25](#).)
- [53] Y.C. Fan, X.L. Gong, S.H. Xuan, W. Zhang, J. Zheng, and W.Q. Jiang. Interfacial friction damping properties in magnetorheological elastomers. Smart Materials and Structures, 20(035007):1–8, 2011. (Cited on page [12](#).)
- [54] M. Farshad and A. Benine. Magnetoactive elastomer composites. Polymer Testing, 23:347–353, 2004. (Cited on pages [12](#), [18](#), and [25](#).)
- [55] M. Farshad and M. Le Roux. A new active noise abatement barrier system. Polymer Testing, 23:855–860, 2004. (Cited on pages [13](#) and [25](#).)
- [56] M. Farshad and M. Le Roux. Compression properties of magnetostrictive polymer composite gels. Polymer Testing, 24:163–168, 2005. (Cited on page [18](#).)
- [57] S.Y. Fu, X.Q. Feng, B. Lauke, and Y.W. Mai. Effects of particle size, particle/matrix interface adhesion and particle loading on mechanical properties of particulate-polymer composites. Composites: Part B, 39:933–961, 2008. (Cited on page [26](#).)
- [58] E. Galipeau and P. Ponte Castañeda. The effect of particle shape and distribution on the macroscopic behavior of magnetoelastic composites. International Journal of Solids and Structures, 49:1–17, 2012. (Cited on page [64](#).)
- [59] E. Galipeau and P. Ponte Castañeda. A finite-strain constitutive model for magnetorheological elastomers: Magnetic torques and fiber rotations. Journal of the Mechanics and Physics of Solids, 61:1065–1090, 2013. (Cited on pages [16](#) and [65](#).)
- [60] E. Galipeau and P. Ponte Castañeda. Giant field-induced strains in magnetoactive elastomer composites. Proceedings of the Royal Society A, 469(20130385), 2013. (Cited on pages [16](#) and [65](#).)
- [61] E. Galipeau, S. Rudykh, G. DeBotton, and P. Ponte Castañeda. Magnetoactive elastomers with periodic and random microstructures. International Journal of Solids and Structures, 51:3012–3024, 2014. (Cited on pages [16](#) and [120](#).)
- [62] A.N. Gent and B.K. Park. Failure processes in elastomers at or near a rigid spherical inclusion. Journal of Materials Science, 19:1947–1956, 1984. (Cited on page [26](#).)

- [63] J.M. Ginder, S.M. Clark, W.F. Schlotter, and M.E. Nichols. Magnetostrictive phenomena in magnetorheological elastomers. Journal of Modern Physics B, 16(17 & 18):2412–2418, 2002. (Cited on pages 20, 28, and 30.)
- [64] J.M. Ginder, M.E. Nichols, L.D. Elie, and S.M. Clark. Controllable-stiffness components based on magnetorheological elastomers. Smart Structures and Materials, 3985:418–425, 2000. (Cited on pages 10, 12, 25, and 64.)
- [65] J.M. Ginder, M.E. Nichols, L.D. Elie, and J.L. Tardiff. Magnetorheological elastomers: properties and applications. SPIE Proceedings, 3675:131–138, 1999. (Cited on pages 10, 20, and 64.)
- [66] X.L. Gong, L. Chen, and J.F. Li. Study of utilizable magnetorheological elastomers. Journal of Modern Physics B, 21(29):4875–4882, 2007. (Cited on pages 11 and 25.)
- [67] X.L. Gong, X.Z. Zhang, and P.Q. Zhang. Fabrication and characterization of isotropic magnetorheological elastomers. Polymer Testing, 24:669–676, 2005. (Cited on pages 12 and 25.)
- [68] S.R. Gorodkin, R.O. James, and W.I. Kordonski. Magnetic properties of carbonyl iron particles in magnetorheological fluids. Journal of Physics: Conference Series, 149(012051):1–4, 2009. (Cited on page 35.)
- [69] A.E Green and J.E Adkins. Large Elastic Deformations. Clarendon Press, Oxford, 1970. (Cited on page 85.)
- [70] H. Gross, F. Blechinger, and B. Aichtner. Handbook of Optical Systems. Wiley-VCH, Berlin, 2005. (Cited on page 41.)
- [71] X.C. Guan, X.F. Dong, and J.P. Ou. Magnetostrictive effect of magnetorheological elastomer. Journal of Magnetism and Magnetic Materials, 320:158–163, 2008. (Cited on pages 25 and 51.)
- [72] D. Günther, D.Y. Borin, S. Günther, and S. Odenbach. X-ray micro-tomographic characterization of field-structured magnetorheological elastomers. Smart Materials and Structures, 21(015005):1–7, 2012. (Cited on page 12.)
- [73] M. Guyot. Mesure des paramètres magnétiques fondamentaux des matériaux ferromagnétiques ou ferrimagnétiques, chapter Rappels sur les paramètres fondamentaux du magnétisme, pages 5–24. CNRS Formation, Meudon, 1994. (Cited on page 12.)
- [74] E.H. Hall. On a new action of the magnet on electric currents. American Journal of Mathematics, 2(3):287–292, 1879. (Cited on page 42.)
- [75] B. Hamrock. Mechanical Engineers’ Handbook: Materials and Mechanical Design. John Wiley and Sons, Columbus, Ohio, 2006. (Cited on page 24.)

-
- [76] Y. Han, A. Mohla, X. Huang, W. Hong, and LE. Faidley. Magnetostriction and field stiffening of magneto-active elastomers. International Journal of Applied Mechanics, 7(1550001), 2015. (Cited on page 53.)
- [77] J.A. Harvey. Smart Materials. In Mechanical Engineers' Handbook, volume 1. Wiley, 3rd edition, 2006. (Cited on pages 9 and 10.)
- [78] Z. Hashin. Analysis of composite materials. Journal of Applied Mechanics, 50:481–505, 1983. (Cited on page 46.)
- [79] W.M. Haynes. CRC Handbook of Chemistry and Physics. CRC Press, Florida, 2013. (Cited on pages 34 and 38.)
- [80] Y. Hu, Y.L. Wang, X.L. Gong, X.Q. Gong, X.Z. Zhang, W.Q. Jiang, P.Q. Zhang, and Z.Y. Chen. New magnetorheological elastomers based on polyurethane/si-rubber hybrid. Polymer Testing, 24(3):324–329, 2005. (Cited on page 11.)
- [81] D. Ivaneyko, V. Toshchevikov, D. Borin, M. Saphiannikova, and G. Heinrich. Mechanical properties of magneto-sensitive elastomers in a homogeneous magnetic field: Theory and experiment. Macromolecular Symposia, 338(1):96–107, 2014. (Cited on page 64.)
- [82] Y. Jansen, T. Karrer, and J. Borchers. Mudpad: tactile feedback and haptic texture overlay for touch surfaces. Proceedings of the ACM International Conference on Interactive Tabletops and Surfaces, pages 11–14, 2010. (Cited on page 13.)
- [83] A. Javili, G. Chatzigeorgiou, and P. Steinmann. Computational homogenization in magneto-mechanics. International Journal of Solids and Structures, 50(25-26):4197–4216, 2013. (Cited on pages 16 and 120.)
- [84] M.R. Jolly, J.D. Carlson, B.C. Munoz, and T.A. Bullions. The magnetoviscoelastic response of elastomer composites consisting of ferrous particles embedded in a polymer matrix. Journal of Intelligent Material Systems and Structures, 7:613–622, 1996. (Cited on pages 12, 16, 20, 25, and 65.)
- [85] JP. Joule. On the effects of magnetism upon the dimensions of iron and steel bars. The London, Edinburgh, and Dublin Philosophical Magazine and Journal of Science, 30:76–87, 1847. (Cited on page 27.)
- [86] J. Kaleta, M. Krolewicz, and D. Lewandowski. Magnetomechanical properties of anisotropic and isotropic magnetorheological composites with thermoplastic elastomer matrices. Smart Materials and Structures, 20(085006):1–13, 2011. (Cited on page 11.)
- [87] K.A. Kalina, P. Metsch, and M. Kästner. Microscale modeling and simulation of magnetorheological elastomers at finite strains: A study on the influence of mechanical preloads. International Journal of Solids and Structures, 102-103:286–296, 2016. (Cited on pages 16 and 120.)

-
- [88] M. Kallio. The elastic and damping properties of magnetorheological elastomers. PhD thesis, Tampere University of Technology, 2005. (Cited on pages [11](#), [12](#), [18](#), [19](#), [25](#), and [30](#).)
- [89] S.V. Kankanala. On finitely strained magnetoelastic solids. PhD thesis, University of Michigan, 2007. (Cited on pages [20](#) and [25](#).)
- [90] S.V. Kankanala and N. Triantafyllidis. On finitely strained magnetorheological elastomers. Journal of the Mechanics and Physics of Solids, 52:2869–2908, 2004. (Cited on pages [5](#), [6](#), [16](#), [21](#), [25](#), [65](#), [71](#), [72](#), [74](#), [79](#), [80](#), [81](#), [85](#), [97](#), [106](#), [120](#), and [122](#).)
- [91] S.V. Kankanala and N. Triantafyllidis. Magnetoelastic buckling of a rectangular block in plane strain. Journal of the Mechanics and Physics of Solids, 56:1147–1169, 2008. (Cited on page [52](#).)
- [92] L. Kari. Magneto-sensitive elastomers - theory and applications, chapter Constitutive Models for Rubber VIII Chapter 2, pages 13–18. CRC Press 2013, 2013. (Cited on pages [12](#) and [16](#).)
- [93] M-A. Keip and M. Rambausek. A multiscale approach to the computational characterization of magnetorheological elastomers. International Journal of Numerical Methods in Engineering, 107(4):338–360, 2016. (Cited on pages [16](#), [64](#), and [120](#).)
- [94] M-A. Keip and M. Rambausek. Computational and analytical investigations of shape effects in the experimental characterization of magnetorheological elastomers. International Journal of Solids and Structures, 121:1–20, 2017. (Cited on page [64](#).)
- [95] M.S. Kim, K.M. Yang, S.H. Lee, J.H. Yoon, U.C. Jeong, I.H. Yang, and J.E. Oh. US 8844914 B2. Variable differential mount apparatus using magnetorheological elastomer, 2014. (Cited on pages [13](#) and [25](#).)
- [96] J.H. Koo, A. Dawson, and H.J. Jung. Characterization of actuation properties of magnetorheological elastomers with embedded hard magnetic particles. Journal of Intelligent Material Systems and Structures, 23(9):1049–1054, 2012. (Cited on page [12](#).)
- [97] A. Kovetz. Electromagnetic Theory. Oxford, New York, 2000. (Cited on page [120](#).)
- [98] K.U. Kyung, J.U. Lee, S. Park, H. Prahlad, and P. von Guggenberg. Flexible visio-haptic display. Haptics: Perception, Devices, Mobility, and Communication, 7283:206–209, 2012. (Cited on page [13](#).)
- [99] C.H. Lee and M.G. Jang. Virtual surface characteristics of a tactile display using magneto-rheological fluids. Sensors, 11(3):2845–2856, 2011. (Cited on page [13](#).)
- [100] V. Lefèvre, K. Danas, and O. Lopez-Pamies. A general result for the magnetoelastic response of isotropic suspensions of iron and ferrofluid particles in rubber, with applications to spherical and cylindrical specimens. Journal of the Mechanics and Physics of Solids, 107:343–364, 2017. (Cited on pages [16](#), [65](#), [120](#), and [144](#).)

-
- [101] M. Lokander. Performance of magnetorheological rubber materials. PhD thesis, KTH Stockholm, 2004. (Cited on page [12](#).)
- [102] M. Lokander and B. Stenberg. Performance of isotropic magnetorheological rubber materials. Polymer Testing, 22:245–251, 2003. (Cited on page [25](#).)
- [103] O. Lopez-Pamies. A new i1-based hyperelastic model for rubber elastic materials. Comptes Rendus Mecanique, 338(1):3–11, 2009. (Cited on pages [86](#) and [132](#).)
- [104] J. Maas and D. Uhlenbusch. Experimental and theoretical analysis of the actuation behavior of magnetoactive elastomers. Smart Materials and Structures, 25(10):104002, 2016. (Cited on page [64](#).)
- [105] J.E. Martin, R.A. Anderson, D. Read, and G. Gulley. Magnetostriction of field-structured magnetoelastomers. Physical Review E, 74(051507):1–17, 2006. (Cited on pages [12](#), [16](#), [19](#), [25](#), [27](#), [28](#), and [29](#).)
- [106] J.E. Martin, R.A. Anderson, and C.P. Tigges. Simulation of the athermal coarsening of composites structured by a uniaxial field. Journal of Chemical Physics, 108(9):3765–3787, 1998. (Cited on page [11](#).)
- [107] J.E. Martin, E. Venturini, G.L. Gulley, and J. Williamson. Using triaxial magnetic fields to create high susceptibility particle composites. Physical Review E, 69(021508):1–15, 2004. (Cited on page [11](#).)
- [108] J.E. Martin, E. Venturini, J. Odinek, and R.A. Anderson. Anisotropic magnetism in field-structured composites. Physical Review E, 61(3):2818–2830, 2000. (Cited on page [11](#).)
- [109] P.R. Marur. US 0087985 A1. Magneto-rheological elastomer-based vehicle suspension, 2013. (Cited on pages [13](#) and [25](#).)
- [110] G.A Maugin and A.C Eringen. A continuum theory of deformable ferrimagnetic bodies. i. field equations. Journal of Mathematical Physics, 13(9):143–155, 1972. (Cited on page [65](#).)
- [111] G.A Maugin and A.C Eringen. A continuum theory of deformable ferrimagnetic bodies. ii. thermodynamics, constitutive theory. Journal of Mathematical Physics, 13(9):1334–1347, 1972. (Cited on page [65](#).)
- [112] D.C. Meeker. FEMM - finite element method magnetics version 4.2, November 2013. (Cited on page [19](#).)
- [113] C. Miehe and J. Keck. Superimposed finite elastic-viscoelastic-plastoelastic stress response with damage in filled rubbery polymers. Experiments, modelling and algorithmic implementation. Journal of the Mechanics and Physics of Solids, 48:323–365, 2000. (Cited on pages [26](#) and [46](#).)

- [114] C. Miehe, D. Vallicotti, and S. Teichtmeister. Homogenization and multiscale stability analysis in finite magneto-electro-elasticity. application to soft matter ee, me and mee composites. Computer Methods in Applied Mechanics and Engineering, 300:294–346, 2016. (Cited on pages 16, 120, and 121.)
- [115] F.C. Moon and Y.H. Pao. Magnetoelastic buckling of a thin plate. Journal of Applied Mechanics, 35(1):53–58, 1968. (Cited on page 48.)
- [116] MSC-Software. Whitepaper. Nonlinear finite element analysis of elastomers, 2010. (Cited on page 17.)
- [117] L. Mullins. Effect of stretching on the properties of rubber. Rubber Chemistry and Technology, 21:281–300, 1948. (Cited on page 26.)
- [118] L. Mullins and N.R. Tobin. Theoretical model for the elastic behavior of filler-reinforced vulcanized rubbers. Rubber Chemistry and Technology, 30(2):555–571, 1957. (Cited on page 26.)
- [119] R.W. Ogden. Mechanics and electrodynamics of magneto- and electro-elastic materials, volume 527, chapter Magnetostatics: from basic principles to nonlinear interactions in deformable media, pages 107–152. Springer Vienna, 2011. (Cited on pages 16 and 25.)
- [120] J.A. Osborne. Demagnetizing factors of the general ellipsoid. Physical Review, 67(11&12):351–357, 1945. (Cited on pages 27, 29, 31, and 67.)
- [121] Y-H. Pao. Electromagnetic forces in deformable continua. Mechanics today, Volume 4, Pergamon Press, Inc, New York, p. 209-305, 1978. (Cited on page 65.)
- [122] Y-H. Pao and C-S. Yeh. A linear theory for soft ferromagnetic elastic solids. International Journal for Engineering Science, 11(4):415–436, 1973. (Cited on page 65.)
- [123] A.C. Pipkin and R.S. Rivlin. The formulation of constitutive equations in continuum physics. I. Archive for Rational Mechanics and Analysis, 4(1):129–144, 1959. (Cited on page 122.)
- [124] P. Ponte Castañeda and E. Galipeau. Homogenization-based constitutive models for magnetorheological elastomers at finite strain. Journal of the Mechanics and Physics of Solids, 59:194–215, 2011. (Cited on pages 16, 25, and 65.)
- [125] T. Pössinger. Experimental Characterization, Modeling and Simulation of Magneto-Rheological Elastomers. PhD thesis, Ecole Polytechnique (Paris), 2015. (Cited on pages 14, 21, and 64.)
- [126] T. Pössinger, C. Bolzmacher, L. Bodelot, and N. Triantafyllidis. Influence of interfacial adhesion on the mechanical response of magneto-rheological elastomers at high strain. Microsystem technologies, 20:803–814, 2014. (Cited on page 35.)

- [127] E. Psarra, L. Bodelot, and K. Danas. Two-field surface pattern control via marginally stable magnetorheological elastomers. Soft Matter, 13(37):6576 – 6584, 2017. (Cited on pages 14 and 15.)
- [128] J. Rabinow. The magnetic fluid clutch. Transactions of the American Institute of Electrical Engineers, 67(2):1308–1315, 1948. (Cited on page 24.)
- [129] Y.L. Raikher, O.V. Stolbov, and G.V. Stepanov. Deformation of a circular ferroelastic membrane in a uniform magnetic field. Technical Physics, 53(9):1169–1176, 2008. (Cited on pages 12 and 16.)
- [130] Z. Rigbi and L. Jilken. The response of an elastomer filled with soft ferrite to mechanical and magnetic influences. Journal of Magnetism and Magnetic Materials, 37:267–276, 1983. (Cited on page 24.)
- [131] A.J.C.B. Saint-Venant. Mémoire sur la torsion des prismes. Mémoires Divers Savants, 14:233–560, 1855. (Cited on page 31.)
- [132] P. Saxena, M. Hossain, and P. Steinmann. A theory of finite deformation magneto-viscoelasticity. International Journal of Solids and Structures, 50:3886–3897, 2013. (Cited on pages 16 and 25.)
- [133] N. Scheerbaum, D. Hinz, O. Gutfleisch, K.H. Müller, and L. Schultz. Textured polymer bonded composites with Ni-Mn-Ga magnetic shape memory particles. Acta Materialia, 55:2707–2713, 2007. (Cited on page 12.)
- [134] G. Schubert. Manufacture, characterisation and modelling of magneto-rheological elastomers. PhD thesis, University of Glasgow, 2014. (Cited on pages 11, 12, 20, 21, 27, and 35.)
- [135] G. Schubert and P. Harrison. Large-strain behaviour of magneto-rheological elastomers tested under uniaxial compression and tension, and pure shear deformations. Polymer Testing, 42:122–134, 2015. (Cited on pages 25 and 30.)
- [136] G. Schubert and P. Harrison. Equi-biaxial tension tests on magneto-rheological elastomers. Smart Materials and Structures, 25(015015), 2016. (Cited on page 25.)
- [137] G. Schubert, P. Harrison, and Z. Guo. The behaviour of magneto-rheological elastomers under equi-biaxial tension. In 19th International Conference on Composite Materials, 2013. (Cited on page 20.)
- [138] Y. Shen, M.F. Golnaraghi, and G.R. Heppler. Experimental research and modeling of magnetorheological elastomers. Journal of Intelligent Material Systems and Structures, 15:27–35, 2004. (Cited on pages 18 and 25.)
- [139] T. Shiga, A. Okada, and T. Kurauchi. Magnetoviscoelastic behavior of composite gels. Journal of Applied Polymer Science, 58(4):787–792, 1995. (Cited on page 12.)

- [140] G.V. Stepanov, S.S. Abramchuk, D.A. Grishin, L.V. Nikitin, E.Y. Kramarenko, and A.R. Khokhlov. Effect of a homogeneous magnetic field on the viscoelastic behavior of magnetic elastomers. Polymer, 48:488–495, 2007. (Cited on page 29.)
- [141] G.V. Stepanov, E.Y. Kramarenko, and D.A. Semerenko. Magnetodeformational effect of the magnetoactive elastomer and its possible applications. Journal of Physics: Conference Series, 412(012031):1–4, 2013. (Cited on pages 10, 14, and 17.)
- [142] O.V. Stolbov, Y.L. Raikher, and M. Balasoiu. Modelling of magnetodipolar striction in soft magnetic elastomers. Soft Matter, 7:8484–8487, 2011. (Cited on page 28.)
- [143] M. Tejedor, H. Rubio, L. Elbaile, and R. Iglesias. External fields created by uniformly magnetized ellipsoids and spheroids. IEEE Transactions on Magnetics, 31(1):830 – 836, 1995. (Cited on page 67.)
- [144] F. Thorsteinsson, I. Gudmundsson, and C. Lecomte. US 0060349 A1. Prosthetic and orthotic devices having magnetorheological elastomer spring with controllable stiffness, 2013. (Cited on pages 10, 13, 17, and 25.)
- [145] H.F. Tiersten. Coupled magnetomechanical equations for magnetically saturated insulators. Journal of Mathematical Physics, 5:1298–1318, 1964. (Cited on page 65.)
- [146] H.F. Tiersten. Variational principle for saturated magnetoelastic insulators. Journal of Mathematical Physics, 6(5):779–787, 1965. (Cited on page 65.)
- [147] C. Truesdell and R. Toupin. The Classical Field Theories. Flügge, S.(Ed.),Handbuch der Physik, Springer, Berlin, 1960. (Cited on page 65.)
- [148] Z. Varga, G. Filipcsei, and M. Zrinyi. Smart composites with controlled anisotropy. Polymer, 46:7779–7787, 2005. (Cited on pages 20 and 30.)
- [149] Z. Varga, G. Filipcsei, and M. Zrinyi. Magnetic field sensitive functional elastomers with tunable elastic modulus. Polymer, 47:227–233, 2006. (Cited on page 20.)
- [150] F. Vidal-Verdu and M. Hafez. Graphical tactile displays for visually-impaired people. IEEE Transactions on Neural Systems and Rehabilitation Engineering, 15(1):119–130, 2007. (Cited on page 13.)
- [151] B. Wei, X.L. Gong, and W.Q. Jiang. Influence of polyurethane properties on mechanical performances of magnetorheological elastomers. Journal of Applied Polymer Science, 116:771–778, 2010. (Cited on page 11.)
- [152] F-L. Xin, X-X. Bai, and L-J Qian. Modeling and experimental verification of frequency-, amplitude-, and magneto-dependent viscoelasticity of magnetorheological elastomers. Smart Materials and Structures, 25(10):105002, 2016. (Cited on page 64.)
- [153] H.M. Yin, L.Z. Sun, and J.S. Chen. Magneto-elastic modeling of composites containing chain-structured magnetostrictive particles. Journal of the Mechanics and Physics of Solids, 54:975–1003, 2006. (Cited on pages 16, 25, and 65.)

-
- [154] G. Zhou and Z. Jiang. Deformation in magnetorheological elastomer and elastomer-ferromagnet composite driven by a magnetic field. Smart Materials and Structures, 13(2):309, 2004. (Cited on page [29](#).)
- [155] M. Zrinyi, L. Barsi, and A. Büki. Deformation of ferrogels induced by nonuniform magnetic fields. J. Chem. Physics, 104(21):8750–8756, 1996. (Cited on pages [13](#), [16](#), and [29](#).)
- [156] M. Zrinyi, L. Barsi, and A. Büki. Ferrogel: a new magneto-controlled elastic medium. Polymer Gels and Networks, 5:415–427, 1997. (Cited on page [12](#).)
- [157] A.Y. Zubarev. On the theory of the magnetic deformation of ferrogels. Soft Matter, 8:3174–3179, 2012. (Cited on pages [12](#) and [16](#).)
- [158] G. Zurlo, M. Destrade, D. DeTommasi, and G. Puglisi. Catastrophic thinning of dielectric elastomers. PHYSICAL REVIEW LETTERS, 118:078001, 2017. (Cited on page [121](#).)

Titre : Modélisation et identification de la loi de comportement des élastomères Magnéto-Rhéologiques.

Mots clés : Caractérisation Expérimentale, Modélisation Théorique, Simulations Numériques, Identification de paramètres matériaux.

Résumé : Ce travail de thèse porte sur une catégorie de matériaux actifs dénommés Elastomères Magnéto-Rhéologiques (EMR). Ces derniers sont composés de particules micrométriques et magnétisables imprégnées dans une matrice élastomère isolante. Il est possible de modifier les propriétés mécaniques de tels matériaux en les soumettant à un champ magnétique externe. Avec pour objectif d'aboutir à une caractérisation couplée (magnéto-mécanique) du comportement des EMRs en grandes déformations et en présence de champs magnétiques élevés, ce travail propose une approche à la fois expérimentale, théorique et numérique.

La première partie de ce travail s'intéresse à des aspects expérimentaux où l'influence de la microstructure (isotrope et transverse isotrope) et l'influence de la fraction volumique de particules sont étudiées. Un échantillon dédié est développé afin d'obtenir simultanément des champs mécaniques et magnétiques les plus homogènes possibles dans celui-ci lors d'une caractérisation couplée. La question de l'adhésion interfaciale entre les particules de fer doux et la matrice en silicone est également traitée et il est montré qu'un traitement chimique des particules est nécessaire afin d'éviter toute décohésion avec la matrice lorsque le matériau est soumis à un champ magnétique externe. Avant d'analyser les données obtenues, le dispositif expérimental permettant d'obtenir de manière simultanée une mesure du champ de déformation en trois dimensions et une mesure des champs magnétiques internes, est décrit. Malgré l'ensemble des difficultés expérimentales en grande partie dues à des phénomènes d'instabilité qui sont omniprésents chez les EMRs, de nombreuses données sont collectées et serviront à la calibration des lois de comportement.

La seconde partie de cette thèse couvre la modélisation couplée magnéto-mécanique des EMRs en s'appuyant sur le cadre théorique général des solides magnéto-élastiques proposé par Kankanala, Triantafyllidis et Danas (2004, 2012, 2014). En parti-

culier, la méthode énergétique (qui s'appuie sur l'utilisation d'une fonction d'énergie libre) est préférée et des formulations variationnelles équivalentes (qui diffèrent entre elles simplement par le choix de la variable magnétique indépendante utilisée pour décrire le problème : B , H ou M) sont proposées et implémentées dans des codes numériques 3D s'appuyant sur la méthode des éléments finis. Ces outils numériques sont combinés à la méthode de minimisation des moindres carrés afin d'obtenir l'ensemble des paramètres matériaux du modèle de comportement des EMRs. L'utilisation de simulations numériques est nécessaire car une approche purement analytique ne permettrait pas de modéliser " l'effet de forme " observé expérimentalement. En effet, il est primordial de modéliser ce dernier car dans le cas contraire les paramètres identifiés dépendraient de la forme de l'échantillon expérimental et ne décriraient pas uniquement le matériau.

La troisième partie de cette étude décrit en détail l'implémentation numérique des différentes formulations variationnelles proposées précédemment. Dans chacun des cas, il est prouvé que l'utilisation d'éléments isoparamétriques est bien adaptée. De nombreuses difficultés numériques ont été observées dans le cas des formulations variationnelles utilisant le champ de déplacement et le potentiel vecteur magnétique comme variables indépendantes. L'ensemble de ces difficultés (comme par exemple la minimisation de l'énergie potentielle sous la contrainte imposée par la jauge de Coulomb) est surmonté dans ce travail. Avant de décrire les différents problèmes tests utilisés pour s'assurer de la validité et de la précision des codes numériques, les différentes étapes nécessaires à la simulation d'un problème aux limites sont expliquées. Plus précisément, les questions liées aux spécificités des conditions aux limites à appliquer sur le potentiel vecteur magnétique ou encore aux conditions de symétries, sont traitées.

Title : Modeling and Identification of the constitutive behaviour of Magnetorheological Elastomers.

Keywords : Experimental Characterization, Constitutive Modeling, Numerical Simulations, Parameter Identification.

Abstract : In this thesis, we study a class of 'active materials' called Magnetorheological elastomers (MRE) which are ferromagnetic impregnated rubbers whose mechanical properties are altered by the application of external magnetic fields. With the purpose of characterizing the behavior of MREs up to large strains and high magnetic fields, this work brings a completely novel experimental, theoretical and numerical approach.

The first part of this study focuses on an experimental investigation of MRE where multiple microstructures (isotropic and transversely isotropic materials) and multiple particles' volume fraction are tested. A special sample geometry is designed in order to increase the uniformity of internal magnetic and mechanical fields measured during coupled-field experiments. The interfacial adhesion between the iron fillers and the silicone matrix is investigated and we show that when specimens are subjected to external magnetic fields, a silane primer treatment of the particles is needed to prevent debonding at the interface particle/matrix. Then, we present the magneto-mechanical testing setup that allows simultaneous 3D mechanical and magnetic measurements before discussing the results. Even if it is found that instabilities are ubiquitous in MREs, lots of useful data are collected and will be used to compute the parameters proposed in the material model.

The second part of the thesis is dedicated to the modeling of isotropic MREs. The continuum description proposed by Kankanala, Triantafyllidis and Danas (2004, 2012, 2014) to derive constitutive laws that account for finite strains is used and, in particular, the energetic approach (that requires an energy density function) is

chosen. Multiple equivalent variational formulation alternatives (based on different choices of the independent magnetic variable used in the energy function: B , H or M) are given and implemented into 3D finite element (FEM) codes. Based on the use of FEM simulation in combination with least square optimization methods, the previously collected experimental data are fitted and all three energy functions ψ_B , ψ_H and ψ_M are computed. The obtained material model proves to have excellent predictive capabilities when compared to other experiments not used in the fitting process. The use of numerical tools is necessary to make sure that the calculated material parameters are not influenced by the shape of experimental specimens.

The last part of this work details the numerical implementation of the different variational formulations. For each one of them, it is found that isoparametric elements are well suited to simulate coupled magneto-mechanical boundary value problems. We show that special care is needed when implementing variational formulations using the displacement vector and the magnetic vector potential as independent variables. Indeed, ensuring the uniqueness of the vector potential requires to numerically enforce the Coulomb gauge, which leads to numerical complications that are addressed in this thesis. Before describing the different patch tests that have been considered to validate the numerical codes, we show which are the valid boundary conditions for the magnetic vector potential and how to use the symmetry properties of a given boundary value problem to reduce its complexity and the computational resources needed to solve it.

